**Doctoral Thesis**

# Continuous microgravity monitoring of the Þeistareykir geothermal field (North Iceland)

**by**

**Florian Forster**

**Cumulative dissertation**

to obtain the academic degree

“Doctor rerum naturalium” (Dr. rer. nat.)

in the scientific discipline Geophysics

Submitted to the

Faculty of Mathematics and Natural Sciences

Institute for Geosciences

at the University of Potsdam, Germany

**Potsdam, 23.11.2021**

Principal supervisor: Prof. Andreas Güntner
Second supervisor: Dr. Philippe Jousset

Reviewers: Prof. Andreas Güntner
Dr. Jacques Hinderer
Prof. Michel Diament

Published online on the
Publication Server of the University of Potsdam:
https://doi.org/10.25932/publishup-54851
https://nbn-resolving.org/urn:nbn:de:kobv:517-opus4-548517

# Statement of originality

I declare that the work presented in this thesis is, to the best of my knowledge and belief, original and my own work. Any use of the works of any other author is properly acknowledged.

Date Signature

# Abstract

In my doctoral thesis, I examine continuous gravity measurements for monitoring of the geothermal site at Þeistareykir in North Iceland. With the help of high-precision superconducting gravity meters (iGravs), I investigate underground mass changes that are caused by operation of the geothermal power plant (i.e. by extraction of hot water and reinjection of cold water). The overall goal of this research project is to make a statement about the sustainable use of the geothermal reservoir, from which also the Icelandic energy supplier and power plant operator Landsvirkjun should benefit.

As a first step, for investigating the performance and measurement stability of the gravity meters, in summer 2017, I performed comparative measurements at the gravimetric observatory J9 in Strasbourg. From the three-month gravity time series, I examined calibration, noise and drift behaviour of the iGravs in comparison to stable long-term time series of the observatory superconducting gravity meters. After preparatory work in Iceland (setup of gravity stations, additional measuring equipment and infrastructure, discussions with Landsvirkjun and meetings with the Icelandic partner institute ISOR), gravity monitoring at Þeistareykir was started in December 2017. With the help of the iGrav records of the initial 18 months after start of measurements, I carried out the same investigations (on calibration, noise and drift behaviour) as in J9 to understand how the transport of the superconducting gravity meters to Iceland may influence instrumental parameters.

In the further course of this work, I focus on modelling and reduction of local gravity contributions at Þeistareykir. These comprise additional mass changes due to rain, snowfall and vertical surface displacements that superimpose onto the geothermal signal of the gravity measurements. For this purpose, I used data sets from additional monitoring sensors that are installed at each gravity station and adapted scripts for hydro-gravitational modelling.

The third part of my thesis targets geothermal signals in the gravity measurements. Together with my PhD colleague Nolwenn Portier from France, I carried out additional gravity measurements with a Scintrex CG5 gravity meter at 26 measuring points within the geothermal field in the summers of 2017, 2018 and 2019. These annual time-lapse gravity measurements are intended to increase the spatial

coverage of gravity data from the three continuous monitoring stations to the entire geothermal field. The combination of CG5 and iGrav observations, as well as annual reference measurements with an FG5 absolute gravity meter represent the hybrid gravimetric monitoring method for Þeistareykir. Comparison of the gravimetric data to local borehole measurements (of groundwater levels, geothermal extraction and injection rates) is used to relate the observed gravity changes to the actually extracted (and reinjected) geothermal fluids. An approach to explain the observed gravity signals by means of forward modelling of the geothermal production rate is presented at the end of the third (hybrid gravimetric) study. Further modelling with the help of the processed gravity data is planned by Landsvirkjun. In addition, the experience from time-lapse and continuous gravity monitoring will be used for future gravity measurements at the Krafla geothermal field 22 km south-east of Þeistareykir.

# Zusammenfassung

In meiner Doktorarbeit beschäftige ich mich mit kontinuierlichen Schweremessungen zum Monitoring des geothermisch genutzten Standorts Þeistareykir in Nordisland. Unter Verwendung von hochpräzisen Supraleitgravimetern (iGravs) untersuche ich unterirdische Massenveränderungen, die durch den Betrieb des isländischen Erdwärmekraftwerks (d.h. durch die Entnahme von Heißwasser und Rückinjektion von Kaltwasser) hervorgerufen werden. Als übergeordnetes Ziel des Forschungsprojektes soll eine Aussage zur nachhaltigen Nutzung des geothermischen Reservoirs gemacht werden, von der auch der isländische Energieversorger und Kraftwerksbetreiber Landsvirkjun profitieren soll.

Als ersten Schritt, zur Untersuchung der Leistungsfähigkeit und Messstabilität der Gravimeter, begleitete ich im Sommer 2017 Vergleichsmessungen in dem gravimetrischen Observatorium J9 in Straßburg. Aus den dreimonatigen Messzeitreihen untersuchte ich Kalibration, Rausch- und Driftverhalten der iGravs im Vergleich zu den betriebssicher laufenden Observatoriums-Supraleitgravimetern. Nach vorbereitender Arbeit in Island (Aufbau der Gravimeter-Stationen und zusätzlicher Messeinrichtung, Einrichtung der Infrastruktur, Gespräche mit Landsvirkjun und Treffen mit isländischen Partnerinstitut ISOR) startete ich mit meinen Kollegen im Dezember 2017 das Gravimeter-Monitoring in Þeistareykir. Anhand der iGrav-Aufzeichnungen der ersten 18 Monaten nach Messbeginn führte ich die gleichen Untersuchungen (zu Kalibration, Rausch- und Driftverhalten) wie in J9 durch, um zu verstehen inwieweit der Transport der Supraleitgravimeter nach Island die Geräteeigenschaften beeinflusst hat.

Im weiteren Verlauf der vorliegenden Arbeit beschäftige ich mich verstärkt mit der Modellierung und Korrektur von oberflächennahen Schwereeffekten in Þeistareykir. Dies umfasst zusätzliche Massenbewegungen durch Regen, Schneefall oder vulkanisch-tektonische Bodenbewegungen, die das geothermische Signal in den Gravimeter-Messungen überlagern. Als Hilfsmittel verwende ich die Datensätze der zusätzlich an jeder Gravimeter-Station eingerichteten Messsensorik und von mir angepasste Modellierungsskripte meiner Gravimetrie-Kollegen.

Als dritten Punkt meiner Dissertation untersuche ich die geothermischen Signale in den Gravimeter-Messungen. Gemeinsam mit meiner PhD-Kollegin Nolwenn Portier

aus Frankreich führte ich in den Sommern 2017, 2018 und 2019 zusätzliche Schweremessungen mit einem Scintrex CG5 Gravimeter an 26 im Geothermie-Feld verteilten Messpunkten durch. Diese jährlich begrenzten Schweredaten dienen der Verbesserung der räumlichen Auflösung unserer kontinuierlichen iGrav-Messungen. Die kombinierten Ergebnisse beider Messmethoden (der CG5 und iGrav Gravimeter), sowie jährlich im Messgebiet durchgeführter Referenz-Messungen mit einem FG5 Absolut-Gravimeter, komplettieren das hybridgravimetrische Monitoring am Messstandort Þeistareykir. Die abschließende Gegenüberstellung der gravimetrischen Daten mit lokalen Bohrlochmessungen (von Grundwasserpegeln, geothermischen Extraktions- und Injektions-Raten) des Kraftwerksbetreibers, ermöglicht einen direkten Vergleich der beobachteten Schwereveränderungen mit den tatsächlich geförderten geothermischen Fluiden. Ein Ansatz zur Erklärung des beobachteten Schweresignals mittels Vorwärtsmodellierung der geförderten geothermischen Förderrate wird im Abschluss der dritten (hybridgravimetrischen) Studie vorgestellt. Weitere Modellierungen unter Verwendung der aufbereiteten gravimetrischen Messdaten sind durch den Kraftwerksbetreibers von Þeistareykir geplant. Außerdem sollen die gesammelten Erfahrungen des gravimetrischen Messnetzes und Monitorings in Þeistareykir zur Durchführung weiterer gravimetrischer Messungen an dem 22 km südöstlich gelegenem Geothermiefeld Krafla genutzt werden.

# Statement of contribution

This cumulative thesis consists of three manuscripts, which are listed in the following.

**Schäfer, F.**, Jousset, P., Güntner, A., Erbas, K., Hinderer, J., Rosat, S., Voigt, C., Schöne, T., & Warburton, R.J. (2020). Performance of three iGrav superconducting gravity meters before and after transport to remote monitoring sites. *Geophysical Journal International*, 223(2), 959-972, https://doi.org/10.1093/gji/ggaa359.

**Forster, F. (né Schäfer)**, Güntner, A., Jousset, P., Reich, M., Männel, B., Hinderer, J., & Erbas, K. (2021). Environmental and anthropogenic gravity contributions at the Þeistareykir geothermal field, North Iceland. *Geothermal Energy*, 9(1), 1-28, https://doi.org/10.1186/s40517-021-00208-w.

Portier, N., **Forster, F. (né Schäfer)**, Hinderer, J., Erbas, K., Jousset, P., Drouin, V., Li, S., Sigmundsson, F., Magnússon, I., Hersir, G.P., Ágústsson, K., Guðmundsson, Á., Júlíusson, E., Hjartasson, H., & Bernard, J.-D. (2021). Hybrid microgravity monitoring of the Theistareykir geothermal reservoir (North Iceland). *Pure and Applied Geophysics*. (Accepted for publication).

**Contributions:** For the three studies listed above, the PhD candidate prepared and participated in the measuring campaigns in France and Iceland; for the first two studies he obtained and analysed the results, prepared all figures, and wrote the manuscripts. For the third (co-author) study he contributed chapter 5.5 (Continuous microgravity monitoring), discussed the results, revised and improved the manuscript. An additional publication during the author's PhD studies is not integrated into the thesis but is listed here for the readers' interest.

Hinderer, J., Warburton, R., Rosat, S., Riccardi, U., Boy, J.-P., **Forster, F. (né Schäfer)**, Jousset, P., Güntner, A., Erbas, E., Little, F., Bernard, J.-D. (2021). Intercomparing superconducting gravimeters records in a dense meter-scale network at the J9 gravimetric observatory of Strasbourg, France. *Pure and Applied Geophysics*. (Accepted for publication).

# Declaration

I, Florian Forster, declare that the thesis titled “Continuous microgravity monitoring of the Þeistareykir geothermal field (North Iceland)” is my own work. The present study, including field work, data analyses, and interpretations, was done by myself jointly with support from others at the GFZ German Research Centre for Geosciences, Potsdam, Germany and colleagues from the Institut Terre et Environnement de Strasbourg, Université de Strasbourg, France.

The collaborative researchers are listed as co-authors in each manuscript separately. Additional work, e.g., field work or provision of data, done by others, is indicated and acknowledged in the corresponding manuscripts.

Installation and measuring start-up of the iGrav superconducting gravity meters at J9 (France) and Þeistareykir (Iceland) were realised with assistance of the technicians Frederic Little (ITES, Université de Strasbourg, France), Tanja Ballerstedt and Stephan Schröder from GFZ, and support (on-site and remote) from the manufacturers Richard Reineman and Richard Warburton (GWR Instruments, Inc., USA). Our GFZ colleagues Tilo Schöne, Nico Stolarczuk, Julia Illigner and Cornelia Zech installed the remotely operated multiparameter stations (ROMPS). Jean-Daniel Bernard (ITES, Université de Strasbourg, France) performed the absolute gravity measurements (FG5#206). Nolwenn Portier (ITES, Université de Strasbourg, France) and I performed the time-lapse gravity measurements (Scintrex CG5) at Þeistareykir.

Date Signature

# Acknowledgements

In the past 5 years, I had the opportunity to contribute to the geothermal research of the GFZ German Research Centre for Geosciences in Potsdam. I experienced a most positive cross-border collaboration between science and industry aiming for sustainable and environmental-friendly energy production, which I believe is one of the cruxes for future life on our planet. Therefore, I want to thank all the people who have supported and accompanied me on this journey:

First and foremost, my supervisors and mentors Andreas Güntner, Philippe Jousset and Kemâl Erbaş for their friendly guidance and encouragement throughout the study.

Second, my colleagues Nolwenn Portier and Jacques Hinderer from the University of Strasbourg who joined us and contributed greatly in our work in France and Iceland.

Anette Kærgaard Mortensen and her colleagues from the National Power Company of Iceland (Landsvirkjun), for their friendly collaboration, supportive provision of borehole monitoring data and for providing the necessary facilities and infrastructures at the Þeistareykir and Krafla geothermal fields.

Richard Reinemann and Richard Warburton for the reliable and ongoing technical assistance and vast transfer of knowledge about the superconducting gravity meters.

Ernst Huenges, for his sympathetic ear and providing me with the opportunity to conduct my PhD study at the Geoenergy section. As well as, my friends and colleagues at the GFZ for creating a warm and joyful work environment, excellent company both in office and during fieldwork as well as many fruitful discussions.

Finally, I thank my family, my lovely parents and grandparents for their warm and unconditional support. In particular, I want to tell my beloved wife, Amy Forster, that meeting you is the happiest moment and greatest fortune in my life. I am very excited and looking forward to starting the next chapter together, and meeting the rest of our family from the land down under!

# Table of contents

# List of figures

# List of tables

# List of acronyms and symbols

## Abbreviations

| | |
|---|---|
| AG | Absolute gravity meter |
| AQG | Absolute quantum gravity meter |
| CT | Compact superconducting gravity meter |
| DEM | Digital elevation model |
| FAG | Free-air vertical gravity gradient |
| FES | Finite element solution (ocean tidal model) |
| GNSS | Global navigation satellite system |
| GPS | Global positioning system |
| GPXC | gPhone, central station (later SCGC, s. below) |
| GWL | Groundwater levels |
| HyGra | Hydro-gravitational modelling |
| IERS | International Earth Rotation and References Systems Service |
| IGETS | International Geodynamics and Earth Tide Service |
| iGrav | Superconducting gravity meter with integrated electronics |
| InSAR | Interferometric synthetic aperture radar |
| KMT | Krafla Magma Testbed |
| NLNM | New Low Noise Model |
| NVZ | Northern Volcanic Zone |
| OSG | Observatory superconducting gravity meter |
| PSD | Power spectral density |
| RG | Relative gravity meter |
| ROMPS | Remotely operated multi-parameter station |
| SCGC | Superconducting gravity station, central position |
| SCGE | Superconducting gravity station, eastern position |
| SCGR | Superconducting gravity station, reference position |
| SCGW | Superconducting gravity station, western position |
| SD | Standard deviation |
| SG | Superconducting gravity meter |
| SPA | Snow pack analyser |

| | |
|---|---|
| SWE | Snow water equivalent |
| TCCM | Three-channel correlation method |
| TFZ | Tjörnes Fracture Zone |
| WDD | Wahr-Dehant-Defraigne (tidal model) |

## Symbols

| | | |
|---|---|---|
| $A$ | Amplitude | µGal |
| $B$ | Instrumental constant | $m\ s^{-2}\ A^{-2}$ |
| $d$ | Distance | m |
| $F$ | Force | $kg\ m\ s^{-2}$ |
| $g$ | Gravity | µGal (1 µGal = 10 $nm\ s^{-2}$) |
| $G$ | Gravitational constant | $6.67\ 10^{-11}\ m^3\ kg^{-1}\ s^{-2}$ |
| $h$ | Water level variation | m |
| $I$ | Electric current | A |
| $L$ | Instrumental constant | $m\ s^{-2}\ A^{-2}$ |
| $R^2$ | Regression coefficient | - |
| $SF$ | Scale factor | $nms^{-2}\ V^{-1}$ |
| $t$ | time | s |
| $T_c$ | Critical temperature | K |
| $V$ | Volume | $m^3$ |
| $z$ | Depth | m |
| $\Delta C$ | Scale factor variation | $nms^{-2}\ V^{-1}$ |
| $\Delta g$ | Gravity difference | µGal |
| $\delta g/\delta h$ | Vertical gravity gradient | µGal $m^{-1}$ |
| $\Delta h$ | Vertical surface displacement | m |
| $\Delta V$ | Volume change | $m^3$ |
| $\nu$ | Poisson ratio | - |
| $\pi$ | Pi | ≈ 3.14 |
| $\rho$ | Density | $kg\ m^{-3}$ |
| $\sigma$ | Standard error | µGal |
| $\tau$ | Time constant | - |
| $\varphi$ | Porosity | % |

# Chapter 1

# Introduction

## 1.1 Background

Gravimetry is a non-destructive geophysical method to investigate underground mass distributions. Gravity measurements can help to reveal groundwater aquifers, geological strata and deposits, or other specific subterranean structures. The first relative gravity meters, based on the spring balance principle were introduced in 1930 and achieved measuring uncertainties between 0.2 and 0.5 mGal (1 mGal = $10^{-5}$ m $s^{-2}$) (Krynski, 2012). After several technical improvements, the LaCoste & Romberg gravity meter (Weber and Larson, 1966) was one of the most commonly used instruments. With measuring uncertainties between 0.01 and 0.05 mGal (Krynski, 2012) the LaCoste & Romberg gravity meters are still deployed for field experiments in present day (Al-majid and Mutib, 2018; Berrino, 2020; Fukuda et al., 2021). At the end of the 1980s, the new Scintrex automated relative gravity meter was invented and received increasing attention due to several innovations (fused quartz sensor with automatic electrostatic feedback, automatic conversion of raw signal and correction for tilts and Earth tides), which enabled superior data repeatability and user-friendly application in rough field terrain (Hugill, 1988). The new instrument design allowed for further reduction of the measuring uncertainty to 5 µGal for measurements with the Scintrex CG3 and CG5 types (Jousset et al., 1995; Sugihara, 2004). These instruments are well suited for creating gravity-depth profiles of subsurface geological formations, or for time-lapse gravimetry, i.e. repeated gravity observations at one or serval points within a network (Jousset, 1996). However, high temporal resolution of the gravity signal can only be obtained by continuous monitoring with a permanently installed gravity meter.

The monitoring of subsurface mass changes is of significant importance to understand the relation between observations at the Earth's surface (like water outflow or ground subsidence) and processes in subterranean geosystems. Apart from geoelectric and magnetic measurements, gravimetric monitoring is the only non-destructive method that can tell about underground mass distribution changes over time. The most stable, long-term gravity time series are obtained from permanently installed instruments at gravimetric observatories. This helps to quantify global gravity contributions from large-scale hydrology (Wziontek et al., 2009) and atmospheric pressure changes (Boy and Hinderer, 2006; Klügel and Wziontek, 2009), or calculate and improve tidal models (Melchior, 1974; Ducarme et al., 2004; Agnew, 2015). The main semidiurnal lunar waves M2 can already be accurately determined after a three month record. Whereas for a complete tidal analysis, including the long periodic wave group SA, up to 18.6 years of gravity records from observatory instruments are needed (Wenzel, 1997). For example, the superconducting gravity meter (SG) C-026, currently operating at the gravimetric observatory J9 in Strasbourg, is recording continuously since 1996 (Rosat et al., 2015).

For monitoring specific local geophysical phenomena, field measurements are performed with smaller more user-friendly instruments, like spring gravity meters (Parseliunas et al., 2011; Schilling and Gitlein, 2015), the iGrav SG (Warburton et al., 2010) or the newly developed absolute quantum gravity meter (Ménoret et al., 2018). A wide variety of gravimetric field studies examine near-surface hydrological mass changes (Creutzfeldt et al., 2010; Kennedy et al., 2014; Reich et al., 2019; Watlet et al., 2020). Other gravity observations are performed on volcanoes to understand magma-induced or hydrothermal mass changes (Jousset and Okada, 1999; Jousset et al., 2000; Carbone et al, 2017, 2019). For the monitoring of geothermal fields, most studies to date are restricted to time-lapse measurements with spring and/or absolute gravity meters (Sugihara and Ishido, 2008; Oka et al., 2012; Portier et al., 2018). To the authors knowledge, there exist only trial runs of continuous gravimetry for geothermal reservoir monitoring (Sugihara et al., 2011).

The gravimetric monitoring method is suited to complement traditional geothermal monitoring techniques like geochemical, magnetotelluric or seismic measurements

(Gudmundsson and Arnórsson, 2002; Peacock et al., 2012; Taira et al., 2018; Toledo et al., 2020). On the other hand, important supplementary data may be received for interpretation of the gravity time series from other geophysical observations. Interferometric synthetic aperture radar (InSAR) provide additional information about surface deformation (e.g. subsidence due to fluid extraction) of the geothermal field (Carnec and Fabriol, 1999), which can be applied for gravity reduction of vertical displacement in addition to local geodetic (levelling, GPS, GNSS) observations. Local groundwater level monitoring (Bromley, 2009) can help to quantify the observed gravity changes in terms of hydrological mass changes of the geothermal system. Finally, well logs about flow rates and temperatures of the geothermal fluids (Bixley et al., 2009) can be used to directly relate the gravity observations to mass extraction, injection and recharge of the reservoir.

For the application of gravimetry as a method for geothermal monitoring, the following general research questions are considered in this thesis:

1) What is the benefit of gravimetry compared to other observation techniques?
2) Which supplementary methods are useful / needed for the interpretation of gravimetric monitoring?
3) Which gravity meter types are suited for geothermal monitoring and which instruments can be used for complementary measurements?
4) What can be done to ensure reliability of comparative measurements between different gravity meter types?
5) What is the best arrangement of the gravity stations within (and outside) the geothermal field?
6) Is it possible to observe and quantify gravity changes, and relate them to mass changes of the geothermal reservoir?
7) Which observations can be used to make a statement about the sustainability of the geothermal field?
8) What are the “lessons learned” from the specific study area that can be transferred to other geothermal sites?

## 1.2 Objectives

As an overall objective of this study, I want to quantify gravity changes in terms of mass movements due to the exploitation of a geothermal field. With this knowledge I want make an estimation about the sustainability of the geothermal reservoir during exploitation by the power plant. The main scientific questions of this thesis are specified as:

1) What are the instrumental characteristics of the iGrav superconducting gravity meters in terms of calibration, noise and drift, and how are they influenced by transport to a new location?
2) What is the share of environmental contributions (from global effects, local hydrology, snow and vertical surface displacement) and how can they be removed from the continuous gravity signals?
3) Which of the observed gravity changes can be attributed to exploitation-induced mass changes of the geothermal reservoir?

In the following chapters, I address the above-defined questions systematically. As a first step, the instrumental performance of the iGrav SGs are quantified, and compared before and after transport to the remote monitoring stations in Iceland. This is of fundamental importance to assure that the instruments provide reliable data, which can be used for any further analyses and interpretations. Ideally, comparative measurements under the same conditions are performed for all gravity meters in a sheltered and stable environment before the start of field investigations. Such ideal conditions are created at specialised measuring sites like geodetic or gravimetric observatories. The observatories may host one or several SGs that provide continuous long-term gravity time series, like the T-012 in Cantley, Canada since 1990, the C-026 in Strasbourg, France since 1996 and the CD-034 in Moxa, Germany since 1999 (Voigt et al., 2016). Up to date there are 35 worldwide distributed SG stations with freely available continuous gravity time series, provided by the International Geodynamics and Earth Tide Service (IGETS; http://isdc.gfz-potsdam.de/igets-data-base/). The permanent observatory SGs provide a reliable reference for calibration, noise and drift analyses of any portable gravity meters. These “best performance” instrumental parameters can then be used as reference

for field studies when the gravity meters are installed at different observations sites and subjected to diverse environmental conditions. As additional reference for the field measurements, comparison to an absolute gravity meter should be performed for estimation of instrumental drift, which may have changed for the relative gravity meters after transport to the remote monitoring stations.

As a second step, for the field observations, all environmental parameters causing mass changes that superimpose onto the target gravity signal need to be quantified and reduced from the gravity time series. Gravity contributions from global effects like polar motion, non-tidal ocean loading, atmospheric and hydrological mass changes can be calculated by elaborate models for many places on Earth (Rodell et al., 2004; Boy and Lyard, 2008; Klügel and Wziontek 2009; Stephenson et al., 2016). Local gravity contributions resulting from vertical surface displacement and mass accumulations after rain or snowfall can be observed by additional sensors and monitoring systems installed at the gravity stations (Schöne et al., 2013). Any additional mass variations from e.g. nearby lake level or groundwater level changes, should be included if data is available from water gauge or monitoring wells (Harnisch and Harnisch, 2006; Creutzfeldt et al., 2010; Reich et al., 2019). Additionally for volcanically active regions, there can be magmatic mass movement, which is difficult to measure directly. These mass changes may be modelled from the reduced gravity signals in combination with surface deformation monitoring from InSAR data and/or levelling (Jousset et al., 2003; Tizzani et al., 2015; Carbone et al., 2017).

As a final step, after all instrumental and environmental contributions are reduced, focus will be on the geothermal target signal within the gravity time series. The residuals of SG observations provide a high temporal resolution of the local mass changes. If the gravity stations are ideally positioned above the geothermal extraction and injection zones, the gravity observations can be related to extracted and reinjected masses in the underground. However, positioning and installation of the SG stations are restricted to local conditions. There needs to be a relatively flat surface, which provides enough space for the food print of the building, and there should be a direct connection between the bedrock and a decoupled gravity meter pillar so that no artificial noise (e.g. wind forcing on the container) is transmitted to

the gravity signal. Additionally for operation of the SGs a continuous power supply has to be connected to the gravity station, which rules out measuring sites in far distance to the electrical grid. This may restrict the measuring site selection to locations that are not directly positioned above the main extraction or injection zones of the geothermal reservoir. To fill these potential measuring gaps and increase the spatial resolution of the continuous observations, it is beneficial to perform additional time-lapse gravity measurements at several positions within the study area. This complementary method of combining continuous, time-lapse and absolute gravity observations is known as hybrid gravimetry (Okubo et al., 2002; Sugihara and Ishido, 2008; Hinderer et al., 2016).

With focus on the continuous gravity observations, the aims of the present study can be summarised as:

1) Comparing gravity measurements under observatory conditions and repeated performance analyses after transport to the Icelandic remote gravity stations.
2) Observation of local environmental parameters (by soil moisture, snow and GNSS measurement) at Þeistareykir, modelling of the contribution within the gravity signal and combined reduction for each of the gravity time series.
3) Combination of continuous (iGrav), time-lapse (CG5) and absolute (FG5) gravity observations, and comparison to groundwater levels, geothermal extraction and reinjection flow rates to estimate the sustainability for operation of the Þeistareykir power plant.

## 1.3 Thesis organisation

This publication-based thesis consists of three peer-reviewed articles published in (or submitted to) scientific journals, with focus on the above-mentioned scientific questions. Chapter 2 introduces the Icelandic study area and the gravimetric methods applied at the Þeistareykir geothermal field. The first two articles (chapter 3 and 4) address the comparative gravity measurements, instrumental setup and reduction of gravity time series in preparation for the geothermal analysis of Þeistareykir, which is approached towards the end of chapter 4. The third article (chapter 5) presents the hybrid gravity method to examine the geothermal gravity

contributions from different perspectives. Chapter 6 provides a summary and discussion of the main results, highlights the overall conclusions of this thesis and recommendations for future work, and gives an outlook with suggestions for future studies. Further details about the three studies are summarised in the following.

**Chapter 3: Performance of three iGrav superconducting gravity meters before and after transport to remote monitoring sites** (Schäfer et al., 2020; published in Geophysical Journal International)

This chapter addresses the first scientific question (What are the instrumental characteristics of the iGrav superconducting gravity meters in terms of calibration, noise and drift, and how are they influenced by transport to a new location?) by examining the instrumental parameters of three iGrav superconducting gravity meters. I describe the comparative measurements at the gravimetric observatory J9 near Strasbourg (France) for determining calibration, noise and drift behaviour of the instruments. Then I show the setup and measurements at the Icelandic remote stations and examine how transport may affect the iGrav instrumental parameters.

**Chapter 4: Environmental and anthropogenic gravity contributions at the Þeistareykir geothermal field, North Iceland** (Forster et al., 2021; excepted for publication in Geothermal Energy)

In this chapter, I focus on the environmental observations at Þeistareykir to answer the second scientific question (What is the share of environmental contributions (from global effects, local hydrology, snow and vertical surface displacement) and how can they be removed from the continuous gravity signals?). Global models and local observations of soil moisture, snow and vertical displacement are presented, from which I calculated the associated gravity contributions for the Icelandic gravity stations and derived a combined gravity reduction for each iGrav time series. Then, in order to approach the third scientific question, I compare and discuss the obtained gravity residuals with regard to the local groundwater levels and the geothermal flow rates of the Þeistareykir power plant.

**Chapter 5: Hybrid microgravity monitoring of the Theistareykir geothermal reservoir (North Iceland)** (Portier et al., 2021; submitted to Pure and Applied Geophysics)

In order to investigate the third scientific question (Which of the observed gravity changes can be attributed to exploitation-induced mass changes of the geothermal reservoir?), this study gives insight into exploration, exploitation and hydrological monitoring at Þeistareykir, conducted by Landsvirkjun the National Energy Company of Iceland. It introduces the hybrid gravity method as combination of continuous, time-lapse and absolute gravity measurements at Þeistareykir. The combined (hybrid) gravity results are presented in comparison with observed groundwater levels and geothermal flow rates. The study closes by an approach of forward modelling of the produced geothermal fluid to explain the residual gravity observations.

# Chapter 2

# Study site and gravimetric methods

## 2.1 Geodynamic and geothermal setting of the study area

Iceland is subject to active volcanism due to its unique geographic position on the tectonic boundary between the North American and Eurasien plates. Interactions between the Icelandic mantle plume and Mid-Atlantic ridge spreading of about 2 cm $yr^{-1}$ led to a formation of about 32 volcanic systems (Sigmundsson et al., 2020). Figure 1 shows the volcanic active zone stretching from the Reykjanes Ridge in the southwest to the Tjörnes Fracture Zone in the northeast. The six major geothermal power plants are located on the Reykjanes peninsula (Svartsengi and Suðurnes), at the Hengill volcano (Nesjavellir and Hellisheiði) and north of Lake Mývatn (Krafla and Þeistareykir) supplying the Icelandic population with 26% of electricity and almost 90% of heat demand (Stober and Bucher, 2020). The study site is located at the newest of the six power plants in Þeistareykir. Exploration studies at the Þeistareykir geothermal field indicated a highly permeable reservoir with fluid temperatures above 280°C (Ármannsson, 2009). After drilling of the first 10 deep wells, the electricity generation capacity has been estimated at 104 MWe for 100 years or 348 MWe for 30 years power plant operation (Óskarsson, 2015). In November 2017, the power plant started operation and produces 90 MWe since April 2018 (Knútsson et al., 2018).

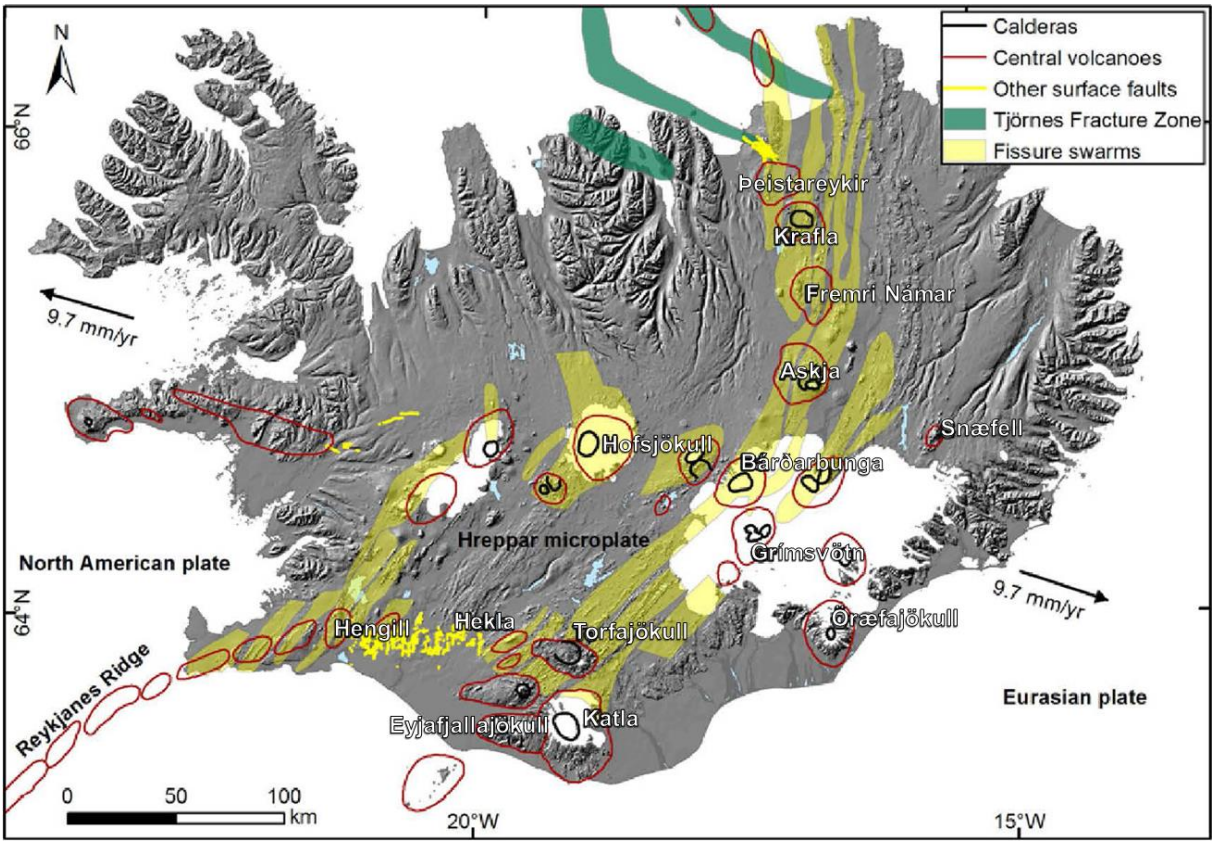


**Figure 1.** Geodynamic map of Iceland with names of the tectonic plates and selected volcanic systems; the study site is located in Þeistareykir in the northeast (modified from Sigmundsson et al., 2020).

## 2.2 Gravimetric monitoring of a geothermal system

### 2.2.1 Fundamental concept

Figure 2 shows a sketch of the basic field setup with two gravity stations (for time-lapse and/or continuous observations) located in the vicinity of the geothermal extraction and reinjection wells. The gravity stations A and B need to be positioned close enough to the wells so that the subsurface feed zones (for extracted or injected fluids) lie within the coverage of the gravity meters (visualised by green triangular shapes). The third gravity station C is located outside the geothermal field. If the local environmental gravity contributions (from e.g. vertical surface displacement, local hydrology, snow, etc.) are roughly the same at all three sites, station C can be used for reference measurements. The reference gravity signal is subtracted directly from

the signals at gravity stations A and B to reduce the additional environmental gravity contributions and identify the purely geothermal related signals.

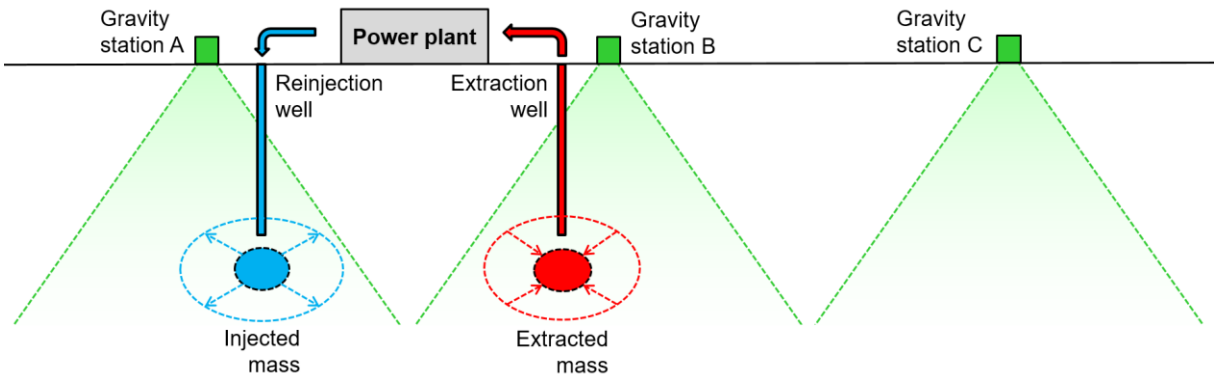


**Figure 2.** Conceptual 2D sketch of gravimetric monitoring during geothermal operation with three gravity stations. The stations A and B are positioned in the vicinity to the geothermal extraction and reinjection wells for observations of the underground mass changes due to extracted and injected geothermal fluids (depicted as decreasing red and increasing blue circles respectively), station C is positioned outside the geothermal field for reference measurements; triangular bright green coloured areas mark the subsurface coverage of the gravity sensors.

### 2.2.2 Setup at the Þeistareykir geothermal field in North Iceland

The location of the study area in North Island and the positions of five gravity monitoring stations are shown in Figure 3. The reference station is located 17 km to the northwest close to the road, which connects Þeistareykir to the coastal town Húsavík. Another gravity station is positioned 22 km southeast of Þeistareykir in the Krafla geothermal field, which was initially intended to be the main study site for gravimetric monitoring. However, the Krafla geothermal system has been exploited for a long period since 1977 (Ármannsson et al., 1987), which suggests that subsurface mass changes have become stationary over time. For the newly commissioned power plant at Þeistareykir larger mass changes are expected, due to the “sudden” extraction of water from (and reinjection into) an undisturbed reservoir. Therefore, this study focuses on the Þeistareykir geothermal field, which is shown in the enlarged section in Figure 4 with three gravity monitoring stations and the time-lapse gravity network. The aerial view of Þeistareykir in Figure 5 shows the positions of the continuous gravity stations (indicated by white arrows) and the geothermal

power plant, which began operation in autumn 2017. Shortly after, in December 2017, the iGrav SGs started continuous monitoring at Þeistareykir. In the initial setup, iGrav015 was deployed at the reference station, iGrav032 at the east station close to the geothermal extraction wells and iGrav006 at the west station next to the reinjection wells. Due to gravity contributions, which could not be explained by drift analysis or from locally observed environmental parameters, in June 2019, iGrav015 was moved from the reference station to Þeistareykir and continued monitoring at the central station within the geothermal field.

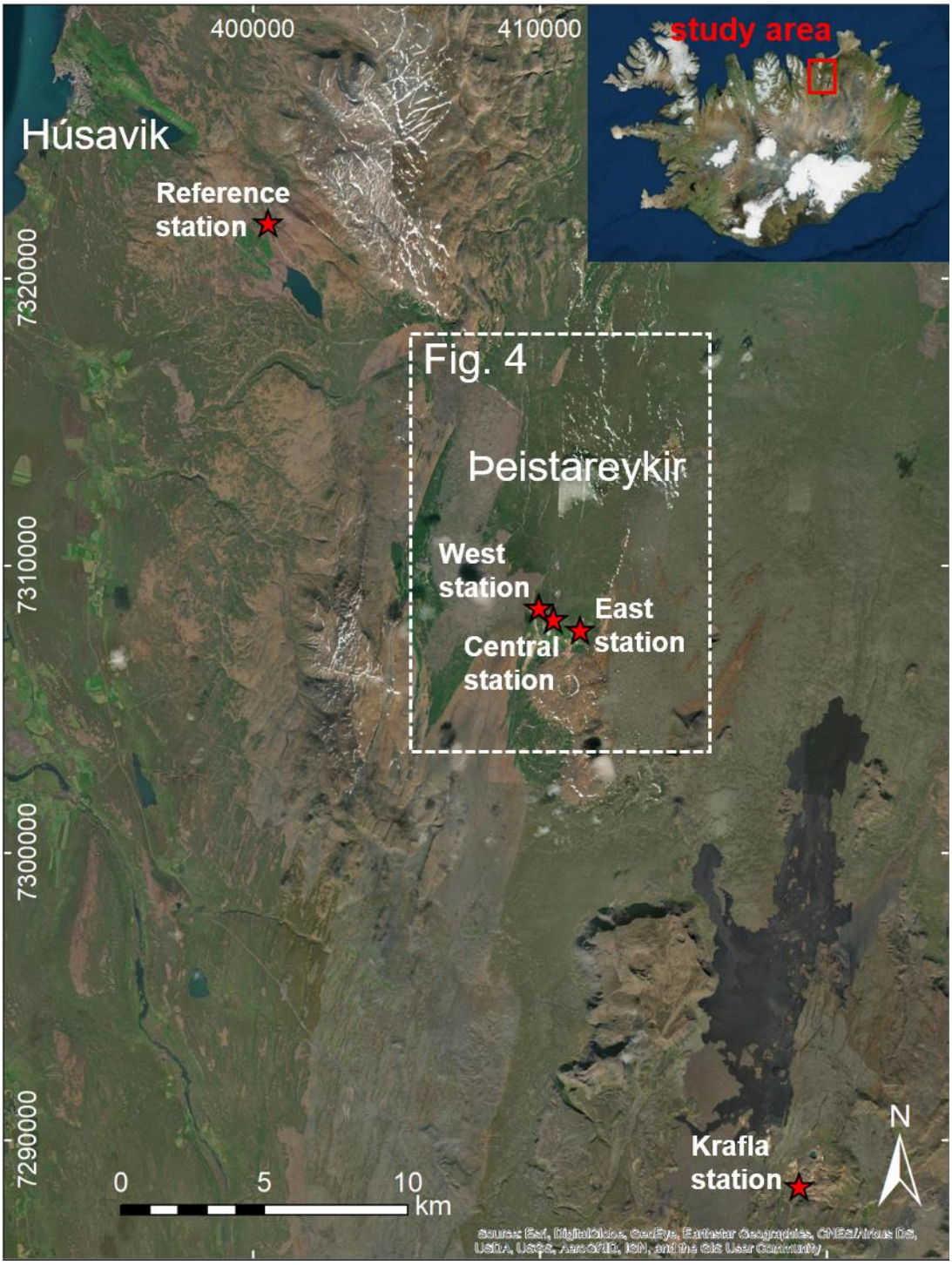


**Figure 3.** Location of the study area in North Iceland with the positions of the five gravity stations marked by red stars, Þeistareykir is located 25 km southeast of the coastal town Húsavík and 22 km northwest of the Krafla geothermal field; enlarged section (white box) shown in Fig. 4.

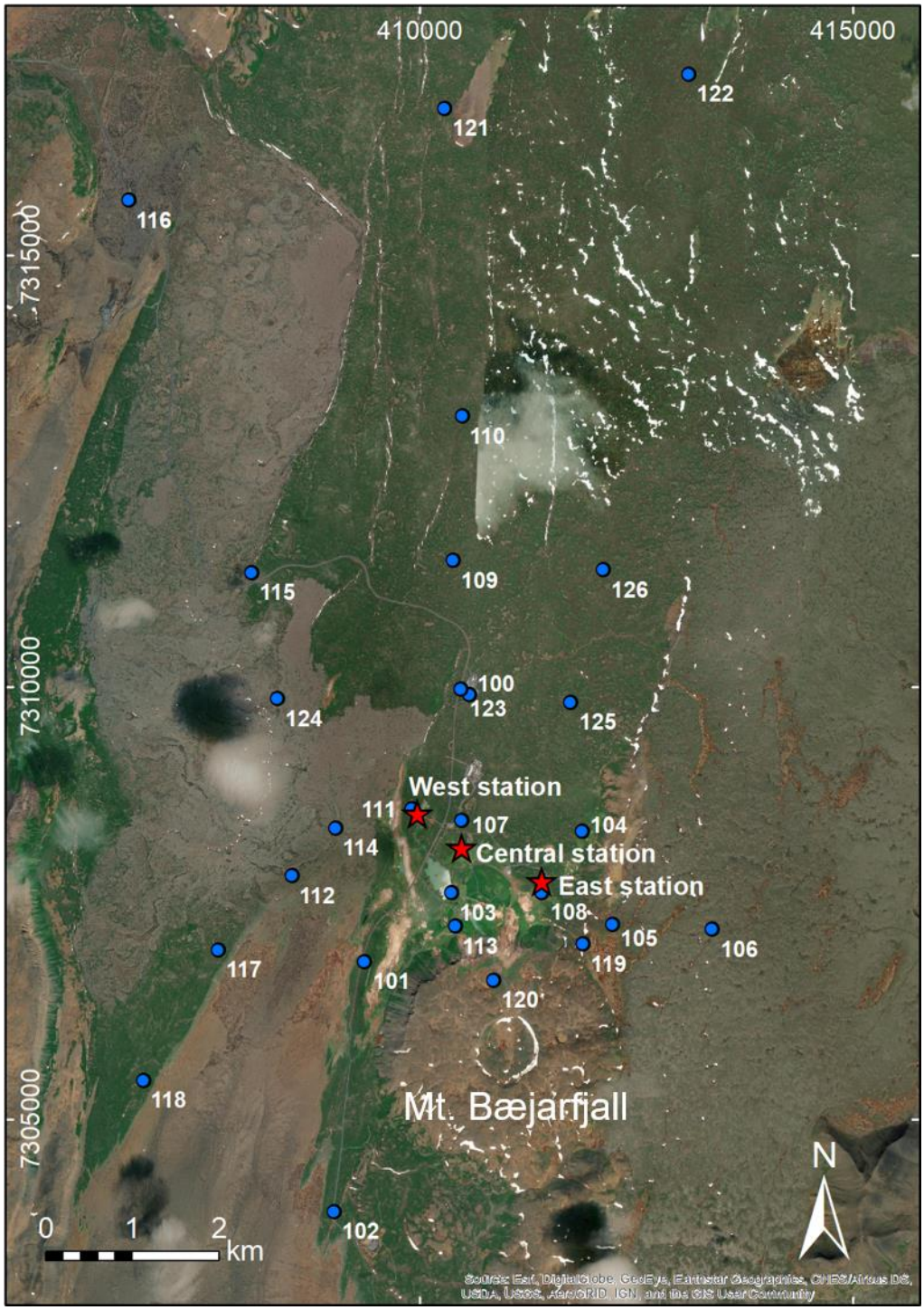


**Figure 4.** Satellite image of Þeistareykir showing the positions of the three continuous gravity stations (red stars) and the 27 stations of the time-lapse gravity network (blue dots).

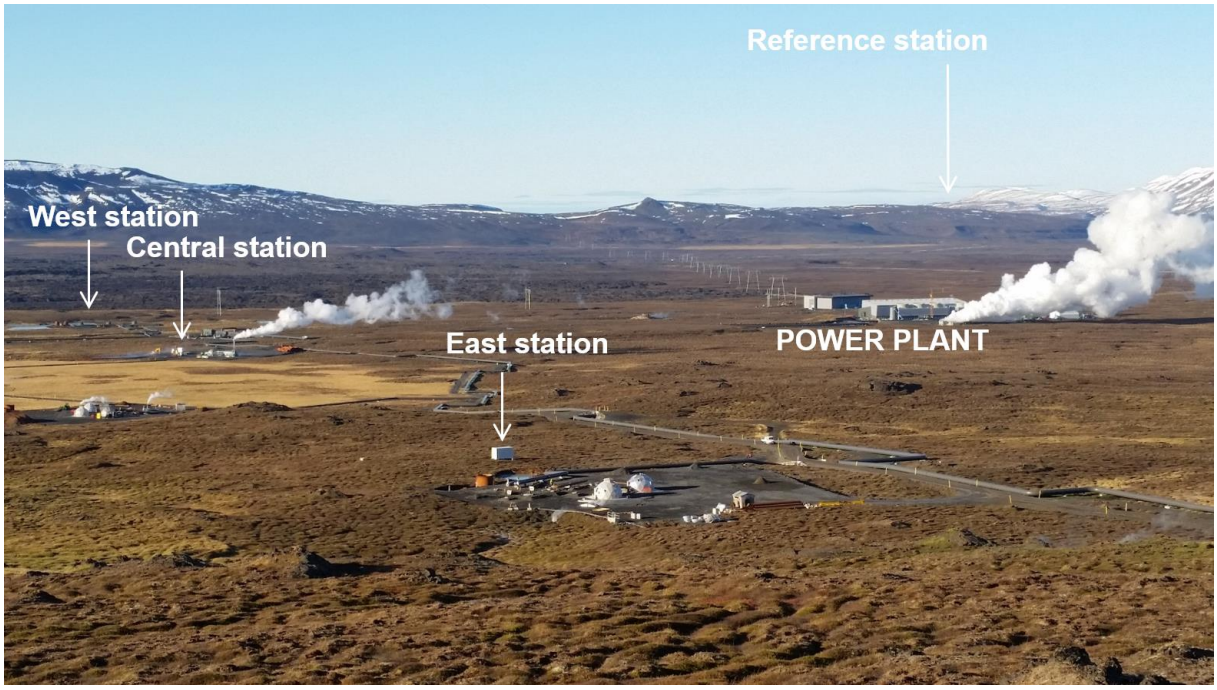


**Figure 5.** Aerial view (from the southeast) of the Þeistareykir geothermal field, showing the positions of the east and central stations close to the production wells, and the west station at the reinjection site, the reference station is positioned about 17 km to the northwest outside the geothermal field (see Fig. 6).

## 2.3 Instruments and data processing

This thesis comprises measurements from three types of gravity meters. The Scintrex CG5 spring gravity meter was used for annual (time-lapse) gravity measurements and the iGrav SG for continuous gravity observations. Additional annual measurements with an FG5 absolute gravity meter were performed as reference for the relative (CG5 and iGrav) measurements. The specifications for each gravity meter are listed in Table 1. Details about each method are described in the following subchapters.

**Table 1.** Specifications of the three gravity meter types used in this study.

| Name | **Scintrex CG5** | **iGrav** | **FG5** |
|---|---|---|---|
| Manufacturer | Scintrex Ltd. | GWR Instruments, Inc. | Micro-g Solutions, Inc. |
| Classification | Relative gravity meter | Relative gravity meter | Absolute gravity meter |
| Sensor type | Spring suspension | Superconducting sphere | Free-fall chamber |
| Measuring period | Few minutes | Continuous | 24 hours |
| Resolution | 1 µGal | 1 nGal | 1 µGal |
| Field deployment | ~1 min setup | ~5 hrs setup | ~1 hr setup |
| Weight | 8 kg | 40 kg | 127 kg |
| Site requirements | poss. sun or wind protection | Sheltered environment (container or housing) | Sheltered environment (container) |
| Additional requirements | | permanent power supply, He gas filling | permanent power supply |

### 2.3.1 Time-lapse gravity observations

In many gravity field studies spring gravity meters are used for monitoring groundwater flow, volcanic activities and geothermal reservoirs (Jousset et al., 2000; De Zeeuw-van Dalfsen et al., 2006; Jacob et al., 2010; Portier et al., 2018). Due to easy transportability, simple handling and quick application (of a few minutes per measurement), these gravity sensors are suited for measurements within a network with several measuring points (Parseliunas et al., 2011). High spatial resolution of gravity anomalies and their annual variations within the study area can be obtained by measuring (and remeasuring) the gravity changes at different points of the network. However, especially for remote study areas, these field campaigns require planning and logistical efforts, which may constrain the project to few years of annual repetition measurements. Figure 6 shows the field deployment of the Scintrex CG5 spring gravity meter during the study at the Þeistareykir geothermal field.

**Figure 6.** Time-lapse measurements with the Scintrex CG5 relative gravity meter at the Þeistareykir geothermal field.

### 2.3.2 Absolute gravity measurements

Additional to the relative gravity observations, an FG5 absolute gravity meter was deployed for measurements at each gravity monitoring station at Þeistareykir (and Krafla), providing absolute reference for the time-lapse gravity network, and calibration and drift correction for the iGravs. Figure 7 shows the setup for the FG5#206, installed on the large concrete pillar in the front room of the gravity station.

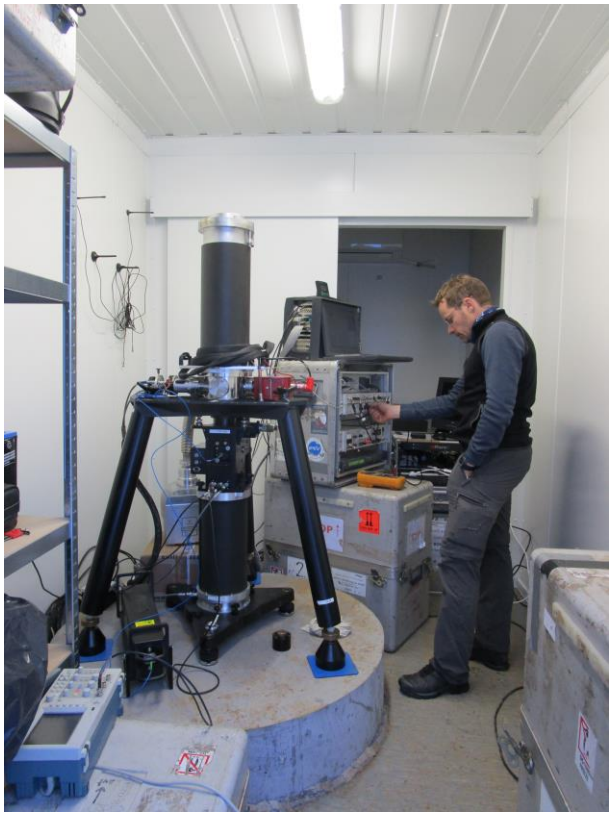

**Figure 7.** Absolute gravity measurements with the FG5#206 positioned on a large decoupled concrete pillar in the front room of the gravity stations at Þeistareykir; setup shown for east station.

### 2.3.3 Continuous gravity monitoring

Continuous gravity monitoring is suited for long-term studies, like tidal measurements in gravimetric observatories. For field operation, a sheltered gravity station with connection to uninterrupted power supply needs to be set up before the gravity meter can be installed for continuous measurements. Gravity monitoring and data transfer may be resumed remotely, and subsequent field work can be reduced to short-term visits for maintenance. In this work, three iGravs were deployed for high-resolution continuous gravity monitoring of the Þeistareykir geothermal field. Figure 8 shows the iGrav setup for one of the four gravity stations at Þeistareykir.


**Figure 8.** Continuous gravity observations with the iGrav superconducting gravity meter (SG) installed on a decoupled concrete pillar in the back room of the gravity stations at Þeistareykir; setup shown for iGrav015 at the reference station.

### 2.3.4 Processing of continuous gravity time series

Figure 9 summarises the principle steps for processing time series from continuous operating gravity meters. For all pre-processing steps, I used the TSoft software package (Van Camp and Vauterin, 2005). The steps 2 to 5 are exemplarily shown for the iGrav006 signal separation in Figure 10.

In step 1, the temporal resolution of the gravity signal is reduced to enable further computation of long-term (up to several years of) gravity data. This step has to be omitted when high temporal resolution of the gravity signal is needed (e.g. for noise analysis, chapter 3.4). For the iGrav data, I applied a least squares low pass filter with cut-off frequency of 0.03 Hz to reduce the sample rate from seconds to minutes.

Step 2 of data pre-processing consists of converting the raw output signal to gravity units. For the iGrav SGs this is done with the help of a specific calibration factor, which converts the instrumental feedback voltage to nm $s^{-2}$ and is obtained by comparative measurements with either an absolute gravity meter or an accurately calibrated relative gravity meter. More information about the iGrav calibration is given in chapter 3.3 of this thesis.

Step 3 and 4 consist of reduction of the gravity contributions with the largest amplitudes (i.e. theoretical tides and pressure effects) that superimpose all remaining gravity signals. For the iGrav monitoring sites, I applied the Wahr-Dehant-Defraigne (WDD) model for solid Earth tides (Dehant et al., 1999) and a finite element solution (FES2014b) model for ocean tide loading (Carrere et al., 2015). Then I removed the contribution of air masses, with the help of ambient pressure measurements (simultaneously recorded by each gravity meter) and the standard barometric admittance factor of -3.5 nm $s^{-2}$ $hPa^{-1}$ (Crossley et al., 1995).

In step 5, the time series are corrected for "artefacts", i.e. spikes and offsets that disturb the further gravity analysis. Spikes are visible as short-period deviations of the gravity signal due to earthquakes or artificially caused vibrations of the sensor. Data offsets usually result from instrumental issues like power failure. For the iGrav time series, I applied the TSoft automatic spike correction and manual correctors for offsets. One major offset of -730 nm $s^{-2}$ in June 2019, which had to be corrected for iGrav006 (Fig. 10d) resulted from replacement of the iGrav coldhead during maintenance work.

In the final pre-processing step 6, the theoretical tidal signal (that was removed in step 3) is added (i.e. restored) to the gravity residuals. Then, in step 7, the gravity time series can be used for tidal analysis, in order to calculate a local tidal model for the individual observation site, which can then be used for further reduction of the gravity signal. I used the program ANALYZE from the ETERNA 3.4 package (Wenzel, 1996) for computation of the local tidal parameters. The adjusted tidal parameters are given for each of the Icelandic observations sites (Appendix B, B1 to B3).

Figure 10f shows the iGrav006 pre-processed residuals (red line) and the subsequently reduced signal (black line) after restoring the theoretical tides and removing the local tidal model (step 8 in Fig. 9). Details about the further processing steps (9 to 11) can be found in chapter 3.5 for drift correction and chapters 4.2 and 4.3 for reduction of global and local gravity contributions. The final processing step 12 of subtracting a reference gravity signal is demonstrated in Figure 17 of chapter 3.5 and Figure 24 of chapter 4.3.3.

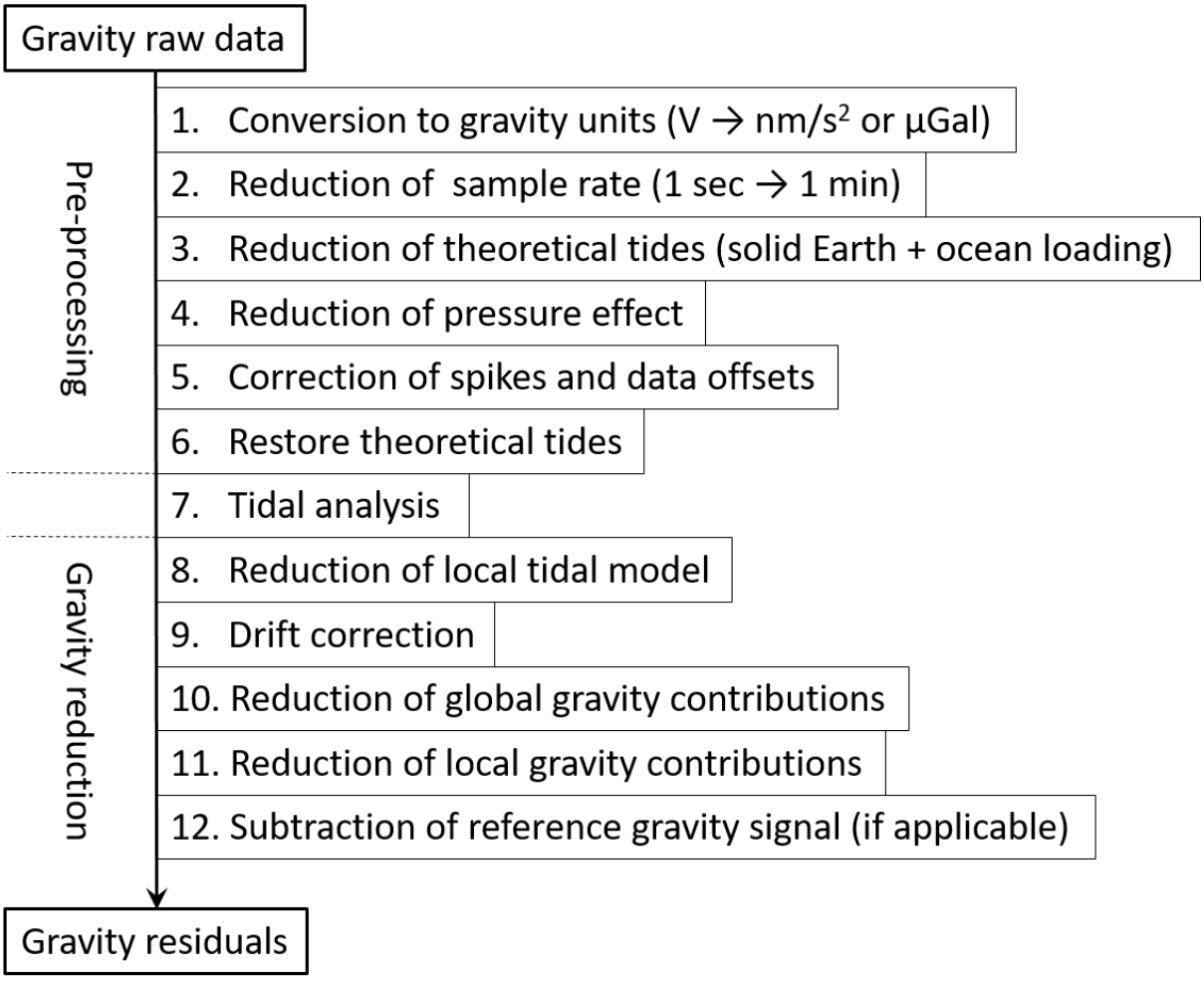


**Figure 9.** Simplified processing scheme with steps for the analysis of continuous gravity time series; note that raw data units (volts and seconds) apply for superconducting gravity meters and can vary for different sensor types.

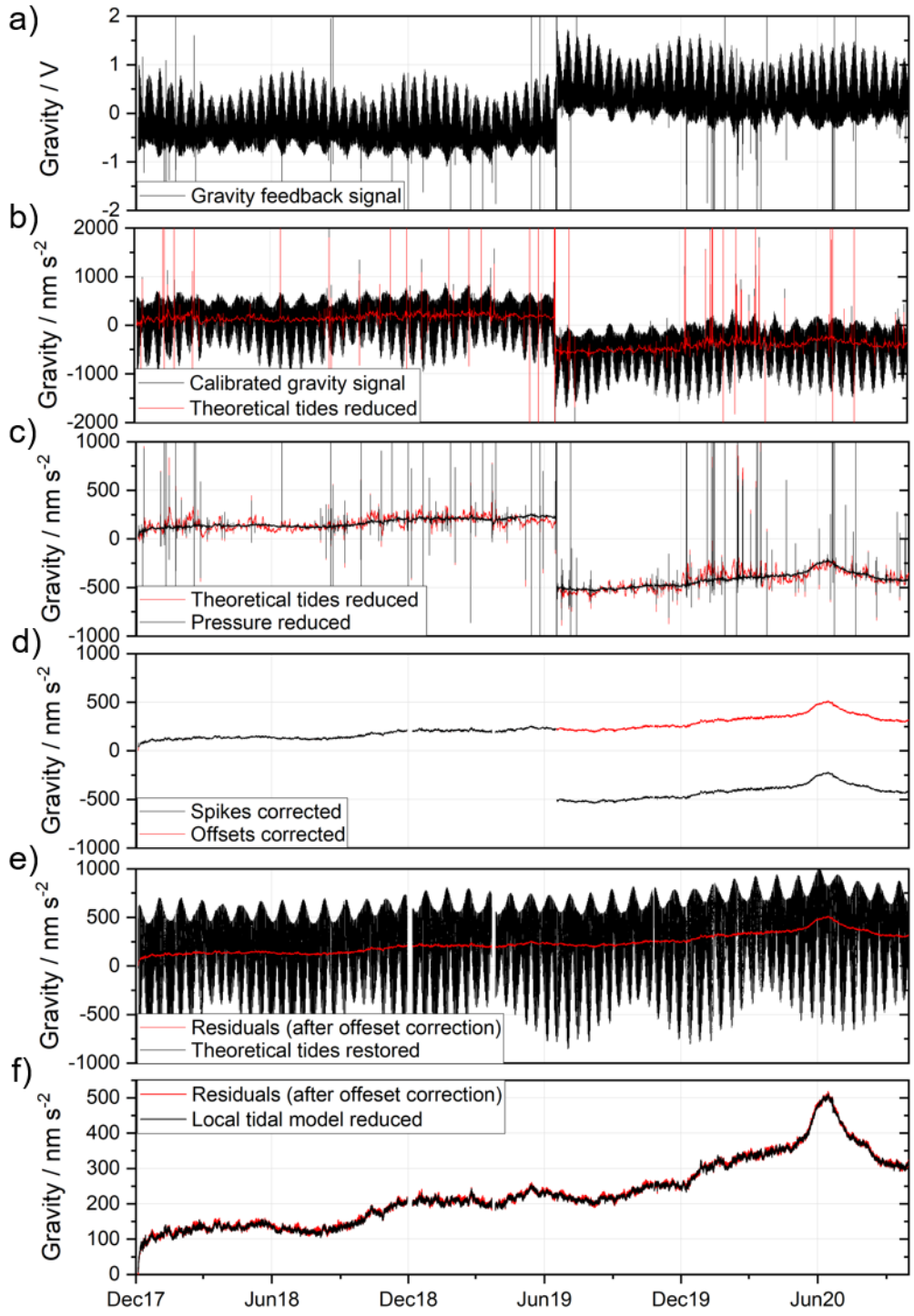


**Figure 10.** Processing steps exemplarily shown for the gravity time series of iGrav006 recorded at Þeistareykir west station; (a) raw signal is the gravity meter feedback voltage, (b) the signal is converted to nm $s^{-2}$ by a specific calibration factor (-914.27 nm $s^{-2}$ $V^{-1}$ for iGrav006) and theoretical tides (solid Earth and ocean loading) are removed, (c) reduction of locally observed pressure effects, (d) correction of spikes and data offsets, (e) theoretical tides are restored for tidal analysis, (f) local tidal model removed from residual signal; please note the different scaling of the axes.

# Chapter 3

## Performance of three iGrav superconducting gravity meters before and after transport to remote monitoring sites

*The content of this chapter has been published in Schäfer, F., Jousset, P., Güntner, A., Erbas, K., Hinderer, J., Rosat, S., Voigt, C., Schöne, T., & Warburton, R.J. (2020). Performance of three iGrav superconducting gravity meters before and after transport to remote monitoring sites. Geophysical Journal International, 223(2), 959-972, https://doi.org/10.1093/gji/ggaa359.*

High spatial and temporal resolution of gravity observations allows quantifying and understanding mass changes in volcanoes, geothermal or other complex geosystems. For this purpose, accurate gravity meters are required. However, transport of the gravity meters to remote study areas may affect the instrument's performance. In this work, we analyse the continuous measurements of three iGrav superconducting gravity meters (iGrav006, iGrav015 and iGrav032), before and after transport between different monitoring sites. For four months, we performed comparative measurements in a gravimetric observatory (J9, Strasbourg) where the three iGravs were subjected to the same environmental conditions. Subsequently, we transported them to Þeistareykir, a remote geothermal field in North Iceland. We examine the stability of three instrumental parameters: the calibration factors, noise levels and drift behaviour. For determining the calibration factor of each instrument, we used three methods: First, we performed relative calibration using side-by-side measurements with an observatory gravity meter (iOSG023) at J9. Second, we performed absolute calibration by comparing iGrav data and absolute gravity

measurements (FG5#206) at J9 and Þeistareykir. Third, we also developed an alternative method, based on intercomparison between pairs of iGravs to check the stability of relative calibration before and after transport to Iceland. The results show that observed changes of the relative calibration factors by transport were less than or equal to 0.01%. Instrumental noise levels were similar before and after transport, whereas periods of high environmental noise at the Icelandic site limited the stability of the absolute calibration measurements, with uncertainties above 0.64% (6 nm s 2 V 1). The initial transient drift of the iGravs was monotonically decreasing and seemed to be unaffected by transport when the 4K operating temperatures were maintained. However, it turned out that this cold transport (at 4K) or sensor preparation procedures before transport may cause a change in the long-term quasi-linear drift rates (e.g. iGrav015 and iGrav032) and they had to be determined again after transport by absolute gravity measurements.

## 3.1 Introduction

For more than 50 years, continuous gravity observations have been performed across the globe to gain knowledge about spatial and temporal gravity changes. This helps to quantify local subsurface mass changes (Jousset et al., 2000; Harnisch and Harnisch, 2006; Jacob et al., 2009) or to improve tidal models by identifying the share of regional and global gravity effects, like solid Earth tides, ocean loading or polar motion (Melchior, 1974; Francis and Mazzega, 1990; Agnew, 2015). Superconducting gravity meters (SG) have proven their value for such observations, especially for long-term measurements.

Most SGs installed to date are large, heavy, and require significant amounts of power and, in some cases, refills with liquid helium (Tab. 2). A more flexible approach for continuous high-resolution gravimetry is achieved by using smaller and easier-to-handle instruments like the SG with integrated electronics (iGrav) of GWR Instruments, Inc. The iGrav Dewar is much smaller and weighs less than the Dewars of the Compact (CT) and Observatory SG (OSG), although it uses the same refrigeration system. Furthermore, it operates remotely after an initial filling with helium gas and does not depend on a regular refill with liquid helium (Warburton et al., 2010). Finally, the electronics require less power than the OSG. This makes it

more adapted for operation in harsh or remote environments (Kennedy et al., 2014, 2016; Fores et al., 2017; Carbone et al., 2017, 2019).

**Table 2.** Comparison of three SG Dewars from GWR Instruments, Inc.: Compact (CT), observatory (OSG) and with integrated electronics (iGrav); giving the Dewar weight, demand on power supply for electronics, requirement for regular refill with liquid helium (values obtained from Warburton et al., 2010 and Hinderer et al., 2015).

| SG type | Weight (kg) | Power supply for electronics (W) | Liquid helium refill required |
|---|---|---|---|
| CT | 90 | 250 | Yes (up to 100L/yr) |
| OSG | 69 | 250-600 | No |
| iGrav | 40 | 250 | No |

While these technological developments make it easier to transport the gravity meters from one monitoring site to another, the question arises whether specific instrument parameters and characteristics (i.e. calibration, noise and drift behaviour) determined at one location can be transferred to another site to simplify processing and evaluation of the gravity signals. The calibration converts the sensor output voltage into gravity units. Noise is instrumental noise and/or geophysical signal, which may limit the accuracy and precision with which gravity signals of interest can be identified in the data. The drift is an instrumental artefact in the gravity record that contaminates the measured values of true gravity changes. The drift for most SGs is generally assumed to consist of a transient function followed by a linear trend and is determined by comparison to co-located AG measurements (Crossley et al., 2004; Van Camp and Francis, 2007). Schilling and Gitlein (2015) described the variability of these parameters for a spring gravity meter (gPhone98) at different measuring stations in Germany. There are several studies that have involved moving SGs. Wilson et al. (2012) reported on the first field test of a transportable OSG. Kennedy et al. (2014) transported iGravs 004 and 006 by truck with sensor spheres levitated. Later, Güntner et al. (2017) transported iGrav006 from GWR (San Diego, USA) to the Wettzell geodetic observatory (Germany) and deployed it in a customised field enclosure. However, there are no studies so far that report on how the iGrav instrumental parameters may be influenced by either preparation for cold transport

(i.e. transport while maintaining the sensor operation temperature at 4K) or the cold transport itself to a new location.

In this study, we assess the performance of three iGravs (006, 015 and 032) before and after transport. First, we deployed the three iGravs for continuous measurements at the gravimetric observatory J9 in Strasbourg (France) for instrumental calibration and for estimation of the noise levels. For determination of the iGrav drifts at J9, we included measurements of one OSG with integrated electronics (iOSG023) as a reference (Rosat and Hinderer, 2018). Next, we transported the three iGravs to Þeistareykir (pronounced: 'Thest-a-rey-kir'), a geothermal site in North Iceland. For drift characterisation and calibration check of the scale factors at the Icelandic remote sites, we used an FG5 absolute gravity meter (FG5#206; Amalvict et al., 2001; Van Camp et al., 2003). At both sites (J9 and Iceland), we used a three-channel correlation method (TCCM; Rosat and Hinderer, 2018) to discriminate common environmental noise from instrument-specific noise. In this study, we do not address the interpretation of the gravity signals with regard to local mass changes due to geothermal activity, which will be discussed in subsequent analyses.

## 3.2 Instruments, sites and transport

### 3.2.1 Instrument specifics

The first iGravs were introduced about 10 years ago and since then approximately 45 iGrav SGs have been manufactured. During this time, several modifications were made to the iGravs to improve their performance. Early iGrav bodies (serial no. 001 to 020) were made shorter than previous SG bodies to reduce Dewar height and weight so as to increase portability. The shorter body reduced the length of the Niobium shield and its shielding effectiveness (sensor design illustrated in Fig. A1, Appendix A; and Hinderer et al., 2015). As a result, magnetic signals produced by building elevators or nearby parked cars were observed in early iGravs. To remedy this problem, a lead shield was added outside of the vacuum can so that it enclosed the open end of the Niobium shield. Although this proved effective, iGrav bodies (serial no. 021) returned to the original SG design and as a result their Dewars are 10 cm taller; and have a larger volume and hold time for liquid helium during transport. iGrav015 was also retrofitted into a larger Dewar.

An additional change that was implemented for serial no. 015, 017 and above, was the introduction of side coils and 'flux trapping' to raise the frequency of the commonly observed orbital sphere resonance (Hinderer et al., 2015) out of the long-period seismic band. To accomplish this, four small side coils were placed at sphere height with their axes perpendicular to the axis of the levitation magnets. These were wired so that a current through the coils produced a dipole magnetic field in the vicinity of the sphere, coils, and shield. This change results in the ability to trap the magnetic flux in the sphere, coils and shield, by a specific procedure called 'flux trapping'. 'Flux trapping' consisted of heating the body to 32K (well above $T_c$), applying a current to the side coils, activating the getter to add helium gas to the vacuum can to cool the sensor to 4K, and turning off the current. The use of trapped flux was very effective at raising the mode frequency and no abnormal drifts have been reported for dozens of iGravs operated for many years at stationary observatories.

### 3.2.2 Co-located gravity measurements at the gravimetric observatory J9 in Strasbourg

J9 has been a gravimetric observatory since 1971 (Arnoso et al., 2014; Rosat et al., 2015). We installed our three iGravs within 2 to 10 meters from each other at J9, where they were operating for up to four months between June and October 2017. Figure 11 shows the positions of the iGravs and of the other gravity meters at the observatory. iOSG023 has been recording at J9 since February 2016 and, therefore, provides good reference for our instruments (Rosat and Hinderer, 2018). Operational setup is shown in the Appendix A (Fig. A2).

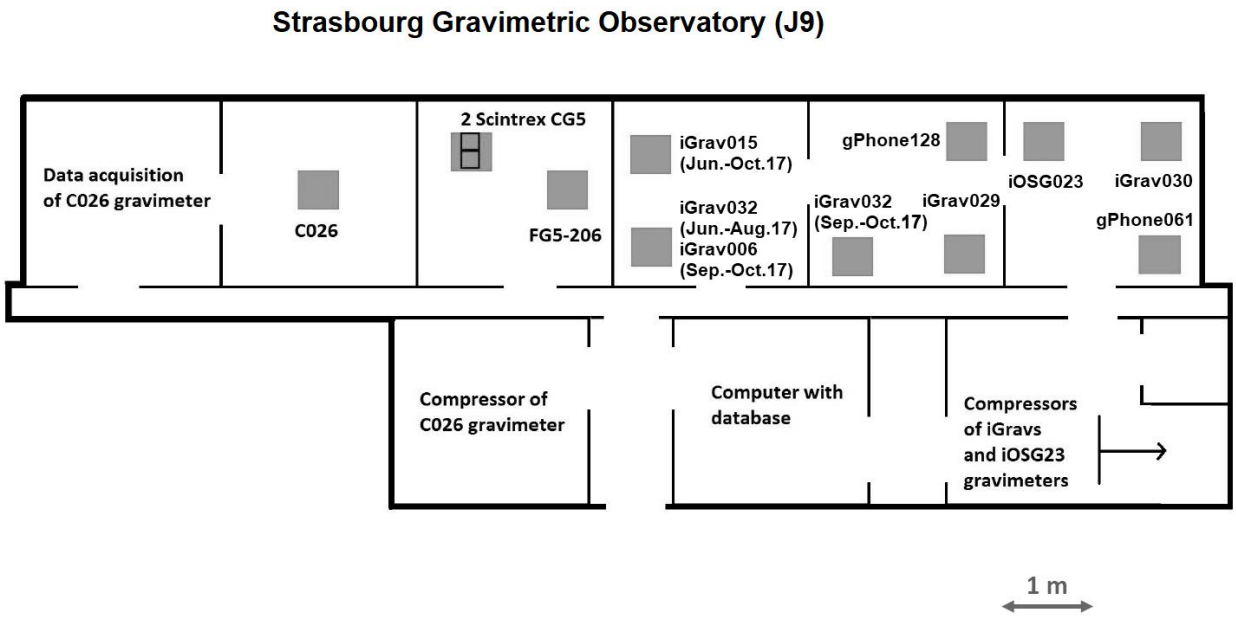


**Figure 11.** Site map of the underground observatory J9 with the positions of the three iGravs (006, 015, 032) and the observatory instruments (iGrav029, iOSG023) included in this study (modified from Hinderer et al., 2018).

### 3.2.3 Remote operation at a geothermal field in North Iceland

On 04 December 2017, we started recording with the gravity meters at Þeistareykir in North Iceland (Fig. 12). iGravs 006 and 032 were set up inside the geothermal field within two kilometres of each other. iGrav015 was initially located outside the geothermal field, 17 kilometres to the northwest, for reference measurements. In June 2019, we relocated iGrav015 to the central position between iGravs 006 and 032. GPS positions of the four monitoring sites are given in the Appendix A (Tab. A1).

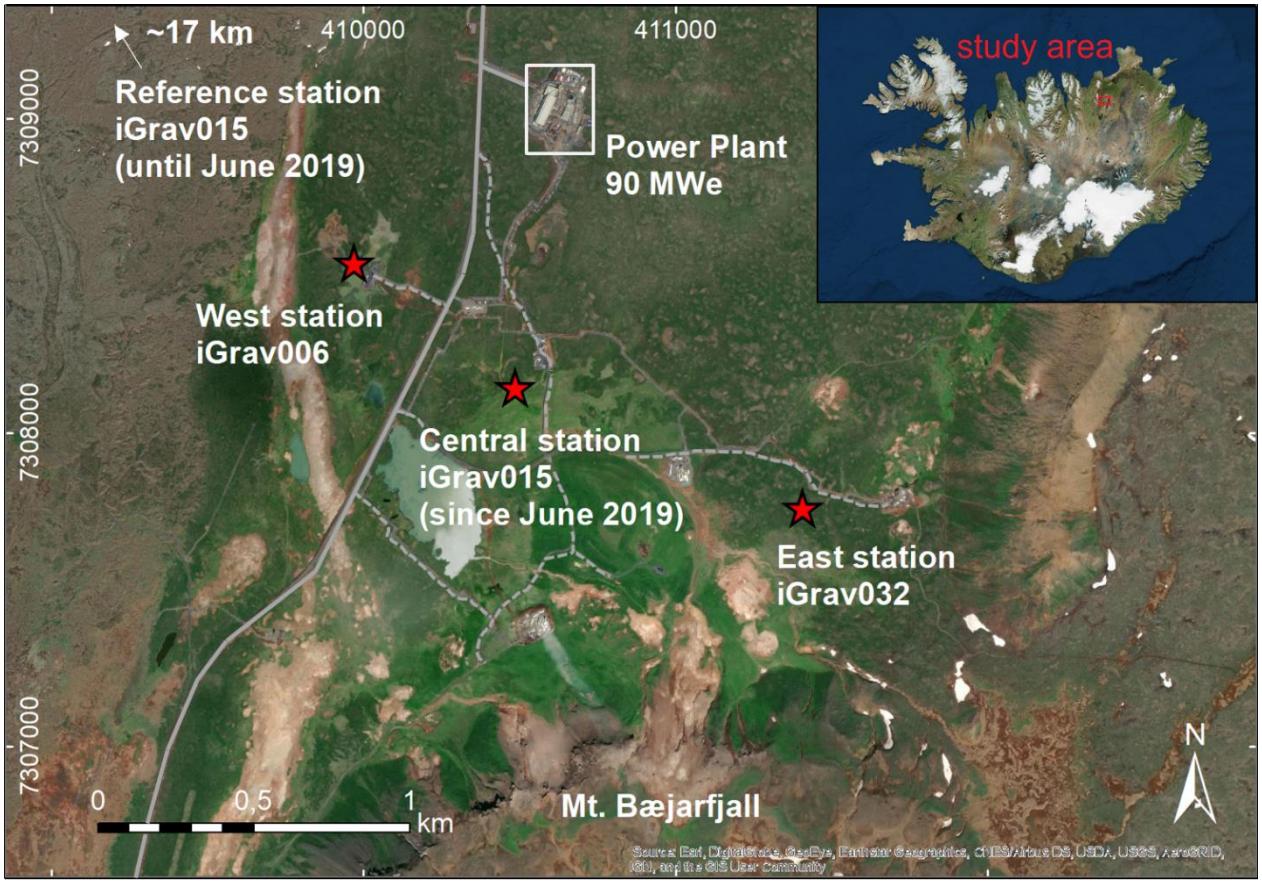


**Figure 12.** Location of the geothermal field in North Iceland and positions of the gravity stations for each iGrav, iGrav015 was moved from reference to central station in June 2019 (maps compiled with ArcGIS 10.5.1, map.is/os, UTM Zone 28N).

All monitoring sites have similar configuration (Fig. A3, Appendix A). They comprise an isolated container with two rooms, each housing a circular concrete pillar. Both pillars are decoupled from the container and attached to the subsurface (bedrock where possible). The continuously operating gravity meter is set up on the pillar in the rear room. The pillar in the entrance room is used for performing calibration measurements with an absolute gravity meter. Each container is equipped with a heater and air conditioning system to keep a constant room temperature of approximately 16°C. A remotely operated multi-parameter station (ROMPS) (Schöne et al., 2013) outside the container monitors hydro-meteorological parameters including barometric pressure, air temperature, precipitation, wind speed, soil moisture and soil temperature. Snow weight, snow height and snow water equivalent

are monitored at the east station (iGrav032) only. At every gravity station, we deployed geodetic GNSS receivers for continuous observations of ground motion. Three cameras at each site allow visual inspections of the surroundings and estimation of snow heights at the container corners.

### 3.2.4 Instrument transport and timeline of gravity measurements

Figure 13 summarises the different periods of gravity measurements performed at the J9 observatory in Strasbourg and the Icelandic remote monitoring sites in Þeistareykir. Each change of location of a particular instrument marks a transport and may influence the subsequent gravity records. At the end of October 2017, we removed the three iGravs from the measuring site in Strasbourg for transport to Iceland. Transport from J9 to Þeistareykir is illustrated in the Appendix A (Fig. A4).Typically, SGs are transported at room temperature without liquid helium inside the Dewar of the gravity meter, and several weeks are required to cool the system to operating temperature (4K) for helium liquefaction and filling. For our study, we targeted to transport the iGrav Dewars at 4K with liquid helium filled (cold transport marked grey in Fig. 13) to avoid the time-consuming cooling phase and the associated generation of significant initial drift rates. Only iGrav006 was transported at room temperature and had to be cooled down to 4K before the start of measurements at J9. For iGrav015 and iGrav032 we successfully realised cold transport for every transport from GWR / San Diego, USA to J9 (truck and airfreight) and J9 to Iceland (truck and ship's freight). At Þeistareykir iGrav006 had to be re-cooled from only slightly increased temperature (8K) after cold transport. This results from the larger Dewar volumes and associated longer helium hold times for 015 and 032 compared to 006.

We noticed that two of the instrumental iGrav parameters (i.e. noise and drift) are directly dependent on the sensor preparation procedures for cold transport. It turned out that high-temperature annealing before transport causes a reduction in mode frequency and a reduction of drift rates observed for iGrav015 and iGrav032 at the remote monitoring sites, discussed in detail in sections 3.4 and 3.5.

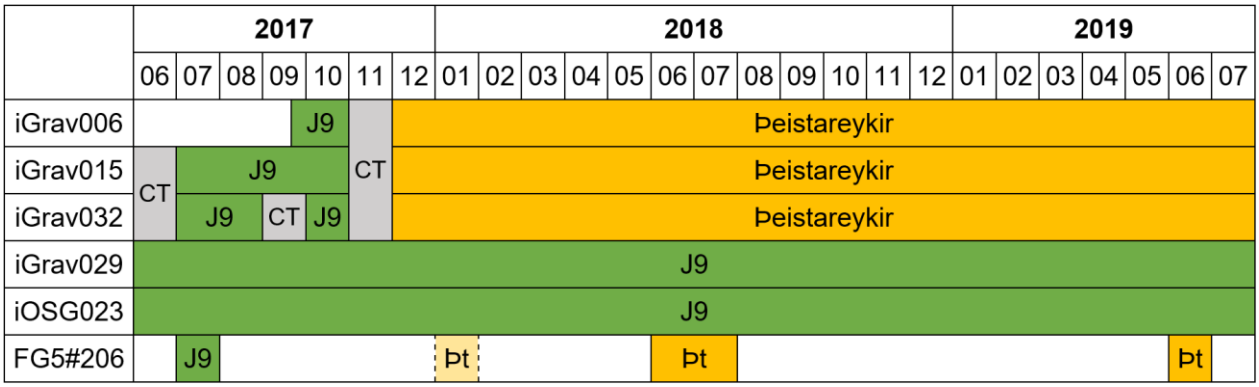


**Figure 13.** Timeline of gravity measurements at J9 (Strasbourg, France) and Þeistareykir (Iceland) with the following operating periods at J9: 21.09.2017-23.10.2017 for iGrav006, 21.06.2017-24.10.2017 for iGrav015, 17.06.2017-29.08.2017 and 28.09.2017-24.10.2017 for iGrav032; periods of cold transport at 4K (CT; marked grey) occurred in September 2017 when iGrav032 had to be sent to GWR (San Diego, USA) for maintenance and in November 2017 when all three iGravs were shipped to Iceland; last line shows AG measurements performed with the FG5#206 at J9 and Þeistareykir; FG5 values from January 2018 (dashed margins) are not included in this study because of large measuring uncertainties due to increased ground vibration in the Icelandic winter.

## 3.3 Calibration factors

Every iGrav needs a scale factor to convert the measured output feedback voltage to gravity units. We used two methods for estimating the scale factor from the local tidal signal, calibrating the iGrav measurements with either an absolute gravity meter (AG calibration) (Riccardi et al., 2012; Crossley et al., 2018) or side-by-side measurements with an accurately calibrated relative gravity meter (RG calibration) (Meurers, 2012; Hinderer et al., 2015).

For AG calibration, the absolute gravity meter is positioned next to the SG. The AG drop values (in nm $s^{-2}$) are then least-squares fitted to the SG output voltage to calculate the scale factor (in nm $s^{-2}$ $V^{-1}$) (Hinderer et al., 2015). Results from AG calibration using FG5#206 at J9 and Þeistareykir are shown in Table A2 in the Appendix A. Uncertainty values of the AG calibrations are up to 3.3 times larger for the Icelandic remote monitoring sites than at J9. One possible reason are the different solid Earth tidal amplitudes (511.6 nm $s^{-2}$ at J9 and 356.1 nm $s^{-2}$ at Þeistareykir during AG calibration in June/July 2017), leading to increased AG calibration uncertainties in Iceland by a factor 1.4 (40% increase) assuming a linear

dependence of the uncertainties to tidal amplitude. As another possible reason we suspect increased local noise at the remote sites from wind, breaking ocean waves, tectonic and geothermal activities, which is negatively affecting AG measurements. In particular, noise from geothermal activities is likely at the iGrav032 and iGrav006 sites due to their short distances to the geothermal well pads.

For RG calibration, a relative gravity meter with known calibration (e.g. by former AG calibration) is positioned next to the SG. Then, analogous to AG calibration both sets of measurements are compared and the data is fitted by a least-squares adjustment from one instrument to the other (Riccardi et al., 2012; Hinderer et al., 2015). We performed RG calibration using one of the observatory superconducting gravity meters (iOSG023) at J9 for all three iGravs in October 2017. The iGrav scale factors obtained by RG calibration at J9 are given in Table A3 in the Appendix A. The results shown in Tables A2 and A3 reveal that AG and RG calibrations are very similar and that the uncertainties of RG calibrations are much smaller. However, for a fair comparison between RG and AG calibration factors, one has to consider the absolute calibration uncertainty of the reference gravity meter (2 nm $s^{-2}$ $V^{-1}$ for iOSG023).

Due to the lack of AG calibration for iGrav006 at J9 and for iGrav032 at Þeistareykir as well as the increased absolute calibration uncertainties for the remote sites, we consider an alternative approach to determine the scale factor stability after transport to Iceland. Instead of comparing the individual iGravs 006, 015 and 032 to either iOSG023 or FG5#206 we compare them to each other using their RG calibrations determined at J9 (from Tab. A3) as reference. The resulting scale factors are shown in Table 3. To determine the scale factors for Þeistareykir we used iGrav data sets of 8 days in June/July 2019. During this period, iGrav015 was located on the second pillar of the central station (cf. Fig. 12) at about 0.7 km distance to iGrav006 and 1.0 km distance to iGrav032. The increasing distances between the instruments may explain the scale factor differences between J9 and Þeistareykir, with smallest differences for the iGrav006-iGrav015 pair located closest to each other (Fig. 12 and Tab. 3, cols. 7 and 8). To correct for the different locations and elevations of the three iGravs at Þeistareykir, we calculate the scale factors between theoretical tides, using Wahr-Dehant-Defraigne (WDD) solid Earth tides (Dehant et al., 1999) and ocean tide

loading (FES2014b; Carrere et al., 2015) models for each of the iGrav locations and multiply the scale factors in column five by this correction factor. As shown in column 11, the differences of the RG calibrations observed between J9 and Þeistareykir are reduced to less than or equal 0.01% when taking into account the tidal correction. We conclude that the RG calibrations have not changed after transport, within 0.01% uncertainty.

**Table 3.** Stability of iGrav scale factors determined by RG calibration between iGrav pairs before and after transport to Iceland; column 1 shows the iGrav for which the scale factors are calculated using the respective iGrav in column 2 (calibrated to iOSG023, Tab. A3) as reference; columns 3 to 6 show the resulting scale factors (SF) and standard deviations (SD) for J9 and Þeistareykir; column 8 shows the distances (Dist.) between each iGrav pair; column 9 shows the correction factors (CF) due to the tides in order to account for the different geographical locations between the iGravs and column 10 shows the therewith corrected scale factors (SFC) for Þeistareykir; columns 7 and 11 show the percentage differences (SFD) between the J9 and Þeistareykir (geographically corrected, SFDC) scale factors.

| **iGrav** | | **Scale factor** | | | | **DIFF** | **Geographic correction** | | | **DIFF** |
|---|---|---|---|---|---|---|---|---|---|---|
| **pair** | | J9 | | Þeistareykir | | J9-Þei | Þeistareykir | | | J9-Þei |
| 1 | 2 | 3 | 4 | 5 | 6 | 7 | 8 | 9 | 10 | 11 |
| **Obj** | Ref | SF | SD | SF | SD | SFD | Dist. | CF | SFC | SFDC |
| | | $nms^{-2}V^{-1}$ | $nms^{-2}V^{-1}$ | $nms^{-2}V^{-1}$ | $nms^{-2}V^{-1}$ | % | km | | $nms^{-2}V^{-1}$ | % |
| **006** | 015 | -914.29 | 0.0040 | -914.24 | 0.0032 | 0.0055 | 0.66 | 1.00012 | -914.35 | 0.0065 |
| **006** | 032 | -914.23 | 0.0075 | -914.01 | 0.0055 | 0.0241 | 1.64 | 1.00021 | -914.20 | 0.0031 |
| **015** | 006 | -930.11 | 0.0041 | -930.16 | 0.0032 | 0.0054 | 0.66 | 0.99988 | -930.05 | 0.0066 |
| **015** | 032 | -930.14 | 0.0067 | -929.97 | 0.0051 | 0.0183 | 1.00 | 1.00009 | -930.05 | 0.0093 |
| **032** | 006 | -895.77 | 0.0074 | -895.98 | 0.0054 | 0.0234 | 1.64 | 0.99979 | -895.79 | 0.0024 |
| **032** | 015 | -895.85 | 0.0065 | -896.02 | 0.0050 | 0.0190 | 1.00 | 0.99991 | -895.94 | 0.0100 |

The stability of calibration factors examined above can also be considered with regard to the change of the local value of g between J9 and Þeistareykir. A more detailed description and related calculations for the ‘variation of SG calibration caused by change in latitude or elevation’ are given in the Appendix.

## 3.4 Noise analyses

A combination of instrumental noise (e.g. data acquisition noise or sphere resonance effects; Imanishi, 2005; Rosat et al., 2015) and/or environmental noise (of e.g. seismic or meteorological origin) may limit the precision with which gravity signals of interest can be measured. We expect lower environmental noise to be present at a quiet, isolated site like J9 in Strasbourg, compared to an active geothermal site like Þeistareykir. In addition, we expect to observe larger gravity signals (ocean load and waves) at the Icelandic remote sites, due to their short distance to the coastline (8 km for the reference station). In this study, we applied the three-channel correlation method (TCCM) initially proposed by Sleeman et al. (2006) and adapted to SGs by Rosat and Hinderer (2018) in order to extract the incoherent noise (containing the iGrav self-noise) from ambient noise common to the three channels (here instruments). This method consists of calculating the Power Spectral Densities (PSDs) and cross-spectra of calibrated gravity records from three SGs applying a modified smoothed Welch periodogram estimator. We used calibrated gravity signals in nm $s^{-2}$ with 1 Hz sampling rate from which we compute the PSDs. As a consistent time-window for all monitoring sites, we chose gravity records of seven days during 'quiet' periods (no obvious earthquakes or other disturbances).

For J9 a direct comparison of the three iGravs is severely limited by the short record length of iGrav006 (cf. Fig. 13). Instead, we compare each of the three iGravs independently to two SGs (iGrav029 and iOSG023) which were continuously recording during our observation period at J9. We chose records from 20.08.2017 to 26.08.2017 for iGravs 015 and 032, and from 03.10.2017 to 09.10.2017 for iGrav006. As shown in Figure 14, iGrav015 and iGrav032 have average self-noise levels of -180 dB at intermediate frequencies (from $10^{-3}$ to $10^{-1}$ Hz) similar to those of iGrav029 and iOSG023, and in consistence with the observations from Rosat and Hinderer (2018) of low self-noise levels for different iGravs at J9. Only iGrav006 shows about 10 dB higher self-noise. Most likely, this increased noise of iGrav006 is a consequence of improper alignment of the coldhead isolation frame, so that the coldhead is in contact with the inside of the Dewar neck and vibrations from the coldhead are being directly transmitted to the gravity sensor. The sharp peaks at

higher frequencies (between 100 and 350 mHz) have also been observed for other SGs at J9 (Rosat and Hinderer, 2018) but the cause has not been identified yet.

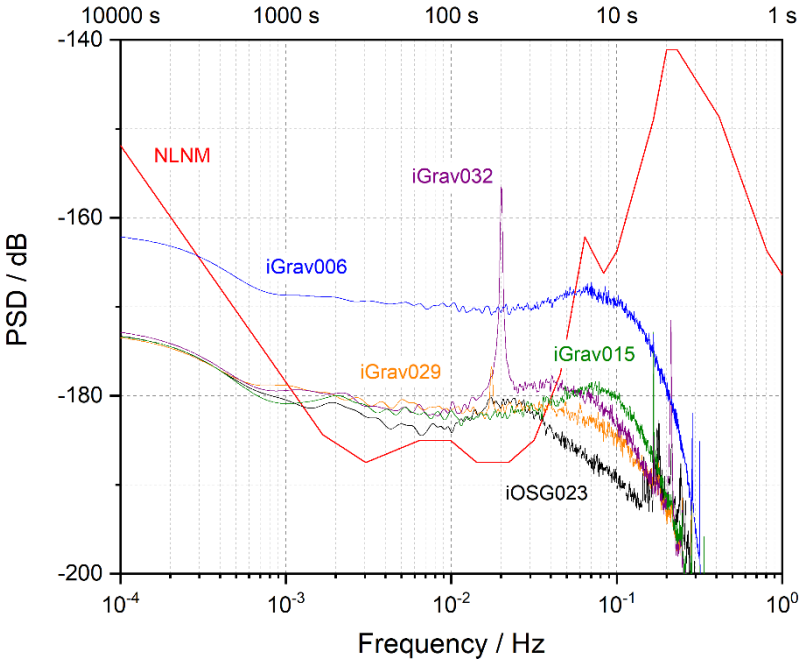


**Figure 14.** The instrument-specific noise levels resulting from the three-channel correlation method (TCCM) applied on 1-second data (1 Hz) of iGravs 006, 015 and 032 during seven 'quiet' days at J9 in comparison to iGrav029 and iOSG023; Noise levels computed as Power Spectral Densities (PSD) relative to 1 (m s 2)2 Hz 1; New Low Noise Model (NLNM; Peterson, 1993) shown for reference.

For Þeistareykir we chose records from 15.07.2019 to 21.07.2019, after relocation of iGrav015 to the central station, to directly apply the TCCM to the nearby located iGravs. The results from Þeistareykir (Fig. 15) show similar self-noise between -180 and -170 dB among the three iGravs. Compared to J9 we observe slightly increased noise levels by approximately 5 dB for iGravs 015 and 032 at the remote stations. At frequencies around 0.2 Hz we observe microseismic peaks (up to -165 dB), which do not appear in the PSDs from J9. This is likely caused by incoherent microseismic signals between the sites at Þeistareykir. We must note that in the TCCM, we assume that the ambient environmental noise is common to the three instruments. Since the three iGravs are located at different positions within the geothermal field, with slightly different environmental conditions, the self-noise extraction is less efficient than at J9, where the three gravity meters are collocated within a few

meters. As a result, cancellation of environmental noise between the remote stations is less efficient in the TCCM. Non-coherent part of the environmental noise will remain and be interpreted as instrumental noise, which could lead to the increased self-noise observed for the remote stations. Another observation is that the microseismic peak for iGrav015 is about 3 to 4 dB lower than for iGrav006 and iGrav032. Possible reasons could be the slightly different response functions or the larger calibration uncertainties among the iGrav pairs containing iGrav015 (Tab. 3, col. 11). It could also be caused by differences from the iGrav remote installations. For example, the terrain at the central station (iGrav015) is characterised by higher amounts of bedrock than the west and east stations, which may favour a better decoupling for the iGrav pillar and thus less microseismic noise being transmitted to iGrav015.

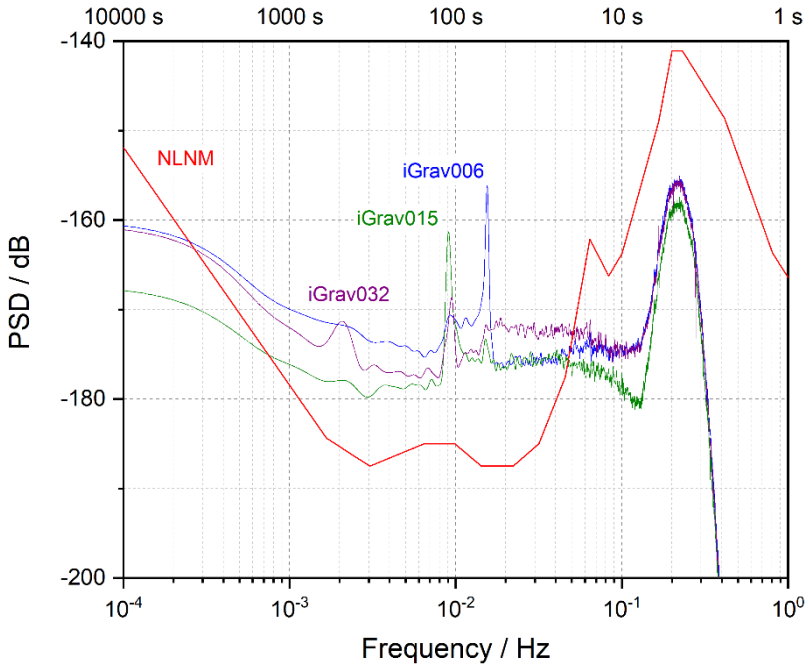


**Figure 15.** The instrument-specific noise levels resulting from the three-channel correlation method (TCCM) applied on 1-second data (1 Hz) of iGravs 006, 015 and 032 during seven ‘quiet’ days at the three remote stations within the Þeistareykir geothermal field; Noise levels computed as Power Spectral Densities (PSD) relative to 1 (m s 2)2 Hz 1; New Low Noise Model (NLNM; Peterson, 1993) shown for reference.

At frequencies around $10^{-2}$ Hz (between 9 and 20 mHz), the graphs show distinct spikes, visible in the plots for J9 and Þeistareykir (Figs. 14 and 15). This effect has been called 'the parasitic mode' (Richter et al., 1995; Van Camp, 1999) and is due to horizontal displacements of the sphere that turn into an orbital mode (Hinderer et al., 2015). At J9 we note sphere parasitic resonance at 20 mHz for iGrav032 (Fig. 14). At Þeistareykir the orbital mode frequencies of iGrav015 and iGrav032 are reduced to about 9 mHz (Fig. 15) because both sensors were heated above 32K at J9 before shipment to Iceland (see also discussion about high-temperature annealing in section 3.5). Note that during the three-channel correlation process, the cross-PSD of two instruments is subtracted from the third one resulting in the contamination to all PSDs by these parasitic peaks.

## 3.5 Instrumental drift

Every relative gravity meter, including SGs, is characterised by a distinctive instrumental drift behaviour. Drift functions for most SGs are normally toward increasing gravity and combine exponential components that decay with time constants from weeks to months, with a small linear term that varies from 16 to 49 nm $s^{-2}$ per year for nine SGs operating in Europe (Crossley et al., 2004; Hinderer et al., 2015). This transient drift behaviour can be described as:

$$g_{recorded} = g_{true} + ae^{-kt} + bt \quad (1)$$

with gravity (g), time (t), the exponential terms (a and k) and the linear term (b).

To identify the instrumental drift of the three iGravs we removed the tidal signals, as well as the effect of air masses (barometric admittance) from the calibrated gravity time series. As a standard tool for gravity reduction, we applied tidal modelling (Francis and Mazzega, 1990; Merriam, 1992; Agnew, 2015) to determine the residual time series for each monitoring site. For computation of local tidal models and the barometric admittance, we used the program ANALYZE from the ETERNA 3.4 package (Wenzel, 1996).

From our measurements at J9, we calculated the gravity residuals by reduction of local tidal parameters and atmospheric admittance factors available from long-term

gravity analysis at the observatory (Calvo et al., 2014, 2016). Figure 16 shows a comparison of the three iGravs and iOSG023 residual time series at J9. For further reduction of the remaining gravity effects including local hydrology, we subtracted the residual (reference) signal of iOSG023 from the iGrav residuals shown in Figure 17. It is noticeable that the iGrav time series are much smoother than in Figure 16 because most of the higher frequency gravity changes are present in all four gravity signals (of iOSG023, iGrav006, iGrav015 and iGrav032) and hence disappear in the difference. To isolate the initial exponential drift and quantify the linear long-term component we applied a linear drift correction for iGrav015 and iGrav032 (dashed black lines in Fig. 17). The time series of iGrav006 and iGrav032 after reinstallation (after day 90 in Fig. 16) were too short to apply linear drift corrections. We calculated the linear term by:

$$g = g_0 + xt \tag{2}$$

with initial gravity at t = 0 ($g_0$) and the drift rate (x). As approximation for the initial drift, we used a two-term exponential decay function:

$$g = g_0 + A_1 e^{-(t-t_0)/\tau_1} + A_2 e^{-(t-t_0)/\tau_2} \tag{3}$$

with initial time ($t_0$), the amplitudes ($A_1$ and $A_2$) and time constants ($\tau_1$ and $\tau_2$); the exponential curve-fittings are shown as dashed red lines in Figure 17. The parameters of the linear and exponential approximations for J9 are summarised in Table A4 in the Appendix A. From the exponential fit, iGrav006, which had to be cooled down from room temperature before the start of measurements, shows largest amplitudes compared to iGrav015 and iGrav032, which were transported cold, at their 4K operating temperature from GWR to J9. However, the time constants of exponential decay are similar for all three iGravs.

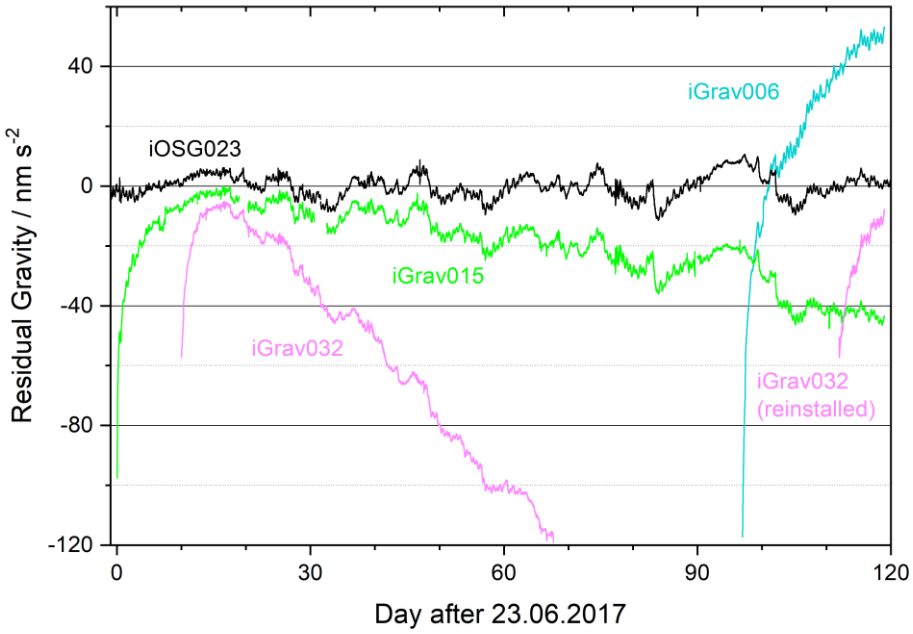


**Figure 16.** Time series from J9, showing gravity residuals of iOSG023, iGrav006, iGrav015 and iGrav032 after reduction of local tides and atmospheric pressure effects.

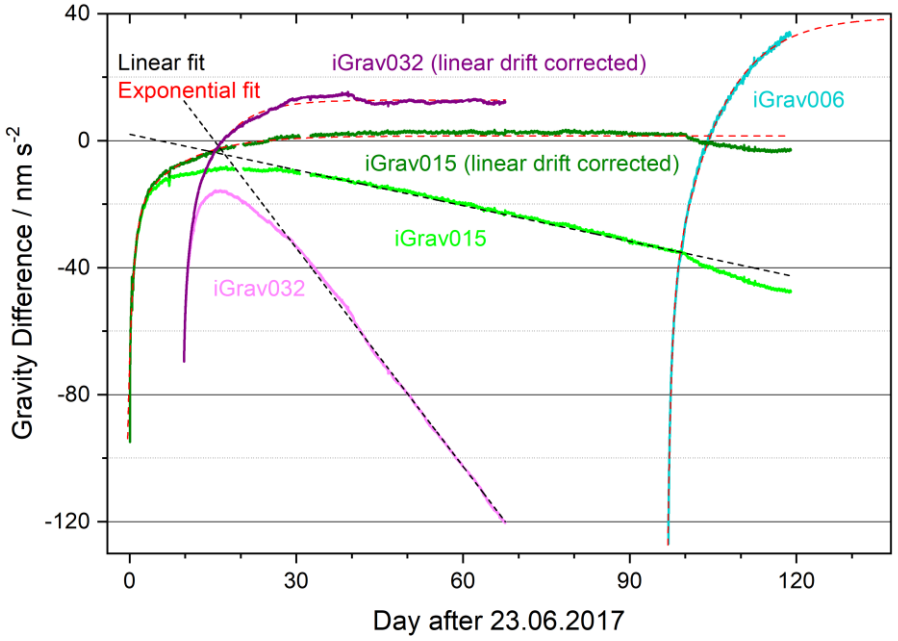


**Figure 17.** Time series from J9, showing gravity differences to the reference iOSG023 and subsequent linear drift correction for iGrav015 (dark green) and iGrav032 (purple), no linear drift corrections were done for iGrav006 and the reinstalled iGrav032 (after day 90 in Fig. 16) because of too short time series; dashed lines show linear (black) and exponential (red) curve-fittings for drift estimation; exponential fit for iGrav006 is extrapolated for days 120 to 137.

At Þeistareykir, the gravity monitoring sites are located at distances of several kilometres to each other (up to ~2 km at the geothermal field and ~17 km apart from iGrav015). For this reason, satisfactory reduction of site-dependent gravitational effects like solid Earth tides or ocean loading cannot be achieved by calculating gravity differences between two instruments as at J9 (in Fig. 17), where the gravity meters were installed inside the same building. Instead, we calculated local tidal models for each of the remote monitoring sites and used them for reduction of the iGrav time series.

Figure 18 shows the iGrav residual time series for the first 18 months of observation at the Þeistareykir remote monitoring sites. For instrumental drift characterisation, we used AG measurements (Hinderer et al., 2015) from two FG5#206 campaigns at Þeistareykir in June/July 2018 and June 2019. With the FG5 measurements as benchmark, we corrected the long-term linear drift of each iGrav. After AG correction, we used Eq. 3 to approximate the initial transient drift. The parameters for the linear and exponential corrections are summarised in the Appendix A (Tab. A5). Out of the three instruments, only iGrav006 shows the initial exponential behaviour as observed from the measurements at J9. At the Icelandic remote monitoring site, however, the exponential component of the iGrav006 residuals has smaller amplitude and time constants and is visible only for a few days after installation (see also Fig. A5, Appendix A).

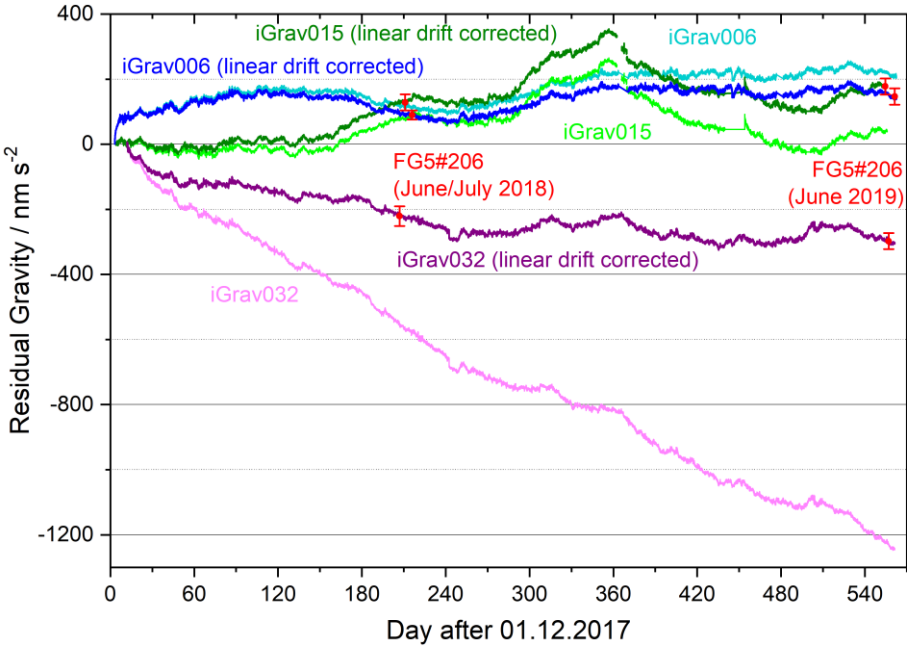


**Figure 18.** Time series from Þeistareykir, showing gravity residuals of the 3 iGravs (bright colours), long-term drift estimations by comparison to FG5#206 absolute measurements in summer 2018 and summer 2019 (red dots with error bars) and the resulting drift corrected iGrav residuals (bold colours).

A comparison of the linear long-term drift rates for J9 and Þeistareykir is shown in Table A6 in the Appendix A. The results from J9 show negative drift rates of -137 nm $s^{-2}$ per year for iGrav015 and -837 nm $s^{-2}$ per year for iGrav032. After transport to Iceland, we observe reduced negative drift rates of -92 nm $s^{-2}$ per year for iGrav015 and -597 nm $s^{-2}$ per year for iGrav032, and a positive drift rate of +70 nm $s^{-2}$ per year for iGrav006.

From our observations at J9 and Þeistareykir, only iGrav006 shows the expected drift behaviour of an initial transient function followed by a small linear term. The drift curves observed for both iGrav015 and iGrav032 were anomalous and can be described by a transient decay toward increasing gravity followed by a much larger negative drift. The problem was most likely caused by shipping iGravs 015 and 032 after side coils had been used to trap flux in the sphere, coils and shield. GWR attempted to remove the trapped flux from both iGravs by heating the sensors inside the vacuum can (above 32K) and letting them slowly recool to 4K, before shipment to Iceland. In later analysis, it was realised that this high-temperature annealing would

generally reduce the magnitude of the negative drift but would not eliminate it completely. In retrospect, it could have been more beneficial to warm these two iGravs to room temperature, subsequently recool to 4K at J9, and then activate them in Iceland without using the side coils.

The drift rates of iGrav015 and iGrav032 both decreased after transport to Iceland (Tab. A6, Appendix A). This reduction in drift rate most likely indicates that the high-temperature annealing of the sensor at J9 was effective. However, it has not been proven that the negative anomalous drift magnitude is linear. An alternative explanation is that the negative drift could also have an exponential component and that its magnitude slowly decreased in the time elapsed between operation at J9 and installation in Iceland.

## 3.6 Conclusions

We analysed continuous gravity measurements of three superconducting iGravs before and after transport to remote monitoring sites. We focused our investigation on calibration, noise and drift, and the influence of transport on these instrumental parameters. For calibration, we used AG (FG5#206) and RG (iOSG023) calibration methods. The stability of the AG calibration factors after transport from J9 to Þeistareykir was limited to 0.64% uncertainty, presumably by high noise disturbances on the AG measurements, from the nearby operating well pads at Þeistareykir. In contrast, the stability of the RG calibration factors was determined to better than 0.01%. For noise analyses, we used a three-channel correlation method. The comparison of noise levels confirms that the iGravs show resonance effects of the sphere and indicate a possible minor change of the iGrav self-noise of about 5 dB after transport to Iceland, although field conditions are also different from the conditions at J9. We estimated the instrumental drift by linear and exponential fitting of the iGrav time series. The results show that there is an exponential component, which presumably started after first initialisation of the iGravs. For iGrav006 (smaller Dewar and no side coils), the initial transient behaviour is also visible at Þeistareykir, which could have started after the sensor warmed up to 8K during shipment to Iceland. For iGravs 015 and 032 which both have side coils we observe negative

drifts after preparing and transporting at 4K (cold transport). The cause of the negative drifts is not yet understood. In fact, iOSG023, which has side coils, was also transported cold from GWR to J9 and its drift curve conforms to typical drift behaviour expected with SGs. Negative drifts have been observed not only in shipping iGravs from GWR to J9, and from J9 to Iceland, but also from GWR to other locations. The problem was diagnosed and removed from other iGravs (by warming the sensors to room temperature and re-cooling to 4K) about one year after the start of installations in Iceland. For the three sites in Þeistareykir, we plan further AG campaigns to validate and improve the long-term drift characterisation.

Our analyses revealed that:

1. Calibration is not affected by transport,
2. Noise is dependent on local conditions mostly, with only minor changes of the iGrav self-noise after transport,
3. Initial transient drift is reduced when the SGs are transported cold, but long-term drift rates cannot be transferred from one site to another without validation by repetitive AG measurements.

Our findings from the comparison measurements at J9 and the first results from the remote sites at Þeistareykir provide a promising basis for continuation of the long-term monitoring of the geothermal field. Further comparison to time-lapse micro-gravimetry carried out at Þeistareykir (Portier et al., 2020), is planned to improve the understanding of the general spatial distribution of the gravity changes within the geothermal field.

# Chapter 4

## Environmental and anthropogenic gravity contributions at the Þeistareykir geothermal field, North Iceland

*The content of this chapter has been accepted for publication in Geothermal Energy.*

Continuous high resolution gravimetry is increasingly used to monitor mass distribution changes in volcanic, hydrothermal or other complex geosystems. To quantify the often small target signals, gravity contributions from, e.g., atmospheric mass changes, global and local hydrology should be accounted for. We set up three iGrav superconducting gravity meters for continuous monitoring of the Þeistareykir geothermal field in North Island. Additionally, we installed a set of hydrometeorological sensors at each station for continuous observation of local pressure changes, soil moisture, snow and vertical surface displacement. We show that the contribution of these environmental parameters to the gravity signal does not exceed 10 µGal (1 µGal = $10^{-8}$ m $s^{-2}$), mainly resulting from vertical displacement and snow accumulation. The seasonal gravity contributions (global atmosphere, local and global hydrology) are in the order of ±2 µGal at each station. Using the environmental observations together with standard gravity corrections for instrumental drift and tidal effects, we comprehensively reduced the iGrav time series. The gravity residuals were compared to groundwater level changes and geothermal mass flow rates (extraction and injection) of the Þeistareykir power plant. The direct response of the groundwater levels and a time-delayed response of the gravity signal to changes in extraction and injection suggest that the geothermal system is subject to a partially

confined aquifer. Our observations indicate that a sustainable “equilibrium” state of the reservoir is reached at extraction flow rates below 240 kg $s^{-1}$ and injection flow rates below 160 kg $s^{-1}$. For a first-order approximation of the gravity contributions from extracted and injected masses, we applied a simplified forward gravity model. Comparison to the observed gravity signals suggest that most of the reinjected fluid is drained off through the nearby fracture system.

## 4.1 Introduction

Many geoscientific studies make use of continuous terrestrial gravity measurements to estimate subsurface mass changes associated with, for example, groundwater flow (Watlet et al., 2020), volcanic activity (Jousset et al., 2000; Carbone et al., 2019) or exploitation of geothermal reservoirs (Portier et al., 2018). Additional gravity effects from environmental phenomena, like Earth tides, atmospheric pressure changes, rain and snowfall superimpose onto the target signals of the gravity time series and have not been always considered, making interpretation inaccurate when gravity variations are small. The amplitudes of the environmental contribution in the recorded gravity signals range from a few hundred nGal (e.g. sea level rise) to several hundreds of µGal (e.g. large volcanic eruptions) and vary from seconds to years (Boy and Hinderer, 2006; Damiani, 2014). Mikolaj et al., (2019) pointed out the need to account for gravity contributions from atmospheric mass displacement, large-scale hydrology and nontidal ocean loading when performing local geophysical applications of terrestrial gravity measurements. They quantified the uncertainties of these corrections to be in the order of a few µGal, depending on the locations and the time scale of the mass variations of interest. Gitlein et al. (2013) modelled the combined gravity contributions of local and global atmospheric mass changes and applied them for reduction of superconducting gravity data, which improved the residuals by about 15% compared to the standard air pressure reduction with an admittance of -0.3 µGal $hPa^{-1}$. Voigt et al. (2021) used a superconducting gravity meter for hydrological monitoring of Mount Zugspitze and identified the snowpack as the primary contributor to seasonal water storage variations, with a snow-gravimetric footprint (i.e. snow related gravity contributions $>10^{-4}$ µGal) of up to 4 km distance around the gravity meter. In addition to environmental gravity contributions, artefacts

of the gravity meter like instrumental drift or self-noise may decrease the accuracy of the target signal (Crossley et al., 2004; Rosat and Hinderer 2018). With respect to long-term drift rates, Schäfer et al. (2020) showed the impact of transporting a superconducting gravimeter. Therefore, an accurate estimation and reduction of instrumental drift and environmental contributions is essential before we can interpret the gravity residuals accurately with respect to a specific geophysical phenomenon.

With the aim of estimating subsurface mass changes associated with geothermal exploitation (geothermal fluid extraction and reinjection), we set up a network of three continuously recording and remotely operated iGrav superconducting gravity meters, together with GNSS stations and hydrometeorological sensors (humidity sensors, snow gauges, pressure sensors, temperature sensors, etc.) at Þeistareykir, a geothermal field in North Iceland. This region is part of the North Volcanic Zone and is located close to the Husavik fault (Gudmundsson et al., 1993) and the Krafla Caldera (Ármannsson et al., 1987). Surface deformation and seismic activity associated to the mid-oceanic ridge have been monitored in Iceland for over 50 years (Sturkell et al., 2006). Surface explorations at Þeistareykir in the 1970s and 1980s suggested beneficial reservoir temperatures (< 280°C), which was confirmed after exploration well drilling between 2002 and 2012 (Óskarsson, 2015). We started our observations in December 2017 shortly after a new geothermal power plant (with 90 MWe total capacity) started operation in Þeistareykir. Figure 19 shows the location of the three superconducting gravity (SCG) stations. The east station (SCGE, iGrav032) is positioned in the vicinity of the geothermal extraction wells and the west station (SCGW, iGrav006) is located close to the reinjection wells. In June 2019, we started continuous measurements with iGrav015 at the central station (SCGC), in the transient area between geothermal extraction and injection. Schäfer et al. (2020) provide further details about the gravity station setup and the continuous observation chronology. Gravity observations are subject to various environmental contributions (e.g. rain, snow and soil humidity). Therefore, we deployed a series of instruments for measuring environmental parameters, which contribute to the total recorded gravity signal. Over more than three years, we acquired a unique data set of high-resolution gravity and environmental time series. We developed and applied an approach to reduce all environmental effects that may hide the geothermal mass changes.

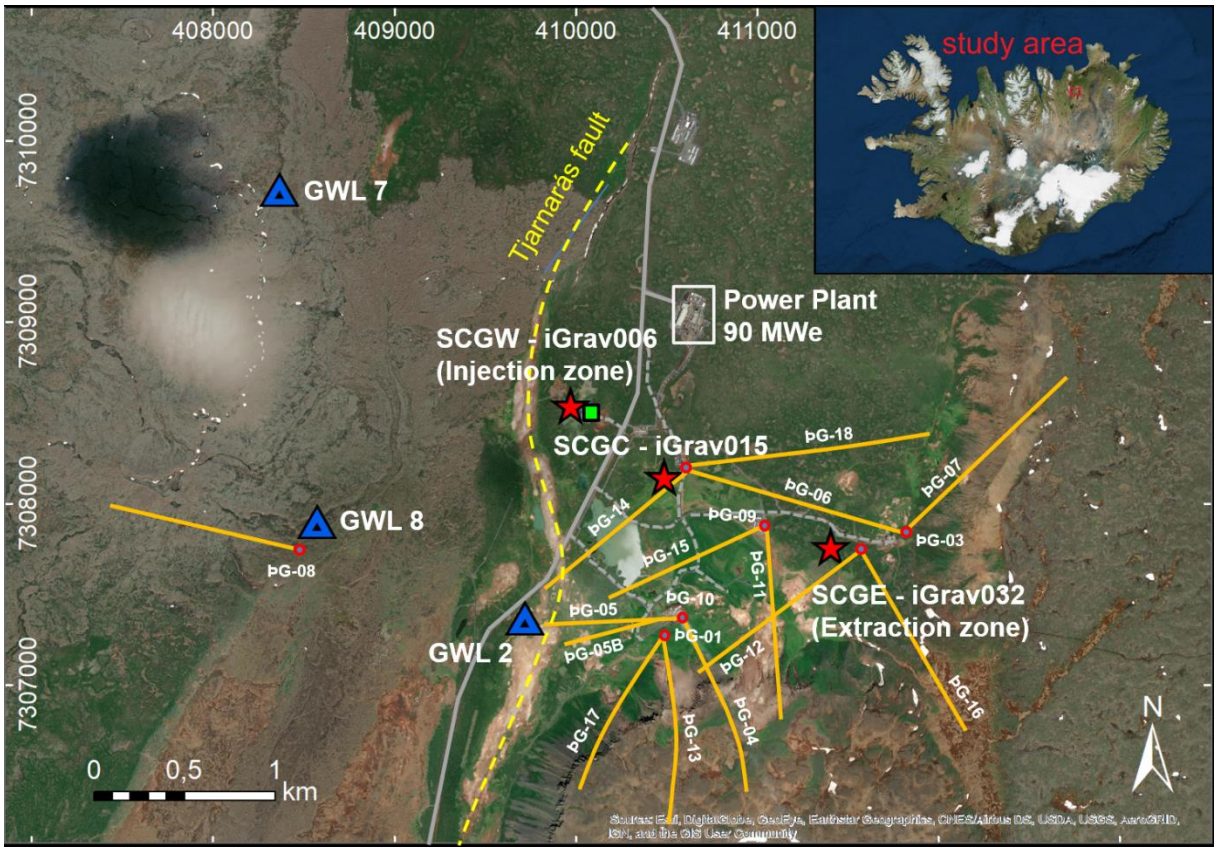


**Figure 19.** Location of the three continuous gravity stations (red stars) at Þeistareykir geothermal field in North Iceland; the east station (SCGE, iGrav032) is positioned in the vicinity of the geothermal extraction wells (well pads marked by red circles, orange lines show subsurface well paths), the west station (SCGW, iGrav006) is positioned in the vicinity of the reinjection well pad (green square) close to the Tjarnarás fault (yellow dashed line), the central station (SCGC, iGrav015) is positioned between the extraction and injection zones; groundwater level monitoring wells (GWL, blue triangles).

## 4.2 Methods for quantifying the gravity contributions

In this work, we assess the contributions of different geophysical phenomena to the observed gravity signals, based on observations and models. Equation 4 shows the gravity contributions examined in our study.

$$\Delta g_{obs} = \Delta g_{tide} + \Delta g_{atm} + \Delta g_{pm} + \Delta g_{glob} + \Delta g_{hydr} + \Delta g_{snow} + \frac{\delta g}{\delta h} * \Delta h + \Delta g_{geoth} + Error \quad (4)$$

These include gravitational effects induced by solid Earth and ocean tides $\Delta g_{tide}$, local atmospheric mass changes $\Delta g_{atm}$, polar motion $\Delta g_{pm}$, global atmosphere, large-scale hydrology and nontidal ocean loading $\Delta g_{glob}$, local hydrology in terms of soil moisture

changes $\Delta g_{hydr}$, snow $\Delta g_{snow}$, vertical surface displacement $\Delta h$ with the vertical gravity gradient $\delta g/\delta h$ and geothermal mass changes $\Delta g_{geoth}$. The "Error" in equation 4 consists of further gravity contributions like magma-induced mass changes from volcanic activity that are neglected in this study. For interpretation of geothermal related mass changes, we identified and reduced the interfering gravity effects that superimpose onto the target signal. To assess the contribution of the local environmental parameters in the gravity records, we analysed the continuous hydrometeorological measurements from remotely operated multiparameter stations (ROMPS; Schöne et al., 2013) at each site. Figure B1 in the Appendix B shows top view sketches of the ROMPS sensors and gravity containers for the three gravity stations. In the following subsections, we describe details of the instruments, the methods and the models for these individual gravity contributions, and we show the observed environmental signals recorded at Þeistareykir. In addition to the environmental parameters from equation 4, we also give a summary about the contribution and correction of instrumental drift.

### 4.2.1 Earth tides, local pressure effects, polar motion and instrumental drift

The largest gravity signal results from the solid Earth and ocean tides and is estimated by tidal modelling (Agnew, 2015). Besides the tidal parameters, we also estimated the barometric admittance factor for each station to be later used for the local pressure residual of the total atmospheric effect (see "global gravity contributions" below). Both, local tidal models and barometric admittance factors were computed for each gravity station at Þeistareykir using the ETERNA 3.4 package (Wenzel, 1996). Results of the tidal analyses are given in the Appendix B (chap. B1, B2 and B3). Due to the small distance of less than 2 km between the gravity stations, no significant changes of the tidal parameters were observed; with the main tidal waves varying by less than 1% in amplitude factors and less than 1 degree in phase. Therefore, we applied one uniform model for all three stations comprising the modelling results of SCGW and theoretical long period tidal parameters from solid Earth and ocean tides models (chap. B4, Appendix). The polar motion effect is provided as Earth orientation parameter file by the International Earth Rotation and References Systems Service (IERS;

https://hpiers.obspm.fr/eoppc/eop/eopc04/, Accessed 02 July 2021). We used the TSoft package (Van Camp and Vauterin, 2005) for computation of the associated gravity contributions. Detailed explanation of these standard corrections is given in Schäfer et al. (2020).

We examined and corrected the individual drift behaviour of the instruments by comparison to absolute gravity measurements (Hinderer et al., 2015). For this, we performed absolute gravity campaigns (with FG5#206) at each station once every year and adjusted the continuous time series to the absolute values. Figure B2 in the Appendix shows the drift corrections for the iGrav time series between December 2017 and October 2020. The uncertainties of the FG5#206 measurements at the three gravity stations (in summers 2018, 2019 and 2020) range between ±0.9 µGal and ±2.0 µGal. Initial exponential drift of a few days is removed for iGrav006. Schäfer et al. (2020) showed an overall reduction of drift rates for iGrav015 and iGrav032 suggesting that these two instruments may have exponential drift components with slowly decreasing magnitudes. This could be a reason for the strong initial gravity decrease of iGrav032 (-12 µGal after 40 days). However, for the long-term drift rates linear adjustments could be determined for all three iGravs (+6.1 µGal $yr^{-1}$ for iGrav006, +5.2 µGal $yr^{-1}$ for iGrav015 and -53.9 µGal $yr^{-1}$ for iGrav032) within the uncertainties of the FG5#206 measurements.

### 4.2.2 Global gravity contributions

In order to determine the contribution of global atmospheric mass variations in the gravity signal, we used the Atmacs model (Klügel and Wziontek, 2009). Besides the correction of the atmospheric effect by Atmacs, we additionally calculated the local pressure residuals and applied the remove-restore method suggested by the Atmacs service (http://atmacs.bkg.bund.de/docs/computation.php, Accessed 02 July 2021), using Atmacs model pressure and the locally recorded pressure at each station. The large-scale hydrological effects on gravity by continental water storage variations were considered by using the simulated soil moisture and snow water equivalent (SWE) of the land surface model NOAHv21 of the GLDAS model (Rodell et al., 2004). In addition, we computed nontidal ocean loading with the OMCTv06 model

(Dobslaw et al., 2017). The simulated storage and mass variations from both models were converted to gravity effects using the mGlobe toolbox (Mikolaj et al., 2016).

### 4.2.3 Local hydrology

At each station we recorded the variations of soil water content with in-situ soil moisture sensors. The sensors are arranged at different depths within soil profiles and at different distances to the gravity meter pillar (Table 4). From the soil moisture time series of all three gravity stations, we calculated the mean water content variations and their associated standard deviation at the four measurement depths (10 cm, 30 cm, 50 cm, 80 cm) and assigned those to the respective soil layers (0-20 cm, 20-40 cm, 40-65 cm, 65-95 cm). Assuming that the temporal variability of soil moisture decreases linearly with depth, we used the observed depth-dependence of the standard deviation to extrapolate at which depth it becomes zero, i.e., the threshold at which depth temporal variations of soil water content can be expected to vanish (Fig. B3, Appendix B). The soil moisture variations of the deepest observation depth at 80 cm were accordingly extrapolated to this threshold depth (here 1.8 m, see Fig. B3, Appendix B).

The calculated soil water content variations at the different depths, expressed in millimetre water equivalent were used as input variable to model the local hydrological gravity effects. Further, we included local digital elevation models (DEM) to account for topographic characteristics (i.e. relative height changes of the soil layers with regard to the gravity sensor). The hydro-gravitational modelling (HyGra) is based on the method of Leirião et al. (2009) and was adapted to gravimetric observatory buildings by Reich et al. (2019). HyGra is a spatially distributed model that enables the setup of a nested component grid (grid containing smaller grids of refined cell discretisation) with adjustable radii around the gravity station. We chose a small lateral discretisation (of 0.1 m) for the model cells closest to the gravity sensor (radius of 50 m) and larger model cells with increasing distance (1 m cells for 50 to 300 m radius and 10 m cells for 300 to 3000 m radius), and a vertical discretisation (cell height) of 0.1 m for every cell. The gravity sensor height above the ground surface of the DEM is 1.0 m. For the volume of the field container and the sub-surface column below the container, no (hydrological) mass changes were assumed

because the building shields the natural underground from direct infiltration of rain or snwomelt (“umbrella effect”, Creutzfeldt et al., 2008).

**Table 4.** Distribution of soil moisture sensors installed at different depths around each gravity station; some soil profiles are deployed at equal distances to the iGrav pillar (e.g. two profiles with 12.1 m distance at the SCGW), in these cases the sensors are installed below different micro-topographic features (e.g. small hills or terrain depressions).

| Gravity station | Nr. of sensors | Nr. of profiles | Profile distance to iGrav pillar [m] | Sensor depths [m] |
|---|---|---|---|---|
| SCGW | 14 | 4 | 6.5, 7.5, 12.1, 12.1 | 0.1 (4x), 0.3 (4x), 0.5 (4x), 0.8 (2x) |
| SCGC | 13 | 5 | 10.3, 11.9, 11.9, 13.4, 13.4 | 0.1 (5x), 0.3 (4x), 0.5 (3x), 0.8 (1x) |
| SCGE | 13 | 4 | 8.1, 8.4, 11.4, 11.4 | 0.1 (4x), 0.3 (4x), 0.5 (3x), 0.6 (1x), 0.8 (1x) |

### 4.2.4 Snow

To determine the mass changes of the snow cover around the monitoring stations in the course of snowfall and snowmelt, we continuously measured (every 15 minutes) the SWE, i.e., the amount of water that is stored in the snow cover in solid and liquid state by two snow monitoring instruments at SCGE (Fig. 20). We used a snow scale to determine the SWE by weighing the column of snow that is on top of a pressure pillow of 6.72 m² in size. Additionally, we used a snow pack analyser system (Sommer Messtechnik) equipped with strap sensors that measure (with an electro-magnetic approach) the specific volume contents of ice, water and air within the snow cover, from which the snow density is calculated. Snow depth is derived from travel time measurement of the pulse between an ultrasonic sensor and the snow surface. Snow density and snow depth are then used to calculate the SWE. We used the mean SWE of the time series of both measuring systems (snow scale and snow pack analyser) as input to calculate the gravity effect of snow with the HyGra model. It should be noted that the calculation of the snow gravity effect considered the actual thickness of the snow cover relative to the gravity meter sensor height, so that both positive and negative gravity contributions may occur, depending on whether parts of the snow cover are below or above the sensor, respectively. Piling up of snow on top of the gravity container was minimal because of the windy conditions at the sites, as

confirmed by daily photos of automatic cameras (see Fig. B1, Appendix B) deployed at each station. Also, based on the camera observations, no snow mass accumulation was observed within the first two meters around the container due to snow drift by wind. Thus, the snow mass in the near field of the gravity meter was neglected when computing the gravity effect of the snow cover.

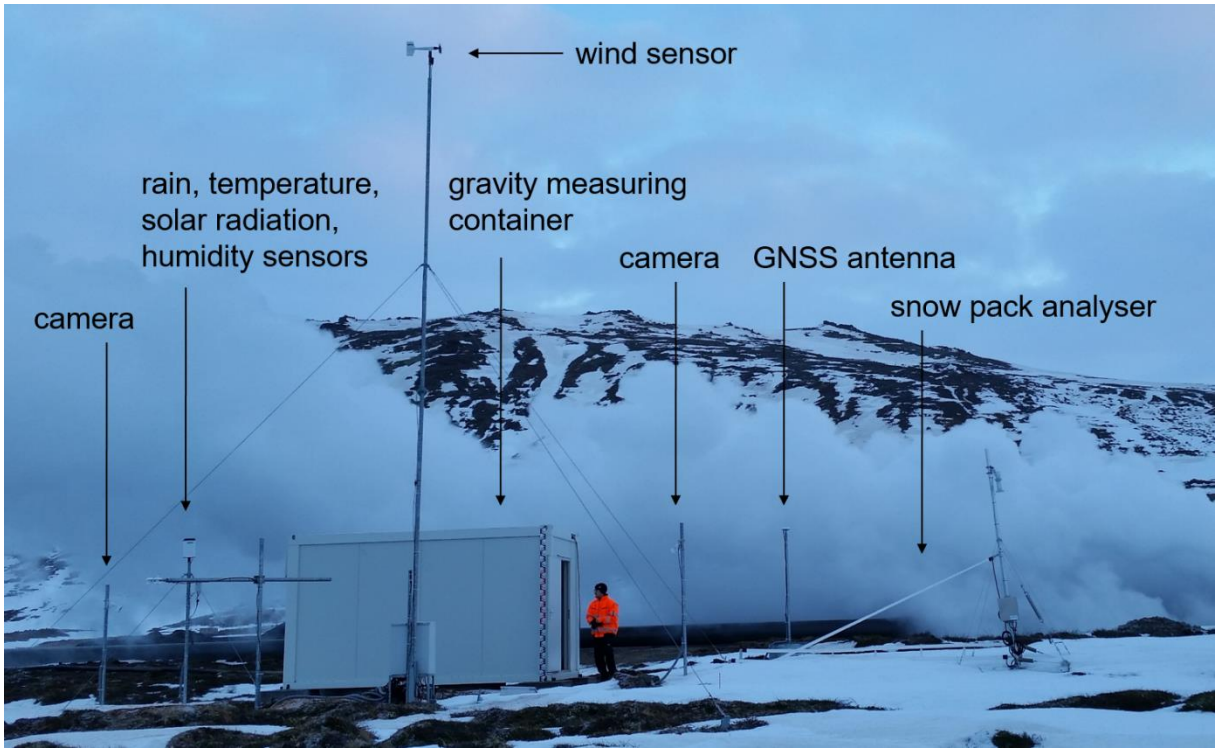


**Figure 20.** East station (SCGE) showing the container hosting iGrav032 and the outside setup of the remotely operated multiparameter station, the snow pack analyser is positioned on the right.

### 4.2.5 Vertical surface displacement

We used GNSS data observed at each gravity station at Þeistareykir to estimate the vertical surface displacement. The GNSS processing was performed using GFZ's EPOS.P8 software based on a classical network approach while introducing satellite orbits, clock corrections, and Earth rotation parameters from GFZ repro3 solution (Männel et al., 2020, 2021). According to the current IERS Conventions 2010 (Petit and Luzum, 2010) nontidal surface loading was not corrected.

To account for the contribution of the observed height changes to gravity we used the free-air vertical gravity gradient (FAG) measured by a Scintrex CG5 gravity meter (Portier et al., 2020). This method (Hunt et al., 2002) was realised by gravity

measurements with a tripod (at different heights above the concrete pillar) at each of the three gravity stations (Fig. B4, Appendix). We observed -319 µGal $m^{-1}$ for SCGW (iGrav006), -330 µGal $m^{-1}$ for SCGC (iGrav015) and -307 µGal $m^{-1}$ for SCGE (iGrav032).

## 4.3 Gravity contributions and geothermal signals

### 4.3.1 Local environmental observations at Þeistarykir

Figure 21 displays the measured environmental parameters for the three years study period at the Þeistareykir site. Table 5 gives the minimum and maximum values, and standard deviations for each parameter. The time series show daily values, representing the smallest common time interval of the obtained data.

Figure 21a shows the relative soil water content variations at different depths averaged from all soil moisture measurements at the three Þeistareykir gravity stations. The short and long-term soil water content variations are similar in their overall dynamics in all depth layers, but their amplitudes decrease with depth. We observe largest soil water content variations at 10 cm depth with a standard deviation of 1.45 Vol% and decreasing variations with increasing depth (SD of 1.10 Vol% at 80 cm depth, see also Figure B3, Appendix B).

The results of the snow measurements are shown in Figure 21b. The SWE time series from the snow pack analyser (black line) and the snow scale (red line) show simultaneous responses to snow mass accumulation during the three winter periods. However, there is a large difference in amplitude between the two monitoring systems, with signals more than ten times larger for the snow pack analyser than for the snow scale. This can partly be explained, by the different positions of the two instruments at SCGE (Fig. B5, Appendix B). As a result of different wind exposure, the snow cover can be expected to be different at the two installation sites. This is also confirmed by time-lapse photos taken by the automatic cameras at the site. Snow conditions at SCGE in the course of one year are shown in Figure B6 in the Appendix B. The differences between the two time series could also be due to systematic measurement errors of the devices. The snow scale is known to underestimate SWE because of the internal cohesion of the snowpack, i.e., the formation of snow or ice bridges between the snow pack on top of the scale and the

surrounding snow cover (e.g., Grossi et al., 2017). On the other hand, the lowest monitoring strap of the snow pack analyser used here for deriving SWE may tend to overestimate SWE because of the more compacted, denser snow pack at this depth, compared to the lower density snow in upper parts of the snow cover. To model the gravity effect of the snow mass, we used mean SWE values (blue line) from the two measuring systems.

In Figure 21c we show vertical surface displacement observed from GNSS monitoring at the three gravity stations at Þeistareykir (blue, green and red dots). The periodical variations of approximately ±5 mm per 3 months are caused by nontidal loading. For calculation of the vertical velocities, we applied a linear fit on the three years GNSS data (coloured lines in Fig. 21c). This revealed a significant subsidence of -11.1 mm $yr^{-1}$ for SCGW (blue line) and small trends of -1.5 and -0.3 mm $yr^{-1}$ for SCGC and SCGE (green and red lines). These values coincide with InSAR observations from the Iceland GeoSurvey (ÍSOR), which show increased subsidence rates of -7 to -8 mm $yr^{-1}$ in the injection zone (SCGW) between summer 2018 and 2019 (Drouin et al., 2020). For the subsequent gravity reductions, we only used the contributions from the vertical velocities (linear trends) of the GNSS data.

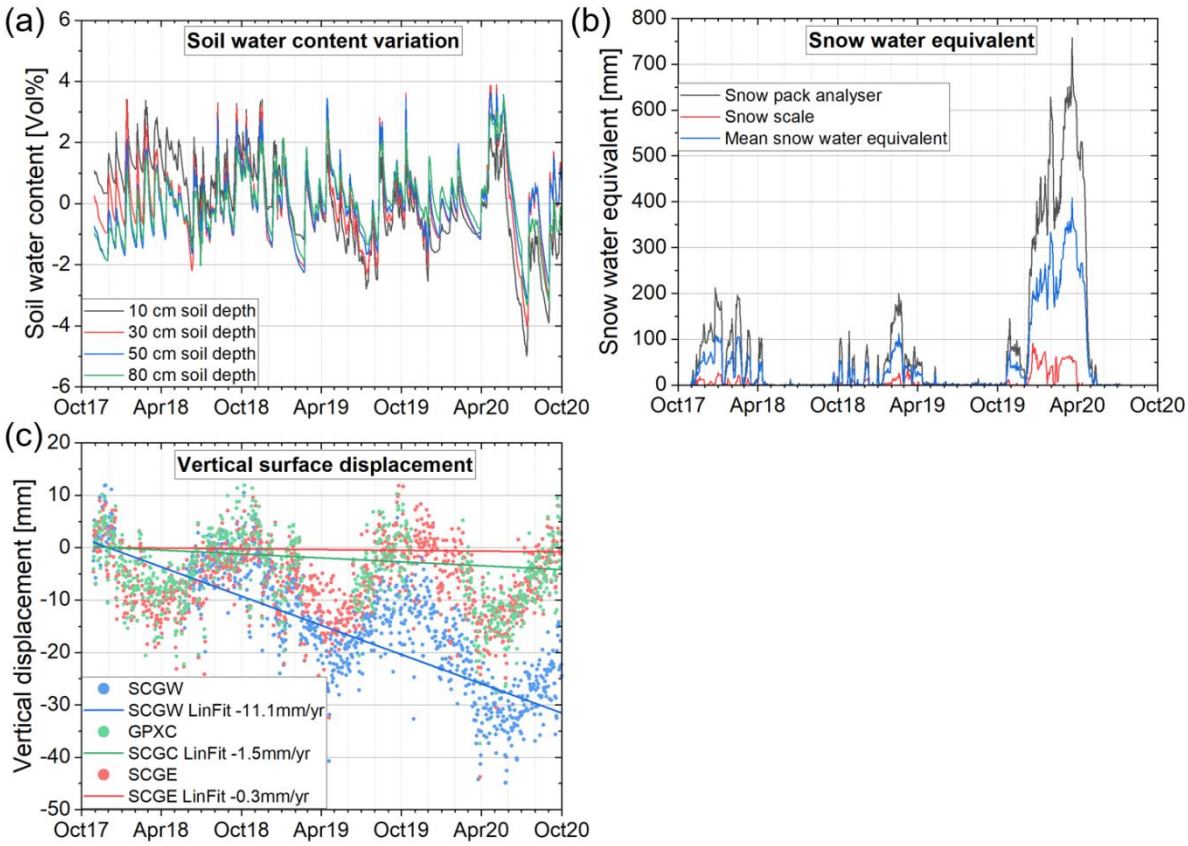


**Figure 21.** Environmental observations at Þeistareykir between November 2017 and October 2020; including (a) soil water content variations at different depths, averaged from soil moisture measurements at the three Þeistareykir gravity stations, (b) snow water equivalent observed from snow pack analyser and snow scale at SCGE, and (c) vertical surface displacement observed from continuous GNSS measurements at the three gravity stations and linear approximations; data gaps in the GNSS records (Dec. 2017 to May 2018 for SCGW, Feb. 2019 to June 2019 and Oct. 2019 to Feb. 2020 for SCGC) are due to receiver malfunctions.

**Table 5.** Quantities of environmental parameters (except tides) determined for the three gravity stations at Þeistareykir; including minima, maxima and standard deviations for soil water content variations at different soil depths, snow water equivalent and vertical surface displacement.

| Environmental parameters | | Unit | Min | Max | SD |
|---|---|---|---|---|---|
| **Soil water content variation** | 10cm depth | Vol% | -4.98 | 3.41 | 1.45 |
| | 30cm depth | | -4.00 | 3.89 | 1.26 |
| | 50cm depth | | -3.12 | 3.63 | 1.19 |
| | 80cm depth | | -3.33 | 3.52 | 1.10 |
| **Snow water equivalent** | Snow pack analyser | mm | 0.00 | 758.06 | 159.10 |
| | Snow scale | | 0.00 | 91.55 | 16.33 |
| | Mean snow water equivalent | | 0.00 | 408.13 | 86.02 |
| **Vertical surface displacement** | SCGW | mm | -51.51 | 11.89 | 11.58 |
| | SCGW linear trend | | 0.00 | 31.56 | 0.26 |
| | SCGC | | -37.39 | 18.21 | 7.03 |
| | SCGC linear trend | | 0.00 | 4.22 | 0.23 |
| | SCGE | | -43.78 | 15.42 | 6.98 |
| | SCGE linear trend | | 0.00 | 0.84 | 0.22 |

### 4.3.2 Environmental gravity reductions

Figure 22 shows the gravity contributions from global models (for the entire study area) and the observed environmental parameters (from Fig. 21) expressed in µGal for each of the three gravity stations at Þeistareykir. Table 6 gives the minimum, maximum and standard deviation for each parameter.

Among the global gravity contributions (Fig. 22a), the atmospheric effect (green line) shows the largest gravity contribution of more than 2 µGal. The gravity contributions modelled for global hydrology (red line) are dominated by a seasonal component, whereas the gravity signal of nontidal ocean loading (blue line) is of higher frequency. Both components have a minor effect for the reduction of the local gravity residuals. We expect mean uncertainties of 0.38 µGal for global hydrology and 0.17 µGal for nontidal ocean loading, based on the uncertainty assessment of Mikolaj et al. (2019). The total effect (black line) of these large-scale contributions to the local gravity observations has a seasonal amplitude of up to 4 µGal peak-to-peak and a standard deviation of about 1 µGal (Figure 22a, Table 6).

From all environmental contributions vertical surface displacement at SCGW (-11.1 mm $yr^{-1}$; see also Fig. 21) causes the largest gravity effect of up to 10 µGal over the entire observation period (Fig. 22d). Global gravity contributions and variations in soil water content only exhibit a very small contribution to the gravity variations observed by all three iGravs. For the reduction of snow, the gravity effect for SCGE and SCGC are larger than for SCGW, visible between December 2019 and May 2020 (Fig. 22c). This can be explained by the different topography surrounding the three gravity stations, considered as input parameter for the snow effect modelling. At SCGW with several little hills around it, a larger amount of snow cover is located at elevations higher than the gravity sensor of iGrav006. This creates a partly negative gravity effect and reduces the net gravity reduction of snow mass changes for SCGW.

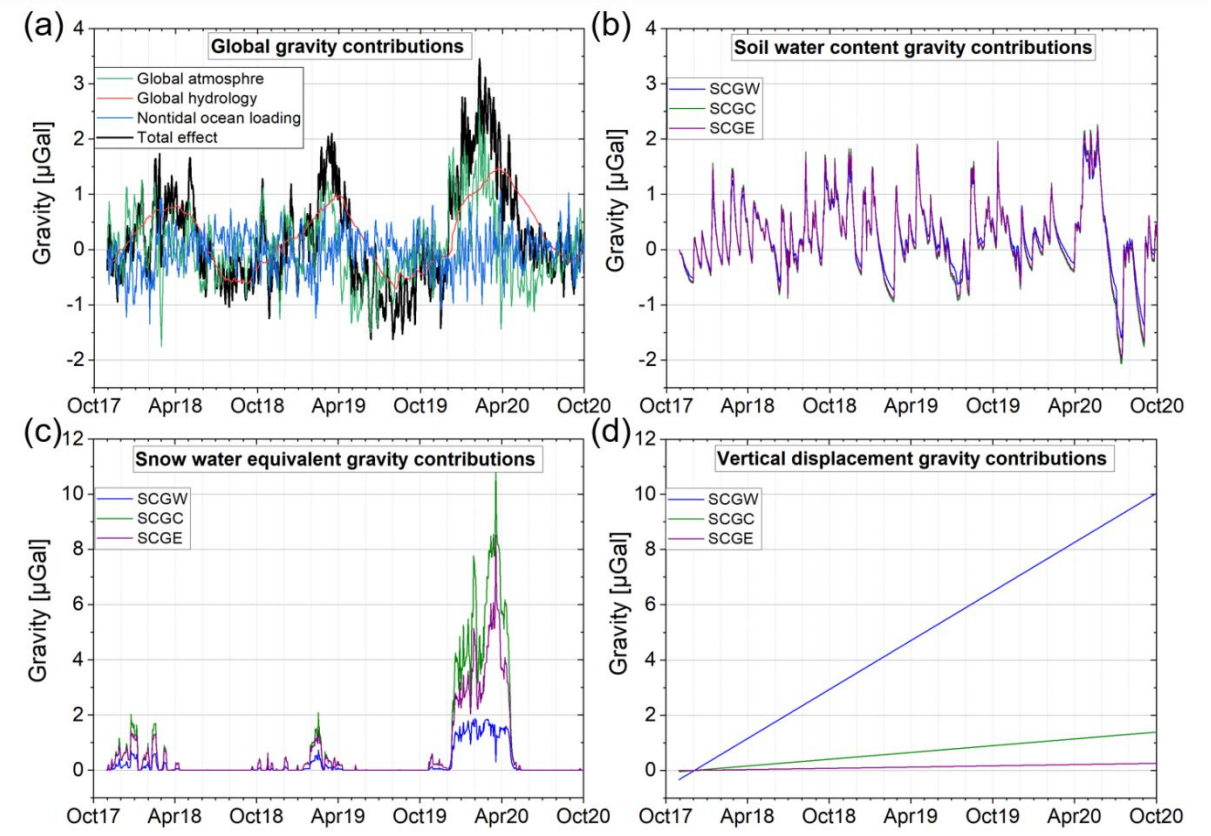


**Figure 22.** Environmental gravity contributions in µGal for each gravity station; (a) global gravity contributions, (b) soil water content variations, (c) snow water equivalent, and (d) vertical surface displacement derived from linear velocities.

**Table 6.** Quantities of environmental parameters (in µGal) determined for the three gravity stations at Þeistareykir; including minima, maxima and standard deviations for global gravity contributions, soil water content variations, snow water equivalent and vertical surface displacement.

| Environmental parameters | Station | Min | Max | SD |
|---|---|---|---|---|
| Global atmosphere | Entire area | -1.76 | 2.60 | 0.63 |
| Global hydrology | Entire area | -0.71 | 1.49 | 0.55 |
| Nontidal ocean loading | Entire area | -1.35 | 1.39 | 0.37 |
| **Total global effect** | Entire area | -1.62 | 3.45 | 0.91 |
| **Soil water content variation** | SCGW | -1.60 | 2.05 | 0.58 |
| | SCGC | -2.07 | 2.27 | 0.69 |
| | SCGE | -1.97 | 2.21 | 0.66 |
| **Snow water equivalent** | SCGW | 0.00 | 1.87 | 0.47 |
| | SCGC | 0.00 | 11.07 | 1.85 |
| | SCGE | 0.00 | 8.52 | 1.25 |
| **Vertical surface displacement** | SCGW | 0.00 | 10.92 | 3.26 |
| | SCGC | 0.00 | 1.51 | 0.45 |
| | SCGE | 0.00 | 0.28 | 0.08 |

### 4.3.3 Gravity residuals

In Figure 23 we compare the time series of gravity residuals of iGrav006, iGrav015 and iGrav032, before and after the combined environmental reductions of global effects, soil water content, snow water equivalent and vertical surface displacement. The initial residuals (before the aforementioned environmental reductions were applied) have been derived by reducing Earth and ocean tides, polar motion, local pressure and instrumental drift, as well as removing spikes and offsets (caused by earthquakes and other disturbances) from the original gravity time series (Schäfer et al., 2020). Reductions of the individual environmental gravity contributions for each iGrav are shown in Figures B7 to B9 in the Appendix B.

From linear regression of the reduced time series, depicted by dashed lines in Figure 24, we determined a gravity increase of 2.2 µGal $yr^{-1}$ for SCGW (iGrav006) and a gravity decrease of -9.0 µGal $yr^{-1}$ for SCGE (iGrav032). Figure 24 also shows the gravity differences between the iGrav residuals after reduction of the environmental contributions. The gravity differences of two instruments exhibit an additional reduction of variability and amplitudes, i.e. they are smoother than the

iGrav residuals themselves. This is because gravity changes that similarly appear at two stations cancel out to some extent in the differences. The remaining gravity variations can be attributed to effects that are locally different at the two stations and have not been reduced by the applied reduction models. Assuming that the local and large-scale gravity contributions as described above are precisely evaluated based on the in-situ observations and the standard models, these remaining variations can be mainly attributed to geothermal mass changes ($\Delta g_{geoth}$ in equation 4), induced by mass extraction in the vicinity of SCGE (iGrav032) and reinjection of effluent water close to the SCGW (iGrav006). For iGrav015, the gravity signal is more similar to iGrav032 than to iGrav006, which is clearly visible in the lower residual amplitudes of the differences between iGrav032 and iGrav015 (red line) compared to the differences between iGrav006 and iGrav015 (orange line). This suggests that SCGC receives a larger contribution to the gravity signal from mass extraction (depth ~2 km) rather than from mass reinjection (depth ~400m).

One particular phenomenon is the large gravity increase of about 10 µGal between May and July 2020, which is most pronounced in the signal from iGrav006. We assume this is due to local accumulation of snowmelt water (see also higher values of soil water content for that time; Fig. 22b) which drains off more easily at the other stations. At SCGW there is a small nearby lake which may contribute to this pronounced water storage increase for a period of several weeks. This anomaly (dotted sections in iGrav residuals in Fig. 24) was excluded for the linear approximations of iGrav006 and iGrav032.

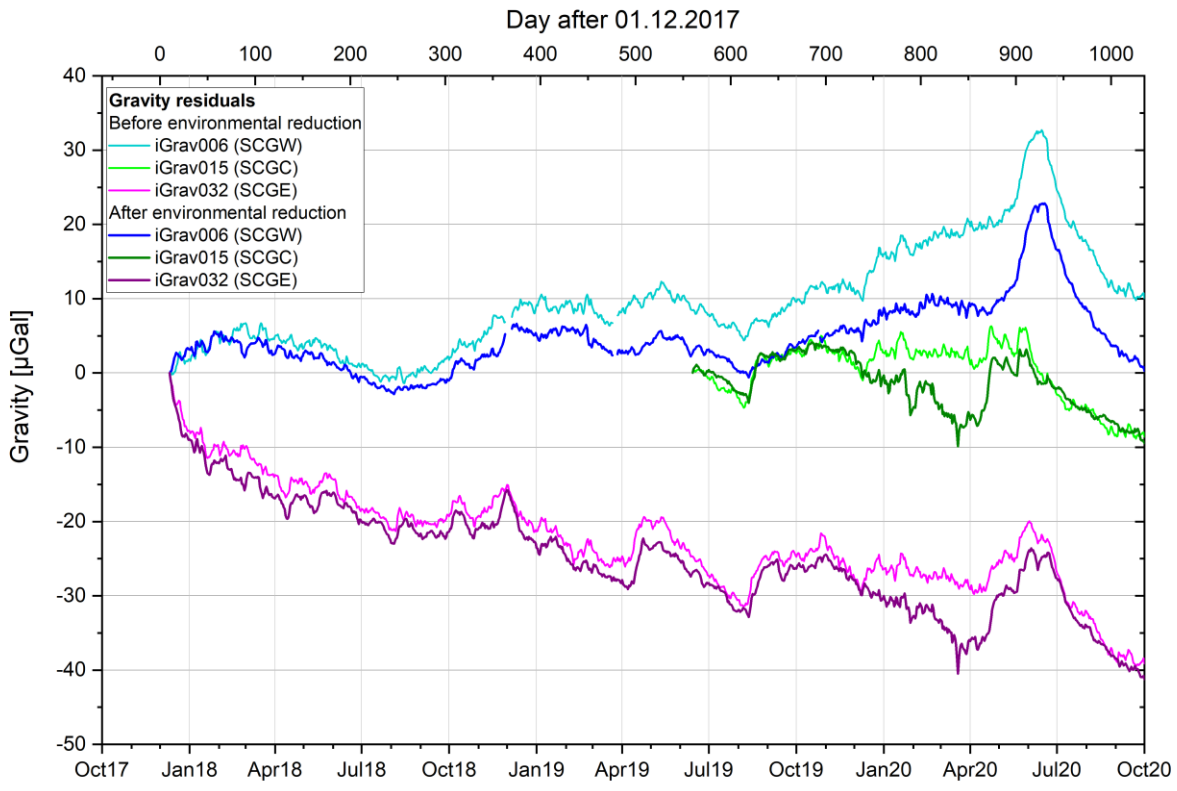


**Figure 23.** Gravity residuals of the three iGravs at Þeistareykir before and after the combined reduction of environmental effects including global effects, soil water content variations, snow water equivalent and vertical surface displacement (see Figs. B7 to B9 Appendix B for individual environmental contributions).

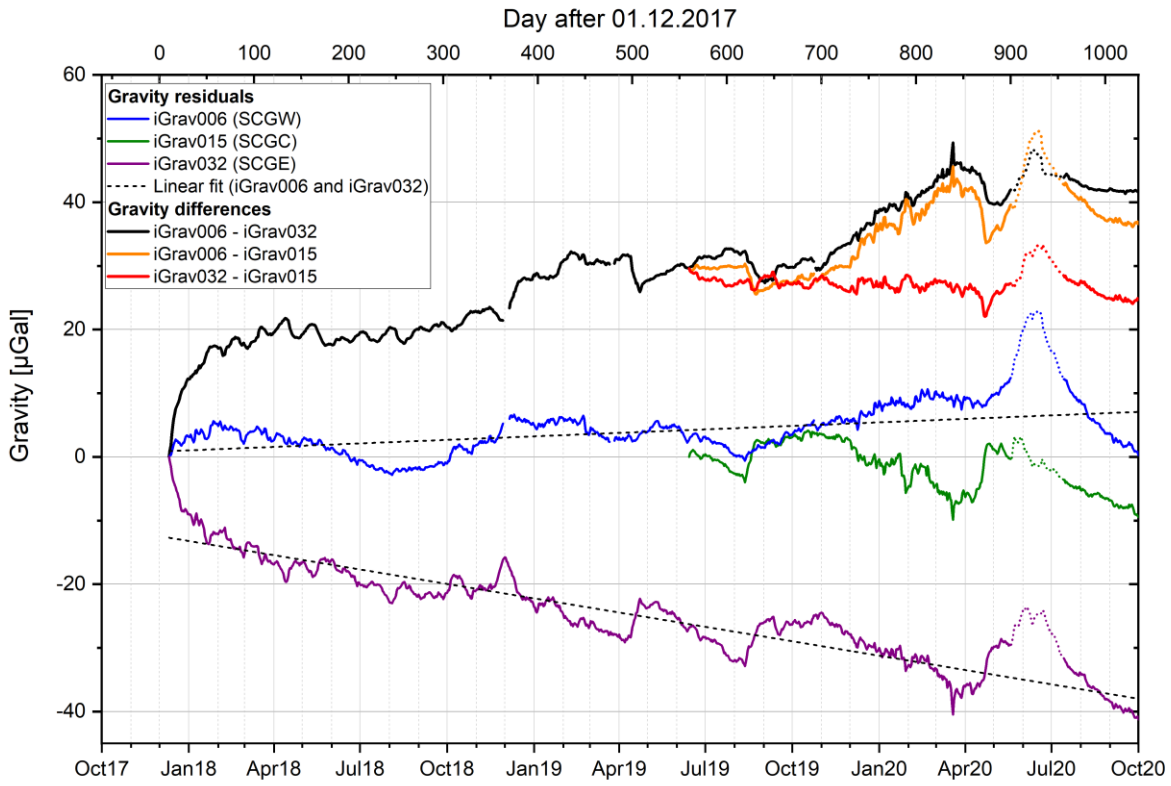


**Figure 24.** Gravity residuals and differences between iGrav006, iGrav015 and iGrav032 after reduction of global effects, soil water content variations and vertical surface displacement; dotted sections of gravity residuals show possible effects of snow melting between May and July 2020, which are excluded for the linear approximations for iGrav006 and iGrav032 (black, dashed lines).

### 4.3.4 Geothermal signals

We investigate the subsurface mass changes that are primarily caused by geothermal fluid extraction and reinjection activities at the Þeistareykir power plant. For this purpose, we compare the gravity residual time series (from Fig. 24) with relative groundwater levels (GWL) and geothermal flow rates at Þeistareykir. The latter two were supplied as local monitoring data by the power plant operator (Landsvirkjun). The locations of the GWL monitoring wells and the injection well pad are depicted in Figure 19. As shown in Figure 25, during the initial period, when injection flow is increased to just below 120 kg $s^{-1}$ (May 2017 until January 2018), only a slight increase of GWL of about 2 m occurs. After January 2018, when injection flow is increased above 180 kg $s^{-1}$, GWL increases at a higher rate and by

about 6 m until July 2018. For the subsequent periods of reduced geothermal flow rates (start of extraction and injection declines indicated by dashed arrows in Fig. 25) we notice an immediate descending response in the GWLs followed by a rebound when the flow rates are increased again. The direct response in the GWLs during periods of high extraction and injection flow rates suggests that the subsurface hydrology consists of pressure controlled systems. When the injection flow rates are reduced below 160 kg $s^{-1}$, pressure reduces instantaneously indicating that the reinjection system is open with a natural westward outflow in the order of the same amount towards the GWL monitoring wells. We observe similar effects for the gravity time series, like the long-term increasing trend in the differences (iGrav006 - iGrav032) and short-term gravity responses (decrease in the differences and increase in the iGrav015 and iGrav032 residuals; marked by A, B, C and D in Fig. 25) after reduced geothermal flow rates in March to April 2019 and July to September 2019. However, the gravity responses show time delays of several days up to weeks in comparison to the injection rates and GWL changes. For iGrav006 these responses are missing (or barely visible) in the gravity residuals. Although GWL observation wells are missing in the eastern (extraction) area of the geothermal field, these observations are indicating a boundary between the injection and extraction areas that can be assumed between SCGW and SCGC (s. below).

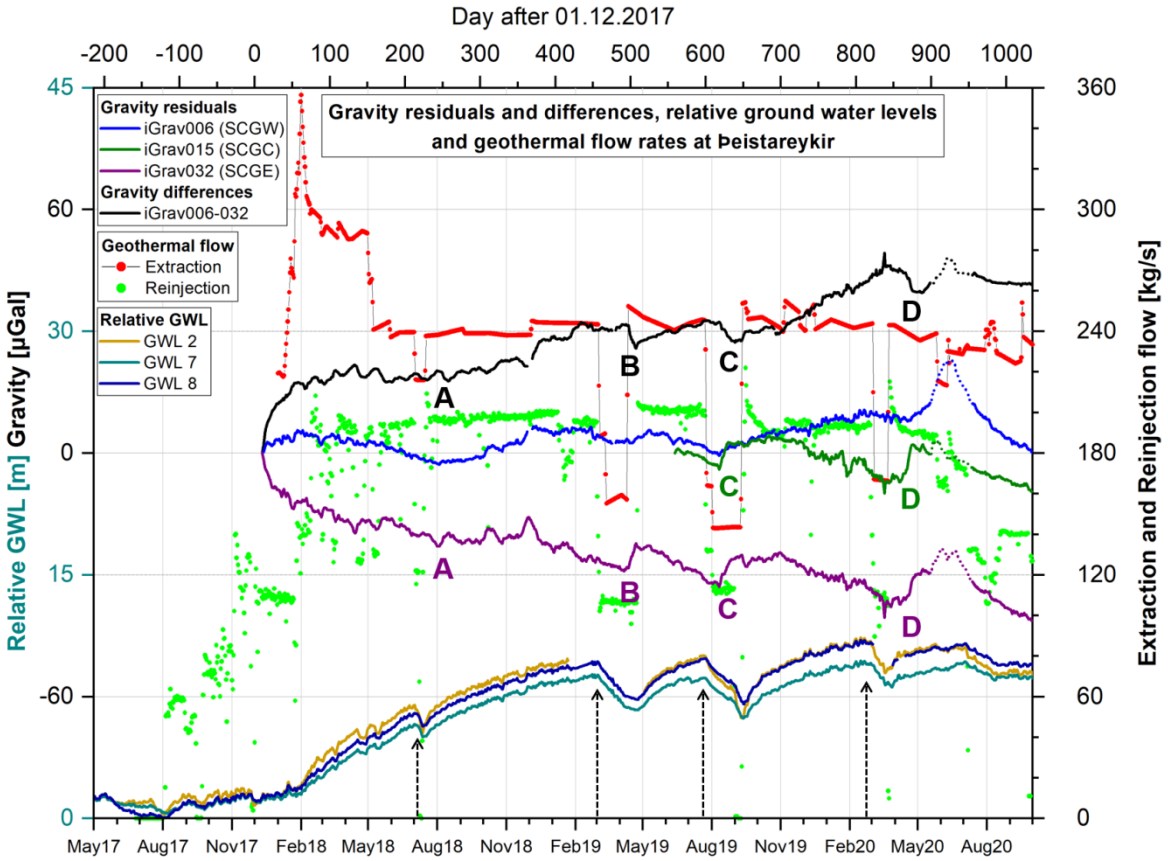


**Figure 25.** Comparison of iGrav residuals and gravity differences between iGrav006 and iGrav032 with relative groundwater levels (GWL 2, 7 and 8) and with geothermal extraction and injection flow rates of the Þeistareykir power plant from July 2017 until October 2020; dashed arrows mark the beginning of periods with reduced geothermal flow rates and capital letters mark possible response in the gravity residuals and differences (A, B, C and D; with same colour as the corresponding gravity time series).

## 4.4 Geothermal interpretation

### 4.4.1 Implications from gravity, groundwater and geothermal observations

Following temporary reduction in extraction and injection rates, the GWL data show a direct response, indicating that the reinjection aquifer is confined at high injection rates (above 180 kg $s^{-1}$) and that the observed response is relative to pressure change in the aquifer. The delayed responses in the gravity data indicate that groundwater is moving with different time constants in the extraction and injection areas, possibly due to pressure induced changes in permeability. These time delays may also be attributed to a season depended natural recharge in the area of the

extraction wells, resulting from e.g. rainfall or snowmelt events that recharge the groundwater system at larger distances from the monitoring site, e.g., on the surrounding volcano ridges, and that are thus not registered by the local hydrometeorological sensors at the gravity stations. In May 2020, injection and extraction were more permanently reduced, and the response of the gravity meters is also delayed. In addition, the gravity difference (iGrav006 - iGrav032) is not raising any more, suggesting that the mass difference may have become stationary between extraction and recharge, and injection and outflow. This could indicate that the system may has attained “equilibrium / steady state” conditions.

The gravity responses from iGrav015 and iGrav032 (marked by A, B, C and D in Fig. 25) are missing (or barely visible) in the iGrav006 residuals. This suggests that reinjected fluids cause a much lower gravity contribution, compared to extraction although the injection depth is much shallower than for extraction, which is another indication for an (to some extend) open injection aquifer. The varying gravity responses between SCGW and SCGE/SCGC additionally indicate that there is a boundary between the reinjection area in the west and the extraction area in the east. The location of this boundary may be indicated by the surface appearance of the Tjarnarás fault (yellow dashed line in Fig. 19). In order to understand and quantify those data, one should model the hydraulic features and adjust hydraulic parameters such as hydraulic diffusivity and consider other influences, such as the temperature and density of the fluid injected, and the detailed geology of the reservoir, as known from exploration drilling at Þeistareykir (Kewiy 2013; Óskarsson 2015; Gudjónsdóttir 2018).

In a first order approximation, from the GWL data observation, it seems that the “equilibrium / steady state” conditions for the injection aquifer may be reached when injection rate is around 140 kg $s^{-1}$ after about three years of power plant operation. Above that injection value, the pressure in the aquifer increases. This indicates that the aquifer is a partly open system with additional storage capacities for the reinjected fluids. Correlation between changes in reinjection and GWL changes west of the Tjarnarás fault system suggest that there is good pressure connection in the western compartment of the Þeistareykir geothermal reservoir. When injection rates are very low, the aquifer system tends to return to the initial state, prior the start of

reinjection. The data after June 2020, when power production was reduced by approximately 30% and extraction rates are in the order of 220 kg $s^{-1}$ (and ~140 kg $s^{-1}$ injection) suggests “steady state conditions” for such operation modus after about 3 years of operation. This hypothesis is also supported by the gravity observations in Figure 25: The difference between the gravity variations at SCGW and SCGE that was continuously increasing changes slope and remains more or less constant for the time interval observed after extraction decrease (June 2020).

Our continuous gravity monitoring results were also used in a hybrid gravity study including measurements of the three iGravs and a Scintrex CG5 gravity meter at Þeistareykir (Portier et al., 2021). The study with both gravity meter types confirms our observation of long-term gravity decrease at the extraction zone and minor gravity changes at the injection zone.

### 4.4.2 Newtonian gravity model of extracted and injected geothermal fluids

Using production data from Landsvirkjun (extracted geothermal fluid and injected water), we can compute the total mass extracted during the period from 2018 to 2020 (3 years, Fig. 26). This allows us to estimate a first order of magnitude of the expected gravity signal. The following modelling approach is based on the studies from Jousset et al. (2000).

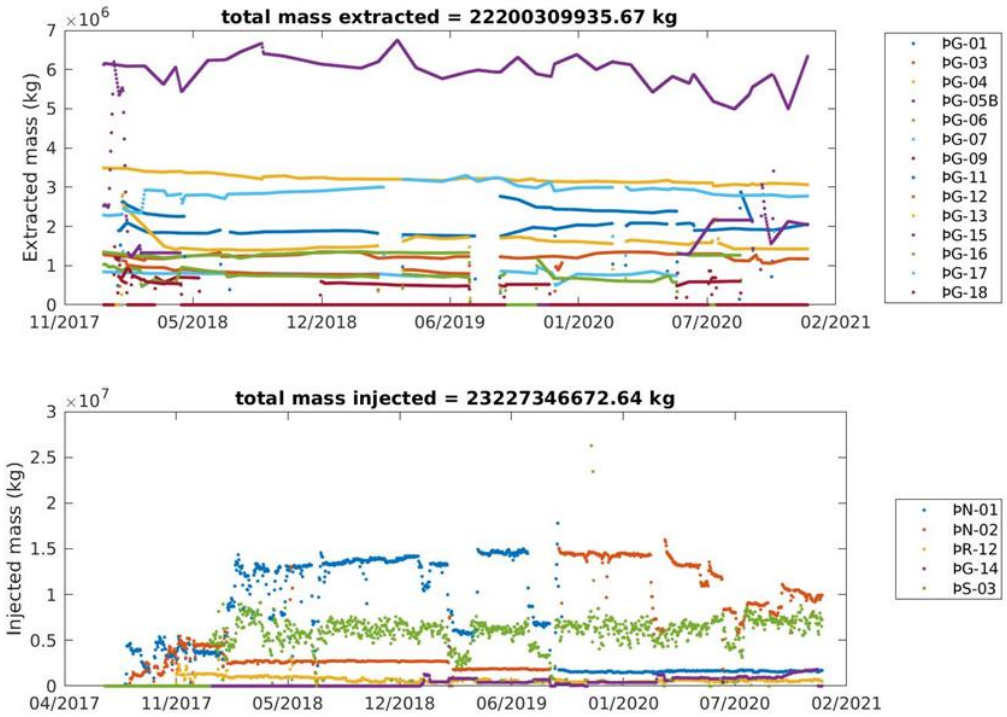


**Figure 26.** Daily mass transfer measured by Landvirskjun for each well (2018-2020); (top) extracted mass, (bottom) injected mass; note that injected mass is slightly larger than extracted mass due to an additional small amount from the cooling tower processes (different of about less than 5%) corresponding to an average mass transfer of about 235 to 245 kg $s^{-1}$.

As first estimation of the expected gravity signal, we computed separately the contributions of extracted and injected masses, assuming that there is only one well which extracts (or injects) the total mass (~2.3 $10^{10}$ kg) between starting and end point. As we are in volcanic terrain, we assume that masses are extracted from and injected to a single layer at the bottom depth of the wells below surface, ~2000 m for extraction and ~400 m for injection. We assume the thickness of the layer to be 20 m, with porosity of 10%. When mass is extracted (or injected) the affected volume is supposed to be confined in the layer, and we assume that the influence is isotropic. Therefore, the affected area of the model has a cylindrical shape. Equation 5 and Table 7 show the results for such configuration. The final radius of the cylinder is less than 2000 m. For the extraction (depth 2000 m), the amplitude of the gravity signal above the cylinder is of the order of -20 to -30 µGal at the surface. For the injection

(depth 400 m), the amplitude of the gravity is about +60 to +70 µGal. The net gravity should then increase, by about 30 to 50 µGal.

$$g = 2 * \pi * G * \rho * \varphi * (h + \sqrt{z * z + r * r} - \sqrt{(z + h) * (z + h) + r * r}) \quad (5)$$

**Table 7.** Estimation of the gravitational attraction associated with a cylinder a depth.

| Parameter | Symbol | Value |
|---|---|---|
| Gravitational constant | G | 6.67 $10^{-11}$ $m^3$ $kg^{-1}$ $s^{-2}$ |
| Volumic mass cylinder | ρ | 1000 kg $m^{-3}$ |
| thickness cylinder | h | 20 m |
| height above cylinder | z | 2000 m |
| Porosity | φ | 0.1 |
| Mass considered | M | 23652000000 kg |
| Fluid volume | $V_{fluid} = M/\rho$ | 236520000 $m^3$ |
| Rock total volume | $V_{total\ rock} = (M/\rho)/\varphi$ | 2365200000 $m^3$ |
| Volume cylinder | $V_{cyl} = \pi*r*r*h$ | |
| Radius cylinder | $r_{cyl} = sqrt(V/(\pi*h))$ | 1940 m |
| Gravity (including porosity) | g | 2.35 $10^{-7}$ m $s^{-2}$ |

As a further attempt to describe more accurately the gravity changes and follow temporal evolution, we computed the daily mass transfer contribution of each well (extraction and injection) for each gravity station (SCGW, SCGC and SCGE). Assuming that each well affects a cylindrical area surrounding the feed zone location at depth, we computed the attraction due to mass extraction and injection for each gravity station with time (1 value per day). Figure 27 shows the locations of the iGravs and the feed zones for each well. Figure 28 shows the results of the continuous gravity model for each gravity station. The largest gravity contributions result from the injection wells (near SCGW) because the injection depth is closer to the surface than for extraction.

The orders of magnitude found from both computations are larger than the observed gravity amplitudes. In particular, for injection, those results suggest that most of the injected fluid is transported away through the Tjarnarás fault system, leaving the geothermal area or returning into the deep reservoir. More detailed computations are required to better understand the influence of the heterogeneous reservoir parameters and to conclude on recharge processes and long-term behaviour of the geothermal field.

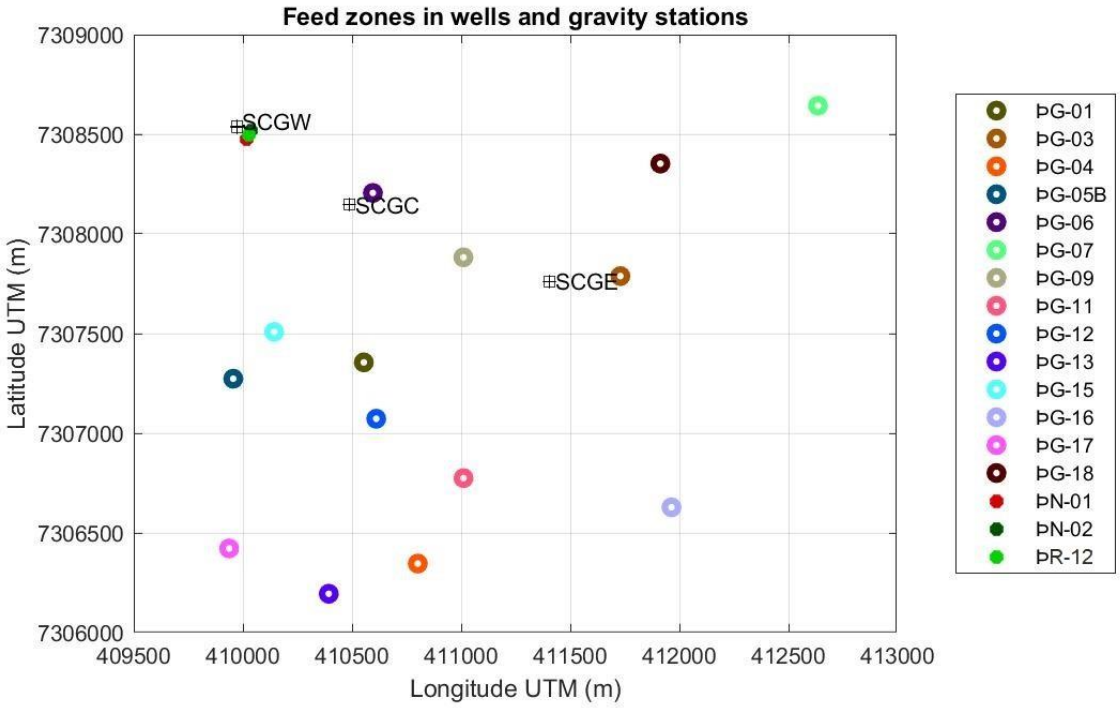


**Figure 27.** Feed zone and gravity station locations.

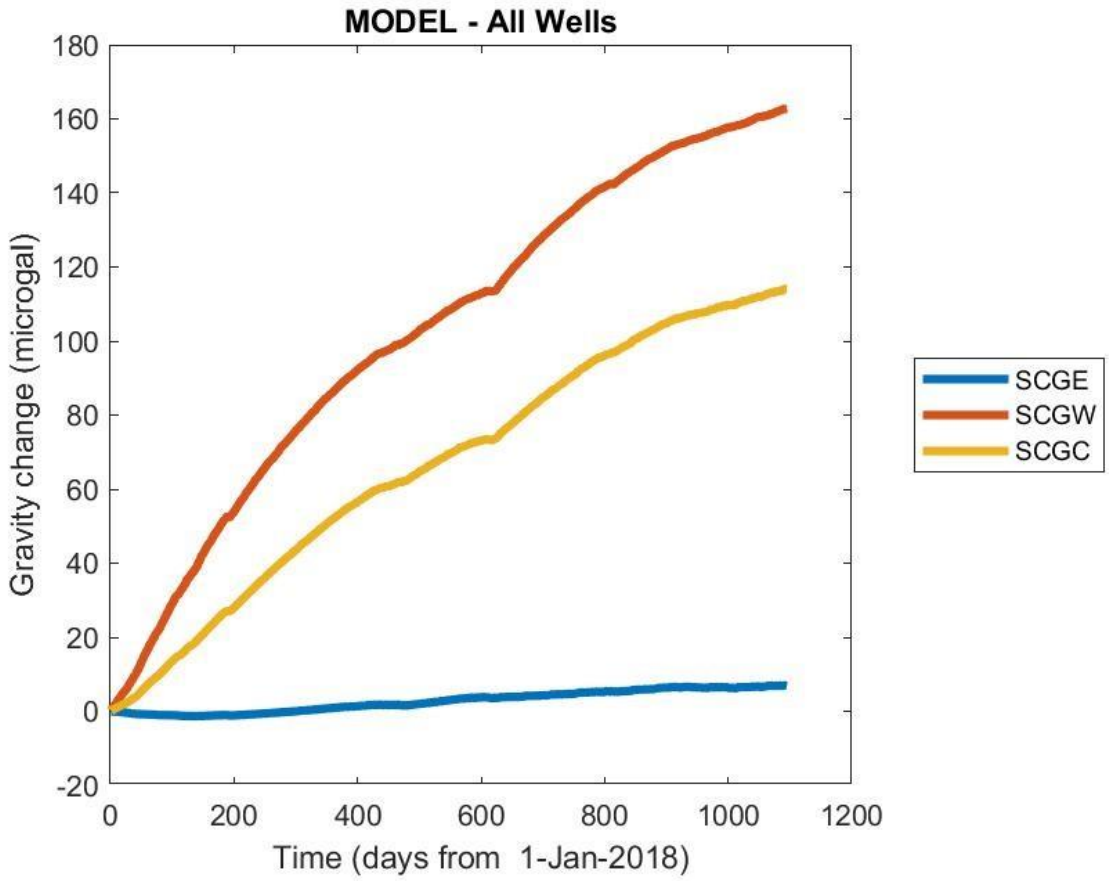


**Figure 28.** Gravity modelled for the three gravity stations considering masses extracted/injected from all wells. Although the mass balance is close to zero in the modelling, gravity increases as the injected mass is located closer to the surface, explaining that the modelled total contribution is positive at all three locations.

## 4.5 Conclusions

We deployed and maintained a network of multiparameter stations including three iGravs superconducting gravity meters for more than three years at the Þeistareykir geothermal field in North Iceland. This allows us to monitor and detect mass changes associated with environmental and geothermal phenomena. The continuous gravity records were reduced from environmental contributions by means of accurate measurements and modelling of global effects, hydrology, snow and vertical surface displacement. The amplitudes of the environmental contributions never exceeded 10 µGal (except tides). Residuals were interpreted in terms of groundwater level

changes and redistribution of geothermal fluids. The analysis of the continuous observation data revealed:

- Gravity increase of 2.2 µGal $yr^{-1}$ at the site above injection (as expected due to the injected water mass).
- Gravity decrease of -9.0 µGal $yr^{-1}$ at the site above the extraction of mass.
- Direct correlation between groundwater levels/pressures and injection flow rates, which indicates that the reinjection system is subject to a confined aquifer.
- Delayed responses in the gravity signals only above the extraction zone, indicating that there is a reservoir boundary between the reinjection and the extraction areas.
- The observed responses in groundwater levels and gravity indicate that the hydraulic response of the hydrothermal system is mainly governed by a partially filled aquifer up to injection flow rates of 140 kg $s^{-1}$ for which the system may have reached steady state conditions between extraction, natural recharge, injection and outflow. Above this value the injection system is over-pressurised.
- Comparison to a simplistic gravity model of the extracted and injected water masses shows larger amplitudes than the observed gravity signals at the injection zone, which indicates a quick fracture-favoured run off of the reinjected fluids. However, due to the very heterogeneous underground, refined computations are required to fully understand the complex mass transport processes within the geothermal system.

This study demonstrates that a network of multiple gravity stations is useful for monitoring geothermal reservoirs and for determining steady state injection and extraction conditions. In addition, it shows that observations of environmental parameters are fundamental to obtain accurate estimations of geothermal signals in volcanic environments. This study may also be useful for understanding gravity changes occurring at active volcanoes, where the effects of environmental parameters must be accurately evaluated, in order to understand volcano-related mass changes.

# Chapter 5

## Hybrid microgravity monitoring of the Theistareykir geothermal reservoir (North Iceland)

*The content of this chapter has been submitted to Pure and Applied Geophysics.*

The Theistareykir geothermal field is located in North Iceland on the Mid-Atlantic ridge. A power plant produces 90 MWe using two 45 MWe turbines in operation since autumn 2017 and spring 2018, respectively. We performed hybrid microgravity measurements from 2017 to 2019 to monitor the short-term mass redistribution induced by geothermal production.

Time-lapse microgravity surveys conducted each summer with a Scintrex CG5 gravimeter reveal the spatial gravity variations with respect to a reference, where the temporal gravity changes are monitored by absolute gravity measurements done with FG5#206 from Micro-g Solutions. In parallel, continuous gravity changes are recorded by a network of several GWR Instruments iGrav superconducting gravimeters and spring gravimeter located in the injection and production areas. The gravity data are reduced for the contribution of vertical displacement.

We notice a regular residual gravity decrease in the production area versus a stable behaviour in the injection area. Time-lapse gravity measurements reveal a minimal value of -38 +/- 10 µGal (1 µGal = $10^{-8}$ m $s^{-2}$) in 2019 with respect to 2017. A simplistic forward modelling of the produced geothermal fluid using a multiple Mogi sphere model can partly explain the residual gravity decrease. This would suggest that a significant part of the injected geothermal fluid flows away, maybe drained by

the Tjarnarás fault to the South where an increase of the water table level is observed. However, further modelling work would be needed to confirm this result.

## 5.1 Introduction

Iceland is subject to intensive volcanic activity induced by the interaction between a hot spot due to a deep-sealed mantle plume (Wolfe et al., 1997) and the Mid-Atlantic ridge. This makes it a suitable place to harness geothermal energy. Geothermal energy is produced both for direct use (~61%), especially heating houses, and for power generation (~39%) in Iceland (Ragnarsson et al., 2020). In 2019, it represents around 30% of the produced electricity in the country with a cumulative capacity of geothermal plants being equal to 755 MWe (Ragnarsson et al., 2020). At the Theistareykir geothermal plant, 90 MWe is generated using two 45 MWe turbines in operation since autumn 2017 and spring 2018, respectively.

This renewable energy is not always sustainable (Axelsson, 2011). The sustainability of the exploitation can be assessed by establishing the balance in heat and flow transfer (outflow for production, and inflow by reinjection).

Microgravity monitoring is a key tool to study mass redistribution induced by geothermal production and to understand fluid recharge of the reservoir (Oka et al., 2012; Guðnason et al., 2015; Portier et al., 2018; Hersir et al., 2020). Previous studies highlighted the efficiency of this non-destructive geophysical and quick implementation method. The undisputed advantage of microgravity monitoring is its uniqueness to quantify the recharge of a geothermal system. Consequently, we choose to apply a complete hybrid microgravity experiment in the Theistareykir geothermal field using superconducting gravimeters (continuously measuring), an absolute gravimeter (yearly measurements at specific stations) and a relative spring gravimeter (yearly repetition of a micro-gravity network). This study began in summer 2017 before the start of the geothermal exploitation and especially the beginning of the injection, thus allowing the investigation of the initial short-term mass redistribution.

## 5.2 The Theistareykir geothermal field

The Theistareykir geothermal field is located in North Iceland on the boundary between the North American and the Eurasian tectonic plates, which drift apart with a

velocity of 18-19 mm $yr^{-1}$ (Sigmundsson et al., 2020). The Northern Volcanic Zone (NVZ) intersects the active transform Tjörnes Fracture Zone (TFZ) (Fig. 29a), resulting in a highly fractured area with a preferential North-South orientation. Both sub-glacial eruption products (hyaloclastites typically formed of pillow basalts, breccias and tuffs) and recent basaltic lava flows (younger than 10,000 years) constitute its bedrock (Fig. 29c).

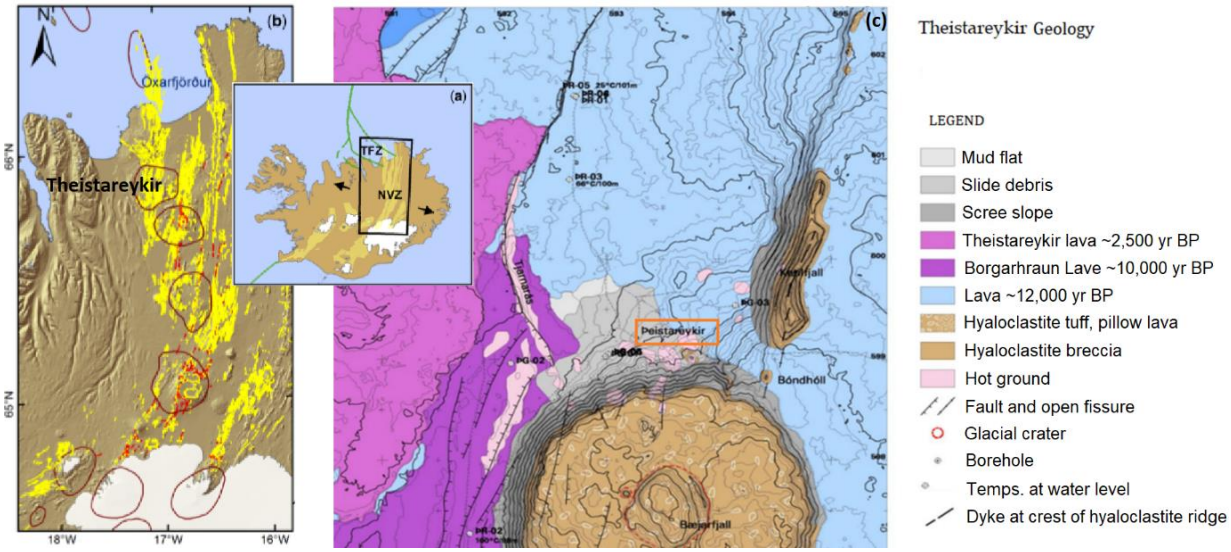


**Figure 29.** The Theistareykir geothermal field in the Icelandic Northern Volcanic Zone (NVZ (a) Map of Iceland showing the Northern Volcanic Zone (NVZ) and the Tjörnes Fracture Zone (TFZ). The green lines indicate the offshore tectonic plate boundary. (b) Location of the Theistareykir geothermal field in the NVZ (black rectangle on the map (a)). Fractures and eruptive fissures are drawn in yellow and red, respectively. The brown circles mark the central volcanoes. (c) Geological map of the Theistareykir geothermal field.) ((a) and (b) from Hjartardóttir et al., 2016; (c) from Saemundsson, 2008).

### 5.2.1 Exploration

Surface exploration of the 11 $km^2$ Theistareykir geothermal area started in the 1970s. Gravity measurements were performed in 1981-1983 (Gíslason et al., 1984). The produced Bouguer-map indicates a large gravity depression stretching from NW of Mt. Bæjarfjall to NE of Lambafjöll. This large depression is where two low-gravity structures meet; one N-S trending which appears to follow the Theistareykir fissure swarm and another NW-SE trending (north of Lambafjöll) which is likely to be connected to the Húsavík Fracture Zone. From 1981 to 1984, Ármannsson et al. (1986) studied the gas geothermometers of 34 fumaroles, from which they divided Theistareykir into five subareas (Fig. 30). Three of them were selected as a potential target for geothermal production: the Ketilfjall A, the Theistareykjagrundir C and the

Tjarnarás D zones. In order to study the temporal temperature evolution of the three subareas (A, C and D), new chemical analyses of fumaroles were performed between 1991 and 1997, and then between 2012 and 2013 (Óskarsson, 2015). The temperature of the Theistareykir geothermal reservoir was estimated to be at least around 280°C. They also showed that the geothermal fluid would originate far from the South; it would be older than 100 years (Ármannsson, 2008).

Following the exploratory drilling of four shallow wells to characterize the groundwater table, first productive wells ThG-01 and ThG-02 were drilled in 2002 in the C area and in 2003 in the D area, respectively (Fig. 30). In 2008, the geothermal field counted six wells. Transient electromagnetic and magnetotelluric measurements were also performed in 2004-2006 and 2009-2011 to highlight four alteration zones, which define the resistivity structure of the geothermal area (Karlsdóttir et al., 2012; Kahwa, 2015). The new information deduced from the well logs and drill cuttings combined with the results of surface exploration, resistivity data and fluid samples enabled Guðmundsson et al. (2008) to define a model of the geothermal reservoir (Fig. 30). The conceptual model assumes a 300°C vapour at around 2 km depth subjected to thermal upflow, which is most pronounced in the C subarea. In this area, the vapour would migrate and condensate to supply shallower cavities with a 250-280°C liquid phase. Then, a secondary steam would be created by the reduced thermal upflow and reaches the surface. This seems to be confirmed by the geothermal surface activity (fumaroles, mud and hot springs) observed on the northwestern side of the Bæjarfjall volcano (in the C and D subareas). Within the D area, one part of the primary steam would be cooled to 200°C in open fractures whereas another part, as residual steam, would directly reach the surface. Guðmundsson et al. (2008) estimated the potential of the geothermal system to be 104 MWe for 100 years of production.

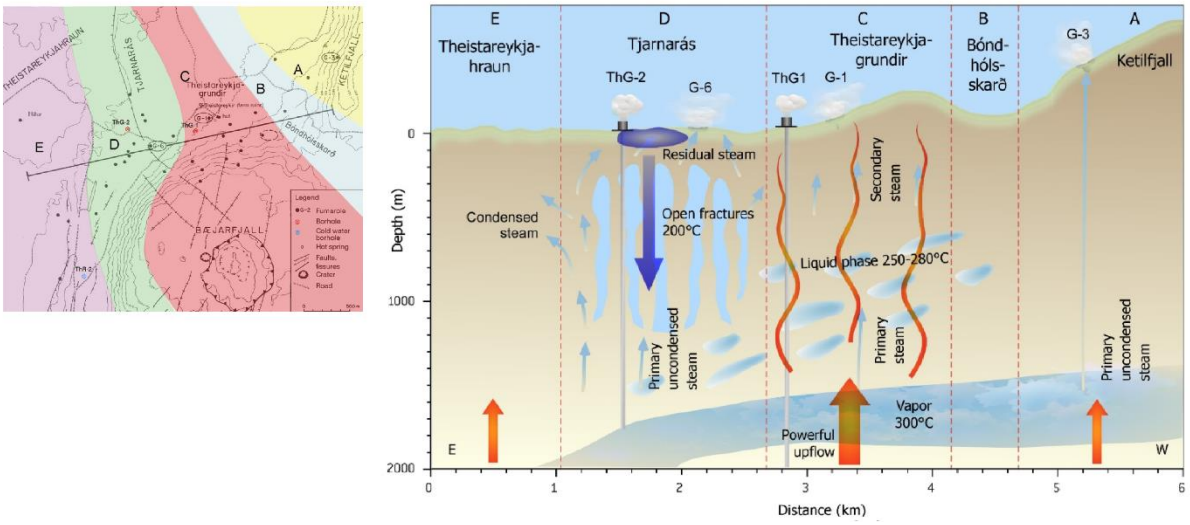


**Figure 30.** Map of the five subareas (A, B, C, D and E) (from Ármannsson et al., 1986) and conceptual model profile of the Theistareykir geothermal field (from Óskarsson, 2015).

Assuming a lithostatic pressure gradient of 23 kPa $m^{-1}$, a pressure of 45 MPa (450 bars) would be reached at 2000 m depth. The temperature of the produced geothermal fluid is around 300°C. In these pressure and temperature conditions, the density $\rho_0$ of the geothermal vapour (brine) would vary between 750 and 1050 kg $m^{-3}$, assuming a NaCl concentration between 6 and 26% (Vishal and Singh, 2016) (Fig. 31).

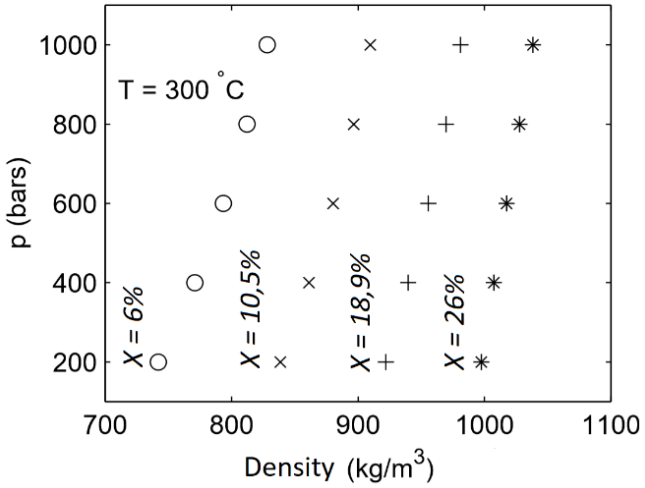


**Figure 31.** Density variation (kg $m^{-3}$) of a brine with NaCl concentration X, at temperature T of 300°C, as a function of pressure p (bar) (from Vishal and Singh, 2016).

### 5.2.2 Exploitation

Following the environmental impact assessment carried out by Kristinsdóttir and Thóroddsson (2015), the building of the geothermal plant started in April 2015. Nine new wells were drilled between 2016 and 2017 (Fig. 32). In 2017, 13 wells of around 2 km depth are used to extract the geothermal fluid: ThG-01, ThG-03, ThG-04, ThG-05b, ThG06, ThG-07, ThG-09, ThG-12, ThG-13, ThG-15, ThG-16, ThG-17 and ThG-18. The first production phase began in autumn 2017 and the second one in spring 2018 to reach a total capacity of 90 MWe. The total production flow rate is around 21 kt $d^{-1}$ (243 L $s^{-1}$ assuming a density of 1 kg $L^{-1}$); well ThG-05b shows the highest flow rate of up to 6 kt $d^{-1}$. The geothermal fluid is reinjected at around 450 m depth by three co-located wells (ThN-01, ThR-12 and ThN-02). The mean injection flow rate is 18 ML $d^{-1}$ (208 L $s^{-1}$). Simultaneously, water is extracted with a mean flow rate of 120 L $s^{-1}$ around 3 km NW of the geothermal area from 113 m depth and then, injected with a mean flow rate of 67 L $s^{-1}$ near the cooling tower at 83 m depth. Injection flow rates at the cooling tower are approximated from the water level measurement of a retention basin with a water weir**.**

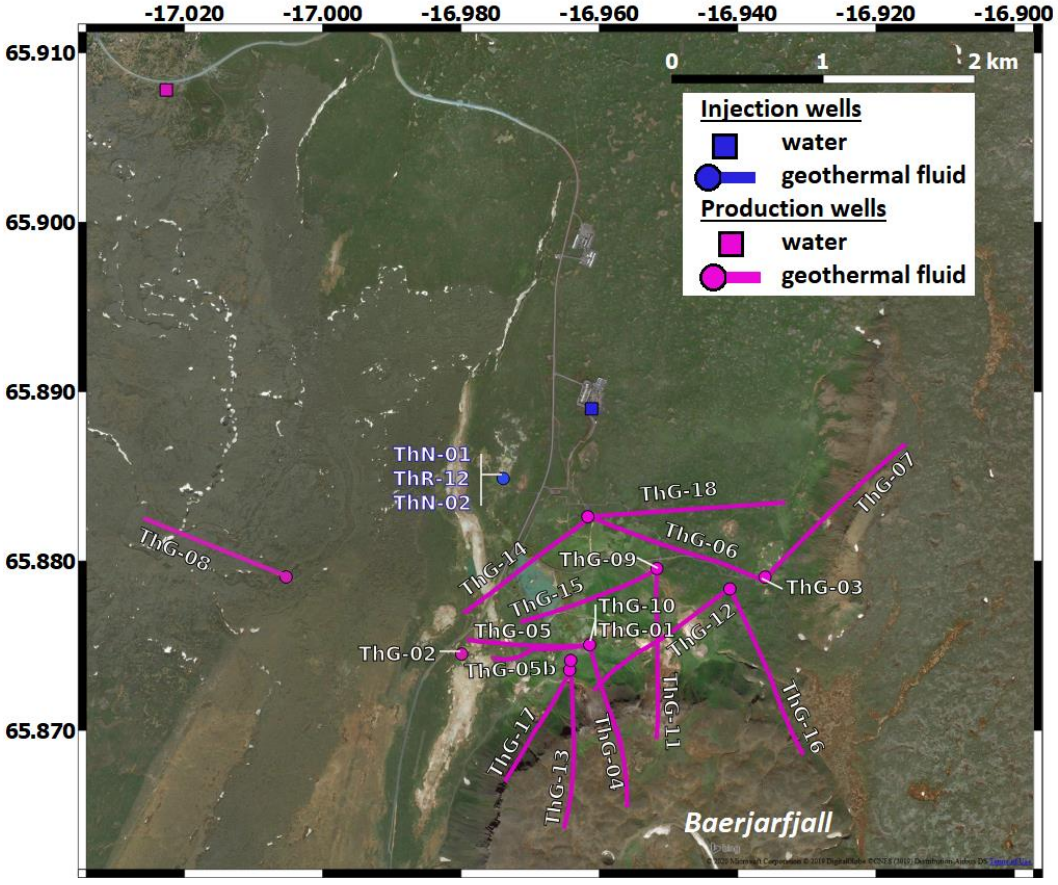


**Figure 32.** Projection of the well paths from production (pink) and injection (blue) wells in the Theistareykir geothermal area.

### 5.2.3 Hydrology

Water level measurements are performed at seven piezometers (Fig. 34). Figure 33 shows these relative variations from 01/01/2015 for wells TH-1, TH-2, TH-7, TH-8, TH-10, TH-15 and from 09/08/2017 for well TH-17. The first measurement is set to zero. It was equal to 223.97 m, 277.4 m, 235.13 m, 240.65 m, 236.24 m, 201.56 m and 219.96 m for TH-1, TH-2, TH-7, TH-8, TH-10, TH-15 and TH-17, respectively. The hydrological gradient points northward to the sea.

From January 2015 to July 2018, we notice an overall decrease of the water level at TH-1, TH-10 and TH-15 of around 7 m. Similar trends are observed for TH-2, TH-7 and TH-8 before stabilization in July 2016. Then, following the beginning of the geothermal fluid injection in August 2017, their water table level increases. This increase is particularly visible when the two 45 MWe turbines of the Theistareykir geothermal plant are working and the maximum flow rate of around 200 L $s^{-1}$ is reached in February 2018. Hence, from February 2018 to January 2019, the water level increase is around 7 m. The water level of TH-2 is the first to respond to the geothermal fluid injection. The sensibility of these three wells to the change of injection flow rate becomes clearly visible during the turbines maintenance in March/April 2019 and in July 2019. Injection flow rates are reduced to half (to ~100 L $s^{-1}$) which induces a 2 m decrease of the water table level. Finally, the water table level of TH-17 slowly increases from October 2018. A small concomitant decrease and subsequent increase of the injection flow rate of TH-17 occur during the first turbine maintenance in March/April 2019.

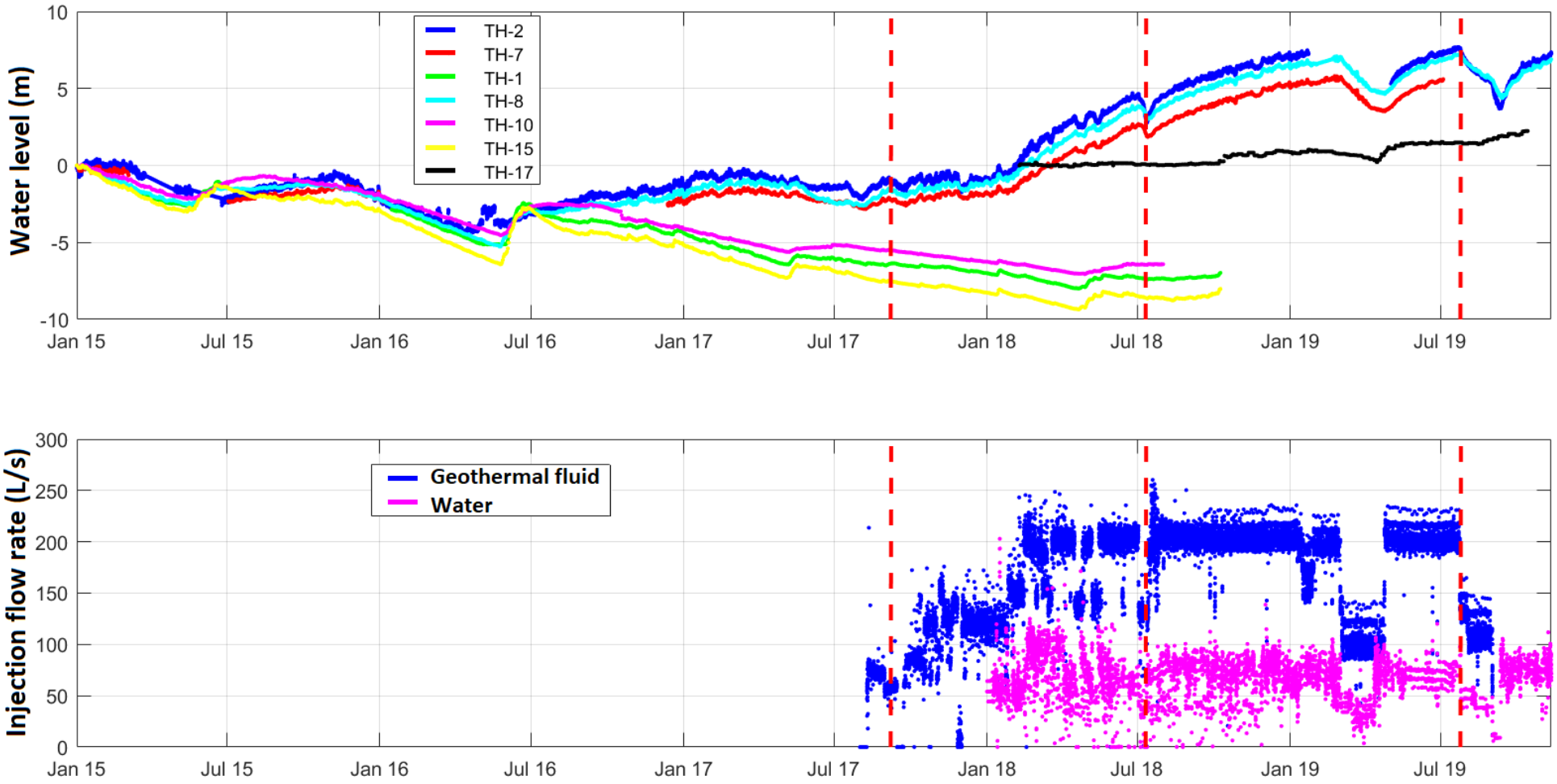


**Figure 33.** Graph of water level variations (m) measured at TH-1, TH-2, TH-7, TH-8, TH-10, TH-15 and TH-17 and graph of cold water (purple) and geothermal fluid (blue) injection flow rates (L $s^{-1}$) (Landsvirkjun, personal communication). Data of the water injection flow rates are incomplete: we do not know when the injection started. Dotted red lines show the dates of the time-lapse microgravity surveys.

## 5.3 The hybrid microgravity method

The hybrid microgravity method is a powerful tool to estimate temporal and spatial gravity changes with an accuracy of a few microgals. It has been shown to efficiently determine temporal and spatial mass changes in many fields, such as hydrology (Jacob et al., 2010), glaciology (Mémin et al., 2011), volcanology (Jousset et al., 2000) and geothermics (Sugihara and Ishido, 2008).

Three types of gravimeters were used to focus on the same target (Okubo et al., 2002; Hinderer et al., 2016):

- A spring relative gravimeter to measure punctually the microgravity variation at several stations with respect to the reference one and hence to spatially cover the gravity variations of the studied area.
- One or several permanent relative gravimeters to measure and assess continuously the gravity changes at some specific stations.
- A ballistic absolute gravimeter for repeated measurements co-located with the permanent gravimeters to establish the long-term reference.

After the effect of solid tides is corrected, the instrumental drift of the spring gravimeter observations is retrieved from the data using the PyGrav Python program (Hector and Hinderer, 2016) (Appendix C3) before we calculate the gravity double differences $\Delta g_{x_1-x_0}^{t_1-t_0}$(Hinderer et al., 2015). This difference describes the gravity *g* at a station $x_1$ and a time $t_1$ with respect to a reference station $x_0$ and a reference time $t_0$ (Eq. 6).

$$\Delta g_{x_1-x_0}^{t_1-t_0} = \left(g_{x_1} - g_{x_0}\right)_{t_1} - \left(g_{x_1} - g_{x_0}\right)_{t_0} \tag{6}$$

The square root of the sum of the variances of the uncertainty of the four gravity terms $\sigma_{g_{x_i}^{t_j}}(i,j \in \{0,1\})$ defines the error $\sigma_{\Delta g_{x_1-x_0}^{t_1-t_0}}$ (Eq. 7).

$$\sigma_{\Delta g_{x_1-x_0}^{t_1-t_0}} = \sqrt{\sigma_{g_{x_1}^{t_1}} + \sigma_{g_{x_0}^{t_1}} + \sigma_{g_{x_1}^{t_0}} + \sigma_{g_{x_0}^{t_0}}} \tag{7}$$

To highlight the mass redistribution, microgravity measurements need to be reduced for the effect of vertical displacement (Hunt et al., 2002) (section 5.4.1). The gravity variation measured at the reference station is also taken into account (section 5.4.2).

Driven by the success of previous microgravity studies, we choose to apply the hybrid microgravity method to the Theistareykir geothermal area in order to monitor

its short-term evolution and thus address the question of its sustainable management (e.g. Portier, 2020).

The Theistareykir repetition network consists of 26 microgravity stations (Fig. 34), including 16 stations measured previously by Magnússon (2016) in 2011 and 2015 (Appendix C1). Measurements were performed in summers 2017, 2018 and 2019 with the Scintrex CG5 gravimeter #41224 (Appendix C2). Observed gravity values have a standard deviation of around 4 µGal. We used 13 loops with 5 measurements beginning and ending at the reference station to correct the instrumental drift. The drift of the Scintrex CG5 gravimeter can reach tens or hundreds of µGal $d^{-1}$. One station is measured two times in a same loop to have 50% redundancy.

Three GWR Instruments Inc. iGrav superconducting gravimeters and one Micro-g Lacoste Inc. gPhone spring gravimeter record continuously the gravity variations at four stations since December 2017 (Erbas et al., 2020) (Appendix C2). Two superconducting gravimeters are located in the geothermal area, i.e. close to the injection wells (SCGW) and in the production zone (SCGE). The gPhone gravimeter is operating between them (GPXC). The third superconducting gravimeter was located at a remote station (SCGR), around 17 km to the northwest of the geothermal plant and relocated to GPXC in June 2019. Each permanent station has two circular pillars inside a 16°C air-conditioned container. At each station, weather sensors record the wind speed, the rainfall, the atmospheric pressure, the temperature and the humidity. Three cameras monitor levelling rods showing the snow level. Seismometers are also continuously recording at each permanent station. Furthermore, the SCGE station has supplementary sensors to study the snow properties.

Absolute measurements were performed with a Micro-g Solutions Inc. FG5 gravimeter at the permanent stations in 2018 and 2019 as well as at reference station 100 of the repeated microgravity surveys in 2017, 2018 and 2019. The measurement accuracy is between 1 and 2 µGal.

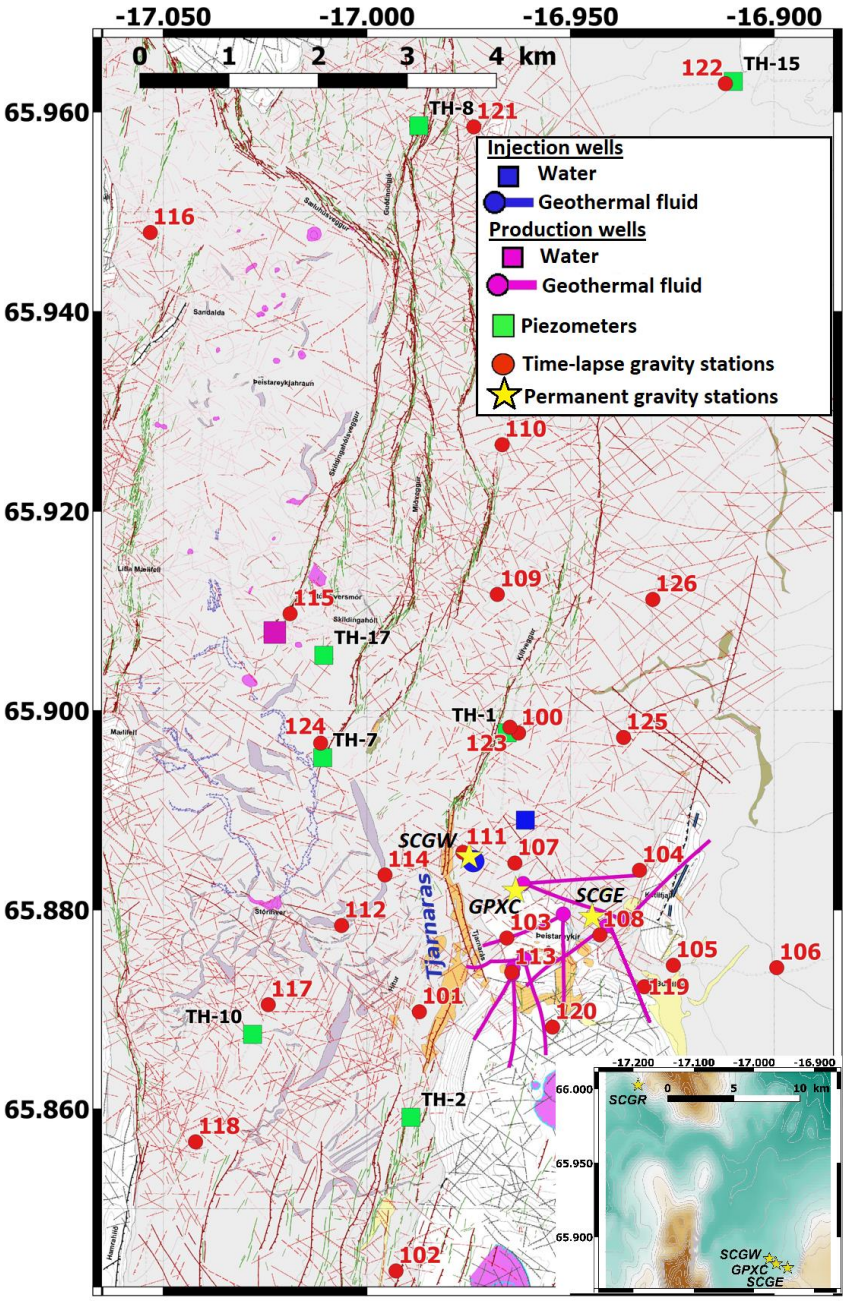


**Figure 34.** The hybrid microgravity network of the Theistareykir geothermal field. Time-lapse and permanent gravity stations are indicated by red dots and yellow stars, respectively. The location of permanent station SCGR is shown on the insert: it is around 17 km to the northwest of the geothermal power plant. Absolute measurements were performed at all permanent stations and at time-lapse reference station 100. The production and injection wells are depicted in pink and in blue, respectively. Water (square) and geothermal fluid (circle) exploitations are distinguished. The location of the piezometers is marked by green squares. The background shows the fractures identified by aerial images and hillshade (from Khodayar and Björnsson, 2013). The position of the Tjarnarás fracture is emphasised, as it represents a possible drainage system for the injected geothermal fluid (section 5.6). Old fractures (>15000 years) are in black; the youngest ones (<15000 years) are in green (open fractures) or in red (undifferentiated fractures). Dotted lines are used when there is a doubt on the presence of a fracture. Yellow/orange mark surface alterations. Craters are coloured purple.

## 5.4 Time-lapse microgravity data processing

### 5.4.1 Vertical displacement

Drouin et al. (2020) studied vertical displacement from 2015 to 2019 at the Theistareykir geothermal field. The InSAR analysis deduced height variations from the Sentinel-1 A and Sentinel-1 B satellites acquisitions which informs us about ground vertical movement with a resolution of around 37.5 x 37.5 $m^2$. The mean uncertainty of the InSAR measurements is around 2.5 mm $yr^{-1}$ (Drouin and Sigmundsson, 2019).

Following the beginning of the geothermal utilization in autumn 2017, a subsidence rate of around -5 mm $yr^{-1}$ was observed in the production area. Between 2018 and 2019, it reached -8 mm $yr^{-1}$ (Fig. 35). Between 2015 and 2019, the highest subsidence of -17.3 mm (at station 110) and 16.5 mm (at station 121) was measured in the north of the study area, followed by -16.2 mm (at station 103) at the production zone (Appendix C4). However, the positions of maximum subsidence do not coincide with the position of maximum extracted mass at well THG-05b (Fig. 32).

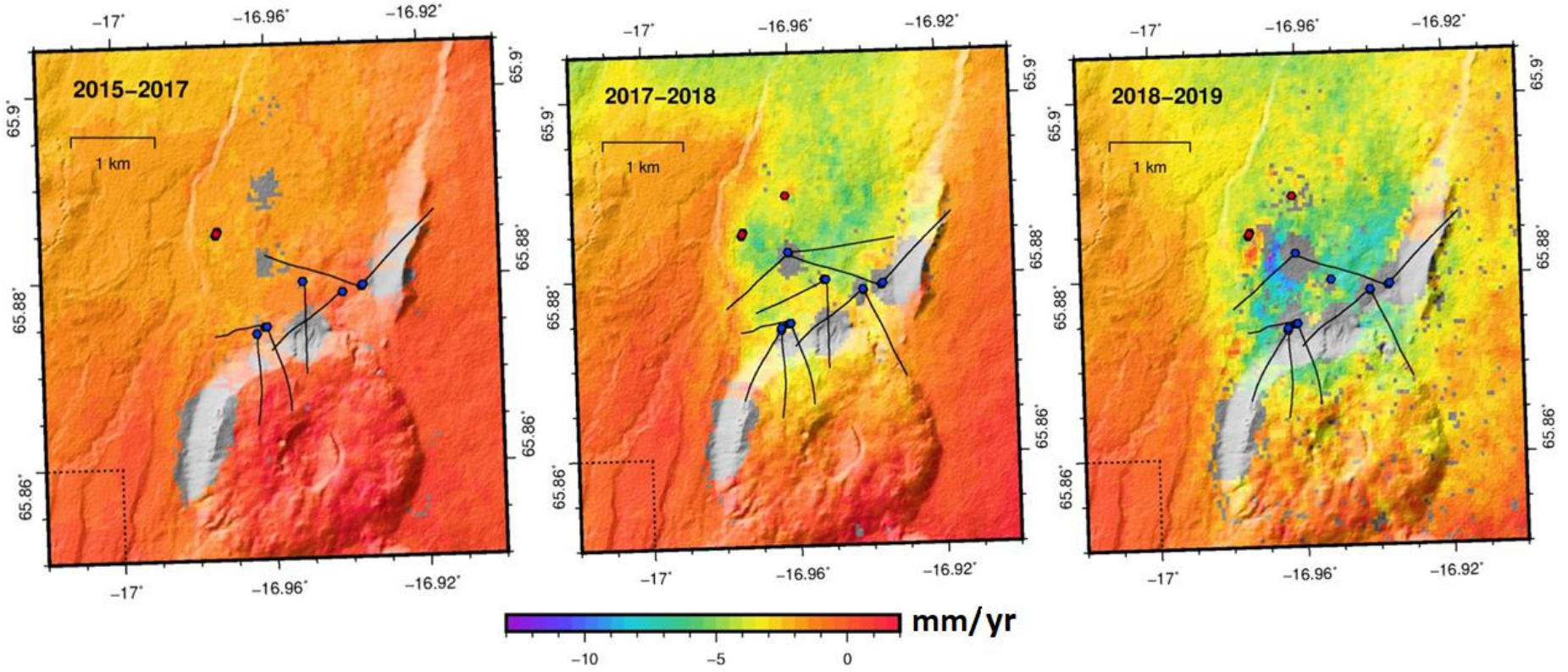


**Figure 35.** Map of vertical displacement (mm $yr^{-1}$) for the 2015-2017, 2017-2018 and 2018-2019 periods deduced from an InSAR analysis (from Drouin et al., 2020). The production and injection wells are in blue and red, respectively. Dotted line surrounds the reference area of the InSAR analysis. The mean uncertainty of the InSAR measurements is around 2.5 mm $yr^{-1}$.

Each gravity measurement is corrected for the gravity change due to vertical displacement deduced from InSAR analysis. Indeed, we do not know vertical displacement given by GPS measurements at all gravity stations. The InSAR results are consistent with the vertical displacements measured by continuous GPS at the three permanent gravity stations SCGE, GPXC and SCGW (Fig. C2 in Appendix C). There, a subsidence of -8.7 +/- 2.5 mm, -6.1 +/- 2.5 mm and -12.0 +/- 2.5 mm occurred from 2018 to 2019, respectively. This comparison suggests that vertical displacements deduced from InSAR analysis are accurate enough to correct the gravity contribution of ground motion, even if we should keep in mind that local displacements will not be detected by this method. Drouin and Sigmundsson (2019) already pointed out the consistency between SAR and GPS in Iceland with difference of about 3.3 mm $yr^{-1}$ for the vertical velocity field.

To reduce the microgravity data for the contribution of the vertical displacement, we measured in 2019 the free-air vertical gravity gradient locally at the permanent stations SCGW, GPXC, SCGE and SCGR as well as time-lapse reference station 100 (Tab. C6 in Appendix C). We assume that the gradient was constant from 2017 to 2019. For correction of the time-lapse gravity measurements, we used the mean value of the free-air vertical gravity gradients measured in the Theistareykir geothermal field (excluding the gradient measured at SCGR which is far outside the geothermal area), which is -316 +/- 9 µGal $m^{-1}$. However, the choice of one instead of another of these measured vertical gravity gradients would only induce a difference lower than 0.2 µGal in the correction of the measured gravity variations.

Except for station 102, all gravity stations observe a subsidence between 2017 and 2019 (Appendix C4) which results in a positive effect on the gravity double differences, considering the mean measured free-air vertical gravity gradient of -316 +/- 9 µGal $m^{-1}$. The effect of vertical displacement varies between -3 and 0 µGal in 2018 and between -5 and 0 µGal in 2019 with respect to 2017. The mean InSAR uncertainty is 2.5 mm $yr^{-1}$, which represents a gravity error of approximately 1 µGal $yr^{-1}$. The mean gravity uncertainty is initially 4 µGal. Taking into account this new uncertainty arising from the effect of vertical displacement, the mean error is $\sqrt{4^2 + 1^2} = 4$ µGal.

### 5.4.2 The absolute gravity variation at reference station 100

Absolute gravity measurements were performed in 2017, 2018 and 2019 at time-lapse reference station 100 (Tab. 8). Data were corrected for the effect of solid Earth and ocean loading tide, atmospheric pressure and polar motion. We notice that the gravity decreased by -1.2 +/- 1.3 µGal in 2018 with respect to 2017 before increasing by 8.0 +/- 1.5 µGal in 2019 with respect to 2018. At the same time, a subsidence of -4.6 +/- 2.5 mm and -4.1 +/- 2.5 mm was measured, respectively. After correction of vertical displacement, we obtain absolute gravity variation of -2.6 +/- 1.5 µGal for the 2017-2018 period and 6.8 +/- 1.7 µGal for the 2018-2019 period.

**Table 8.** Absolute gravity measurements $g_{abs}$ (µGal) at time-lapse reference station 100. $\Delta g_{abs}$ (µGal) are the absolute gravity variations in 2018 and 2019 with respect to 2017. $\Delta g_{abs}$' (µGal) are the absolute gravity variations in 2018 and 2019 with respect to 2017 corrected for vertical displacement $\Delta h_{InSAR}$ (mm) (Appendix C4). The mean InSAR uncertainty is 2.5 mm $yr^{-1}$.

| Date | $g_{abs}$ (µGal) | $\Delta g_{abs}$ (µGal) | $\Delta h_{InSAR}$(mm) | $\Delta g_{abs}$' (µGal) |
|---|---|---|---|---|
| 15/08/2017 | 982293783.83 +/- 0.79 | 0 | 0 | 0 +/- 0. |
| 26/06/2018 | 982293782.62 +/- 1.05 | -1.2 +/- 1.3 | -4.6 | -2.6 +/- 1.5 |
| 06/06/2019 | 982293790.65 +/- 1.01 | 6.8 +/- 1.3 | -8.7 | 4.1 +/- 2.0 |

### 5.4.3 Results

The gravity double differences are corrected for the effect of vertical displacement and the gravity variation measured at time-lapse reference station 100. They are hence the gravity variation at each station of the Theistareykir network with respect to reference station 100 and the summer 2017 reference time.

The gravity double difference measured at station 108 exceeds the 95% confidence interval in 2018 with respect to 2017 (Fig. 36): we observe a decrease of -17 +/-10 µGal. In 2019 with respect to 2017, the gravity decreases at station 108 almost doubles to -38 +/- 10 µGal. Hence, a gravity decrease appears in the production area (Fig. 37), which seems to extend towards the NE and SW (Figs. 38 and 39). In 2019 with respect to 2017, a significant increase of 18 +/- 10 µGal is also observed at station 102 (Fig. 36). These values exceed the mean gravity change of -10 +/-13 µGal $yr^{-1}$ measured between 2011 and 2015, before the beginning of the

geothermal production (Magnússon, 2016) (Appendix C1). The other gravity variations are small and show the limit of the method if we consider the error of the Scintrex CG5 gravimeter, which varies between 5 and 10 µGal. Nevertheless, we will try to model and interpret the results (section 5.6), which seem to show a coherent distribution with a gravity decrease in the production area (Figs. 37, 38 and 39).

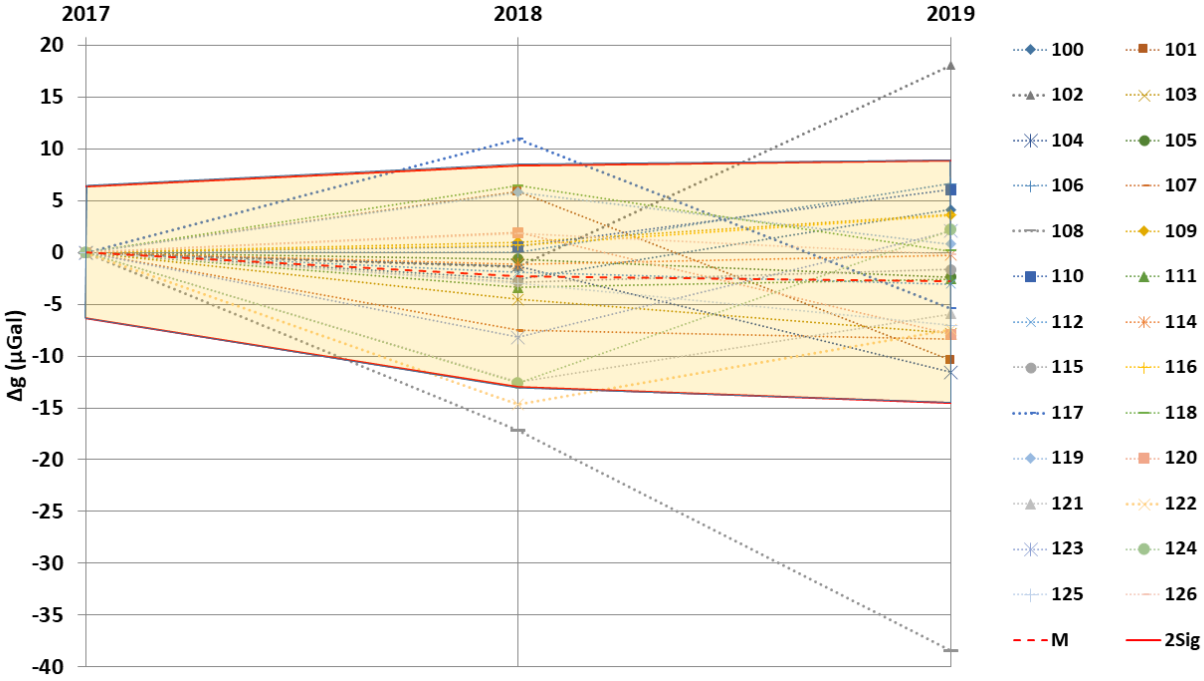


**Figure 36.** Graph of the gravity double differences Δg (µGal) measured in 2018 and 2019 with respect to 2017 at the Theistareykir geothermal field. Data are corrected for the effect of vertical displacement and the gravity variation of reference station 100. The 95% confidence interval (2Sig) is highlighted in orange and it is centred on the mean gravity double difference (M).

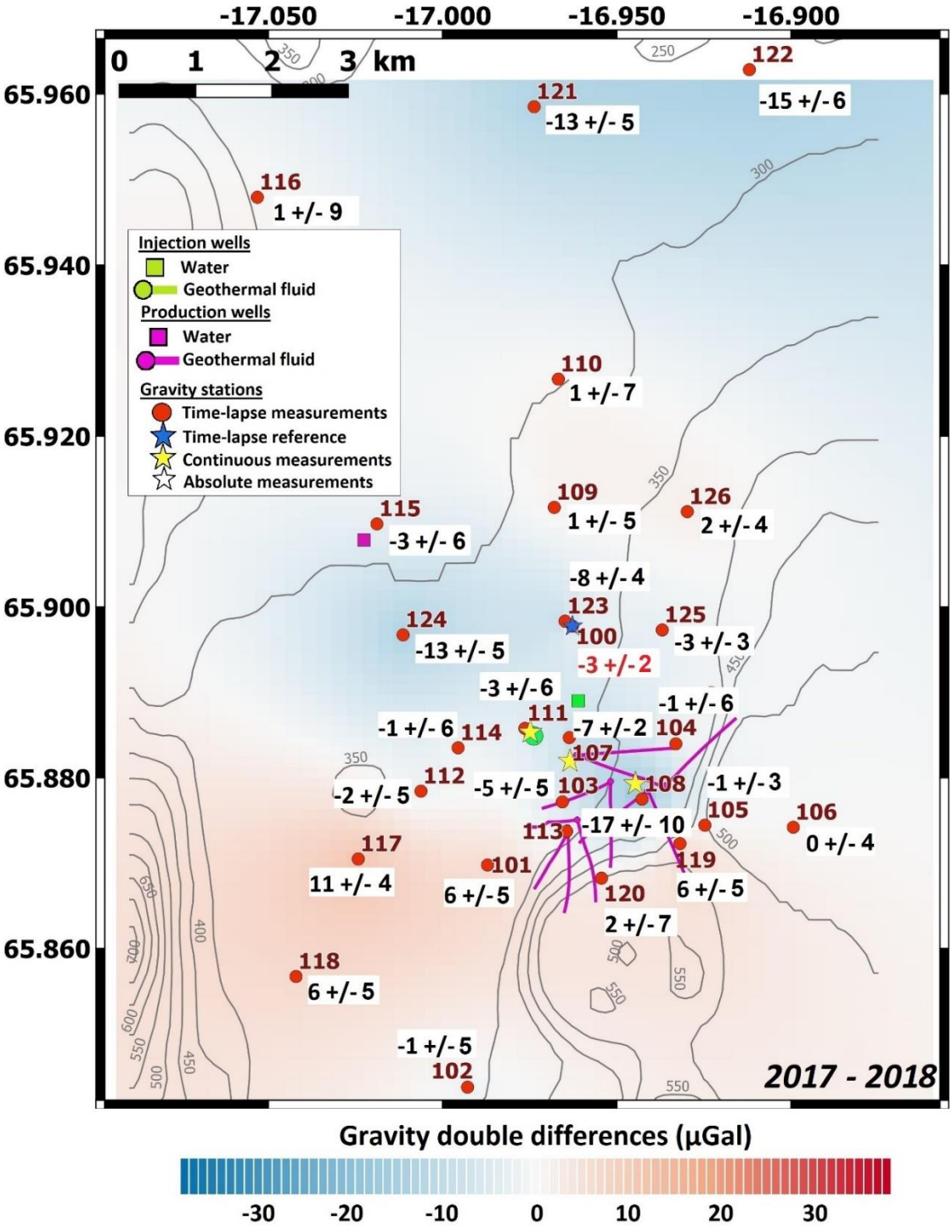


**Figure 37.** Map of the gravity double differences (µGal) measured at the Theistareykir geothermal field between 2017 and 2018. The values and errors are written in black close to time-lapse gravity stations (red dots). The station code is written in brown. The absolute gravity double difference of time-lapse reference station 100 shown by a blue star is written in orange. Yellow stars mark permanent gravity stations. Absolute gravity measurements have been performed at all stations indicated by a star. The gravity double differences are interpolated by kriging method. Altitude isolines are derived from GMTED with 7.5 arc seconds resolution.

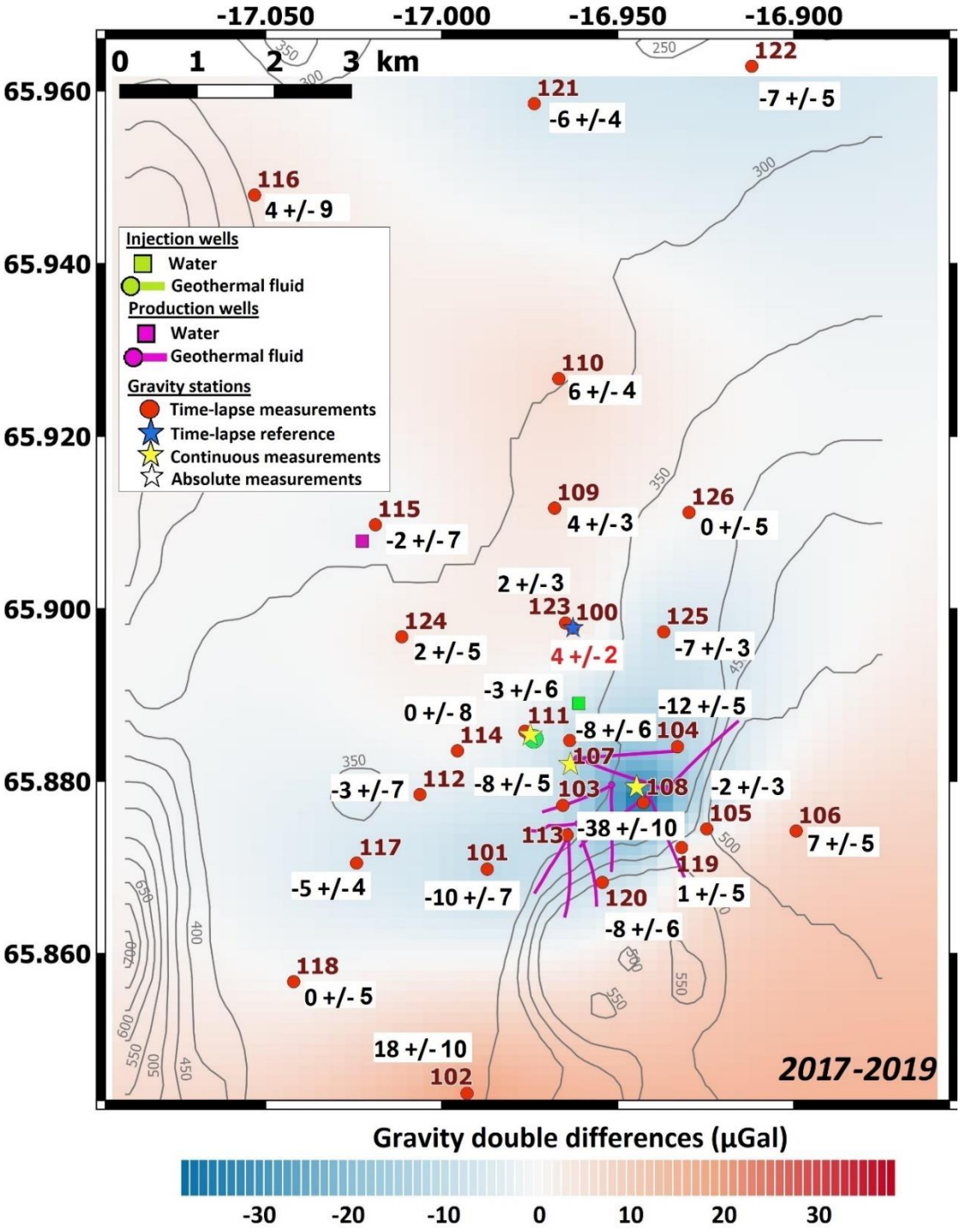


**Figure 38.** Map of the gravity double differences (µGal) measured at the Theistareykir geothermal field between 2017 and 2019. The values and errors are written in black close to time-lapse gravity stations (red dots). The station code is written in brown. The absolute gravity double difference of time-lapse reference station 100 shown by a blue star is written in orange. Yellow stars mark permanent gravity stations. Absolute gravity measurements have been performed at all stations indicated by a star. The gravity double differences are interpolated by kriging method. Altitude isolines are derived from GMTED with 7.5 arc seconds resolution.

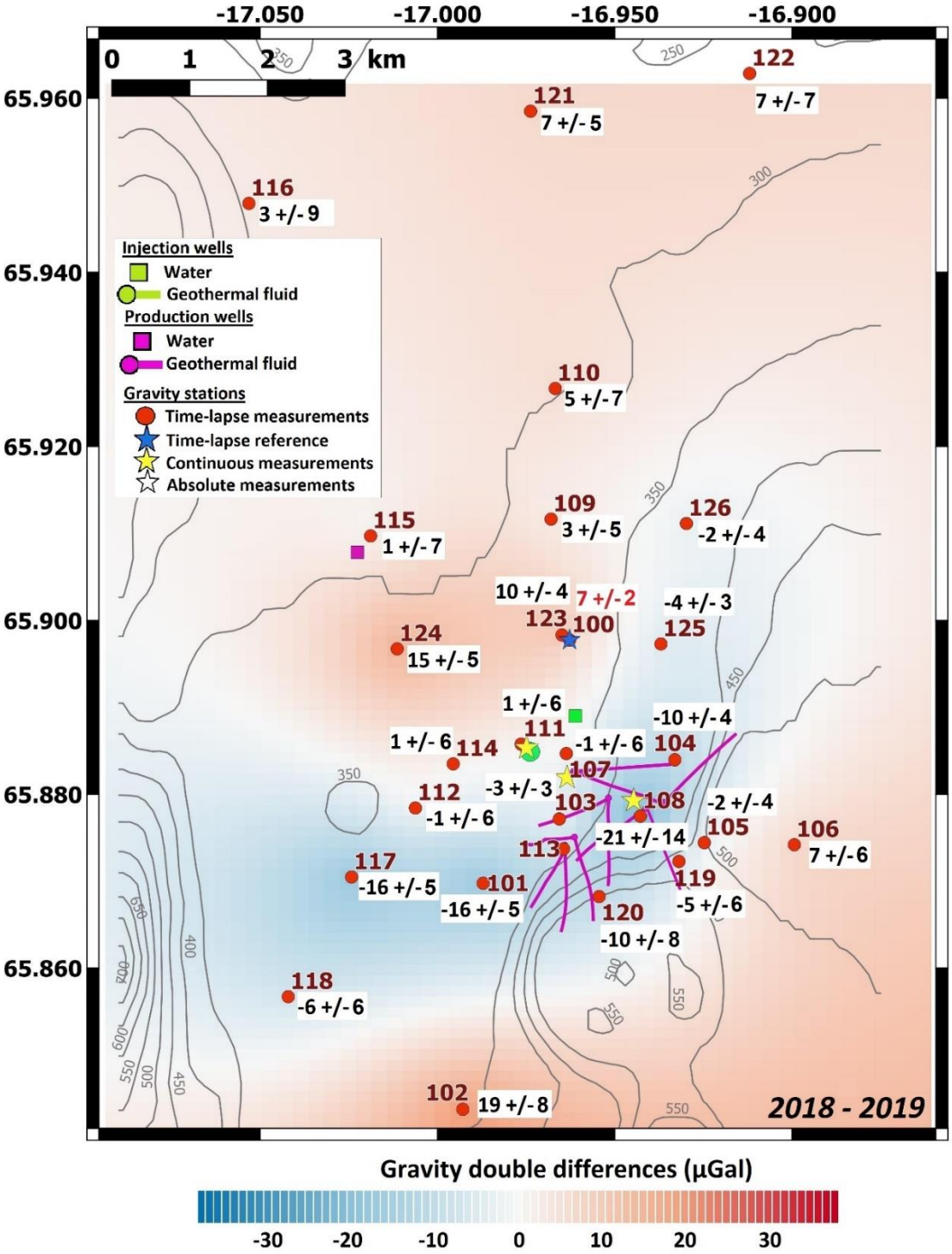


**Figure 39.** Map of the gravity double differences (µGal) measured at the Theistareykir geothermal field between 2018 and 2019. The values and errors are written in black close to time-lapse gravity stations (red dots). The station code is written in brown. The absolute gravity double difference of time-lapse reference station 100 shown by a blue star is written in orange. Yellow stars mark permanent gravity stations. Absolute gravity measurements have been performed at all stations indicated by a star. The gravity double differences are interpolated by kriging method. Altitude isolines are derived from GMTED with 7.5 arc seconds resolution.

## 5.5 Continuous microgravity monitoring

In our hybrid microgravity monitoring of the Theistareykir geothermal site we performed continuous gravity measurements with gPhone128 and the superconducting gravimeters iGrav006, iGrav015 and iGrav032. For the following investigation, we focused on the observations of iGrav032 and iGrav006 at the permanent stations SCGE and SCGW respectively, because they are located most closely to the geothermal production and injection wells (Fig. 34).

### 5.5.1 Description of the applied reductions

For the iGrav time series, we retrieved contributions of tidal and pressure effects, obtained from local tidal modelling and individual barometric admittance factors for each of permanent gravity stations. Further, we corrected the instrumental drift of SCGW/iGrav006 (injection) and SCGE/iGrav032 (production) by two absolute gravity FG5 campaigns at Theistareykir in June/July 2018 and June 2019 (Tab. 9). A detailed explanation of these corrections is given in Schäfer et al. (2020).

**Table 9.** Absolute gravity measurements $g_{abs}$ (µGal) at permanent stations SCGE and SCGW. $\Delta g_{abs}$ (µGal) are the absolute gravity variations in 2019 with respect to 2018. $\Delta g_{abs}$' (µGal) are the absolute gravity variations in 2019 with respect to 2018 corrected for contribution of vertical displacement $\Delta h_{GNSS}$ (mm).

| Station | Date | $g_{abs}$ (µGal) | $\Delta g_{abs}$ (µGal) | $\Delta h_{GNSS}$(mm) | $\Delta g_{abs}$' (µGal) |
|---|---|---|---|---|---|
| **SCGE** | 25/06/2018 | 982282487.70 +/- 1.41 | 0 +/- 1.41 | 0 | 0 +/- 1.41 |
| **SCGW** | 05/07/2018 | 982293480.13 +/- 1.31 | 0 +/- 1.31 | 0 | 0 +/- 1.31 |
| **SCGE** | 12/06/2019 | 982282481.76 +/- 1.99 | -5.9 +/- 2.4 | -2.1 +/- 7.0 | -6.5 +/- 3.3 |
| **SCGW** | 15/06/2019 | 982293486.82 +/- 0.91 | 6.7 +/- 1.6 | -8.4 +/- 8.9 | 4.0 +/- 3.2 |

In addition to the above-mentioned standard corrections we included reductions of global gravity effects by applying established models for atmospheric mass attraction (Klügel and Wziontek, 2009), large-scale hydrological effects (Rodell et al., 2004) and nontidal ocean loading (Dobslaw et al., 2017). For the calculation of local environmental gravity effects, we analysed the continuous measurements from our remotely operated multiparameter stations (ROMPS) (Schöne et al., 2013) which are installed at each of permanent gravity stations. From soil moisture time series, we

calculated the gravity effect of soil water content by applying hydro-gravitational modelling based on the method of Leirião et al. (2009) and adapted to superconducting gravity (SG) observatory buildings by Reich et al. (2019). The effect of vertical displacement was calculated from collocated GNSS time series (Fig. C3 in Appendix C) using the measured free-air vertical gravity gradient (Tab. C6 in Appendix C).

### 5.5.2 Microgravity observations

In Figure 40, we show a compilation of the Theistareykir gravity measurements with all the above described reductions applied to the iGrav time series. The FG5 absolute gravity measurements (used for drift correction) are marked by red squares. Additionally, the time-lapse gravity measurements at station 111 close to SCGW / iGrav006 (injection) and at station 108 close to SCGE / iGrav032 (production) are plotted for the CG5 campaigns in July 2018 and July 2019 (circles in Fig. 40). In the gravity differences between iGrav006 and iGrav032 (stations 111 and 108 respectively) all remaining hydrometeorological and tectonic gravity effects are largely cancelled out, leaving only the effects that are locally varying at the two stations. This comprises in particular the mass differences due to geothermal injection at SCGW and production at SCGE.

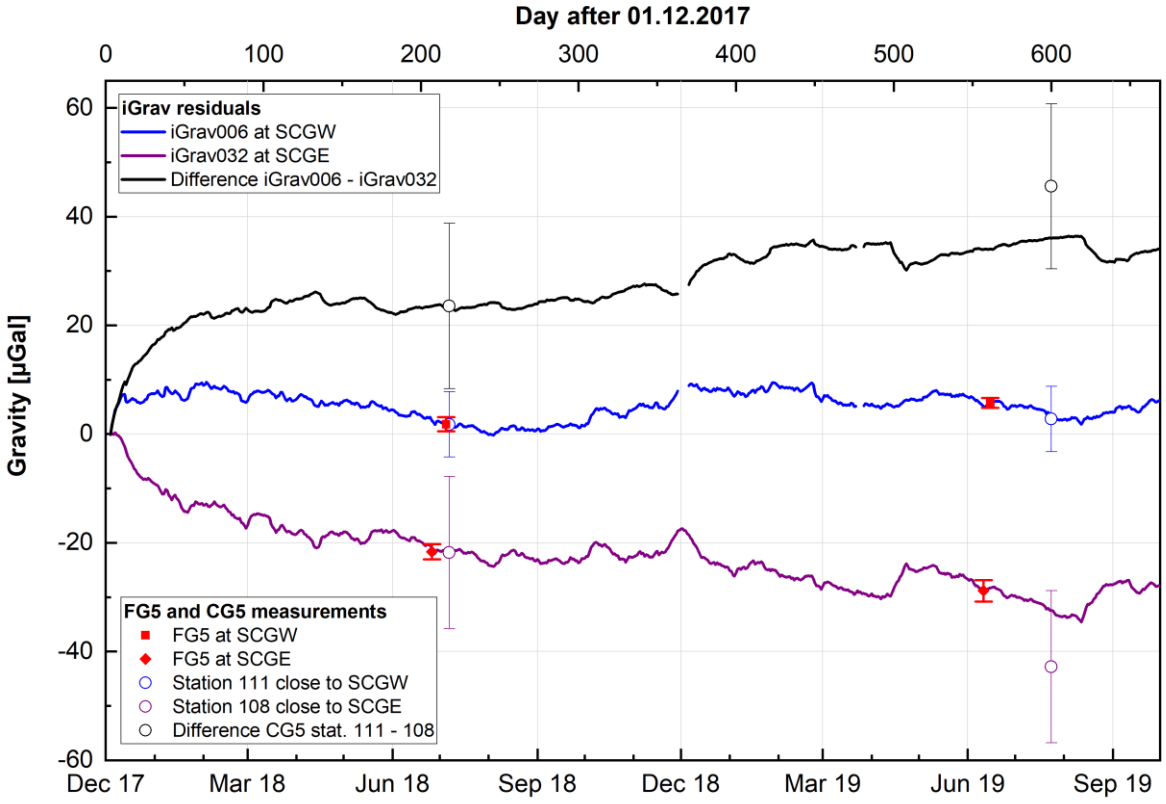


**Figure 40.** Residual corrected time series of iGrav006 (SCGW) and iGrav032 (SCGE) and differences iGrav006 - iGrav032 (dark blue, purple and black), FG5#206 absolute gravity (red squares), and comparison to CG5 measurements and differences (circles with error bars) from the field campaigns in 2018 and 2019.

### 5.5.3 Gravity, injection flow rates and ground water levels

Figure 41 shows a comparison of the gravity differences (iGrav006-iGrav032 and CG5 stations 111-108 from Fig. 40), cold water reinjection and groundwater level (GWL) variations. From the continuous measurements, good correlation is visible between the iGrav differences and GWLs. Only during the “winter periods” the iGrav time series show larger values (less prominent between December 2017 and June 2018, more prominent between November 2018 and May 2019). These winter anomalies cannot be explained so far, by our hydrometeorological and GNSS observations. The comparison of iGrav and CG5 differences, in both cases shows an increase of gravity between summers 2018 and 2019. The same increasing trend we observe for three of the GWLs (TH-02, TH-08 and TH-07) (Fig. 33).

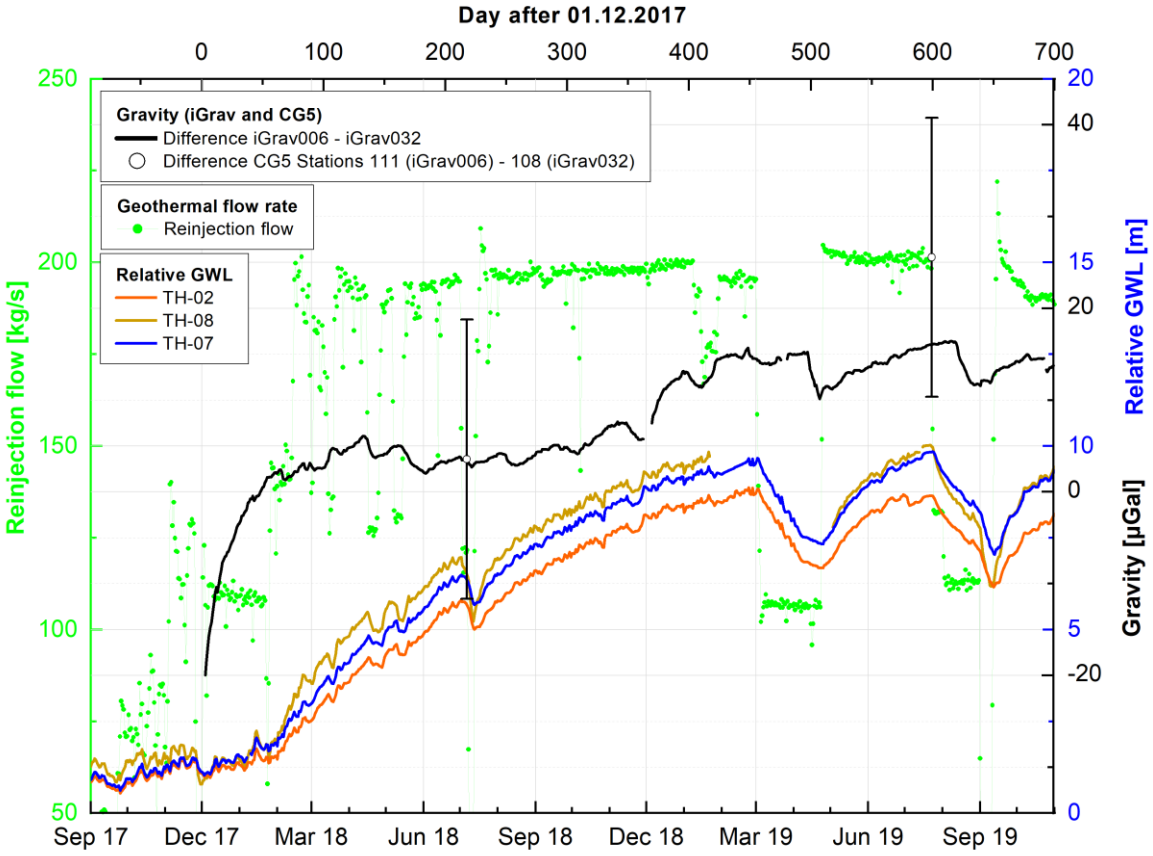


**Figure 41.** Gravity differences between injection and production sites (in black, for iGrav and CG5) compared to geothermal fluid reinjection (bright green) and ground water level variations (brown, blue and orange).

## 5.6 Interpretation

### 5.6.1 Origin of gravity variations

Hunt (2001) enumerates other potential origins for the temporal gravity difference measured at geothermal fields. In our study, we assume that the three main contributions would be:

- ***Changes in groundwater level***

We notice that the water table level (GWL) increases in the wells TH-2, TH-7 and TH-8 following the beginning of geothermal fluid injection (section 5.2.3). On the contrary, the water table level of wells TH-1 and TH-10 decreases since July 2016, which corresponds to the second phase drilling of most of the production wells. We formulate two hypotheses:

1. The injection could create a surplus of water that would stop water to follow the natural flow toward north, making an accumulation of water in the south (well TH-2), whereas the production could create a decrease of water level in the north (well TH-1) that would not be compensated by the reinjection.
2. The water table level increase observed at wells TH-2 and TH-7 would suggest that the injected fluid flows to the east of the geothermal field and/or to the south, maybe drained in the Tjarnarás fault (Fig. 34). Tracer testing support this idea (E. Júlíusson, personal communication).

If the aquifer is unconfined the water table level variation $h$ induces a gravity change $\Delta g_{hydro}$:

$$\Delta g_{hydro} = 2\pi G \rho h \varphi \quad (8)$$

The gravitational constant G is 6.67 $10^{-11}$ $m^3$ $kg^{-1}$ $s^{-2}$. ρ is the water density equal to 1000 kg $m^{-3}$. $\varphi$ is the porosity of the medium. Hence, for 9 m water table level change of an unconfined aquifer, we would expect a gravity change of 18 µGal, taking into account a porosity of 5% (Eq. 8). In this condition, the water table change observed at well TH-2 for the 2017-2019 period could explain the gravity variation measured at nearby station 102 (Fig. 34).

If the aquifer is confined, the observed water table level changes may be due to pressure variation without any mass change. Gautason et al. (2010) explained that ThG-01, ThG-04 and ThG-05 (Fig. 32) crossed over-pressurized aquifers at around 200 m depth. Hence, this hypothesis could explain, for instance, why we observe a gravity decrease at station 124 (-13 +/- 5 µGal) between 2017 and 2018 despite the water table level increase of nearby TH-7 (Fig. 34).

- ***Changes in soil water content in the aeration zone (soil moisture)***

The variations in soil water content near the surface (above 2 m depth) do not affect significantly the microgravity changes measured at the Theistareykir geothermal field. The mean induced difference is lower than 2 µGal which is within the accuracy of the Scintrex CG5 gravimeter.

- ***Mass redistribution in the geothermal system (objective of the study)***

The injection and production of geothermal fluid, the phase change as well as the density variations induced by temperature change and potential alteration generate a mass redistribution (Hunt, 2001). These causes are dependent on each other. In this study, we focus on the effect of injected and produced mass.

It is also worth mentioning three other potential weaker sources at the Theistareykir geothermal field: the gravity contribution due to magma movements, glaciers and tectonics. However, we observed no sign of deep-seated magma movements, which could induce gravity changes. Furthermore, time-lapse gravity measurements were performed each year in summer to minimize seasonal variations; this precaution would reduce the effect of the nearby Vatnajökull glacier. This ice cap is located around 130 km southward of the geothermal area and has a surface of 7900 $km^2$. Hence, a 1 m ice elevation would induce a gravity variation of around 2 $10^{-11}$ µGal at the Theistareykir geothermal field. In addition, we estimate the main contribution of tectonics would be due to vertical displacement that we corrected for.

### 5.6.2 Attempt to model gravity and height data

Considering a geothermal fluid density of 1000 kg $m^{-3}$ (Fig. 31), masses of 3.9 Mt and 10.1 Mt were injected around 450 m depth at the Theistareykir geothermal field in 2017-2018 and 2017-2019 periods, respectively. If those injected masses would stay in the vicinity of the injection well, the gravity increase would amount 128 µGal and 333 µGal. Nevertheless, we measured a residual gravity variation of -3 +/- 6 µGal for both periods at nearby gravity station 111. We conclude that the injected geothermal fluid flows away. Therefore, in the following modelling study, we consider the produced geothermal fluid only.

The microgravity variations show a gravity decrease in the production area. Station 108 observes a maximum decrease equal to -17 +/- 10 µGal (Fig. 37) and -38 +/- 10 µGal (Fig. 38) for the 2017-2018 and 2017-2019 periods, respectively. The area of negative gravity changes overlaps with an area of disk subsidence (Fig. 35). For 2017-2018 and 2018-2019 periods, the deflation at station 108 is -4.7 mm and -5.4 mm with a mean error of 2.5 mm $yr^{-1}$ (Appendix C4). Drouin et al. (2020) propose

that the subsidence in the production area could be due to the extraction of geothermal fluid generating a pressure drop or maybe, a temperature decrease (thermal contraction). The shape of the subsidence area as well as the same negative trend for vertical displacement and the gravity variations observed in 2018 and 2019 with respect to 2017 favours the use the Mogi spherical model.

Observed gravity and vertical displacement observed changes at the Theistareykir geothermal field are small with respect to their uncertainties, which prevents to obtain a well-constrained model (Appendix C5) by inversion (Jousset et al., 2003). Consequently, in the next subsection, we choose to focus our analysis on forward modelling.

The extracted masses are modelled by Mogi spheres (Mogi, 1958) localised at the open holes of the 13 production wells, at measured depth $z_p$ (Tab. C7 in Appendix C). The induced gravity changes $\Delta g_x$ at a station *x*, which is located at a distance $d_x^p$ from the 13 production open-hole *p*, are described by the equation 9. The modelled gravity changes do not consider the effect of vertical displacement; only the Newtonian attraction is considered.

$$\Delta g_x = G\rho_0 \sum_{p=1}^{13} V_p \frac{z_p}{\left(d_x^{p2} + z_p^2\right)^{\frac{3}{2}}} \quad (9)$$

The gravitational constant G is 6.67 $10^{-11}$ $m^3$ $kg^{-1}$ $s^{-2}$ and the geothermal fluid density $\rho_0$ is assumed to be 1000 kg $m^{-3}$ (Fig. 31). $V_p$ refers to the produced volume. The modelled gravity changes are between -6.5 and -1.5 µGal for the 2017-2018 period (Fig. 42a). Between 2017 and 2019, they range from -15 to -4 µGal (Fig.42b). In the production area, 50% of the time-lapse measured gravity variations are explained by this forward model (bold values in Tab. 10). Note that the unexplained values have been measured, in particular at station 108 and at stations 119 and 120, on the Bæjarfjall volcano. Additionally, the 2017-2019 gravity variation is unexplained for station 111, located in the geothermal injection area and we did not consider the injection in this simplistic model.

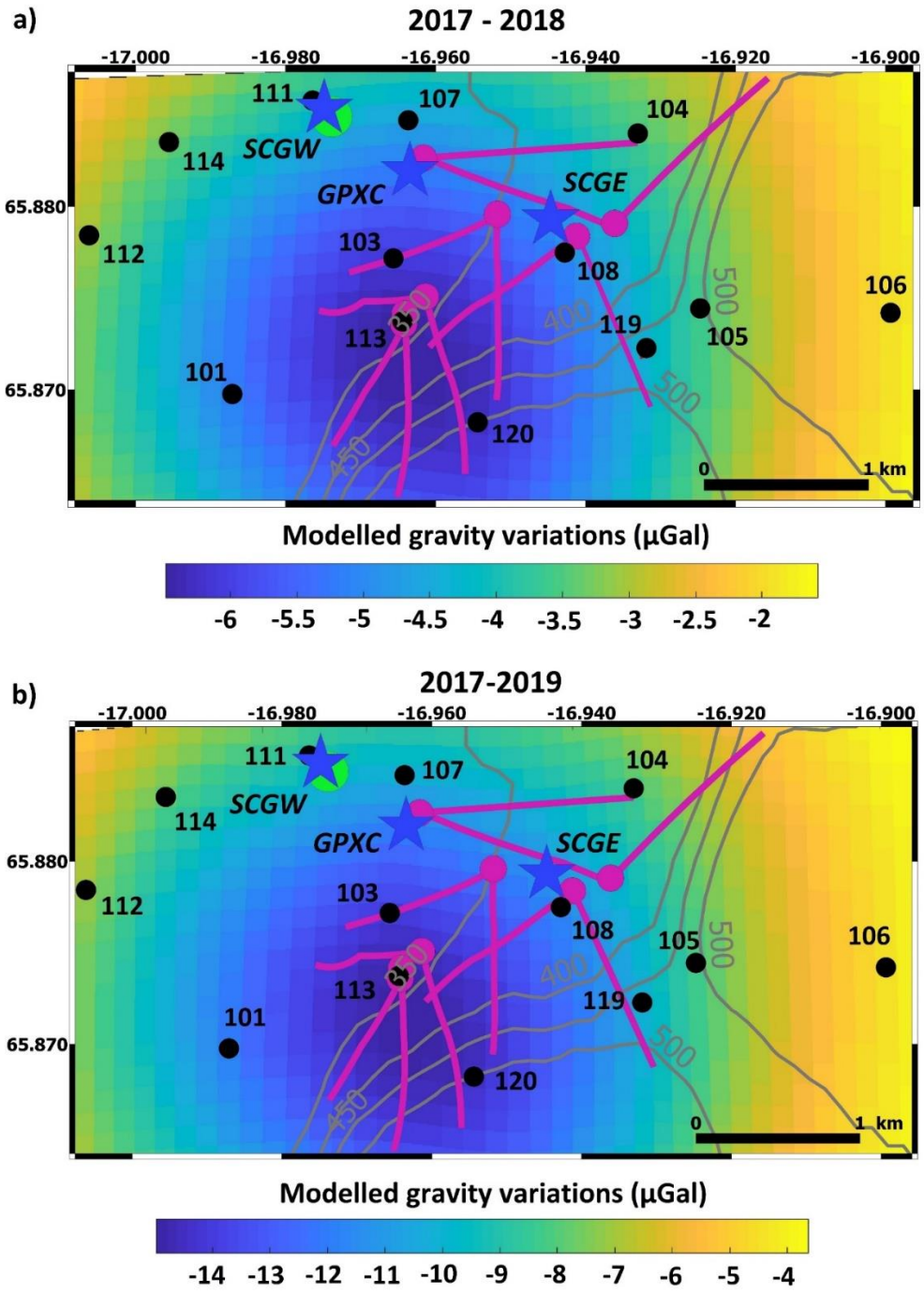


**Figure 42.** Map of the gravity changes (µGal) induced by geothermal fluid production, modelled with several Mogi spheres at the Theistareykir geothermal field for the 2017-2018 (a) and 2017-2019 (b) periods. The production and injection wells are in pink and green, respectively. The blue stars show the positions of permanent gravity stations. The black dots mark time-lapse gravity stations.

**Table 10.** Measured and modelled gravity variations (µGal) for the 2017-2018 and 2017-2019 periods in the production area. The matching values are written in bold.

| Stations | **Δg 2018-2017 (µGal)** | | **Δg 2019-2017 (µGal)** | |
|---|---|---|---|---|
| | Measured | Modelled | Measured | Modelled |
| 101 | 6 +/- 5 | -4 | **-10 +/- 7** | **-9** |
| 103 | -5 +/- 5 | -6 | -8 +/- 5 | -14 |
| 104 | **-1 +/- 6** | **-4** | **-12 +/- 5** | **-8** |
| 105 | **-1+/- 3** | **-4** | -2 +/- 3 | -8 |
| 106 | **0 +/- 4** | **-2** | 7 +/- 5 | -4 |
| 107 | -7 +/- 2 | -4 | **-8 +/- 6** | **-10** |
| 108 | -17 +/- 10 | -5 | -38 +/- 10 | -12 |
| 111 | **-3 +/- 6** | **-5** | -3 +/- 6 | -11 |
| 112 | **-2 +/- 5** | **-3** | **-3 +/- 7** | **-7** |
| 114 | **-1 +/- 6** | **-3** | **0 +/- 8** | **-8** |
| 119 | 6 +/- 5 | -4 | 1 +/- 5 | -10 |
| 120 | 2 +/- 7 | -6 | **-8 +/- 6** | **-14** |

Pascal et al. (2014) specify that the use of a multiple Mogi sphere model to predict vertical displacement is allowed only if the source separations are less than four times the radii of the sources. Here, this criterion is clearly unfulfilled if we impose a reasonable pressure change of $10^6$ Pa: we cannot use this multiple Mogi sphere model to study ground movement. However, we can consider a unique equivalent Mogi sphere to model the vertical displacement $\delta h$above the sphere (Eq. 10):

$$\delta h = \frac{1-\nu}{\pi}\frac{1}{z^2}\Delta V \quad (10)$$

where $\nu$ is the Poisson ratio equal to 0.25 in this study. Considering a geothermal fluid density $\rho_0$ of 1000 kg m$^{-3}$ (Fig. 31), a volume change $\Delta V$ of -6.1231 Mm$^3$ and -14.1637 Mm$^3$ occurred in 2017-2018 and 2017-2019 periods, respectively. The mean depth $z$ is 2373 m (Tab. C7 in Appendix C). These volume changes would induce vertical displacements of -26 cm and -60 cm above the sphere in 2017-2018 and 2017-2019 periods, respectively which is much larger than the subsidence shown by InSAR analysis that is lower than 1.5 cm (Tab. C6 in Appendix C4). This means that a Mogi type model would only work if the induced subsidence is smaller than expected due to smaller pressure inside the reservoir for the same mass effect. One possibility would be to introduce changes in compressibility due to the existence of water vapour. We refer the reader to Currenti (2014) which discusses in details the

possibility to alter the ratio $\delta g/\delta h$ for a Mogi model in the volcanic context. However, the observed dispersion of the $\delta g/\delta h$ data (Fig. C6 in Appendix C) indicates independent responses to pressure changes at each gravity station resulting from the heterogeneity of the geothermal system, which could not be explained by the Mogi model.

## 5.7 Conclusion

We performed time-lapse gravity measurements in 2017, 2018 and 2019 i.e. before and after the beginning of the electricity production in autumn 2017 at the Theistareykir geothermal field. In the production area, after the correction for the gravity contribution of subsidence, this study reveals a residual gravity decrease in 2018 and 2019 with respect to 2017. A minimum change of -38 +/- 10 µGal is measured on the 2017-2019 period. We do not notice any gravity variation nearby the injection area, suggesting that the injected geothermal fluid would be drained away by faults. 2018-2019 continuous microgravity variations recorded with permanent superconducting gravimeters calibrated with absolute measurements further confirm this trend.

A forward modelling study using a multiple Mogi sphere model would partly explain the residual gravity changes in the production area. Because of the weak gravity and vertical displacement observations with respect to their uncertainties, we were not able to retrieve a well-constrained inverse model. However, if the gravity observations continue to decrease during the ongoing exploitation of the geothermal plant, we would expect a stronger cumulative signal in the next years. We would recommend performing new time-lapse gravity surveys in the future in support of continuous measurements. Moreover, the horizontal displacement measurement could also help to define an inverse model explaining our observations.

# Chapter 6

# Discussion and outlook

The overall goal of this thesis is to relate observed gravity changes to underground mass changes induced by exploitation of the Þeistareykir geothermal field, for estimating the sustainability of the geothermal reservoir during power plant operation. In the previous chapters, I analysed continuous gravity measurements: before and after transport to Iceland to determine the instrumental performances (chapter 3), with regard to environmental and anthropogenic gravity contributions at Þeistareykir (chapter 4), and in comparison to time-lapse gravimetry (chapter 5). The combined observations with several gravity meters and locally observed parameters like vertical displacement, groundwater levels and geothermal flow rates provided several findings, which I will discuss in the following sections with regard to the scientific questions defined in chapter 1.2.

## 6.1 Summary and discussion of main results

*1) What are the instrumental characteristics of the iGrav superconducting gravity meters in terms of calibration, noise and drift, and how are they influenced by transport to a new location?*

The results of the first study (chapter 3) revealed some of the challenges for the preparation and implementation of continuous high-resolution gravity measurements at remote monitoring sites. With the demand for most accurate observations at the geothermal field in Iceland, the instruments were calibrated at the gravimetric observatory J9 in Strasbourg. The comparison of calibration results at J9 showed that RG calibration (using a relative gravity meter as reference) could improve the calibration accuracy by several orders of magnitude, compared to AG calibrations (with an absolute gravity meter). Nonetheless, the absolute accuracy of RG

calibrations is always limited by the accuracy of the AG calibration of the reference gravity meter. As another observation, the uncertainties of the AG calibration measurements performed at Þeistareykir were more than three times larger than the J9 observatory measurements, with the AG calibration of iGrav006 showing the largest uncertainty of 10 nm $s^{-2}$ $V^{-1}$ (1.09%). A possible reason could be the short distance of the iGrav006 monitoring site to one of the geothermal well pads (less than 70 m), which produced a considerable amount of local noise during the FG5 measurements. The best stability of the AG calibration with an uncertainty of 6 nm $s^{-2}$ $V^{-1}$ (0.64%) was obtained for iGrav015 at the reference station outside the geothermal field. In contrast, the noise from the geothermal well pads did not affect the stability of the RG scale factors, which was determined to be better than 0.01%.

After applying the corresponding scale factors to each gravity meter, the unfiltered (1 Hz) signals of seven quiet days from J9 and Þeistareykir were used for noise analysis. I applied the three-channel correlation technique from Rosat and Hinderer (2018) to separate the iGrav self-noise from environmental noise at each site. The comparison of self-noise levels showed low noise levels for iGrav015 and iGrav032 similar to iGrav029 and iOSG023 operating at J9. The iGrav006 showed a higher noise level than the J9 SGs, likely due to disturbances of the iGrav006 initialisation procedure during the limited measuring period at J9. After transport to Iceland, the self-noise was similar between the three iGravs and increased by about 5 dB compared to the records of the J9 SGs. A main reason for the increased self-noise could be the local separation of the iGravs within the geothermal field. Different environmental noise between the remote stations could remain unrecognized by the three-channel correlation and be interpreted as instrumental noise.

For correct interpretation of the iGrav residuals, it is important to distinguish between the initial exponential and the long-term drift. Both types of drift could be clearly observed in the iGrav time series from J9, after removing the tidal components and pressure effects with iOSG023 as a reference. Drift identification became more challenging for the gravity time series from Þeistareykir. Due to the different positions of the remote monitoring sites, varying subsurface signals can be expected at every gravity station superimposing the individual drift behaviour of each instrument. The first approach for drift characterization, with the FG5#206 absolute measurements

from summers 2018 and 2019, revealed similar results as for J9, i.e. linear positive drift for iGrav006 and linear negative drift rates for iGrav015 and iGrav032. A third AG campaign in summer 2020 confirmed the long-term drift behaviour, with slightly reduced drift rates for iGrav006 and iGrav032. Figure 43 shows the complete iGrav time series at Þeistareykir before and after drift corrections, with the according linear drift rates given in Table 11. Interestingly the drift behaviour of iGrav015 changed from negative to positive values more similar to iGrav006 after movement from the reference station to the central station. Possible reasons for the changes in drift behaviours are discussed in the following section.

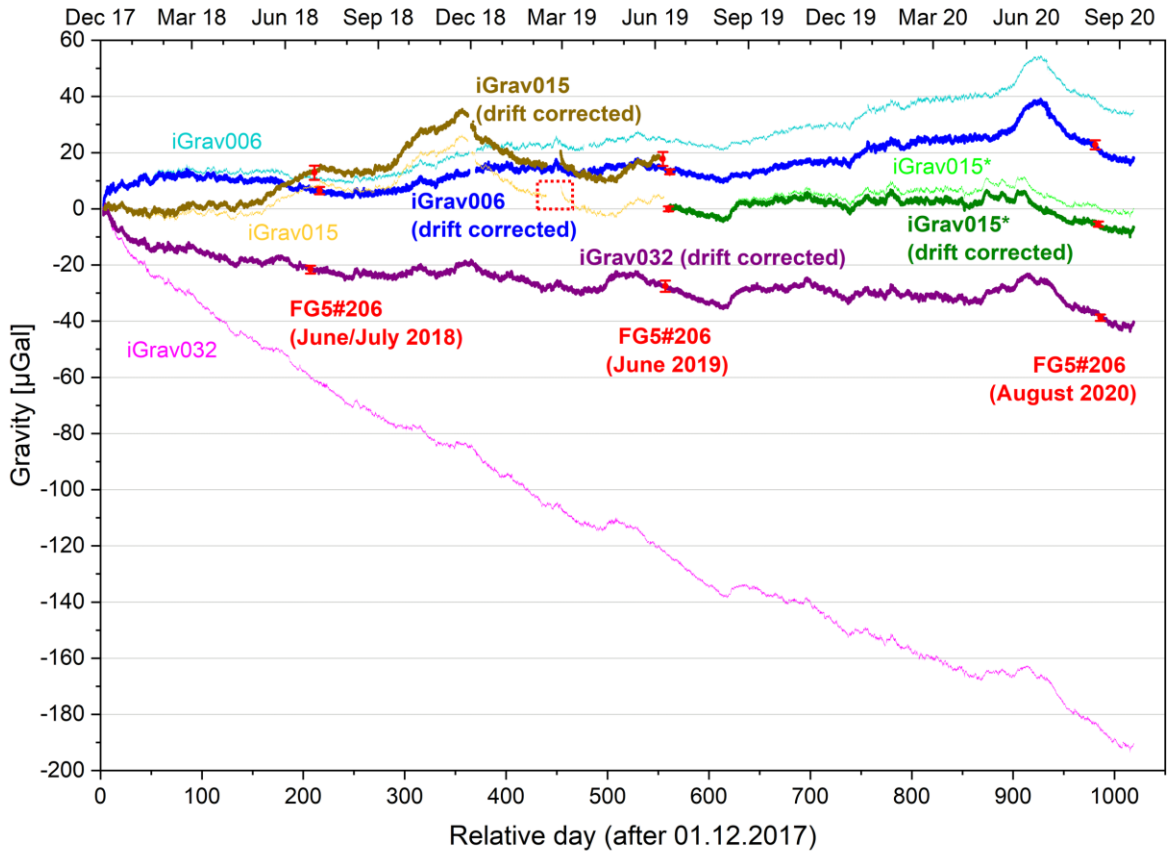


**Figure 43.** Residual gravity time series of the three iGravs at Þeistareykir (light shaded colours), long-term drift estimations by comparison to FG5#206 absolute measurements in summers 2018, 2019 and 2020 (red dots with error bars) and the resulting drift corrected iGrav residuals (dark shaded colours); iGrav015* time series shown in brown colours after movement from reference to central station in June 2019; red dotted box marks iGrav015 data gap due to 14 days power failure at reference station.

**Table 11.** Long-term drift rates (in µGal $yr^{-1}$) of iGrav time-series from Wettzell, J9 and Þeistareykir; in June 2019 iGrav015 was moved from a reference gravity station outside the geothermal field to the central station at Þeistareykir.

| Location | Timeframe | iGrav006 | iGrav015 | iGrav032 |
|---|---|---|---|---|
| Wettzell | 329 days for iGrav006 (May 2015-April 2016) | +9.4 | X | X |
| J9 | 120 days for iGrav015 (June-October 2017) | X | -13.7 | X |
| | 60 days for iGrav032 (July-August 2017) | X | X | -83.7 |
| Þeistareykir | 350 days for each iGrav (June 2018-June 2019) | +7.0 | -9.2 | -59.7 |
| | 779 days for iGrav006 and iGrav032 (June 2018-August 2020) | +6.1 | X | -53.9 |
| | 433 days for iGrav015 (June 2019-August 2020) | X | +5.2 | X |

One goal of this work was to measure the individual drifts of the three iGravs at J9 and then to transport them to Iceland with liquid helium-filled Dewars, at their 4K operating temperature without disturbing the drift behaviour. This goal was only partially fulfilled. iGrav006 was cooled at J9 only 3 weeks before shipping and its Dewar partially warmed to 8K after 13 days in transit, due to delays caused by bad weather during ship transport to Iceland. Therefore, iGrav006 should have a 'normal' drift curve as described above. This appears to be validated by the measured drift of +7.0 µGal per year in Þeistareykir, which is less than the estimated drift of +9.4 µGal per year measured previously in Wettzell (Güntner et al., 2017). In contrast, the drift curves observed at J9 for both iGrav015 and iGrav032 showed an initial exponential behaviour followed by a large negative drift. Different approaches were taken to fix the drift of these two iGravs. iGrav032 was shipped back to GWR to replace its getter, which was diagnosed as a potential cause of the large long-term drift. Unfortunately, this was a misdiagnosis. It is more likely that the problem was caused by shipping iGravs 015 and 032 from GWR to J9 after using the sensor side coils for 'flux trapping' during testing at GWR. This procedure had been instituted to raise the frequency of the commonly observed orbital sphere resonance (Hinderer et al., 2015) out of the long-period seismic band. In retrospect both iGravs 015 and 032 could have been 'repaired' by warming them to room temperature, recooling them to 4K, and reinitializing them without using the side coils to trap flux. This possibility was discussed but it would have delayed the start of gravity monitoring in Iceland by

another month. Therefore, the higher priority was kept, of starting the gravity monitoring as close to the beginning of the power plant operation as possible.

In June 2019, iGrav015 was relocated from the reference station to the central station at Þeistareykir because the gravity signal contained contributions, which could not be explained by drift analysis or from the locally observed environmental parameters (brown line in Fig. 43). As a consequence iGrav015 could not be used with the initial purpose as reference to iGrav006 and iGrav032. The gravity meter was reinstalled at the central station to gain more information about subsurface mass changes in the transition zone between extraction (iGrav032) and injection (iGrav006) zones. The time series of the relocated iGrav015 (dark green line in Fig. 43) shows higher similarity to the other two iGravs and could be included for geothermal interpretation in chapter 4.4. The change from negative to positive drift rates after relocation (see iGrav015 in Fig. 43 and Tab. 11) could be directly caused by the transport of iGrav015 to the central station due a trapped flux in the sensor or by a remaining exponential drift component as discussed above. As an alternative explanation, there could be an error in one of the absolute gravity measurements performed in parallel with iGrav015, or in the correction of the iGrav offsets during pre-processing. Regarding the latter there is one major data gap in the iGrav015 time series due to 14 days power failure in February 2019 (red dotted box in Fig. 43) for which a large offset of 116.5 µGal had to be corrected in the raw data. This may contribute an error to the drift estimation because the true course of the time series remains uncertain for this 14 days period.

*2) What is the share of environmental contributions (from global effects, local hydrology, snow and vertical surface displacement) and how can they be removed from the continuous gravity signals?*

In the course of the second study (chapter 4), I analysed continuous three years long gravity observations of the three iGravs at Þeistareykir. Additionally, I calculated the gravity contributions from locally observed environmental parameters (i.e. atmospheric pressure changes, hydrology, snow and vertical surface displacement) for each gravity station. These results, together with instrumental drift, tidal and global gravity models from the previous study (chapter 3), I used for gravity reduction

of the iGrav time series to improve the resolution and interpretation of geothermally caused signals. From the environmental gravity contributions, global effects and soil water content showed the smallest amplitudes of ±2 to ±3 µGal similarly for each gravity station. Consequently, in the case of Þeistareykir, these contributions have only a minor influence on the overall gravity reduction and the related changes are hardly visible the long-term (three years) iGrav residuals.

Snow mass distributions modelled from SWE measurements resulted in varying gravity contributions among the three sites. The east and central stations showed larger snow contributions (peaks above 8 and 10 µGal in winter 2020) than the west station (below 2 µGal in winter 2020). These differences can be explained by the varying topographies and thus different vertical distributions of the snow cover (above and below the gravity sensor) at each station. It is however arguable if the SWE measurements, which were restricted to the east station only, could be representatively transferred to the other two gravity stations. Locally varying wind exposures may lead to different amounts of snow drift and mass accumulations for each station, where not accounted for by the HyGra model. The setup could be improved by additional data from local weather stations and snow measuring sensors for each station, combined with elaborate snow modelling (e.g. Lehning et al., 2006; Grünewald et al., 2013) to receive a better resolution of the near field snow pack distribution for each gravity sensor.

For vertical surface displacement, the west station receives the largest gravity contribution of 10 µGal from continuous subsidence (-11.1 mm $yr^{-1}$) after the three years observation period, compared to minor subsidence-caused contributions (below 2 µGal) for the central and east stations. These local GNSS observations are in good correlation to the inSAR measurements (shown in chapter 5.4.1). Consequently, both GNSS and inSAR offer reliable data for reduction of the long-term gravity trends induced by vertical displacement. Local height changes can only be observed by GNSS measurements, which are therefore better suited for reduction of the continuous gravity time series. However, the setup at Þeistareykir did not allow reducing the short-term gravity contributions of vertical displacement, because the processed GNSS time series contain periodical variations induced by non-tidal loading effects, which do not coincide with the loading effects observed by the gravity

meters. Several options were discussed and an estimation of the GNSS periodical signals and the linear trends was carried out. Figure 44 shows the GNSS observations and the yearly signals (periodical variations and trends) estimated by least squares regression. For the environmental gravity reductions presented in chapter 4.3.2, only the estimated linear trends were used to account for the contributions of vertical displacement. Another option would be to reduce the GNSS signal by the estimated periodical variations and then use the GNSS residual signal for gravity reduction. This approach is shown in Figure 45 for the 90 days moving average GNSS signals of the four gravity stations. The according gravity contributions are calculated from the GNSS residuals and the locally measured FAGs (see Tab. C5, Appendix C). However, this option was discarded for the present study due to the large GNSS data gaps at the west station (Dec. 2017 to May 2018) and central station (Feb. 2019 to June 2019 and Oct. 2019 to Feb. 2020), which would have been transferred to the iGrav residuals. Note that the amplitudes of these gravity contributions are in the range of ±1 to ±2 µGal (Fig. 45), which would scarcely influence the overall gravity reductions.

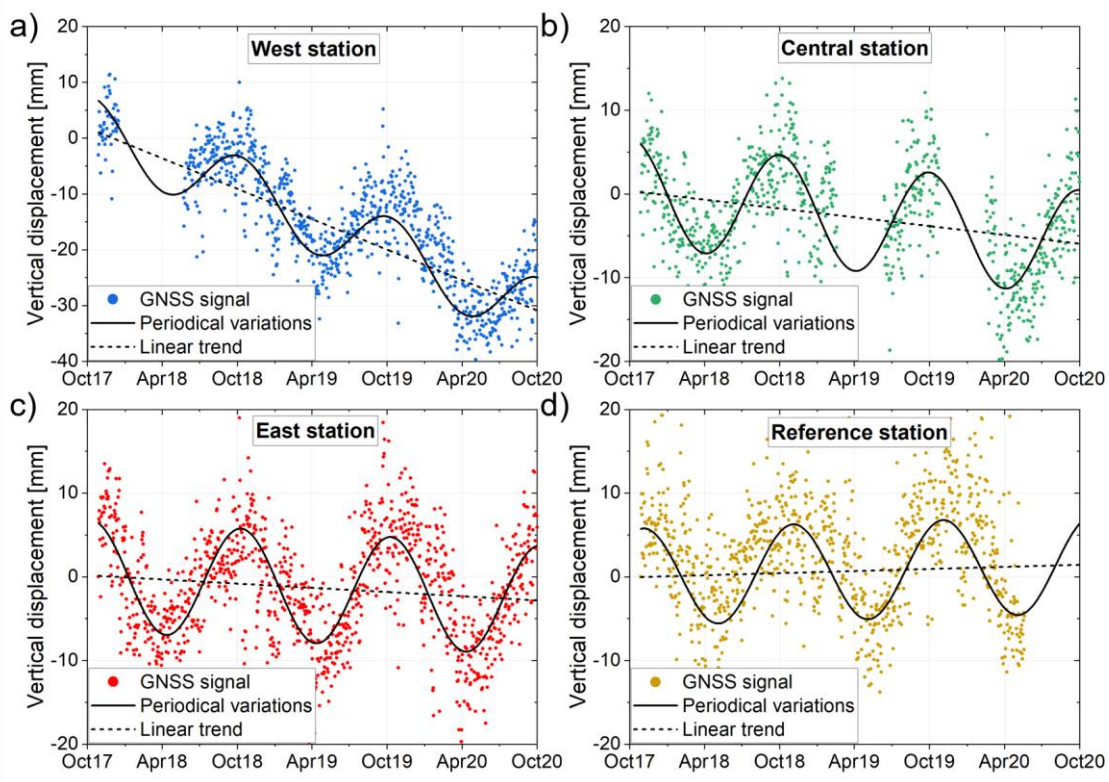


**Figure 44.** GNSS observations at Þeistareykir between November 2017 and October 2020; showing the measured vertical surface displacements (coloured dots), from which the periodical variations (black line) and linear trends (dashed line) are estimated for each gravity station based on the following trigonometric function: y = Amplitude * sin (2π*t + phase) + trend*t.

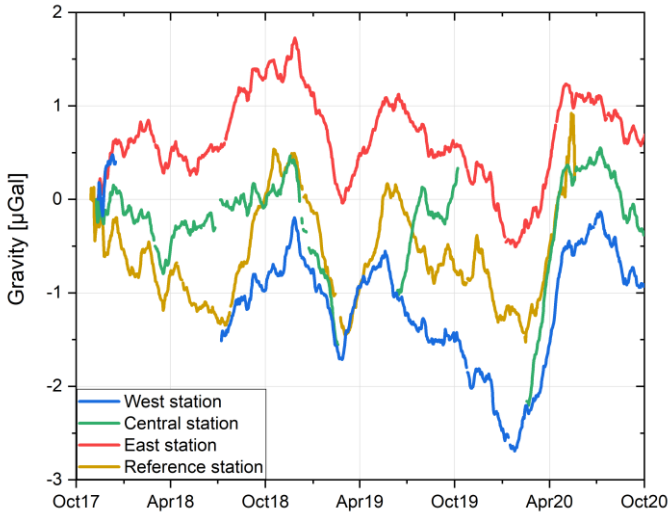


**Figure 45.** Gravity contributions calculated from the 90 days moving average GNSS signals after reduction of estimated periodical variations for the four gravity stations at Þeistareykir.

*3) Which of the observed gravity changes can be attributed to exploitation-induced mass changes of the geothermal reservoir?*

The second part of chapter 4 compares the iGrav residuals (after reduction of the environmental contributions discussed above) to geothermal related subsurface water flow. This comparison revealed a direct correlation between GWLs and injection flow rates, which indicates that the reinjection system is subject to a confined aquifer. Similar responses to the geothermal flow rates could be observed in the gravity time series (iGrav015 and iGrav032) but with time delays of up to several weeks after sudden reduction of the injection flow rate. Comparison with time-lapse gravimetry (presented in chapter 5) showed good agreement of the CG5 measurements at station 111 near the west station (iGrav006) and at station 108 near the east station (iGrav032) to the according iGrav time series. The agreement of the continuous gravity signal within the CG5 error bars can be seen in Figure 46, which shows an extended plot of the gravity (and flow rate) observations from chapter 4 and 5 between June 2017 and December 2020. Both the iGrav and the CG5 measurements show an overall decrease in gravity at (and close to) the east station. This can be generally explained by mass loss due to continuous fluid extraction of (and above) 240 kg $s^{-2}$ between January 2018 and June 2020 (red dots, Fig. 46), which is larger than the recharge of the geothermal reservoir. The gravity measurements at the west station show smaller variations and the gravity signal stays about constant for total the observation period. This suggests that there is no major mass accumulation below the west station, which could have been caused by the large amounts of reinjected fluids above 180 kg $s^{-2}$ after February 2018 (green dots, Fig. 46). The CG5-measured gravity differences between 2017 and 2019 support the above hypothesis by showing largest gravity decrease (-38 ±10 µGal) close to the east station, smallest changes (-3 ±6 µGal) near the west station and intermediate decrease (-8 ±6 µGal) in the transition zone near the central station.

Possible gravity responses to short-term reductions in reinjection or extraction rates (in July 2018, March/April 2019, August 2019, March 2020, June 2020; marked by 1* to 5* in Fig. 46) are more recognizable in the time series of iGrav015 and iGrav032 than for iGrav006. This is another indication that there is no water accumulation below the west station. Direct responses to injection by the GWL monitoring (west of

Tjarnarás fault) suggest outflow of the reinjected fluids into western direction instead (see also geothermal interpretations in chapter 4.4). The delayed gravity increases of up to 10 µGal after reduced extraction rates (most clearly visible for 2* and 3*, Fig. 46) indicate mass accumulations due to temporary recharge of the reservoir. It seems that, after a more permanent reduction of flow rates (extraction <240 kg $s^{-1}$, injection <180 kg $s^{-1}$) after July 2020, the geothermal system may have reached steady state conditions between extraction, natural recharge, injection and outflow.

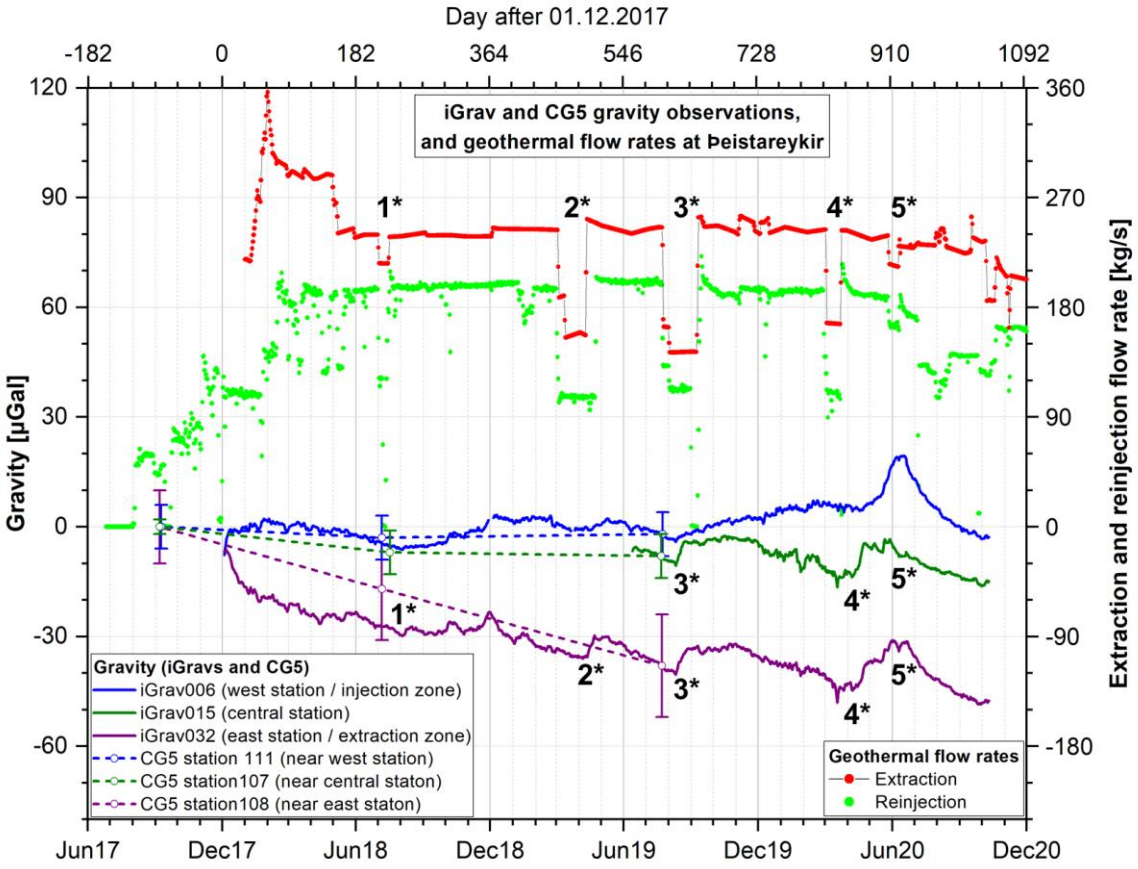


**Figure 46.** Comparison of iGrav and CG5 measurements to extraction and reinjection flow rates at Þeistareykir between June 2017 and December 2020; the CG5 observations are set to zero for the initial 2017 campaign, the iGrav residuals are adjusted to the third (2019) CG5 campaign when all three iGravs were simultaneously measuring at west, central and east stations; possible gravity responses to short-term reduction in geothermal flow rates are marked by 1* to 5*.

## 6.2 General conclusions and recommendations for other work

In this thesis, I presented gravimetry as a monitoring technique to observe reservoir changes during geothermal operation. To understand the advantages and possible limitations of this method, I formulated eight general research questions in chapter 1.1. The subsequent conclusions and implications shall answer these questions with regard to my experience and findings from the gravity measurements at the J9 observatory in France and at the Þeistareykir geothermal field in Iceland.

*1) What is the benefit of gravimetry compared to other observation techniques?*

Gravity measurements allow non-destructive observations of subsurface mass changes, which can be achieved by no other geophysical method. Alternative applications for measurements of electric resistivity or magnetic susceptibility can only be used for indirect assessment of geothermal related mass variations. With the deployment of gravity meters, high temporal resolution (up to 1 second sample rates for the SGs) and high spatial resolution (by repeated measurements within a gravity network) measuring signals can be obtained. Especially the latter time-lapse gravimetric method can be performed with relatively low expenses for the measuring arrangement, compared to cost-intensive drilling of monitoring boreholes, which can only deliver very localised data and would always leave an anthropogenic (intrusive) footprint to the observed underground.

*2) Which supplementary methods are useful / needed for the interpretation of gravimetric monitoring?*

Gravity observations can be ambiguous because of several natural and anthropogenic effects that contribute to the gravity signal. Depending on the amplitudes of the target signal, gravity analysis may require a comprehensive reduction of the superimposing contributions. The methods for measuring these additional gravity contributions are summarised in Table 12. Repeated absolute gravity measurements have to be performed at each of the permanent monitoring stations to check the instrumental drift behaviour of the continuous operating gravity

meters, and as reference for the time-lapse gravity network. Local GPS or GNSS measurements are needed for each (continuous and time-lapse) gravity station as geographical reference and for calculation of theoretical or local tidal models. Information about temporal height changes (from GPS, GNSS, InSAR or levelling measurements) is necessary for gravity reduction of vertical surface displacement. Additional measurements of local environmental parameters (i.e. air pressure, soil moisture and snow) at the permanent stations provide important data for the reduction of the continuous gravity time series. Reduction of GWL can be inferred from local monitoring wells or for comparative analysis, if there is a direct correlation between observed GWL, geothermal flow rates and the gravity residual signal.

**Table 12.** Supportive methods for gravimetric monitoring.

| **Methods** | | **Essential application** | **Notes / further applications** |
|---|---|---|---|
| for continuous and time-lapse gravimetry | Absolute gravimetry | Drift correction (continuous gravity measurements), reference for time-lapse gravity network | Expendable if drift behaviour is well-known or assessable by other (SG) reference measurements |
| | GPS / GNSS (InSAR or levelling) measurements | Geographical referencing, reduction of tides and vertical surface displacement | Comparative InSAR and/or levelling measurements |
| for continuous gravimetry | Pressure measurements | Reduction of air masses | Global pressure models in addition to local measurements |
| | Soil moisture, snow measurements | Reduction of hydrological mass changes | Expendable if insignificant effects (e.g. no rain or snow-free areas) |
| | Borehole monitoring | Reduction of GWL (if no direct correlation to geothermal flow) | Direct comparison to gravity residual signal |

*3) Which gravity meter types are suited for geothermal monitoring and which instruments can be used for complementary measurements?*

The setup of this thesis suggests a combination of three gravity meter types, including the iGrav SG for continuous monitoring, the CG5 Scintrex gravity meter for time-lapse observations and the FG5 absolute gravity meter for reference measurements. This setup is suitable for long-term monitoring of a geothermal field.

As an alternative, the setup could be confined to either continuous and absolute gravimetry or time-lapse and absolute gravimetry, in case that the research should be focussed only on high temporal or high spatial resolution of the gravity signal. Also, the specific gravity meters could be replaced by other gravity meters of a similar type (e.g. iOSG for iGrav, CG6 for CG5, A10 for FG5). Instruments for complementary measurements comprise a GNSS receiver for positioning of the gravity stations and a sensor array (incl. pressure, soil moisture and snow sensors) for assessing the atmospheric and hydrological contributions for each of the permanent gravity stations.

*4) What can be done to ensure reliability of comparative measurements between different gravity meter types?*

For an initial assessment of this question, the instrumental specifications should be compared to see what instrumental performance can be expected for which gravity meter type (see Tab. 1, chapter 2). Calibration, noise and drift behaviour should be checked and optimised for each instrument in advance to the field observations. For side-by-side measurements, an equal measuring setup should be chosen for all instruments (e.g. Figs. 7 and 8, chapter 2) showing FG5 and iGrav positioned on two concrete pillars in the same building). During data analysis, the measurement accuracy (error bars) provides further indication about the reliability of the gravity observations.

*5) What is the best arrangement of the gravity stations within (and outside) the geothermal field?*

The optimal arrangement of gravity stations for continuous monitoring is depicted in the sketch in Figure 2 (in chapter 2), with two stations inside the geothermal field close to the extraction and reinjection wells, and a reference station outside the geothermal field. This arrangement was targeted for Þeistareykir with the initial setup of iGrav032 at the east station (extraction zone), iGrav006 at the west station (injection zone) and iGrav015 at the reference station (cf. Fig. 3, chapter 2).

Unfortunately, it was not possible to quantify the additional environmental gravity contributions at the reference station and iGrav015 was moved to the central station in June 2019. In retrospect, the reference station could have been set up at a different location closer to the geothermal field where there is access to continuous power supply. One possible option could have been a site about 4 km northwest of Þeistareykir, close to the groundwater extraction well (pink square in Fig. 32, chapter 5). For the time-lapse gravity network, it is advisable to include existing stations of former gravity observations, like the stations used by Magnússon (2016) in the case of Þeistareykir (cf. Fig. C1, Appendix C). The past measurements can provide an important reference and extend the overall timeline gravity observations.

*6) Is it possible to observe and quantify gravity changes, and relate them to mass changes of the geothermal reservoir?*

In an ideal scenario, if the geothermal reservoir is in equilibrium, i.e. there is a constant recharge of the same amount as extraction on the one hand, and reinjection equals outflow on the other hand, then there would be no geothermal related gravity changes and the gravity meter would show an unvarying residual signal. This ideal situation may be approached after several years of sustainable geothermal operation. In case of an early phase of power plant operation (like for Þeistareykir), larger amounts of gravity changes are expected, due to alteration of the natural reservoir state and short-term adjustments of extraction and injection rates.

The gravity measurements at Þeistareykir revealed long-term signals that are correlating for time-lapse and continuous gravimetry, with up to 20 µGal $yr^{-1}$ above the extraction zone and minor changes up to 3 µGal $yr^{-1}$ above the reinjection zone. This suggests that the applied extraction flow rates of around 240 kg $s^{-1}$ are larger than the recharge of the reservoir. The gravity signals of iGrav015 and iGrav032 showed delayed gravity increases of about 10 µGal after short-term reductions of the extraction rate below 180 kg $s^{-1}$, which indicates a temporary mass increase within the geothermal reservoir.

*7) Which observations can be used to make a statement about the sustainability of the geothermal field?*

Both time-lapse and continuous gravimetry can provide guidance for sustainable exploitation of a geothermal field. Long-term gravity observations of several years may reveal mass accumulation, depletion or equilibrium of the reservoir. Continuous gravity monitoring has the additional advantage for tracing short-term mass changes in the underground, which can be associated to operational changes of the power plant. For this purpose, it is useful to make a comparative analysis between the gravity residuals and borehole monitoring data of GWL, extraction and reinjection flow rates. As demonstrated for Þeistareykir, this method can be used to relate the observed gravity changes to mass changes of the geothermal reservoir from which a preliminary sustainability assessment can be made. For a more profound evaluation and quantification of the observed gravity in terms of mass changes, it is necessary to model the hydraulic parameters (e.g. hydraulic diffusivity, fluid temperatures and densities) and spatial distributions inside the geothermal system.

*8) What are the "lessons learned" from the specific study area that can be transferred to other geothermal sites?*

In summary of the three scientific questions discussed in chapter 6.1 and the seven general research questions from above, I shortly highlight the lessons learned at Þeistareykir, which should be considered for future monitoring studies:

- The iGravs SGs should only be transported cold (sensor at 4K operating conditions) without 'flux trapping' of the side coils to prevent an alteration of long-term drift rates.
- Absolute gravity meter measurements are essential reference of the time-lapse gravity network and drift correction of the continuous gravity time series.
- For differential analysis, the reference station has to be outside the geothermal field, but close enough to the other stations so that environmental gravity contributions are similar and can be neutralised in the gravity difference.

- Hydrological gravity contributions from changes in snow or water levels of nearby lakes or near surface GWLs have an important influence on the gravity signal but can be difficult to access and quantify due to varying local conditions (e.g. snowdrifts, freezing and melting processes, high pressure and temperature at near-surface).

## 6.3 Outlook

The experience from over three years of time-lapse, absolute and continuous gravity observations at the Icelandic study area provide valuable knowledge for future geothermal research. For Þeistareykir, a continuation of the gravity monitoring is planned with at least one of the currently installed iGrav SGs and the existing infrastructure (gravity station, GNSS, hydro-meteorological sensors, etc.). This will allow for further analyses of the reservoir mass changes to maintain a sustainable power plant operation.

Ongoing research at the 'Krafla Magma Testbed' (KMT; Eichelberger et al., 2018) also provides an opportunity for gravity monitoring. The Krafla geothermal field is located about 22 km to the southeast (Fig. 3, chapter 2) and has one gravity station with equal setup (incl. pillars, power connection and all sensors) like the other four stations at Þeistareykir. Similarly to Þeistareykir, Krafla also provides a gravity network that was formerly used for time-lapse observations (De Zeeuw-van Dalfsen et al., 2006). With this setup, all requirements for hybrid gravity monitoring are fulfilled. Scientific gravimetric questions for KMT may deal with possible mass changes and tracing subsurface flow of cooling water while drilling into the underlying geothermal system.

A promising enhancement for the hybrid gravimetric method could be provided by deployment of the newly developed absolute quantum gravity meter (AQG; Ménoret et al., 2018). First performance tests at laboratory conditions show high sensitivity of 10 nm $s^{-2}$ after 1 h, no significant drift and good correlation of observed gravity changes in comparison to the FG5 and iGrav measurements (Cooke et al., 2021). If the AQG turns out to provide reliable results under field conditions, it may also be used as absolute reference for continuous and time-lapse gravity observations. The

instrument is much smaller, lighter and easier to handle and transport than the FG5 absolute gravity meter. Therewith, the measurement repetition rate could be increased (to more than once a year), which would improve drift estimation for the continuous operating gravity meter, or additional AG measurements could be done at more than one reference point of the time-lapse gravity network to increase the reliability of the spatial gravity observations.

# References

Agnew, D.C., 2015. Earth Tides, in Treatise on Geophysics, vol. 3 Geodesy, second edition, vol. ed. T. Herring, ed. in chief Schubert G., Elsevier, Amsterdam, The Netherlands, 151-178, https://doi:10.1016/b978-0-444-53802-4.00058-0.

Al-majid, M.H. & Mutib, M., 2018. Implications of Latest Earthquakes from Geophysical Surveys in Shaikhan Area Northern Iraq. International Journal of Enhanced Research in Science, Technology & Engineering, 7(11), https://www.researchgate.net/profile/Drmarwan-Mutib/publication/346054529_Implications_of_Latest_Earthquakes_from_Geophysical_Surveys_in_Shaikhan_Area_Northern_Iraq/links/5fb8ebce92851c933f498693/Implications-of-Latest-Earthquakes-from-Geophysical-Surveys-in-Shaikhan-Area-Northern-Iraq.pdf, Accessed 22 November 2021.

Amalvict, M., Hinderer, J., Boy, J.-P. & Gegout, P., 2001. Three Year Comparison Between a Superconducting Gravimeter (GWR C026) and an Absolute Gravimeter (FG5# 206) in Strasbourg (France), Journal of the Geodetic Society of Japan, 47(1), 334-340, https://doi.org/10.11366/sokuchi1954.47.334.

Ármannsson, H., Gíslason, G., and Torfason, H., 1986. Surface exploration of the Theistareykir high-temperature geothermal area, Iceland, with special reference to the application of geochemical methods, Applied Geochemistry, 47-64, https://doi.org/10.1016/0883-2927(86)90037-5.

Ármannsson, H., Gudmundsson, Á., Steingrímsson, B.S., 1987. Exploration and development of the Krafla geothermal area, Jökull, 37:13-30, https://www.researchgate.net/profile/Asgrimur-Gudmundsson/publication/284698694_Exploration_and_development_of_the_Krafla_geothermal_area/links/56e9697208a

e47bc651c716e/Exploration-and-development-of-the-Krafla-geothermal-area.pdf. Accessed 22 November 2021.

Ármannsson, H., 2008. The Theistareykir geothermal system, North East Iceland. Case history, UNU-GPT, KenGen, Kenya, https://orkustofnun.is/gogn/unu-gtp-sc/UNU-GTP-SC-13-0607.pdf. Accessed 22 November 2021.

Ármannsson, H., 2009. Exploration of the Theistareykir geothermal system, NE Iceland, UNU-GTP and LaGeo, Santa Tecla, El Salvador, http://www.os.is/gogn/unu-gtp-sc/UNU-GTP-SC-09-21.pdf, Accessed 22 November 2021.

Arnoso, J., Riccardi, U., Hinderer, J., Córdoba, B. & Montesinos, F.G., 2014. Analysis of co-located measurements made with a LaCoste&Romberg Graviton-EG gravimeter and two superconducting gravimeters at Strasbourg (France) and Yebes (Spain), Acta Geodaetica et Geophysica, 49(2), 147-160, https://doi.org/10.1007/s40328-014-0043-y.

Axelsson, G., 2011. Using long case histories to study hydrothermal renewability and sustainable utilization. Geothermal Resources Council Transactions, 35, 1393-1400, http://www.isor.is/sites/isor.is/files/Using%20Long%20Case%20Histories%20to%20Study%20Hydrothermal%20Renewability%20and%20Sustainable%20Utilization.pdf, Accessed 22 November 2021.

Berrino, G., 2020. The state of the art of gravimetry in Italy. Rendiconti Lincei. Scienze Fisiche e Naturali, 31(1), 35-48, https://doi.org/10.1007/s12210-020-00924-8.

Bixley, P.F., Clotworthy, A.W. & Mannington, W. I., 2009. Evolution of the Wairakei geothermal reservoir during 50 years of production. Geothermics, 38(1), 145-154, https://doi.org/10.1016/j.geothermics.2008.12.007.

Boy, J.-P. & Hinderer, J., 2006. Study of the seasonal gravity signal in superconducting gravimeter data. Journal of Geodynamics, 41(1-3), 227-233, https://doi.org/10.1016/j.jog.2005.08.035.

## References

Boy, J.-P. & Lyard, F., 2008. High-frequency non-tidal ocean loading effects on surface gravity measurements. Geophysical Journal International, 175(1), 35-45, https://doi.org/10.1111/j.1365-246X.2008.03895.x.

Bromley, C.J., 2009. Groundwater changes in the Wairakei–Tauhara geothermal system. Geothermics, 38(1), 134-144, https://doi.org/10.1016/j.geothermics.2008.11.007.

Calvo, M., Hinderer, J., Rosat, S., Legros, H., Boy, J.-P., Ducarme, B. & Zürn, W., 2014. Time stability of spring and superconducting gravimeters through the analysis of very long gravity records, J. of Geodyn., 80, 20-33, https://doi.org/10.1016/j.jog.2014.04.009.

Calvo, M., Rosat, S. & Hinderer, J., 2016. Tidal spectroscopy from a long record of superconducting gravimeters in Strasbourg (France), in: Freymueller J.T., Sánchez L. (eds) International Symposium on Earth and Environmental Sciences for Future Generations. International Association of Geodesy Symposia, vol 147. Springer, Cham, https://doi.org/10.1007/1345_2016_223.

Carbone, D., Poland, M.P., Diament, M. & Greco, F., 2017. The added value of time-variable microgravimetry to the understanding of how volcanoes work, Earth-Science Reviews, 169, 146-179, https://doi.org/10.1016/j.earscirev.2017.04.014.

Carbone, D., Cannavò, F., Greco, F., Reineman, R. & Warburton, R.J., 2019. The benefits of using a network of superconducting gravimeters to monitor and study active volcanoes, Journal of Geophysical Research: Solid Earth, 123, https://doi.org/10.1029/2018JB017204.

Carnec, C. & Fabriol, H., 1999. Monitoring and modeling land subsidence at the Cerro Prieto geothermal field, Baja California, Mexico, using SAR interferometry. Geophysical Research Letters, 26(9), 1211-1214, https://doi.org/10.1029/1999GL900062.

Carrere, L., Lyard, F., Cancet, M. & Guillot, A., 2015. FES 2014, a new tidal model on the global ocean with enhanced accuracy in shallow seas and in the Arctic region. EGUGA, April 2015, Vienna, id.5481.

Cooke, A.K., Champollion, C. & Le Moigne, N., 2021. First evaluation of an absolute quantum gravimeter (AQG# B01) for future field experiments. Geoscientific Instrumentation, Methods and Data Systems, 10(1), 65-79, https://doi.org/10.5194/gi-10-65-2021.

Creutzfeldt, B., Güntner, A., Klügel, T. & Wziontek, H. (2008). Simulating the influence of water storage changes on the superconducting gravimeter of the Geodetic Observatory Wettzell, Germany. Geophysics, 73(6), WA95-WA104, https://doi.org/10.1190/1.2992508.

Creutzfeldt, B., Güntner, A., Wziontek, H. & Merz, B. (2010). Reducing local hydrology from high-precision gravity measurements: a lysimeter-based approach. Geophysical Journal International, 183(1), 178-187, https://doi.org/10.1111/j.1365-246X.2010.04742.x.

Crossley, D.J., Jensen, O.G. & Hinderer, J., 1995. Effective barometric admittance and gravity residuals. Physics of the Earth and Planetary Interiors, 90(3-4), 221-241, https://doi.org/10.1016/0031-9201(95)05086-Q.

Crossley, D., Hinderer, J. & Boy, J.-P., 2004. Regional gravity variations in Europe from superconducting gravimeters, Journal of Geodynamics, 38(3-5), 325-342, https://doi.org/10.1016/j.jog.2004.07.014.

Crossley, D., Calvo, M., Rosat, S. & Hinderer, J., 2018. More Thoughts on AG–SG Comparisons and SG Scale Factor Determinations, Pure and Applied Geophysics, 175(5), 1699-1725, https://doi.org/10.1007/s00024-018-1834-9.

Currenti, G., 2014. Numerical evidence enabling reconciliation gravity and height changes in volcanic areas. Geophysical Journal International, 197(1), 164-173, https://doi.org/10.1093/gji/ggt507.

Damiani, T.M., 2014. Dynamic Effects in Gravimetry: An Assessment of the Current State of Knowledge. NOAA-National Geodetic Survey, 1315 East-West Hwy, SSMC3, Silver Spring, MD 20910, G51B-0362. https://nweb.ngs.noaa.gov/web/science_edu/presentations_library/files/damiani_agu_2014_36x65.pdf. Accessed 22 November 2021.

## References

Dehant, V., Defraigne, P. & Wahr, J.M., 1999. Tides for a convective Earth. Journal of Geophysical Research: Solid Earth, 104(B1), 1035-1058., https://doi.org/10.1029/1998JB900051.

De Zeeuw-van Dalfsen, E., Rymer, H., Williams-Jones, G., Sturkell, E. & Sigmundsson, F., 2006. Integration of micro-gravity and geodetic data to constrain shallow system mass changes at Krafla Volcano, N Iceland. Bulletin of Volcanology, 68(5), 420-431, https://doi.org/10.1007/s0445-005-0018-5.

Dobslaw, H., Bergmann-Wolf, I., Dill, R., Poropat, L., Thomas, M., Dahle, C. & Flechtner, F., 2017. A new high-resolution model of non-tidal atmosphere and ocean mass variability for de-aliasing of satellite gravity observations: AOD1B RL06. Geophysical Journal International, 211(1), 263–269, https://doi.org/10.1093/gji/ggx302.

Drouin, V. & Sigmundsson, F., 2019. Countrywide observations of plate spreading and glacial isostatic adjustment in Iceland inferred by Sentinel-1 radar interferometry, 2015–2018. Geophysical Research Letters, 46(14), 8046-8055, https://doi.org/10.1029/2019GL082629.

Drouin, V., Sigmundsson, F. & Li, S., 2020. Ground deformation at the Theistareykir volcanic system, Iceland 535 following onset of geothermal utilization. In Proceedings World Geothermal Congress 2020, Reykjavik, Iceland.

Ducarme, B., Venedikov, A.P., Arnoso, J. & Vieira, R., 2004. Determination of the long period tidal waves in the GGP superconducting gravity data. Journal of Geodynamics, 38(3-5), 307-324, https://doi.org/10.1016/j.jog.2004.07.004.

Egilson, Þ., 2019. Eftirlitsmælingar arið 2018. Report LV-2019-034.

Eichelberger, J., Ingolfsson, H.P., Carrigan, C., Lavallee, Y., Tester, J. & Markusson, S.H., 2018. Krafla magma testbed: Understanding and using the magma-hydrothermal connection. Transactions-Geothermal Resources Council, 42, 2396-2405,
https://livrepository.liverpool.ac.uk/3027998/1/Eichelberger_GRC_2018_revised.pdf, Accessed 22 November 2021.

Erbas, K., Schäfer, F., Guðmundson, Á., Júlíusson, E., Hersir, G.P., Warburton, R.J., Bernard, J.-D., Portier, N., Hinderer, J., Drouin, V., Sigmundsson, F., Ágústsson, K., Männel, B., Güntner, A., Voigt, C., Schöne, T., Jolly, A., Hjartasson, H., Hernandez, D.F.N., and Jousset, P., 2021. Continuous Microgravity Monitoring in a Volcanic Geothermal Field: Integrated Observational Approach in Þeistareykir, NE Iceland. In Proceedings World Geothermal Congress 2020, Reykjavik, Iceland, https://pangea.stanford.edu/ERE/db/WGC/papers/WGC/2020/13124.pdf, Accessed 22 November 2021.

Fores, B., Champollion, C., Le Moigne, N., Bayer, R. & Chery, J., 2017. Assessing the precision of the iGrav superconducting gravimeter for hydrological models and karstic hydrological process identification. Geophysical Journal International, 208(1), 269-280, http://dx.doi.org/10.1093/gji/ggw396.

Forster, F., Güntner, A., Jousset, P., Reich, M., Männel, B., Hinderer, J. & Erbas, K., 2021. Environmental and anthropogenic gravity contributions at the Þeistareykir geothermal field, North Iceland. Geothermal Energy, (Accepted for publication), https://doi.org/10.21203/rs.3.rs-692087/v1.

Francis, O. & Mazzega, P., 1990. Global charts of ocean tide loading effects, Journal of Geophysical Research: Oceans, 95(C7), 11411-11424, https://doi.org/10.1029/JC095iC07p11411.

Fukuda, Y., Okuno, J.I., Doi, K. & Lee, C.K., 2021. Gravity observations at Jang Bogo Station, Antarctica, and scale factor calibrations of different relative gravimeters. Polar Science, 100702, https://doi.org/10.1016/j.polar.2021.100702.

Gautason, B., Guðmundsson, Á., Hjartarson, H., Blischke, A., Mortensen, A.K., Ingimarsdóttir, A., Gunnarsson, H.S., Sigurgeirsson, M.Á., Árnadóttir, S. & Egilson, Þ., 2010. Exploration Drilling in the Theistareykir High-Temperature Field, NE-Iceland: Stratigraphy, Alteration and Its Relationship to Temperature Structure. In Proceedings World Geothermal Congress 2010, Indonesia, https://www.geothermal-energy.org/pdf/IGAstandard/WGC/2010/1136.pdf, Accessed 22 November 2021.

## References

Gíslason, G., Johnsen, G.V., Ármannsson, H., Torfason, H. & Árnason, K., 1984. Theistareykir. Surface exploration of the high-temperature geothermal area. Orkustofnun, Reykjavík, Rep. No. OS 84089/JHD16, 134.

Gitlein, O., Timmen, L. & Müller, J., 2013. Modeling of atmospheric gravity effects for high-precision observations. International Journal of Geosciences, 4(4), 663-671, https://doi.org/10.15488/1531.

Grossi, G., Lendvai, A., Peretti, G. & Ranzi, R., 2017. Snow Precipitation Measured by Gauges: Systematic Error Estimation and Data Series Correction in the Central Italian Alps. Water, 9(7), 461, https://doi.org/10.3390/w9070461.

Grünewald, T., Stötter, J., Pomeroy, J.W., Dadic, R., Moreno Baños, I., Marturià, J., Spross, M., Hopkinson, C., Burlando, P. & Lehning, M., 2013. Statistical modelling of the snow depth distribution in open alpine terrain. Hydrology and Earth System Sciences, 17(8), 3005-3021, https://doi.org/10.5194/hess-17-3005-2013, 2013.

Gudjónsdóttir, S.R., St. Ásgeirsdóttir, R., Sigurgeirsson, M.Á. & Gudmundsson, Á., 2018. Drilling of nine high temperature wells in the Þeistareykir geothermal field, NE-Iceland, 2016-2017. Overview of the project, geology of the area and interpretation of the lithology and alteration of the sub-surface strata. In EGU General Assembly Conference Abstracts, 1369.

Gudmundsson, A., Brynjolfsson, S. & Jonsson, M.T., 1993. Structural analysis of a transform fault-rift zone junction in North Iceland. Tectonophysics, 220(1-4):205-221. https://doi.org/10.1016/0040-1951(93)90232-9.

Gudmundsson, B.T. & Arnórsson, S., 2002. Geochemical monitoring of the Krafla and Námafjall geothermal areas, N-Iceland. Geothermics, 31(2), 195-243, https://doi.org/10.1016/S0375-6505(01)00022-0.

Guðmundsson, Á., Gautason, B., Axelsson, G., Lacasse, C., Thorgilsson, G., Ármannsson, H., Tulinius, H., Sæmundsson, K., Karlsdóttir, R., Kjaran, S.P., Pálmarsson, S.Ó. & Halldórsdóttir, S.A., 2008. A conceptual model of the geothermal system at Theistareykir and a volumetric estimate of the geothermal potential. Iceland GeoSurvey, Mannvit and Vatnaskil Consulting Engineers, report ÍSOR-2008/024 (in Icelandic).

Guðnason, E.Á., Arnaldsson, A., Axelsson, G., Berthet, J.C.C., Halldórsdóttir, S. & Magnússon, I.Þ., 2015. Analysis and modelling of gravity changes in the Reykjanes geothermal system in Iceland, during 2004-2010. In Proceedings World Geothermal Congress 2015, https://georg.cluster.is/wp-content/uploads/2017/02/13114.pdf, Accessed 22 November 2021.

Güntner, A., Reich, M., Mikolaj, M., Creutzfeldt, B., Schroeder, S. & Wziontek, H., 2017. Landscape-scale water balance monitoring with an iGrav superconducting gravimeter in a field enclosure, Hydrol. Earth Syst. Sci., 21, 3167-3182, https://doi.org/10.5194/hess-21-3167-2017.

Harnisch, G. & Harnisch, M., 2006. Hydrological influences in long gravimetric data series, Journal of Geodynamics, 41(1-3), 276-28, https://doi.org/10.1016/j.jog.2005.08.018.

Hector, B. & Hinderer, J., 2016. pyGrav, a Python-based program for handling and processing relative gravity data. Computers & geosciences, 91, 90-97, https://doi.org/10.1016/j.cageo.2016.03.010.

Hersir, G.P., Sigmundsson, F. & Ágústsson, K. (editors), Magnússon, I.Th., Drouin, V., Vilhjálmsson, A.M., Lanzi, C., Li, S., Geirsson, H. & Hreinsdóttir, S., 2020. Geodetic Observations and Surface Deformation at Krafla mid 2018–2020. Status Report December 2020, Report ÍSOR-2020/037, RH-9-20, LV-2020-036.

Hinderer, J., Crossley, D. & Warburton, R.J., 2015. Superconducting gravimetry, in Treatise on Geophysics, vol. 3 Geodesy, second edition, vol. ed. T. Herring, ed. in chief Schubert G., Elsevier, Amsterdam, The Netherlands, 66–122, https://doi.org/10.1016/B978-0-444-53802-4.00062-2.

Hinderer, J., Hector, B., Mémin, A. & Calvo, M., 2016. Hybrid gravimetry as a tool to monitor surface and underground mass changes. In International symposium on earth and environmental sciences for future generations (pp. 123-130). Springer, Cham, https://doi.org/10.1007/1345_2016_253.

Hinderer, J., Rosat, S., Schäfer, F., Riccardi, U., Boy, J.-P., Jousset, P., Littel, F. & Bernard, J.-D., 2018. Intercomparison of a dense meter-scale network of superconducting gravimeters at the J9 gravimetric observatory of Strasbourg,

France, 1st Workshop on the International Geodynamics and Earth Tide Service (IGETS), Potsdam, Germany, June 2018.

Hjartardóttir, Á.R., Einarsson, P., Magnúsdóttir, S., Björnsdóttir, Þ. & Brandsdóttir, B., 2016. Fracture systems of the Northern Volcanic Rift Zone, Iceland: an onshore part of the Mid-Atlantic plate boundary. Geological Society, London, Special Publications, 420(1), 297-314, https://doi.org/10.1144/SP420.1.

Hugill, A.L., 1988. The new Scintrex CG-3 Autograv gravity meter: description and test results. In ASEG/SEG Conference, Adelaide, Australia.

Hunt, T.M., 2001. Five lectures on environmental effects of geothermal utilization. Geothermal training programme, Orkustofnun, https://orkustofnun.is/gogn/unu-gtp-report/UNU-GTP-2000-01.pdf, Accessed 22 November 2021.

Hunt, T., Sugihara, M., Sato, T. & Takemura, T., 2002. Measurement and use of the vertical gravity gradient in correcting repeat microgravity measurements for the effects of ground subsidence in geothermal systems. Geothermics, 31(5), 525-543, https://doi.org/10.1016/S0375-6505(02)00010-X.

Imanishi, Y., 2005. On the possible cause of long period instrumental noise (parasitic mode) of a superconducting gravimeter, Journal of Geodesy, 78(11-12), 683-690, https://doi.org/10.1007/s00190-005-0434-5.

Jacob, T., Chery, J., Bayer, R., Le Moigne, N., Boy, J.-P., Vernant, P. & Boudin, F., 2009. Time-lapse surface to depth gravity measurements on a karst system reveal the dominant role of the epikarst as a water storage entity, Geophysical Journal International, 177(2), 347-360, https://doi.org/10.1111/j.1365-246X.2009.04118.x.

Jacob, T., Bayer, R., Chery, J. & Le Moigne, N., 2010. Time-lapse microgravity surveys reveal water storage heterogeneity of a karst aquifer. Journal of Geophysical Research: Solid Earth, 115(B6), https://doi.org/10.1029/2009JB006616.

Jousset, P., Van Ruymbeke, M., Bonvalot, S. & Diament, M., 1995. Performance of two Scintrex CG3M instruments at the fourth International Comparison of Absolute Gravimeters. Metrologia, 32(3), 231, https://doi.org/10.1088/0026-1394/32/3/012.

Jousset, P., 1996. Microgravimétrie et gravimétrie en volcanologie: méthodologie et application au volcan Merapi, Java, Indonésie. Doctoral dissertation, Université de Paris 7, France.

Jousset, P. & Okada, H, 1999. Post-eruptive volcanic dome evolution as revealed by deformation and microgravity observations at Usu volcano (Hokkaido, Japan). Journal of Volcanology and Geothermal Research, 89(1-4), 255-273, https://doi.org/10.1016/S0377-0273(99)00003-7.

Jousset, P., Mori, H. & Okada, H., 2000. Possible magma intrusion revealed by temporal gravity, ground deformation and ground temperature observations at Mount Komagatake (Hokkaido) during the 1996–1998 crisis, Geophysical Journal International, 143(3), 557-574, https://doi.org/10.1046/j.1365-246X.2000.00218.x.

Jousset, P., Mori, H. & Okada, H., 2003. Elastic models for the magma intrusion associated with the 2000 eruption of Usu Volcano, Hokkaido, Japan. Journal of volcanology and geothermal research, 125(1-2), 81-106, https://doi.org/10.1016/S0377-0273(03)00090-8.

Kahwa, E., 2015. Geophysical exploration of high temperature geothermal areas using resistivity methods. Case study: Theistareykir Area, NE Iceland. In Proceedings World Geothermal Congress 2015, Melbourne, Australia, http://www.os.is/gogn/unu-gtp-report/UNU-GTP-2012-14-2.pdf, Accessed 22 November 2021.

Karlsdóttir, R., Vilhjálmsson, A.M., Árnason, K. & Beyene, A.T., 2012. Theistareykir geothermal area, Northern Iceland. 3D inversion of MT and TEM data. Iceland GeoSurvey, report ÍSOR-2012, 46.

Kennedy, J., Ferré, T.P.A., Güntner, A., Abe, M. & Creutzfeldt, B., 2014. Direct measurement of subsurface mass change using the variable baseline gravity gradient method, Geophysical Research Letters, 41, 8, 2827-2834, https://doi.org/10.1002/2014GL059673.

Kennedy, J., Ferré, T.P.A. & Creutzfeldt, B., 2016. Time-lapse gravity data for monitoring and modeling artificial recharge through a thick unsaturated zone, Water Resources Research, 52(9), 7244-7261, https://doi.org/10.1002/2016WR018770.

## References

Kewiy, W.R., 2013. Injection and production well testing in the geothermal fields of southern Hengill and Reykjanes, SW-Iceland and Theistareykir, N-Iceland. Geothermal Training in Iceland, 747-768, http://os.is/gogn/unu-gtp-report/UNU-GTP-2013-31.pdf, Accessed 22 November 2021.

Khodayar, M. & Björnsson, S., 2013. Preliminary Fracture Analysis of Theistareykir geothermal field and surroundings, Northern Rift Zone and Tjörnes Fracture Zone. Iceland GeoSurvey, Report íSOR-2013/029, 2.

Klügel, T. & Wziontek, H., 2009. Correcting gravimeters and tiltmeters for atmospheric mass attraction using operational weather models. Journal of Geodynamics, 48(3-5), 204-210, https://doi.org/10.1016/j.jog.2009.09.010.

Knútsson, V., Geirsson, S.B., Hjartarson, H. & Emilsson, J.A., 2018. Theistareykir Geothermal Power Plant, A Sustainable Construction. GRC Transactions, 42, https://publications.mygeoenergynow.org/grc/1034050.pdf, Accessed 22 November 2021.

Kristinsdóttir, R. & Thóroddsson, Th.F., 2015. Theistareykir up to 200 MW geothermal power plant, EIA summary and national planning agency opinion. Report Mannvit, Landsvirkjun.

Krynski, J., 2012. Gravimetry for geodesy and geodynamics-brief historical review. Reports on Geodesy, yadda.icm.edu.pl/yadda/element/bwmeta1.element.baztech-9b53a858-a78b-4caa-9e57-3115c9fc2d97/c/Krynski_gravimetry.pdf, Accessed 22 November 2021.

Lehning, M., Völksch, I., Gustafsson, D., Nguyen, T.A., Stähli, M. & Zappa, M., 2006. ALPINE3D: a detailed model of mountain surface processes and its application to snow hydrology. Hydrological Processes: An International Journal, 20(10), 2111-2128, https://doi.org/10.1002/hyp.6204.

Magnússon, I., 2016. Þyngdarmælingar á Þeistareykjum í júlí til september 2015 og Þyngdarkort af Kröflusvæði (Gravity measurements in Theistareykir in July–September 2015 and Gravity Map of the Krafla Area, in Icelandic). Tech. Rep. LV-2016-090, Iceland GeoSurvey, Reykjavik, Iceland, LV-2016-090.

Männel, B., Brandt, A., Bradke, M., Sakic, P., Brack, A. & Nischan, T., 2020. Status of IGS Reprocessing Activities at GFZ. In International Association of Geodesy Symposia, Springer, https://doi.org/10.1007/1345_2020_98.

Männel, B., Brandt, A., Bradke, M., Sakic, P., Brack, A. & Nischan, T., 2021. GFZ repro3 product series for the International GNSS Service (IGS). GFZ Data Services, https://doi.org/10.5880/GFZ.1.1.2021.001.

Melchior, P., 1974. Earth tides, Geophysical surveys, 1(3), 275-303, https://doi.org/10.1007/BF01449116.

Mémin, A., Rogister, Y., Hinderer, J., Omang, O.C. & Luck, B., 2011. Secular gravity variation at Svalbard (Norway) from ground observations and GRACE satellite data. Geophysical Journal International, 184(3), 1119-1130, https://doi.org/10.1111/j.1365-246X.2010.04922.x.

Ménoret, V., Vermeulen, P., Le Moigne, N., Bonvalot, S., Bouyer, P., Landragin, A. & Desruelle, B., 2018. Gravity measurements below $10^{-9}$ g with a transportable absolute quantum gravimeter. Scientific reports, 8(1), 1-11, https://doi.org/10.1038/s41598-018-30608-1.

Merriam, J.B., 1992. Atmospheric pressure and gravity, Geophysical Journal International, 109(3), 488-500, https://doi.org/10.1111/j.1365-246X.1992.tb00112.x.

Meurers, B., 2012. Superconducting gravimeter calibration by colocated gravity observations; results from GWR C025, International Journal of Geophysics, 2012, 1-12, http://dx.doi.org/10.1155/2012/954271.

Mikolaj, M., Meurers, B. & Güntner, A., 2016. Modelling of global mass effects in hydrology, atmosphere and oceans on surface gravity. Computers and Geosciences, 93, 12–20, https://doi.org/10.1016/j.cageo.2016.04.014.

Mikolaj, M., Reich, M. & Güntner A., 2019. Resolving Geophysical Signals by Terrestrial Gravimetry: A Time Domain Assessment of the Correction-Induced Uncertainty. Journal of Geophysical Research, Solid Earth, 124(2), 2153-2165, https://doi.org/10.1029/2018JB016682.

## References

Mogi, K., 1958. Relations of the eruptions of various volcanoes and the deformations of the ground around them. Bull. Earthq. Res. Inst. Tokyo Univ, 36, 98-134.

Leirião, S., He, X., Christiansen, L., Andersen, O.B. & Bauer-Gottwein, P., 2009. Calculation of the temporal gravity variation from spatially variable water storage change in soils and aquifers. Journal of Hydrology, 365(3-4), 302-309, https://doi.org/10.1016/j.jhydrol.2008.11.040.

Oka, D., Fujimitsu, Y., Nishijima, J., Fukuda, Y. & Taniguchi, M., 2012. Evaluation of geothermal reservoir mass change from the gravity change at the Takigami geothermal area, Oita prefecture, Japan. In Proceedings Thirty-Seventh Workshop on Geothermal Reservoir Engineering Stanford University, Stanford, California, https://pangea.stanford.edu/ERE/pdf/IGAstandard/SGW/2012/Oka.pdf, Accessed 22 November 2021.

Okubo, S., Satomura, M., Furuya, M., Sun, W., Matsumoto, S., Ueki, S. & Watanabe, H., 2002. Grand design for the hybrid gravity network around the Mt. Fuji volcano. In International symposium on geodesy in Kanazawa abstract (pp. 39-40).

Óskarsson, F., 2015. Exploration and development of a conceptual model for the Theistareykir geothermal field, NE-Iceland. Short Course VII on Surface Exploration for Geothermal Resources", organized by UNU-GTP and LaGeo, in Santa Tecla and Ahuachapán, El Salvador, www.os.is/gogn/unu-gtp-sc/UNU-GTP-SC-23-0502A.pdf, Accessed 22 November 2021.

Parseliunas, E., Petroskevicius, P., Birvydiene, R. & Obuchovski, R., 2011. Investigation of the automatic gravimeters Scintrex CG-5 and analysis of gravimetric measurements. In Environmental Engineering. Proceedings of the International Conference on Environmental Engineering. ICEE (Vol. 8, p. 1416). Vilnius Gediminas Technical University, Department of Construction Economics & Property.

Pascal, K., Neuberg, J. & Rivalta, E., 2014. On precisely modelling surface deformation due to interacting magma chambers and dykes. Geophysical Journal International, 196(1), 253-278, https://doi.org/10.1093/gji/ggt343.

Peacock, J.R., Thiel, S., Reid, P. & Heinson, G., 2012. Magnetotelluric monitoring of a fluid injection: Example from an enhanced geothermal system. Geophysical Research Letters, 39(18), https://doi.org/10.1029/2012GL053080.

Peterson, J., 1993. Observations and Modelling of Seismic Background Noise, Open-File Report 93-332, U.S. Department of Interior, Geological Survey, Albuquerque, NM.

Petit, G. & Luzum, B., 2010. IERS conventions (2010). Bureau International des Poids et mesures sevres (france), https://apps.dtic.mil/sti/citations/ADA535671, Accessed 22 November 2021.

Portier, N., Hinderer, J., Riccardi, U., Ferhat, G., Calvo, M., Abdelfettah, Y. & Bernard, J.-D., 2018. Hybrid gravimetry monitoring of Soultz-sous-Forêts and Rittershoffen geothermal sites (Alsace, France). Geothermics, 76, 201-219, https://doi.org/10.1186/s40517-018-0104-5.

Portier, N., 2020. Suivi par gravimétrie hybride et magnétotellurie de réservoirs géothermiques. Doctoral dissertation, Université de Strasbourg, France, https://tel.archives-ouvertes.fr/tel-03218945/document, Accessed 22 November 2021.

Portier, N., Hinderer, J., Drouin, V., Sigmundsson, F., Schäfer, F., Jousset, P., Erbas, K., Magnusson, I., Hersir, G.P., Águstsson, K., De Zeeuw Van Dalfsen, E., Guðmundsson, Á. & Bernard, J.-D., 2020. Time-lapse Micro-gravity Monitoring of the Theistareykir and Krafla Geothermal Reservoirs (Iceland), In Proceedings World Geothermal Congress 2020, Reykjavik, Iceland.

Portier, N., Forster, F., Hinderer, J., Erbas, K., Jousset, P., Drouin, V., Li, S., Sigmundsson, F., Magnússon, I., Hersir, G.P., Ágústsson, K., Guðmundsson, Á., Júlíusson, E., Hjartasson, H. & Bernard, J.-D., 2021. Hybrid microgravity monitoring of the Theistareykir geothermal reservoir (North Iceland). Pure and Applied Geophysics, (In review).

Ragnarsson, Á., Steingrímsson, B. & Thorhallsson, S., 2020. Geothermal development in Iceland 2015-2019. In Proceedings World Geothermal Congress

2020, Reykjavik, Iceland, https://www.geothermal-energy.org/pdf/IGAstandard/WGC/2020/01063.pdf, Accessed 22 November 2021.

Reich, M., Mikolaj, M., Blume, T. & Güntner, A. (2019). Reducing gravity data for the influence of water storage variations beneath observatory buildings. Geophysics, 84(1), EN15-EN31, https://doi.org/10.1190/geo2018-0301.1.

Riccardi, U., Rosat, S., Hinderer, J., Wolf, D., Santoyo, M.A. & Fernandez, J., 2012. On the accuracy of the calibration of superconducting gravimeters using absolute and spring sensors; a critical comparison, Pure and Applied Geophysics, 169(8), 1343-1356, http://dx.doi.org/10.1007/s00024-011-0398-8.

Richter, B., Wenzel, H.-G., Zürn, W. & Klopping, F., 1995. From chandler wobble to free oscillations: comparison of cryogenic gravimeters and other instruments in a wide period range, Phys. Earth Planet. Inter., 91, 131-148, https://doi.org/10.1016/0031 9201(95)03041-T.

Rodell, M., Houser, P.R., Jambor, U., Gottschalck, J., Mitchell, K., Meng, C.J. & Toll, D., 2004. The Global Land Data Assimilation System. Bulletin of the American Meteorological Society, 85(3), 381–394, https://doi.org/10.1175/BAMS-85-3-381.

Rosat, S., Calvo, M., Hinderer, J., Riccardi, U., Arnoso, J. & Zürn, W., 2015. Comparison of the performances of different spring and superconducting gravimeters and STS-2 seismometer at the gravimetric observatory of Strasbourg, France, Studia Geophysica Et Geodaetica, 59(1), 58-82, http://dx.doi.org/10.1007/s11200-014-0830-5.

Rosat, S. & Hinderer, J., 2018. Limits of Detection of Gravimetric Signals on Earth, Scientific reports, 8(1), 15324, https://doi.org/10.1038/s41598-018-33717-z.

Saemundsson, K., 2008. Geology and gradient wells. Short course III on exploration for geothermal resources, UNU-GTP & KenGen, Naivasha, Kenya, UNU-GTP CD SC-07, https://orkustofnun.is/gogn/unu-gtp-sc/UNU-GTP-SC-25-0208.pdf, Accessed 22 November 2021.

Schäfer, F., Jousset, P., Güntner, A., Erbas, K., Hinderer, J., Rosat, S., Voigt, C., Schöne, T. & Warburton R.J., 2020. Performance of three iGrav superconducting

gravity meters before and after transport to remote monitoring sites. Geophysical Journal International, 223(2):959-972. https://doi.org/10.1093/gji/ggaa359.

Schilling, M. & Gitlein, O., 2015. Accuracy estimation of the IfE gravimeters Micro-g LaCoste gPhone-98 and ZLS Burris Gravity Meter B-64, in IAG 150 Years. Springer, Cham., 143, 249-256, https://doi.org/10.1007/1345_2015_29.

Schöne, T., Zech, C., Unger-Shayesteh, K., Rudenko, V., Thoss, H., Wetzel, H-U., Gafurov, A., Illigner, J. & Zubovich, A., 2013. A new permanent multi-parameter monitoring network in Central Asian high mountains – from measurements to data bases, Geosci. Instrum. Method. Data Syst., 2, 97-111, https://doi.org/10.5194/gi-2-97-2013.

Sigmundsson, F., Einarsson, P., Hjartardóttir, Á.R., Drouin, V., Jónsdóttir, K., Arnadottir, T., Geirsson, H., Hreinsdóttir, S., Li, S. & Ofeigsson, B.G., 2020. Geodynamics of Iceland and the signatures of plate spreading. Journal of Volcanology and Geothermal Research, 391, 106436, https://doi.org/10.1016/j.jvolgeores.2018.08.014.

Sleeman, R., Van Wettum, A. & Trampert, J., 2006. Three-channel correlation analysis: A new technique to measure instrumental noise of digitizers and seismic sensors, Bulletin of the Seismological Society of America, 96(1), 258-271, https://doi.org/10.1785/0120050032.

Stephenson, F.R., Morrison, L.V. & Hohenkerk, C.Y., 2016. Measurement of the Earth's rotation: 720 BC to AD 2015. Proceedings of the Royal Society A: Mathematical, Physical and Engineering Sciences, 472(2196), 20160404, https://doi.org/10.1098/rspa.2016.0404.

Stober, I. & Bucher, K., 2020. Geothermie, Springer Spektrum, third edition, Berlin, Heidelberg, https://doi.org/10.1007/978-3-662-60940-8.

Sturkell, E., Einarsson, P., Sigmundsson, F., Geirsson, H., Olafsson, H., Pedersen, R., De Zeeuw-Van Dalfsen, E., Linde, A.T., Sacks, SI. & Stefánsson, R., 2006. Volcano geodesy and magma dynamics in Iceland. Journal of Volcanology and Geothermal Research, 150(1-3), 14-34, https://doi.org/10.1016/j.jvolgeores.2005.07.010.

## References

Sugihara, M., 2004. Gravity monitoring with a CG5 Scintrex autogravimeter. ASEG Extended Abstracts, 2004(1), 1-4, https://doi.org/10.1071/ASEG2004ab144.

Sugihara, M., & Ishido, T., 2008. Geothermal reservoir monitoring with a combination of absolute and relative gravimetry. Geophysics, 73(6), WA37-WA47, https://doi.org/10.1190/1.2991105.

Sugihara, M., Nawa, K., Nishi, Y., Ishido, T. & Sakaguchi, K., 2011. Gravity monitoring at the Hachijojima geothermal field, Japan. In Proceedings of the 10th SEGJ International Symposium (pp. 1-2). Society of Exploration Geophysicists of Japan, https://doi.org/10.1190/segj102011-001.120.

Taira, T.A., Nayak, A., Brenguier, F. & Manga, M., 2018. Monitoring reservoir response to earthquakes and fluid extraction, Salton Sea geothermal field, California. Science advances, 4(1), e1701536, https://doi.org/10.1126/sciadv.1701536.

Tizzani, P., Battaglia, M., Castaldo, R., Pepe, A., Zeni, G. & Lanari, R., 2015. Magma and fluid migration at Yellowstone Caldera in the last three decades inferred from InSAR, leveling, and gravity measurements. Journal of Geophysical Research: Solid Earth, 120(4), 2627-2647, https://doi.org/10.1002/2014JB011502.

Toledo, T., Jousset, P., Maurer, H. & Krawczyk, C., 2020. Optimized Experimental Network Design for Earthquake Location Problems: applications to geothermal and volcanic field seismic networks. Journal of Volcanology and Geothermal Research, 391, 106433, https://doi.org/10.1016/j.jvolgeores.2018.08.011.

Van Camp, M., 1999. Measuring seismic normal modes with the GWR C021 superconducting gravimeter, Phys. Earth Planet. Inter., 116, 81-92, https://doi.org/10.1016/S0031-9201(99)00120-X.

Van Camp, M., Hendrickx, M., Richard, P., Thies, S., Hinderer, J., Amalvict, M., Luck, B. & Falk, R., 2003. Comparisons of the FG5# 101,# 202,# 206 and# 209 absolute gravimeters at four different European sites, Cahiers du Centre Européen de Géodynamique et de Séismologie, 22, 65-73.

Van Camp, M. & Vauterin, P., 2005. Tsoft: graphical and interactive software for the analysis of time series and Earth tides. Computers & Geosciences, 31(5), 631-640, https://doi.org/10.1016/j.cageo.2004.11.015.

Van Camp, M. & Francis, O., 2007. Is the instrumental drift of superconducting gravimeters a linear or exponential function of time?, Journal of Geodesy, 81(5), 337 344, https://doi.org/10.1007/s00190-006-0110-4.

Voigt, C., Förste, C., Wziontek, H., Crossley, D., Meurers, B., Palinkas, V., Hinderer, J., Boy, J.P., Barriot, J.-P. & Sun, H., 2016. Report on the Data Base of the International Geodynamics and Earth Tide Service (IGETS), Scientific Technical Report STR – Data; 16/08, Potsdam: GFZ German Research Centre for Geosciences, http://doi.org/10.2312/GFZ.b103-16087.

Vishal, V. & Singh, T., 2016. Geologic carbon sequestration: Understanding Reservoir Behavior. Springer, https://www.academia.edu/download/53190224/selection.pdf, Accessed 22 November 2021.

Voigt, C., Schulz, K., Koch, F., Wetzel, K.F., Timmen, L., Rehm, T., Pflug, H., Stolarczuk, N., Förste, C. & Flechtner, F., 2021. Introduction of a Superconducting Gravimeter as Novel Hydrological Sensor for the Alpine Research Catchment Zugspitze. Hydrology and Earth System Sciences Discussions, 1-28, https://doi.org/10.5194/hess-25-5047-2021.

Warburton, R.J., Pillai, H. & Reineman, R.C., 2010. Initial results with the new GWR iGravTM superconducting gravity meter, IAG Symposium Proceedings, June 2010, Saint Petersburg, http://www.gwrinstruments.com/pdf/warburton-pillai-reineman-revised.pdf, Accessed 22 November 2021.

Watlet, A., Van Camp, M., Francis, O., Poulain, A., Rochez, G., Hallet, V., Quinif, Y. & Kaufmann, O., 2020. Gravity monitoring of underground flash flood events to study their impact on groundwater recharge and the distribution of karst voids. Water Resources Research, 56(4), e2019WR026673, https://doi.org/10.1029/2019WR026673.

## References

Weber, J. & Larson, J.V., 1966. Operation of LaCoste and Romberg gravimeter at sensitivity approaching the thermal fluctuation limits. Journal of Geophysical Research, 71(24), 6005-6009, https://doi.org/10.1029/JZ071i024p06005.

Wenzel, H.G., 1996. The Nanogal software: Earth tide data processing package ETERNA 3.30, Bull. Inform. Marees Terrestres, 124, 9425-9439, http://www.eas.slu.edu/GGP/ETERNA34/MANUAL/ETERNA33.HTM, Accessed 22 November 2021.

Wenzel, H.G., 1997. Tide-generating potential for the Earth. In Tidal Phenomena. Springer, Berlin, Heidelberg, 9-26, https://doi.org/10.1007/BFb0011455.

Wilson, C.R., Scanlon, B., Sharp, J., Longuevergne, L. & Wu, H., 2012. Field test of the superconducting gravimeter as a hydrologic sensor, Groundwater, 50(3), 442-449, https://doi.org/10.1111/j.1745-6584.2011.00864.x.

Wolfe, C.J., Bjarnason, I.T., VanDecar, J.C. & Solomon, S.C., 1997. Seismic structure of the Iceland mantle plume. Nature, 385(6613), 245-247, https://doi.org/10.1038/385245a0.

Wziontek, H., Wilmes, H., Wolf, P., Werth, S. & Güntner, A., 2009. Time series of superconducting gravimeters and water storage variations from the global hydrology model WGHM. Journal of Geodynamics, 48(3-5), 166-171, https://doi.org/10.1016/j.jog.2009.09.036.

# Appendices

## Appendix A (chapter 3)

### A1) Variation of SG calibration caused by change in latitude or elevation

For SG levitation, the current in the magnet ($I_c$) produces induced currents ($I_{cs}$) in the sphere. Since $I_{cs}$ is proportional to $I_c$, the levitation force ($F_L$) is simply expressed as $F_L(I_c) = L(I_c)^2 = mg$, where L depends on the sphere and magnet geometry and is about 2.5 $m/s^2/A^2$ for the iGrav, with a levitation current A ≈ 2 A; m is the mass of the sphere and g is the local value of gravity. The feedback force is proportional to the product of the current in the feedback coil (i) and the current in the sphere $I_{cs}$. Again, since $I_{cs}$ is proportional to $I_c$, the feedback force can be expressed as $F_{fb}(i) = BiI_c \propto i\sqrt{g}$, with the constant B = 0.05 $m/s^2/A^2$ for a typical iGrav. Therefore, the variation of the iGrav scale factor caused by either a change in elevation or latitude can be calculated by the following formula:

$$\Delta C_n = \sqrt{\frac{g_n}{g_0}} \qquad \text{(A1)}$$

With the absolute gravity values at the station of lowest latitude (J9) $g_0$ = 9.80878 m $s^{-2}$ and at the station of highest latitude (Þeistareykir, reference station) $g_n$ = 9.82312 m $s^{-2}$. The resulting scale factor change is 1.00073 (i.e. 0.073%) after transport from J9 to Þeistareykir. This is a larger uncertainty than the 0.01% determined by RG calibration. However, it is still much smaller than the best stability of AG calibration with an uncertainty of 0.64% (6 nm $s^{-2}$ $V^{-1}$) obtained for iGrav015 (Tab. A2, Appendix A).

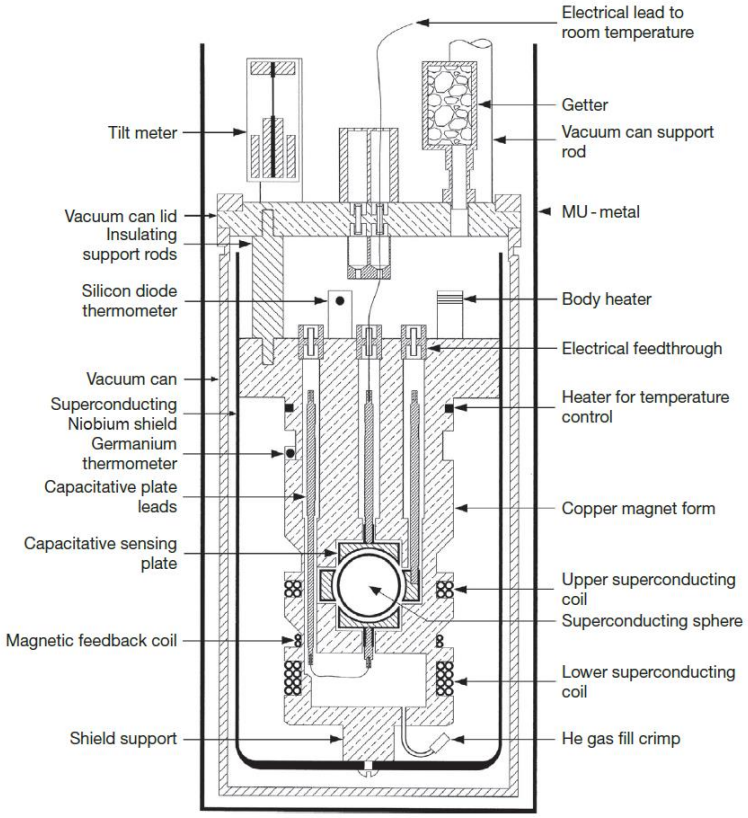


**Figure A1.** Schematic of the gravity sensor inside the iGrav Dewar showing arrangement of the sphere, coils and shielding (modified from Hinderer et al., 2015).

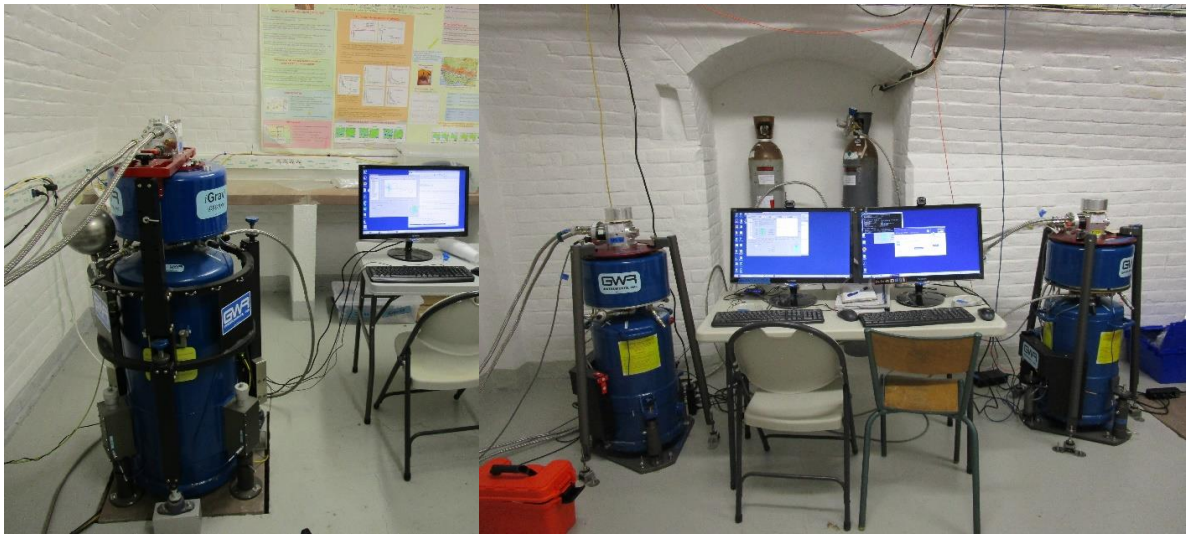

(a) (b)

**Figure A2.** Measuring setup for iOSG023 (a) and iGravs 032 and 015 (b) at the gravimetric observatory J9 in June 2017; with each instrument connected to a separate helium cooling system and data acquisition unit.

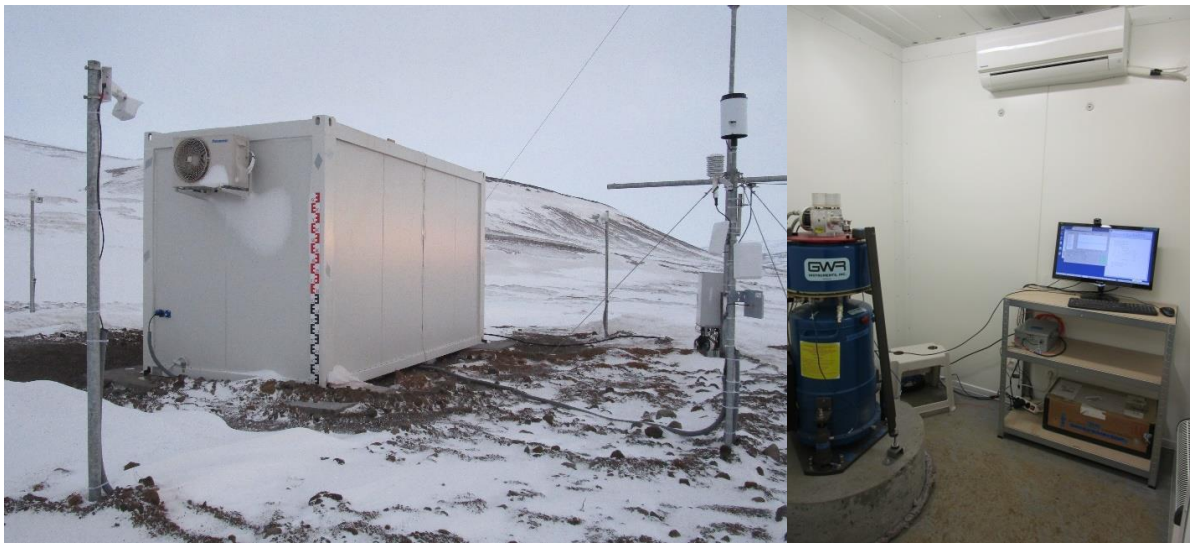

(a) (b)

**Figure A3.** Setup of gravity station similar at all four remote sites (here reference station with iGrav015 shown), GNSS and hydro-meteorological parameters measured outside the container (a); measuring setup inside the container with the iGrav installed on a concrete pillar, decoupled from the surroundings and grounded to the bedrock (b).

(a) (b) (c)

**Figure A4.** Packing and transport of the iGravs with liquid helium filled (4K, cold transport); after securing the Dewar and component parts inside the GWR supplied crates (a and b at J9, Strasbourg), the instruments were transported by truck and ship freight to the remote monitoring sites in Iceland (c).

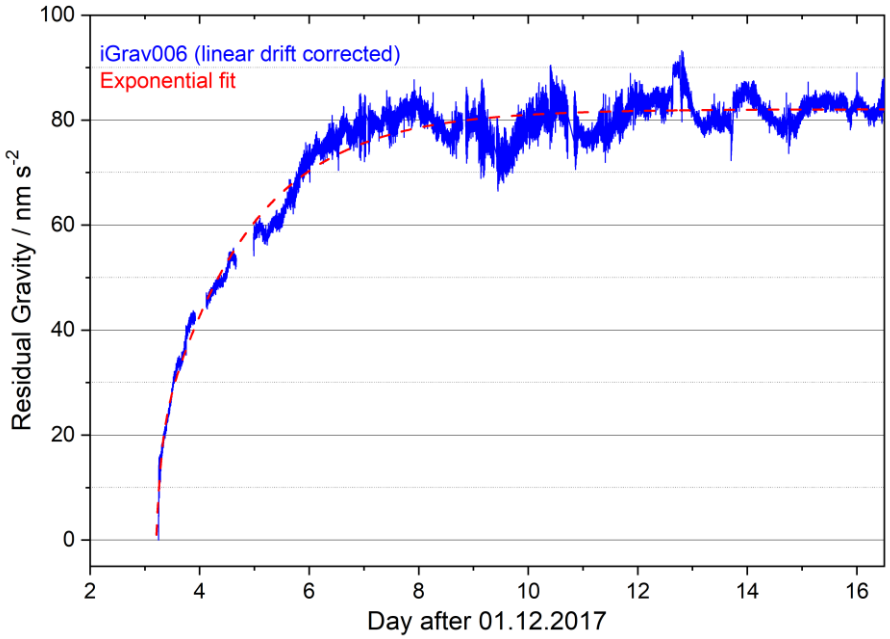


**Figure A5.** Exponential fit of iGrav006 gravity residuals for the initial 13 days after installation at Þeistareykir, subsequent to FG5#206 drift correction; fit function: $g = g_0 - 11e^{(-(t - t_0) / 0.089)} - 62e^{(-(t - t_0) / 1.65)}$.

**Table A1.** Coordinates and heights above sea level for the remote monitoring sites at Þeistareykir, obtained by GPS (Garmin handheld) measurements; iGrav015 moved from reference to central station in June 2019.

| | Latitude (°) | Longitude (°) | Height (m a.s.l.) |
|---|---|---|---|
| iGrav006 (west station) | 65.8853 | -16.9750 | 332 |
| iGrav015 (reference station) | 66.0027 | -17.1925 | 334 |
| iGrav015 (central station) | 65.8819 | -16.9634 | 340 |
| iGrav032 (east station) | 65.8787 | -16.9430 | 378 |

**Table A2.** Absolute gravity (AG) calibration with FG5#206; at J9 for iOSG023 (duration of 6.2 days in September 2016), iGravs 015 and 032 (duration of 7.1 days in July 2017); at Þeistareykir for iGravs 006 and 015 (duration of 5.0 and 4.8 days in June/July 2018); no AG calibrations (X): for iGrav006 at J9 because it was installed in October 2017 when FG5#206 was not available, and for iGrav032 at Þeistareykir because of excessive noise from geothermal well pads during AG measurements at east station; uncertainty of AG calibration factors (from AG-SG least-squares fit) are proportional to uncertainty of the AG drop values (the uncertainty of the SGs being negligible in comparison).

| SG name | J9 | | Þeistareykir | |
|---|---|---|---|---|
| | AG calibration factor ($nm\ s^{-2}\ V^{-1}$) | AG calibration factor uncertainty ($nm\ s^{-2}\ V^{-1}$) | AG calibration factor ($nm\ s^{-2}\ V^{-1}$) | AG calibration factor uncertainty ($nm\ s^{-2}\ V^{-1}$) |
| iOSG023 | -451 | 2 | X | X |
| iGrav006 | X | X | -917 | 10 |
| iGrav015 | -934 | 3 | -935 | 6 |
| iGrav032 | -898 | 3 | X | X |

**Table A3.** Relative gravity (RG) calibration at J9 of iGravs 006, 015 and 032 by fitting to iOSG023; standard deviations (SD) are formal errors for the RG scale factors between iOSG023 and the respective iGrav, smaller than the AG calibration uncertainties because of the large number of SG values sampled at 1 second in the parallel comparison.

| SG name | Scale factor ($nm\ s^{-2}\ V^{-1}$) | SD ($nm\ s^{-2}\ V^{-1}$) |
|---|---|---|
| iGrav006 | -914.27 | 0.0042 |
| iGrav015 | -930.18 | 0.0019 |
| iGrav032 | -895.84 | 0.0065 |

## Appendices

**Table A4.** Parameters of linear and exponential fitting of iGrav gravity differences from J9.

| J9 | | iGrav006 | | iGrav015 | | iGrav032 | |
|---|---|---|---|---|---|---|---|
| | | Value | SD | Value | SD | Value | SD |
| Linear fit | Drift rate ($nm\ s^{-2}\ d^{-1}$) | X | X | -0.375 | 0.00006 | -2.29 | 0.00039 |
| Exponential fit | $A_1$ ($nm\ s^{-2}$) | -63.7 | 0.0729 | -42.3 | 0.106 | -34.4 | 0.0734 |
| | $\tau_1$ (d) | 0.616 | 0.00142 | 0.870 | 0.00432 | 0.744 | 0.00315 |
| | $A_2$ ($nm\ s^{-2}$) | -93.6 | 0.0350 | -25.2 | 0.0704 | -44.3 | 0.0621 |
| | $\tau_2$ (d) | 8.31 | 0.0104 | 8.67 | 0.0257 | 5.67 | 0.00773 |

**Table A5.** Parameters of linear and exponential fitting of iGrav gravity residuals from Þeistareykir.

| Þeistareykir | | iGrav006 | | iGrav015 | | iGrav032 | |
|---|---|---|---|---|---|---|---|
| | | Value | SD | Value | SD | Value | SD |
| Linear fit | FG5#206 diff. ($nm\ s^{-2}$) | 67 | 16 | 51 | 13 | 59 | 24 |
| | Drift rate ($nm\ s^{-2}\ d^{-1}$) | +0.19 | 0.046 | -0.25 | 0.039 | -1.6 | 0.069 |
| Exponential fit | $A_1$ ($nm\ s^{-2}$) | -11 | 0.59 | X | X | X | X |
| | $\tau_1$ (d) | 0.089 | 0.0085 | X | X | X | X |
| | $A_2$ ($nm\ s^{-2}$) | -62 | 0.23 | X | X | X | X |
| | $\tau_2$ (d) | 1.7 | 0.0080 | X | X | X | X |

**Table A6.** Long-term drift rates (in $nm\ s^{-2}\ a^{-1}$) from linear approximations of time series from J9 and Þeistareykir.

| Location | Timeframe | iGrav006 | iGrav015 | iGrav032 |
|---|---|---|---|---|
| J9 | 120 days for iGrav015 (June - October 2017) | X | -137 | X |
| | 60 days for iGrav032 (July - August 2017) | X | X | -837 |
| Þeistareykir | 350 days for each iGrav (June 2018 - June 2019) | +70 | -92 | -597 |

# Appendix B (chapter 4)

## B1) Results of ETERNA 3.4 tidal analysis for iGrav006 (SCGW)

```
 Program ANALYZE, version 3.40 970921               File:   iGrav006
########################################################################
# SCGW                                                                 #
# 65.8853N   16.975W      H331.8M                                      #
# iGrav006                                                             #
# 2018.03.01 - 2020.10.12                                              #
# Theistareykir West                                                   #
#                                                                      #
########################################################################
Latitude: 65.8853 deg, longitude:-16.9750 deg, azimuth:  0.0000 deg.
20180301...20201012     1 blocks. Recorded days in total:    956.999
Hartmann+Wenzel (1995) TGP, threshold: 0.100D-09     12011 waves.
WAHR-DEHANT-ZSCHAU inelastic Earth model used.
UNITY window used for least squares adjustment.
Sampling interval:       60. s
Numerical filter is no filter    with    1 coefficients.

Average noise level at frequency bands in nm/s**2
0.1 cpd   0.471378      1.0 cpd   0.051222        2.0 cpd   0.019616
3.0 cpd   0.011145      4.0 cpd   0.011151    white noise   0.067594

adjusted tidal parameters :

                         theor.
from      to       wave    ampl. ampl.fac.    stdv. ph. lead    stdv.
[cpd]     [cpd]     [nm/s**2 ]                          [deg]    [deg]

0.025811 0.044653 MM    50.8791   1.11639  0.01842   0.4742   0.9407
0.060131 0.080798 MF    96.3258   1.14278  0.00570   0.6297   0.2865
0.096422 0.115412 MTM   18.4433   1.13124  0.01953   0.4300   0.9910
0.130192 0.249952 MQM    2.9457   1.20823  0.07434  -0.8992   3.5268
0.721499 0.833113 SGQ1   1.7126   1.15317  0.02222  -0.8652   1.1039
0.851181 0.870024 SGM1   7.0885   1.14361  0.00462  -2.7001   0.2313
0.887326 0.906316 Q1    44.4207   1.11945  0.00093  -0.8536   0.0475
0.921940 0.940488 O1   232.0049   1.12891  0.00018   0.9228   0.0093
0.958085 0.974189 NO1   18.2367   1.13595  0.00207   2.2021   0.1045
0.989048 1.013690 PSK1 326.1514   1.14758  0.00012   1.1921   0.0061
1.028549 1.044801 J1    18.2433   1.16482  0.00214   0.7074   0.1053
1.064840 1.080945 OO1    9.9794   1.14890  0.00417   0.3904   0.2079
1.099160 1.216398 NU1    1.9111   1.15101  0.02148   1.2756   1.0689
1.719380 1.837970 EPS2   0.9281   1.12937  0.01424   5.1460   0.7225
1.853919 1.872143 2N2    3.8409   1.19854  0.00299   4.2111   0.1431
1.888386 1.906463 N2    24.0490   1.22819  0.00060   2.1624   0.0282
1.923765 1.942754 M2   125.6044   1.24221  0.00012   0.7815   0.0057
1.958232 1.976927 L2     3.5506   1.20886  0.00549   1.0437   0.2601
1.991786 2.013690 S2K2  58.4324   1.23159  0.00026  -1.2136   0.0120
2.031287 2.047391 ETA2   0.8882   1.18625  0.01695  -1.6698   0.8187
2.067578 2.182844 2K2    0.2324   1.15539  0.05787  -5.8825   2.8701
2.753243 3.081255 M3     1.0101   1.07337  0.00822  -5.5396   0.4390

Adjusted meteorological or hydrological parameters:

no. regr.coeff.       stdv.  parameter   unit

  1    -3.79956     0.00295   airpress.  nm/s**2 / hPa

Adjusted TSCHEBYSCHEFF polynomial bias parameters :

block    degree        bias                stdv.

Standard deviation:                  44.768  nm/s**2
Degree of freedom:                 1378034
Maximum residual:                  116.573  nm/s**2
Maximum correlation:                -0.085  airpress. with Y-wave-MF
Condition number of normal equ.      1.276
```

## B2) Results of ETERNA 3.4 tidal analysis for iGrav015 (SCGC)

```
Program ANALYZE, version 3.40 970921               File:   iGrav015
######################################################################
# GPXC                                                               #
# 65.8819N   16.9634W      H340.4M                                   #
# iGrav015                                                           #
# 2019.06.13 - 2020.10.12                                            #
# Theistareykir Central                                              #
#                                                                    #
######################################################################
Latitude: 65.8819 deg, longitude:-16.9634 deg, azimuth:  0.0000 deg.
20190613...20201012     1 blocks. Recorded days in total:    487.217
Hartmann+Wenzel (1995) TGP, threshold: 0.100D-09     12011 waves.
WAHR-DEHANT-ZSCHAU inelastic Earth model used.
UNITY window used for least squares adjustment.
Sampling interval:       60. s
Numerical filter is no filter    with    1 coefficients.

Average noise level at frequency bands in nm/s**2
0.1 cpd   1.168548      1.0 cpd   0.083454        2.0 cpd   0.030888
3.0 cpd   0.020134      4.0 cpd   0.020573    white noise   0.100070

adjusted tidal parameters :

                         theor.
from      to      wave    ampl. ampl.fac.    stdv. ph. lead    stdv.
[cpd]     [cpd]     [nm/s**2 ]                          [deg]    [deg]

0.025811 0.044653 MM    50.8747   1.16853  0.04946   2.8282   2.4036
0.060131 0.080798 MF    96.3173   1.13757  0.01274   0.2619   0.6437
0.096422 0.115412 MTM   18.4417   1.11220  0.04375   0.7169   2.2608
0.130192 0.249952 MQM    2.9455   1.18502  0.16376 -10.0463   7.9347
0.721499 0.833113 SGQ1   1.7128   1.22620  0.03462  -2.6076   1.6168
0.851181 0.870024 SGM1   7.0892   1.14960  0.00712  -2.6214   0.3549
0.887326 0.906316 Q1    44.4255   1.12245  0.00146  -0.9543   0.0743
0.921940 0.940488 O1   232.0298   1.12917  0.00029   0.9374   0.0146
0.958085 0.974189 NO1   18.2386   1.13887  0.00268   2.1272   0.1346
0.989048 1.013690 PSK1 326.1863   1.14735  0.00019   1.2039   0.0097
1.028549 1.044801 J1    18.2453   1.16026  0.00346   0.8509   0.1710
1.064840 1.080945 OO1    9.9805   1.15255  0.00573   0.4741   0.2847
1.099160 1.216398 NU1    1.9113   1.13326  0.02999   2.4183   1.5158
1.719380 1.837970 EPS2   0.9283   1.15714  0.02282   5.4131   1.1301
1.853919 1.872143 2N2    3.8419   1.19331  0.00472   4.4134   0.2266
1.888386 1.906463 N2    24.0554   1.22825  0.00097   2.3991   0.0454
1.923765 1.942754 M2   125.6378   1.24306  0.00020   0.7883   0.0090
1.958232 1.976927 L2     3.5515   1.17776  0.00736   1.1202   0.3579
1.991786 2.013690 S2K2  58.4480   1.23196  0.00041  -1.2763   0.0191
2.031287 2.047391 ETA2   0.8884   1.20327  0.02551  -3.6459   1.2145
2.067578 2.182844 2K2    0.2325   1.23493  0.07369  -1.1502   3.4193
2.753243 3.081255 M3     1.0105   1.11040  0.01507  -5.7103   0.7774

Adjusted meteorological or hydrological parameters:

no. regr.coeff.       stdv.  parameter   unit

  1    -3.78251     0.00407   airpress.  nm/s**2 / hPa

Adjusted TSCHEBYSCHEFF polynomial bias parameters :

block    degree        bias                stdv.

Standard deviation:                  47.290  nm/s**2
Degree of freedom:                   701548
Maximum residual:                    92.673  nm/s**2
Maximum correlation:                 -0.113  airpress. with Y-wave-MF
Condition number of normal equ.       1.462
```

## B3) Results of ETERNA 3.4 tidal analysis for iGrav032 (SCGE)

```
Program ANALYZE, version 3.40 970921               File:   iGrav032
######################################################################
# SCGE                                                               #
# 65.8787N   16.943W      H378.1M                                    #
# iGrav032                                                           #
# 2018.03.01 - 2020.10.12                                            #
# Theistareykir East                                                 #
#                                                                    #
######################################################################
Latitude: 65.8787 deg, longitude:-16.9430 deg, azimuth:  0.0000 deg.
20180301...20201012     1 blocks. Recorded days in total:    957.000
Hartmann+Wenzel (1995) TGP, threshold: 0.100D-09     12011 waves.
WAHR-DEHANT-ZSCHAU inelastic Earth model used.
UNITY window used for least squares adjustment.
Sampling interval:       60. s
Numerical filter is no filter    with    1 coefficients.

Average noise level at frequency bands in nm/s**2
0.1 cpd   0.515649      1.0 cpd   0.055501        2.0 cpd   0.023233
3.0 cpd   0.012482      4.0 cpd   0.011356    white noise   0.084572

adjusted tidal parameters :

                         theor.
from      to      wave    ampl. ampl.fac.    stdv. ph. lead    stdv.
[cpd]     [cpd]     [nm/s**2 ]                         [deg]    [deg]

0.025811 0.044653 MM    50.8707   1.12239  0.02015  -2.3147   1.0239
0.060131 0.080798 MF    96.3098   1.13356  0.00624   0.8037   0.3160
0.096422 0.115412 MTM   18.4403   1.11368  0.02136  -1.7728   1.1013
0.130192 0.249952 MQM    2.9453   1.16246  0.08134  -3.1211   4.0106
0.721499 0.833113 SGQ1   1.7130   1.18983  0.02407   1.9006   1.1590
0.851181 0.870024 SGM1   7.0900   1.15460  0.00500  -1.9895   0.2482
0.887326 0.906316 Q1    44.4302   1.11909  0.00101  -0.6170   0.0515
0.921940 0.940488 O1   232.0543   1.12755  0.00020   0.9652   0.0101
0.958085 0.974189 NO1   18.2405   1.13716  0.00224   2.2595   0.1131
0.989048 1.013690 PSK1 326.2208   1.14659  0.00013   1.2177   0.0067
1.028549 1.044801 J1    18.2472   1.16783  0.00232   0.8827   0.1138
1.064840 1.080945 OO1    9.9816   1.14826  0.00452   0.7711   0.2254
1.099160 1.216398 NU1    1.9115   1.12038  0.02327   4.6679   1.1896
1.719380 1.837970 EPS2   0.9286   1.18337  0.01686   9.1674   0.8162
1.853919 1.872143 2N2    3.8429   1.19379  0.00354   4.8300   0.1701
1.888386 1.906463 N2    24.0615   1.22410  0.00072   2.3554   0.0335
1.923765 1.942754 M2   125.6699   1.24045  0.00015   0.8877   0.0067
1.958232 1.976927 L2     3.5524   1.20004  0.00650   1.2294   0.3102
1.991786 2.013690 S2K2  58.4629   1.23121  0.00031  -1.1088   0.0142
2.031287 2.047391 ETA2   0.8887   1.18160  0.02007  -3.1244   0.9729
2.067578 2.182844 2K2    0.2325   1.28277  0.06851  -8.5912   3.0602
2.753243 3.081255 M3     1.0109   1.06396  0.00920  -2.2433   0.4957

Adjusted meteorological or hydrological parameters:

no. regr.coeff.       stdv.  parameter   unit

  1    -3.68467     0.00371   airpress.  nm/s**2 / hPa

Adjusted TSCHEBYSCHEFF polynomial bias parameters :

block    degree        bias                stdv.

Standard deviation:                  56.013  nm/s**2
Degree of freedom:                 1378035
Maximum residual:                  146.301  nm/s**2
Maximum correlation:                -0.084  airpress. with Y-wave-MF
Condition number of normal equ.      1.275
```

## B4) Theoretical models used for long period tides (SCGW)

Solid Earth tide parameters using Wahr-Dehant-Defraigne (WDD) model:

| Min freq [cpd] | Max freq [cpd] | Amplitude factor [nm s-2] | Phase shift [deg] | Group name |
|---|---|---|---|---|
| 0.000000 | 0.025811 | 1.15800 | 0.0000 | long |

Ocean loading parameters using FES2014b model from H.-G. Scherneck's ocean loading provider:

| Amplitude factor [nm s-2] | Phase shift [deg] | Group name |
|---|---|---|
| 2.0700e-009 | -1.9000 | SSA |

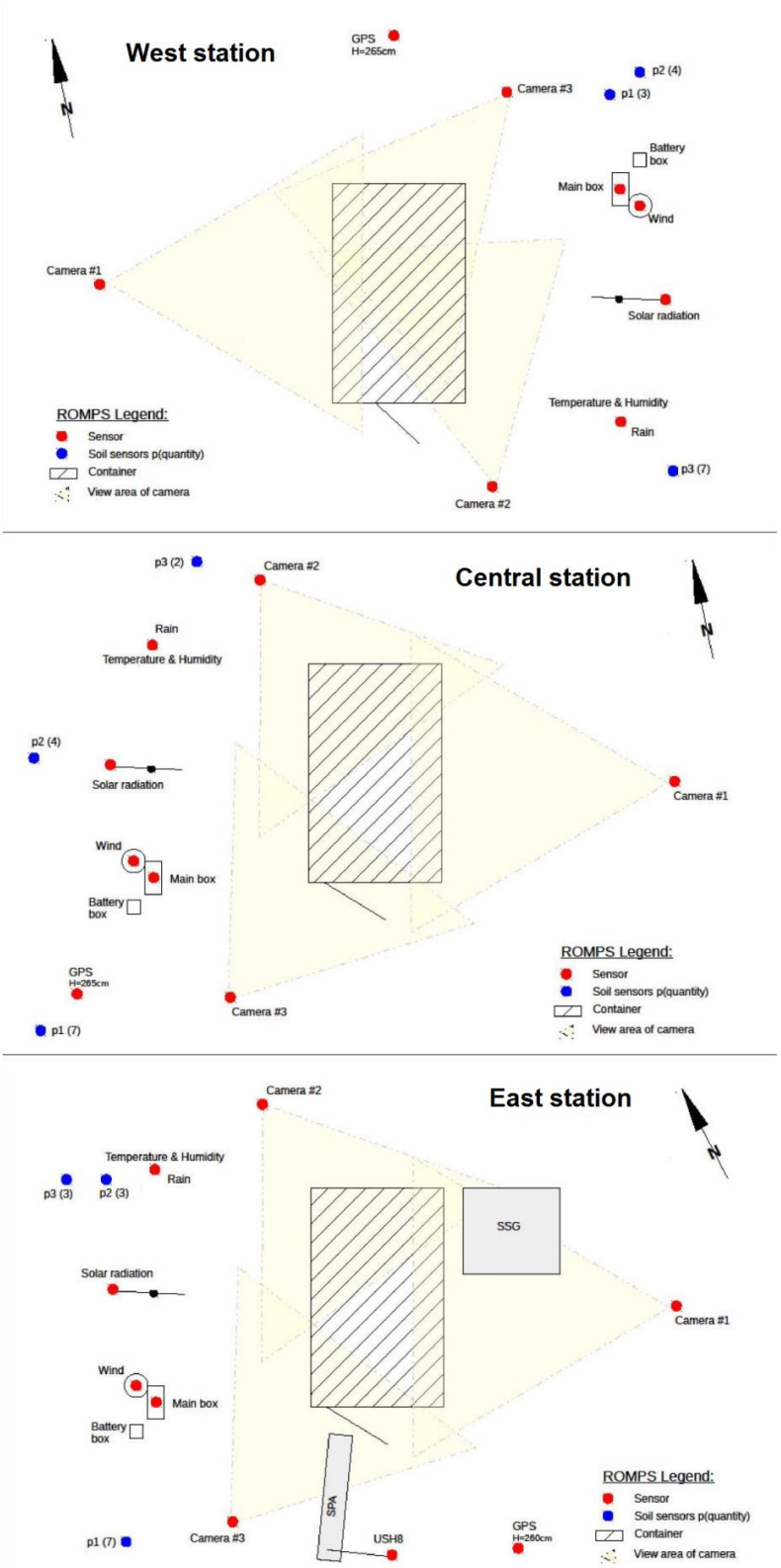


**Figure B1.** Top view sketches of the hydrometeorological sensors (ROMPS) for the three gravity stations at Þeistareykir; bottom image (east station) includes positions of snow scale (SSG) and snow pack analyser (SPA).

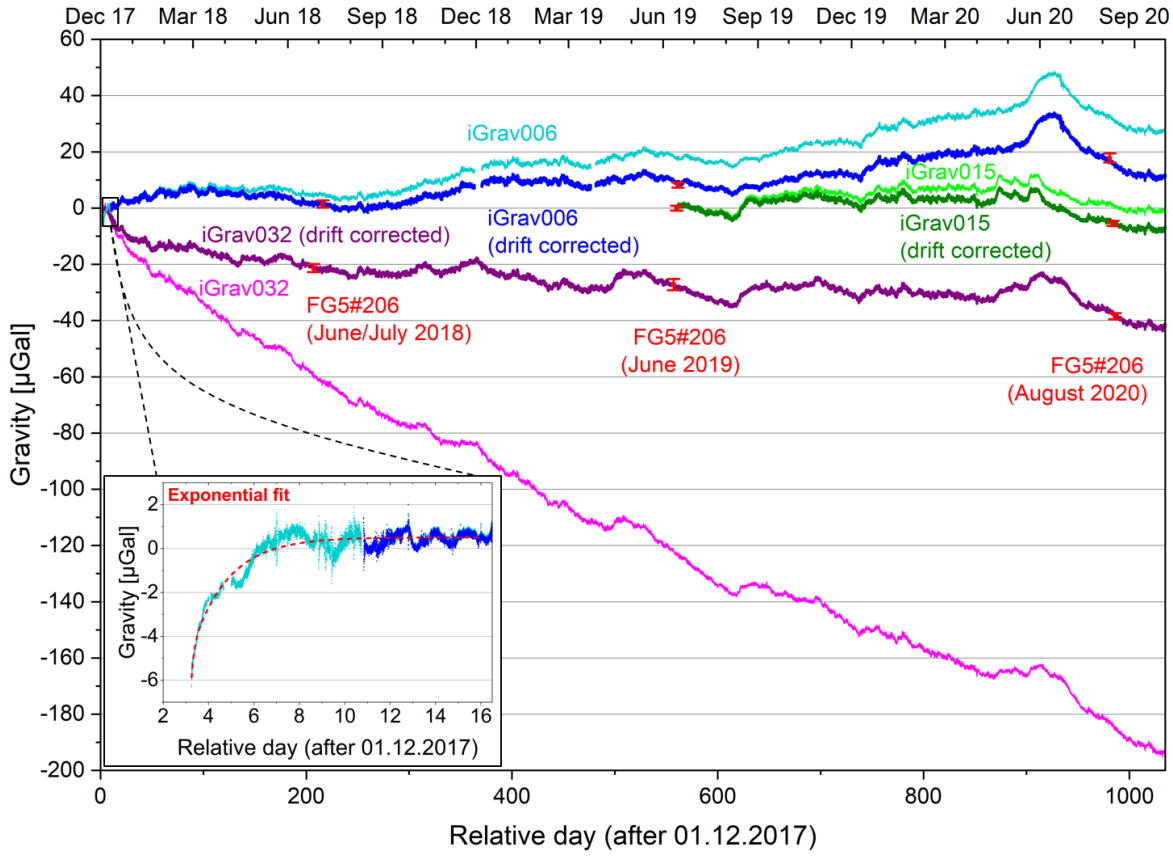


**Figure B2.** Instrumental drift correction for the three iGravs at Þeistareykir by comparison to FG5#206 absolute measurements in summers 2018, 2019 and 2020 (red dots with error bars); drift corrected iGrav residuals shown with dark shaded colours (dark blue, dark green and purple); enlarged section shows initial exponential drift that was removed in iGrav006 residuals.

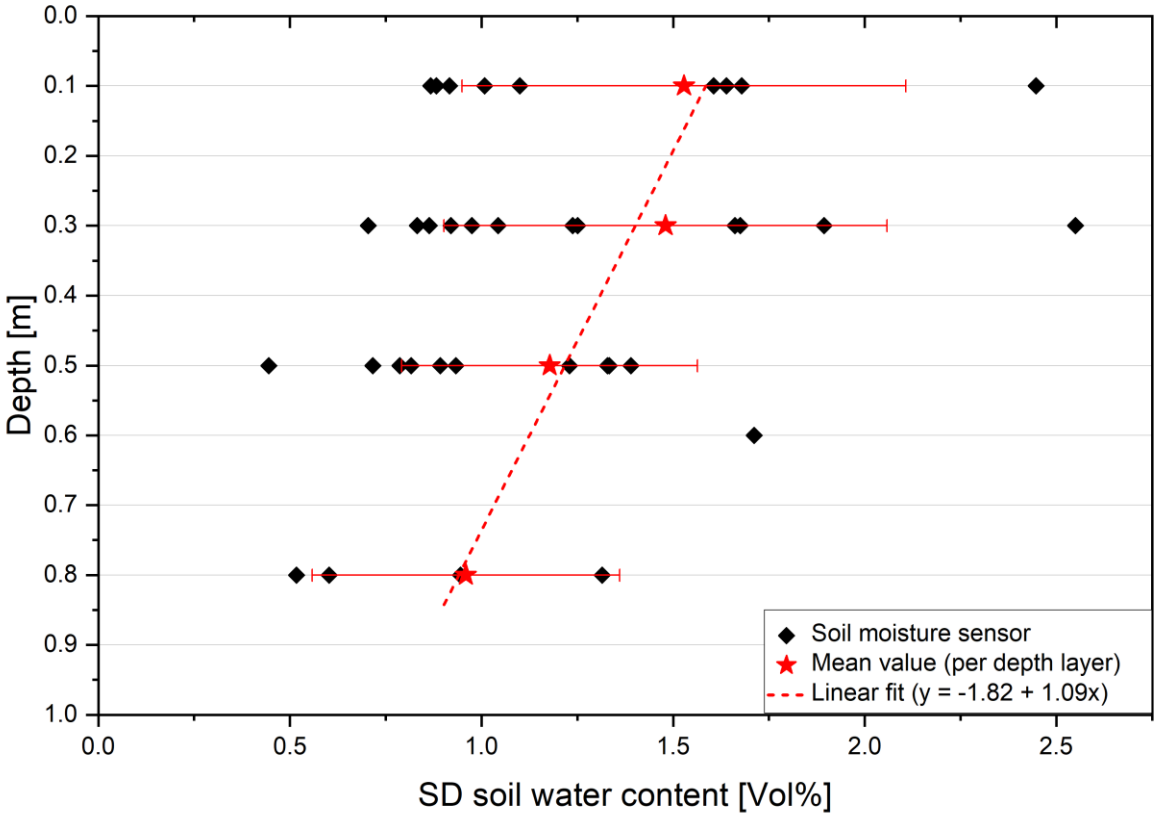


**Figure B3.** Variation of soil water content with depth below surface; black squares show standard deviation of mean soil water content at different depths from all gravity stations, red stars mark mean SD for each depth layer, linear fit of SD mean values (red dashed line) reveals depth of zero soil water content variation at $y_0$ = 1.82 m.

**Figure B4.** Measuring setup at Þeistareykir for determination of the free-air vertical gravity gradient with the help of a CG5 Scintrex gravity meter and a tripod; gravity measurements were performed directly on the concrete pillar, at 60 cm and at 120 cm above the pillar.


**Figure B5.** East station (SCGE) showing positions of snow scale (left) and snow pack analyser (SPA, right); photos taken at the same time (08 February 2020, 13:10) show different snow cover at the two instruments due to varying wind exposure.

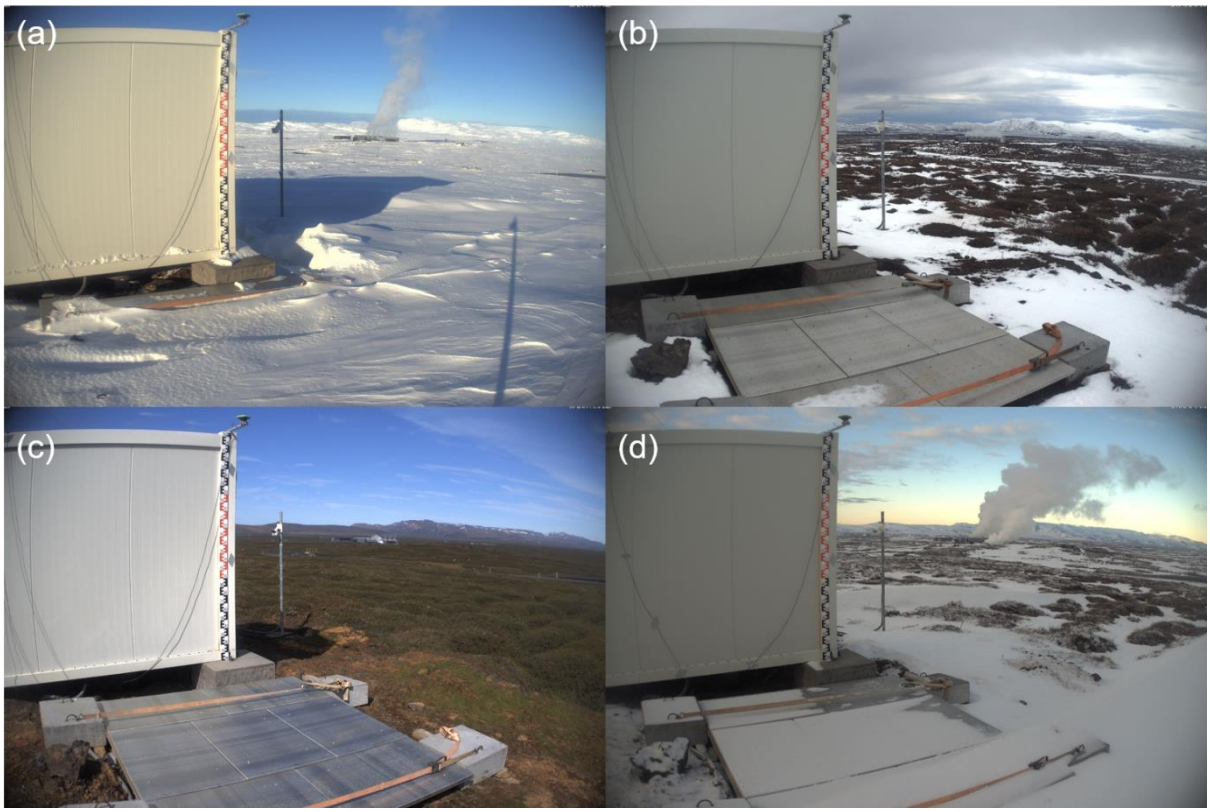


**Figure B6.** East station (SCGE) in the course of the four seasons in 2019: (a) February, (b) May, (c) August and (d) November.

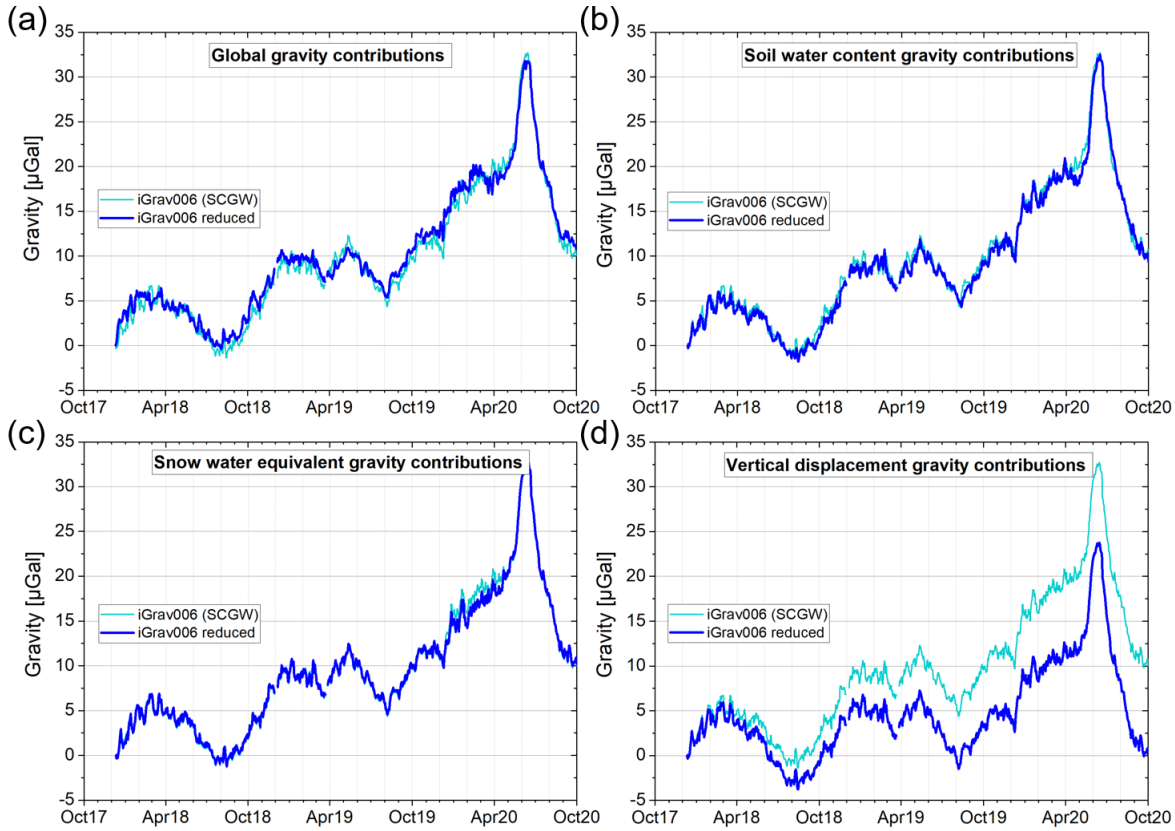


**Figure B7.** Reductions of environmental gravity contributions for iGrav006 (SCGW, 3 years observation period) for (a) global gravity contributions, (b) soil water content variations, (c) snow water equivalent, and (d) vertical surface displacement.

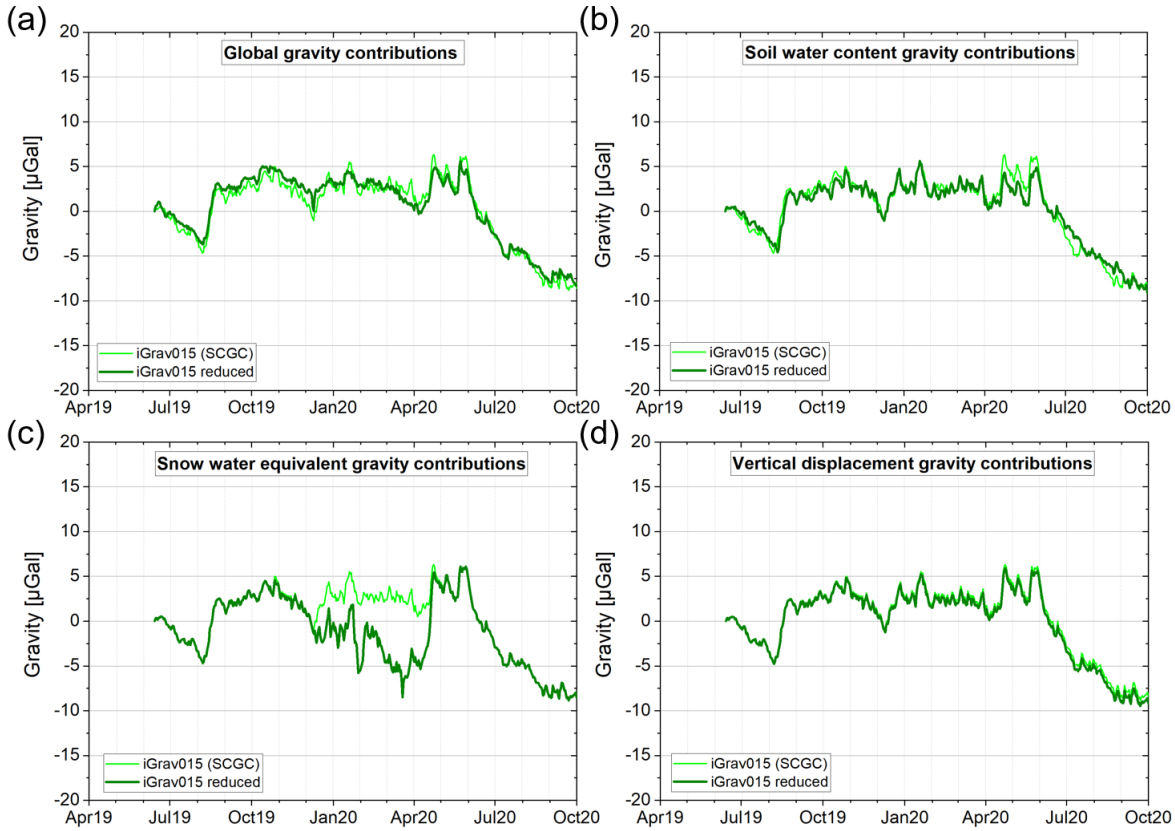


**Figure B8.** Reductions of environmental gravity contributions for iGrav015 (SCGC, 1.3 years observation period) for (a) global gravity contributions, (b) soil water content variations, (c) snow water equivalent, and (d) vertical surface displacement.

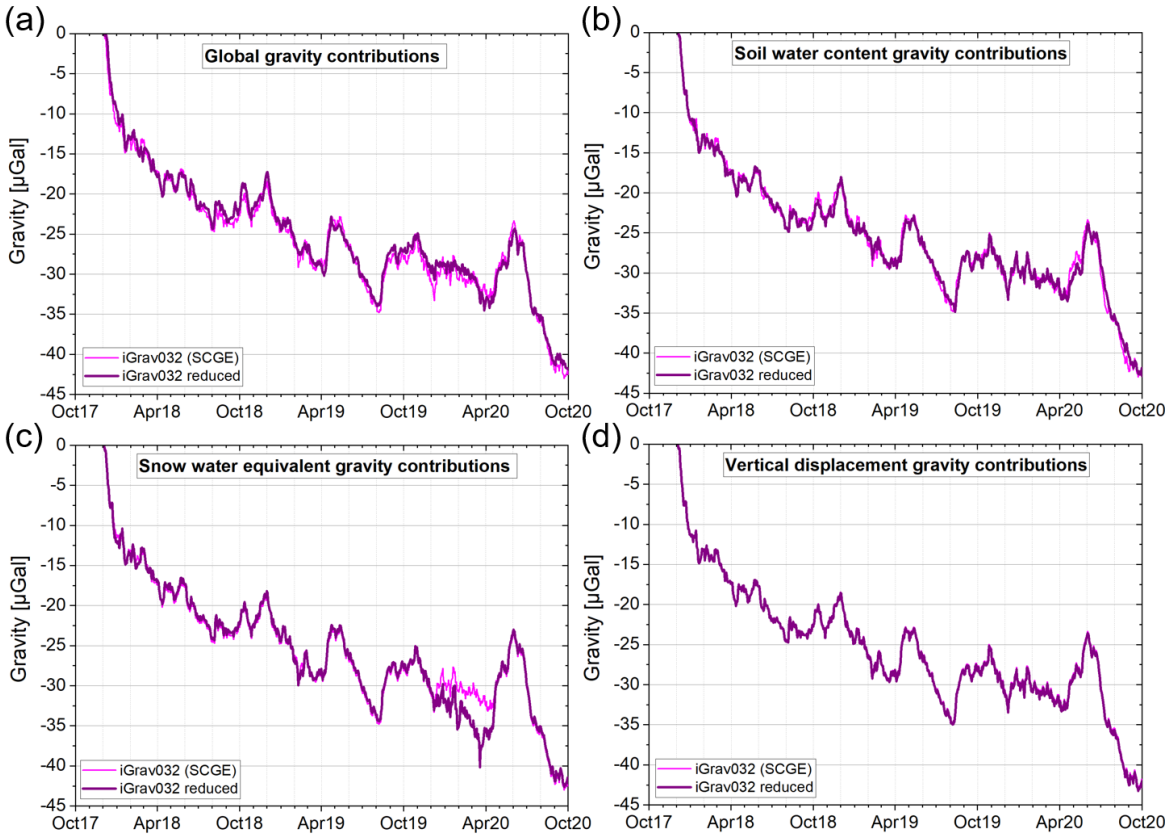


**Figure B9.** Reductions of environmental gravity contributions for iGrav032 (SCGE, 3 years observation period) for (a) global gravity contributions, (b) soil water content variations, (c) snow water equivalent, and (d) vertical surface displacement.

# Appendix C (chapter 5)

## C1) Previous microgravity results

Magnússon (2016) measured 49 gravity stations at the Theistareykir geothermal field using a Scintrex CG3M and CG5 gravimeter in 2011 and 2015, respectively (Tab. C1). To highlight the mass variation, data were corrected for the gravity effect of vertical displacement with the Bouguer vertical gradient (-199.5 µGal $m^{-1}$). Unfortunately, Magnússon (2016) was not able to study the gravity variation at reference station TH10 and assumed that no gravity changes occurred there between 2011 and 2015. A general gravity decrease was observed in the studied area with a mean value of -6 µGal $yr^{-1}$ (Fig. C1). The largest decrease of -10 µGal $yr^{-1}$ was reached in the west of the Bæjarfjall volcano at station TR23. The mean error on the 2011-2015 gravity changes was 14 µGal, taking into account a same mean gravity error of 10 µGal for both years. Between 2011 and 2015, ten wells were already drilled but not yet used for the production at the Theistareykir geothermal field.

Due to time and cost constraints, we only choose 16 stations close to the geothermal field from the above study for repeated gravity measurements in 2017, 2018 and 2019. The code of chosen stations is specified in green in Figure C1. Ten new gravity stations make this network denser within the geothermal field.

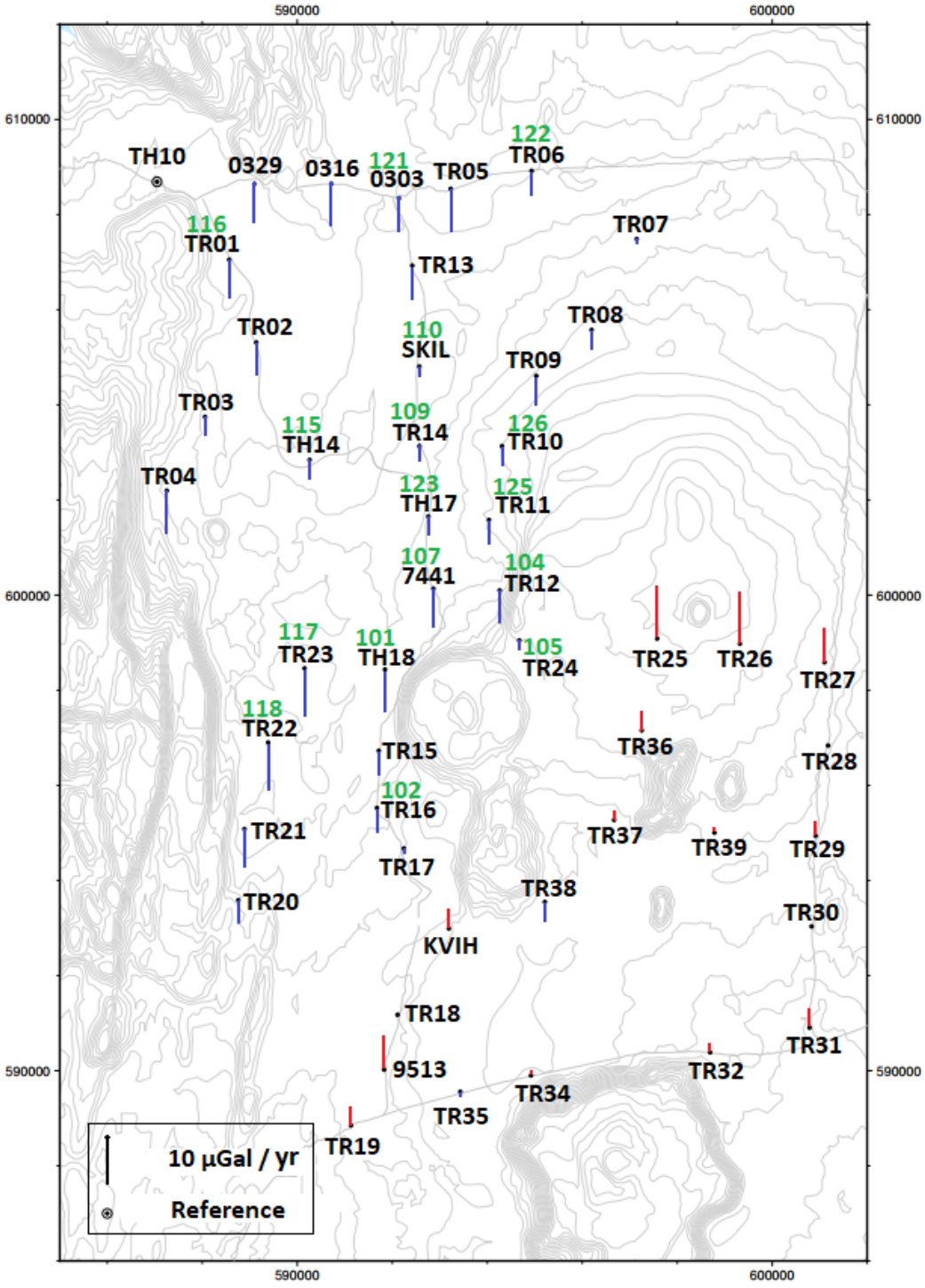


**Figure C1.** Map of the gravity variations (µGal $yr^{-1}$) at the Theistareykir geothermal field between 2011 and 2015 (adapted from Magnússon, 2016). Positive and negative changes are shown in red and blue, respectively. Data are corrected for the gravity effect of vertical displacement using the Bouguer vertical gradient of -199.5 µGal $m^{-1}$. No gravity change is assumed at reference station TH10 between 2011 and 2015. Stations chosen for repeated measurements in our study are labelled with a green three-digit number.

**Table C1.** 2011-2015 gravity change $\Delta g_{2011\text{-}2015}$' (μGal) not corrected for the effect of vertical displacement $\Delta h_{GPS,\ 2011\text{-}2015}$ (mm) (Magnússon, 2016).

| Names | Lat. | Lon. | $\Delta g_{2011\text{-}2015}$' (μGal) | $\Delta h_{GPS,\ 2011\text{-}2015}$ (mm) |
|---|---|---|---|---|
| 303 | 65.95850°N | -16.97372°E | -28 | 5 |
| 316 | 65.96163°N | -17.00480°E | -40 | 12 |
| 329 | 65.96202°N | -17.04041°E | -31 | 5 |
| 7441 | 65.88469°N | -16.96363°E | -32 | 5 |
| 9513 | 65.79436°N | -16.99341°E | 26 | 10 |
| KVIH | 65.82058°N | -16.96150°E | 13 | 7 |
| SKIL | 65.92666°N | -16.96677°E | -4 | -18 |
| TH10 | 65.96300°N | -17.08547°E | 0 | 0 |
| TH14 | 65.90972°N | -17.01883°E | -14 | -7 |
| TH17 | 65.89833°N | -16.96486°E | -15 | -14 |
| TH18 | 65.86977°N | -16.98711°E | -36 | 2 |
| TR01 | 65.94791°N | -17.05316°E | -33 | 8 |
| TR02 | 65.93216°N | -17.04177°E | -29 | -4 |
| TR03 | 65.91844°N | -17.06652°E | -14 | -15 |
| TR04 | 65.90475°N | -17.08527°E | -33 | -15 |
| TR05 | 65.95997°N | -16.94961°E | -38 | 9 |
| TR06 | 65.96283°N | -16.91194°E | -22 | 13 |
| TR07 | 65.94936°N | -16.86433°E | -10 | 20 |
| TR08 | 65.93250°N | -16.88663°E | -18 | 7 |
| TR09 | 65.92416°N | -16.91288°E | -28 | 11 |
| TR10 | 65.91116°N | -16.92977°E | -13 | -16 |
| TR11 | 65.89730°N | -16.93697°E | -19 | 3 |
| TR12 | 65.88397°N | -16.93302°E | -31 | 18 |
| TR13 | 65.94572°N | -16.96858°E | -30 | 2 |
| TR14 | 65.91166°N | -16.96794°E | -10 | -8 |
| TR15 | 65.85450°N | -16.99116°E | -22 | 15 |
| TR16 | 65.84372°N | -16.99283°E | -21 | 13 |
| TR17 | 65.83591°N | -16.98105°E | -6 | 12 |
| TR18 | 65.80461°N | -16.98641°E | 0 | 8 |
| TR19 | 65.78405°N | -17.00944°E | 17 | 5 |
| TR20 | 65.82716°N | -17.05800°E | -23 | 11 |
| TR21 | 65.84055°N | -17.05419°E | -34 | 12 |
| TR22 | 65.85669°N | -17.04205°E | -40 | 0 |
| TR23 | 65.87047°N | -17.02419°E | -42 | 4 |
| TR24 | 65.87444°N | -16.92472°E | -11 | 19 |
| TR25 | 65.87388°N | -16.86116°E | 41 | 15 |
| TR26 | 65.87238°N | -16.82308°E | 42 | 9 |
| TR27 | 65.86833°N | -16.78433°E | 25 | 21 |
| TR28 | 65.85263°N | -16.78408°E | -3 | 13 |
| TR29 | 65.83572°N | -16.79125°E | 10 | 12 |
| TR30 | 65.81866°N | -16.79455°E | 2 | -17 |
| TR31 | 65.79958°N | -16.79711°E | 10 | 22 |
| TR32 | 65.79558°N | -16.84322°E | 7 | 10 |
| TR34 | 65.79236°N | -16.92597°E | 1 | 6 |
| TR35 | 65.78972°N | -16.95866°E | -7 | 14 |
| TR36 | 65.85669°N | -16.86975°E | 15 | 13 |
| TR37 | 65.84002°N | -16.88380°E | 3 | 22 |
| TR38 | 65.82497°N | -16.91694°E | -18 | 18 |
| TR39 | 65.83697°N | -16.83777°E | 2 | 8 |

## C2) The microgravity network

The time-lapse microgravity network of the Theistareykir geothermal field counts 27 stations (Tab. C2). In parallel, the gravity variations are continuously recorded at four permanent stations (Tab. C3).

**Table C2.** Coordinates of 2017, 2018 and 2019 time-lapse gravity stations of the Theistareykir network.

| Codes | Names | GPS Codes | Lat. | Lon. |
|---|---|---|---|---|
| 100 | | | 65.89776°N | -16.96273°E |
| 101 | TH18 | HITR | 65.86977°N | -16.98710°E |
| 102 | TR16 | TR16 | 65.84372°N | -16.99283°E |
| 103 | | TRG1 | 65.87717°N | -16.96562°E |
| 104 | TR12 | TR12 | 65.88398°N | -16.93304°E |
| 105 | TR24 | TR24 | 65.87444°N | -16.92473°E |
| 106 | BOND | BOND | 65.87420°N | -16.89934°E |
| 107 | 7441 | THER | 65.88470°N | -16.96364°E |
| 108 | | TRG2 | 65.87749°N | -16.94277°E |
| 109 | TR14 | TR14 | 65.91166°N | -16.96795°E |
| 110 | SKIL | SKIL | 65.92667°N | -16.96677°E |
| 111 | | | 65.88578°N | -16.97639°E |
| 112 | | | 65.87843°N | -17.00620°E |
| 113 | | | 65.87373°N | -16.96441°E |
| 114 | | TR44 | 65.88351°N | -16.99554°E |
| 115 | TH14 | SKHO | 65.90973°N | -17.01884°E |
| 116 | TR01 | TR01 | 65.94793°N | -17.05316°E |
| 117 | TR23 | TR23 | 65.87048°N | -17.02420°E |
| 118 | TR22 | TR22 | 65.85670°N | -17.04206°E |
| 119 | | | 65.87228°N | -16.93189°E |
| 120 | | | 65.86823°N | -16.95439°E |
| 121 | 0303 | RAUH | 65.95851°N | -16.97372°E |
| 122 | TR06 | TR06 | 65.96284°N | -16.91195°E |
| 123 | TH17 | TH17 | 65.89834°N | -16.96486°E |
| 124 | | THRC | 65.89674°N | -17.01134°E |
| 125 | TR11 | TR11 | 65.89731°N | -16.93696°E |
| 126 | TR10 | TR10 | 65.91116°N | -16.92977°E |

**Table C3.** Coordinates of permanent gravity stations of the Theistareykir network.

| Name | Lat. | Lon. |
|---|---|---|
| SCGR | 66.00275 °N | -17.19222 °E |
| SCGE | 65.87930 °N | -16.94466 °E |
| SCGW | 65.88535 °N | -16.97486 °E |
| GPXC | 65.88193 °N | -16.96343 °E |

## C3) The measured gravity variations

Time-lapse microgravity measurements were performed in 2017, 2018 and 2019 with respect to reference station 100 at the Theistareykir geothermal field (Tab. C4).

**Table C4.** 2017, 2018 and 2019 gravity measurements (µGal) with respect to reference station 100. Data are calibrated (coefficient of 1.0009567 +/- 0.0000165 for the used ScintrexCG5#41224 gravimeter) and corrected for the instrumental drift as well as the effect of solid tides. The gravity variation of reference station 100 is not taken into account (Tab. 8, chapter 5). The gravity contribution of vertical displacement is not corrected (Tab. C6).

| Station | Date | $g_{2017}$ (µGal) | Date | $g_{2018}$ (µGal) | Date | $g_{2019}$ (µGal) |
|---|---|---|---|---|---|---|
| 100 | | 0 +/- 0 | 24/06/2018 | 0 +/- 1 | | 0 +/- 1 |
| 101 | 10/09/2017 | -407 +/- 4 | 07/07/2018 | -400 +/- 1 | 25/07/2019 | -423 +/- 5 |
| 102 | 10/09/2017 | -6115 +/- 5 | 07/07/2018 | -6115 +/- 1 | 23/07/2019 | -6104 +/- 8 |
| 103 | 10/09/2017 | -2177 +/- 4 | 11/07/2018 | -2179 +/- 2 | 25/07/2019 | -2187 +/- 1 |
| 104 | 10/09/2017 | -5976 +/- 5 | 11/07/2018 | -5974 +/- 3 | 25/07/2019 | -5991 +/- 1 |
| 105 | 07/09/2017 | -33450 +/- 1 | 08/07/2018 | -33448 +/- 3 | 25/07/2019 | -33457 +/- 2 |
| 106 | 07/09/2017 | -39220 +/- 2 | 08/07/2018 | -39219 +/- 3 | 25/07/2019 | -39219 +/- 4 |
| 107 | 07/09/2017 | -2055 +/- 1 | 18/07/2018 | -2059 +/- 1 | 23/07/2019 | -2066 +/- 6 |
| 108 | 07/09/2017 | -11206 +/- 2 | 07/07/2018 | -11220 +/- 10 | 24/07/2019 | -11248 +/- 10 |
| 109 | 07/09/2017 | 3978 +/- 1 | 08/07/2018 | 3982 +/- 4 | 24/07/2019 | 3979 +/- 2 |
| 110 | 07/09/2017 | 10151 +/- 2 | 08/07/2018 | 10155 +/- 6 | 24/07/2019 | 10155 +/- 3 |
| 111 | 09/09/2017 | -158 +/- 4 | 07/07/2018 | -159 +/- 4 | 25/07/2019 | -163 +/- 4 |
| 112 | 09/09/2017 | -2865 +/- 4 | 09/07/2018 | -2865 +/- 2 | 27/07/2019 | -2874 +/- 5 |
| 113 | 09/09/2017 | -7135 +/- 5 | x | x | x | x |
| 114 | 09/09/2017 | 758 +/- 5 | 09/07/2018 | 758 +/- 2 | 27/07/2019 | 752+/- 6 |
| 115 | 09/09/2017 | 7992 +/- 4 | 06/07/2018 | 7992 +/- 4 | 23/07/2019 | 7987 +/- 5 |
| 116 | 09/09/2017 | 18514 +/- 6 | 06/07/2018 | 18518 +/- 6 | 23/07/2019 | 18515 +/- 7 |
| 117 | 11/09/2017 | 2743 +/- 1 | 17/07/2018 | 2755 +/- 3 | 28/07/2019 | 2732 +/- 3 |
| 118 | 11/09/2017 | 935 +/- 1 | 17/07/2018 | 943 +/- 4 | 28/07/2019 | 930 +/- 4 |
| 119 | 11/09/2017 | -31335 +/- 1 | 28/06/2018 | -31327 +/- 4 | 27/07/2019 | -31339 +/- 4 |
| 120 | 11/09/2017 | -48549 +/- 1 | 28/06/2018 | -48545 +/- 6 | 27/07/2019 | -48561 +/- 5 |
| 121 | 12/09/2017 | 22100 +/- 2 | 17/07/2018 | 22092 +/- 4 | 28/07/2019 | 22092 +/- 3 |
| 122 | 12/09/2017 | 26814 +/- 2 | 17/07/2018 | 26803 +/- 5 | 28/07/2019 | 26804 +/- 4 |
| 123 | 12/09/2017 | 364 +/- 2 | 17/07/2018 | 359 +/- 2 | 28/07/2019 | 362 +/- 2 |
| 124 | 12/09/2017 | 3129 +/- 3 | 17/07/2018 | 3119 +/- 3 | 28/07/2019 | 3126 +/- 3 |
| 125 | 12/09/2017 | -5131 +/- 2 | 17/07/2018 | -5131 +/- 2 | 29/07/2019 | -5142 +/- 2 |
| 126 | 12/09/2017 | -6503 +/- 3 | 17/07/2018 | -6499 +/- 2 | 29/07/2019 | -6507 +/- 3 |

## C4) Vertical displacement

Drouin et al. (2020) studied vertical displacement from 2015 to 2019 at the Theistareykir geothermal field using the InSAR analysis. Figure C2 describes the values measured at gravity stations for the 2015-2017, 2015-2018 and 2015-2019 periods. Using the mean measured free-air vertical gradient given in Table C5, the gravity effect of vertical displacement is calculated (Tab. C6) and then corrected from the time-lapse microgravity data. Vertical displacement deduced by InSAR analysis at permanent stations is consistent with the continuous GPS measurements (Fig. C3).

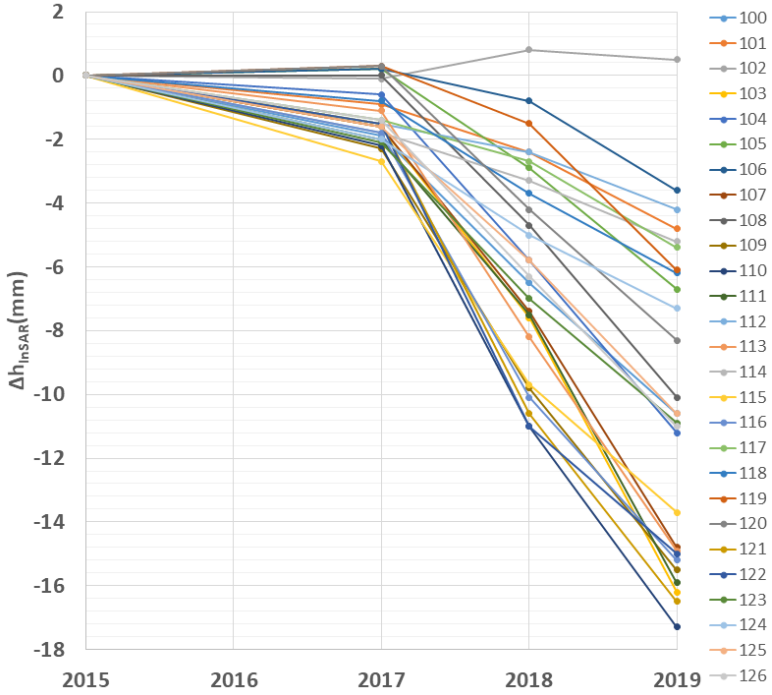


| | 2015-2017 [mm] | 2015-2018 [mm] | 2015-2019 [mm] |
|---|---|---|---|
| 100 | -1.9 | -6.5 | -10.6 |
| 101 | -0.9 | -2.4 | -4.8 |
| 102 | -0.1 | 0.8 | 0.5 |
| 103 | -1.6 | -7.6 | -16.2 |
| 104 | -0.6 | -5.8 | -11.2 |
| 105 | 0.2 | -2.9 | -6.7 |
| 106 | 0.2 | -0.8 | -3.6 |
| 107 | -1.6 | -7.4 | -14.8 |
| 108 | 0 | -4.7 | -10.1 |
| 109 | -2.3 | -9.8 | -15.5 |
| 110 | -2.2 | -11 | -17.3 |
| 111 | -2 | -7.5 | -15.9 |
| 112 | -1.5 | -2.4 | -4.2 |
| 113 | -1.1 | -8.2 | -14.9 |
| 114 | -1.8 | -3.3 | -5.2 |
| 115 | -2.7 | -9.7 | -13.7 |
| 116 | -1.8 | -10.1 | -15.2 |
| 117 | -1.4 | -2.7 | -5.4 |
| 118 | -0.8 | -3.7 | -6.2 |
| 119 | 0.3 | -1.5 | -6.1 |
| 120 | 0.3 | -4.2 | -8.3 |
| 121 | -1.5 | -10.6 | -16.5 |
| 122 | -1.5 | -11 | -15 |
| 123 | -2.1 | -7 | -10.9 |
| 124 | -2 | -5 | -7.3 |
| 125 | -1.6 | -5.8 | -10.6 |
| 126 | -1.4 | -6.3 | -11 |

**Figure C2.** Graph and table of vertical displacement $\Delta h_{InSAR}$ (mm) deduced from InSAR analysis in 2017, 2018 and 2019 with respect to 2015 at gravity stations.

**Table C5.** Measured free-air vertical gravity gradients at permanent stations SCGE, SCGW, GPXC and SCGR and at time-lapse reference station 100.

| Station | Gradient (µGal $m^{-1}$) | Mean gradient (µGal $m^{-1}$) |
|---|---|---|
| SCGE | -307 | -316 +/- 9 |
| SCGW | -319 | |
| GPXC | -330 | |
| 100 | -308 | |
| SCGR | -317 | x |

## Appendices

**Table C6.** Vertical displacement $\Delta h_{InSAR}$ (mm) and the gravity effect $\Delta g_h$ (μGal) for the 2017-2018, 2018-2019 and 2017-2019 periods at time-lapse gravity stations. The mean InSAR uncertainty is 2.5 mm $yr^{-1}$ (Drouin and Sigmundsson, 2019).

| Code | 2017-2018 | | 2018-2019 | | 2017-2019 | |
|---|---|---|---|---|---|---|
| | $\Delta h_{InSAR}$ (mm) | $\Delta g_h$ (μGal) | $\Delta h_{InSAR}$ (mm) | $\Delta g_h$ (μGal) | $\Delta h_{InSAR}$ (mm) | $\Delta g_h$ (μGal) |
| 100 | -4.6 | 1 | -4.1 | 1 | -8.7 | 3 |
| 101 | -1.5 | 0 | -2.4 | 1 | -3.9 | 1 |
| 102 | 0.9 | 0 | -0.3 | 0 | 0.6 | 0 |
| 103 | -6 | 2 | -8.6 | 3 | -14.6 | 5 |
| 104 | -5.2 | 2 | -5.4 | 2 | -10.6 | 3 |
| 105 | -3.1 | 1 | -3.8 | 1 | -6.9 | 2 |
| 106 | -1.0 | 0 | -2.8 | 1 | -3.8 | 1 |
| 107 | -5.8 | 2 | -7.4 | 2 | -13.2 | 4 |
| 108 | -4.7 | 1 | -5.4 | 2 | -10.1 | 3 |
| 109 | -7.5 | 2 | -5.7 | 2 | -13.2 | 4 |
| 110 | -8.8 | 3 | -6.3 | 2 | -15.1 | 5 |
| 111 | -5.5 | 2 | -8.4 | 3 | -13.9 | 4 |
| 112 | -0.9 | 0 | -1.8 | 1 | -2.7 | 1 |
| 113 | -7.1 | 2 | -6.7 | 2 | -13.8 | 4 |
| 114 | -1.5 | 0 | -1.9 | 1 | -3.4 | 1 |
| 115 | -7.0 | 2 | -4.0 | 1 | -11 | 3 |
| 116 | -8.3 | 3 | -5.1 | 2 | -13.4 | 4 |
| 117 | -1.3 | 0 | -2.7 | 1 | -4.0 | 1 |
| 118 | -2.9 | 1 | -2.5 | 1 | -5.4 | 2 |
| 119 | -1.8 | 1 | -4.6 | 1 | -6.4 | 2 |
| 120 | -4.5 | 1 | -4.1 | 1 | -8.6 | 3 |
| 121 | -9.1 | 3 | -5.9 | 2 | -15 | 5 |
| 122 | -9.5 | 3 | -4.0 | 1 | -13.5 | 4 |
| 123 | -4.9 | 2 | -3.9 | 1 | -8.8 | 3 |
| 124 | -3 | 1 | -2.3 | 1 | -5.3 | 2 |
| 125 | -4.2 | 1 | -4.8 | 2 | -9.0 | 3 |
| 126 | -4.9 | 2 | -4.7 | 1 | -9.6 | 3 |

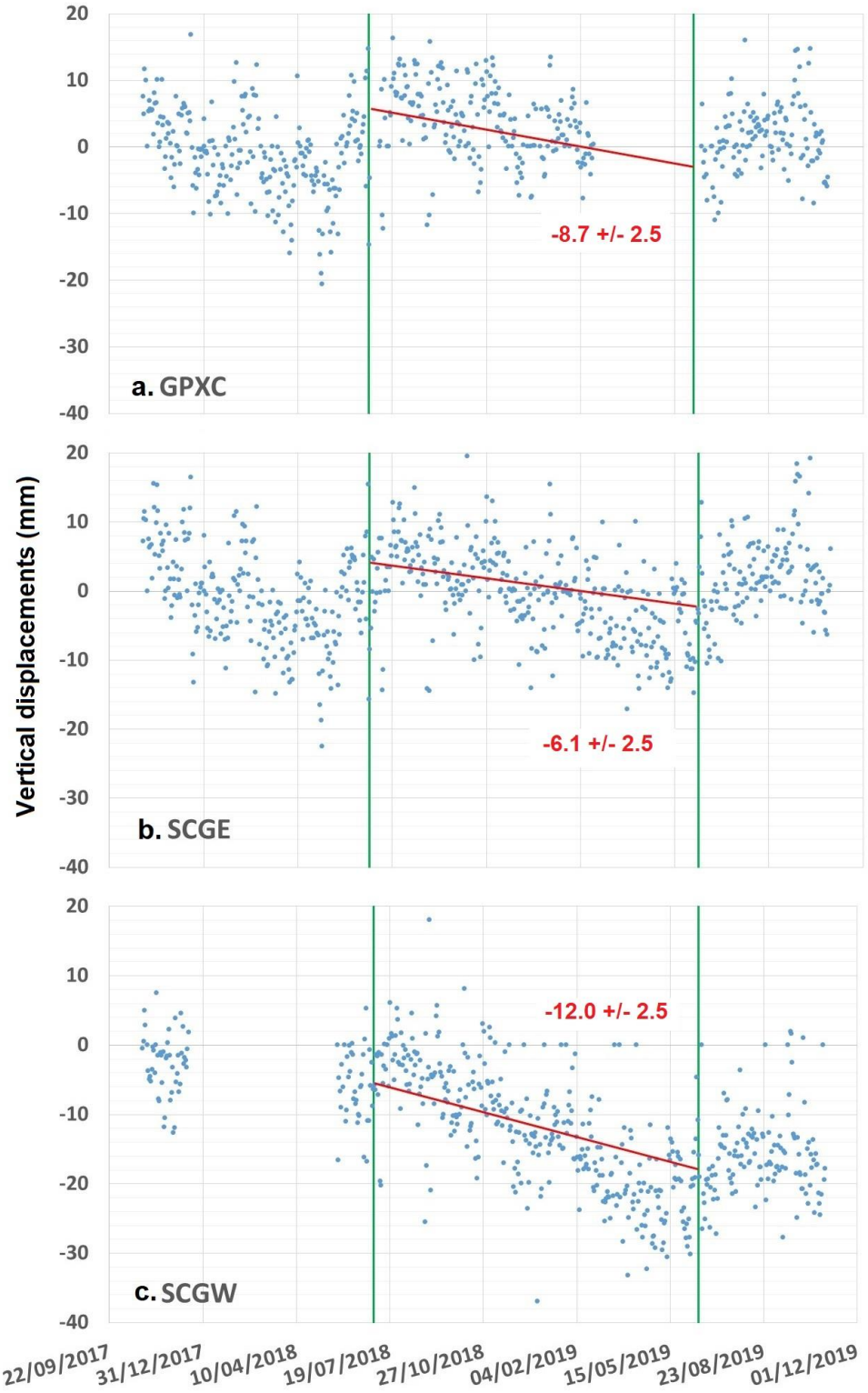


**Figure C3.** Temporal variations of vertical displacement (mm) measured continuously by GNSS at permanent gravity stations GPXC (a), SCGE (b) and SCGW (c). The green vertical lines show the dates of the 2018 and 2019 absolute gravity measurements. The vertical displacements deduced by InSAR analysis are indicated by red lines.

## C5) Inverse model

The gravity and vertical displacement observations at the Theistareykir geothermal field are small with respect to their uncertainties, which prevents to obtain a well-constrained model. Figures C4 and C5 show the measured and modelled gravity and vertical displacement using the single Mogi sphere model, respectively.

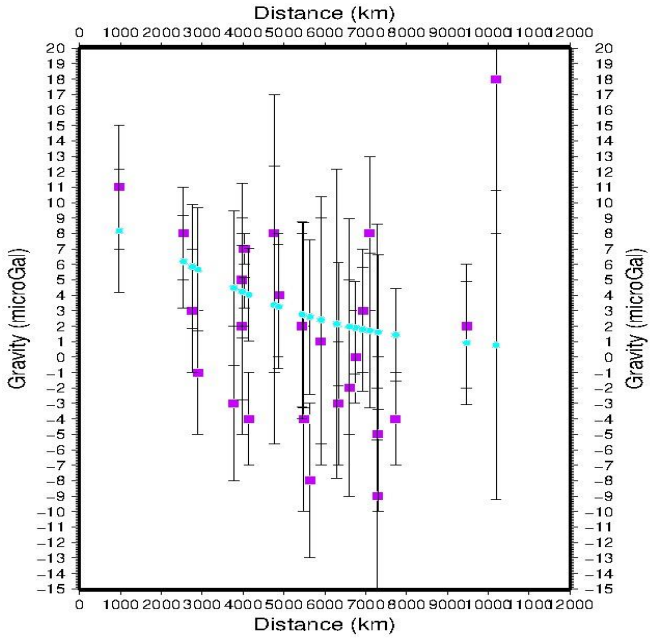


**Figure C4.** Modelled (blue) and measured (purple) gravity changes not corrected for the effect of vertical displacement at the Theistareykir geothermal field as a function of the distance of the Mogi sphere source.

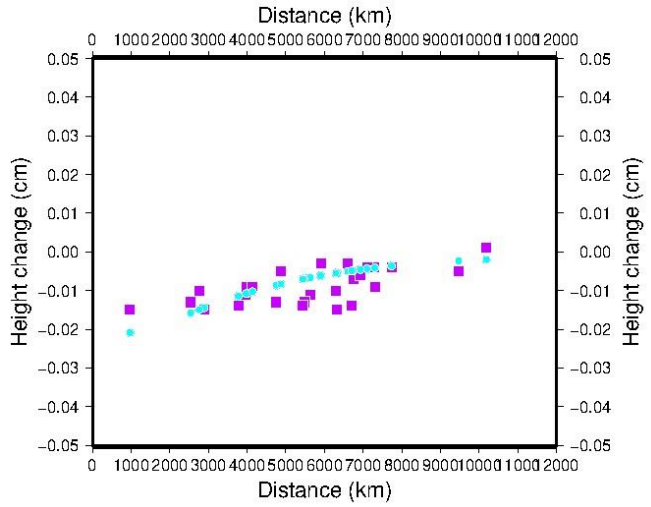


**Figure C5.** Modelled (blue) and measured (purple) vertical displacements at the Theistareykir geothermal field as a function of the distance of the Mogi sphere source. The mean uncertainty of the InSAR measurements is around 2.5 mm $yr^{-1}$.

## C6) Forward model

We apply a forward modelling using multiple Mogi spheres. The spheres are placed at the open-hole of each production well. They represent the real produced masses described in Table C7. Figure C6 shows the vertical displacements in function of the gravity double differences (not corrected for the effect of ground motion).

**Table C7.** Geothermal fluid produced masses (kt) for the 2017-2018 and 2017-2019 periods at the 13 production wells (Landsvirkjun, personal communication). The Mogi spheres are located at the open-hole at measured depth (Óskarsson, 2015; Egilson, 2019).

| Production well | Depth (m) | Mass (kt) 2017-2018 | Mass (kt) 2017-2019 |
|---|---|---|---|
| THG-01 | 1953 | 463.2 | 1094.0 |
| THG-03 | 2659 | 361.1 | 837.2 |
| THG-04 | 1870 | 1009.8 | 2233.6 |
| THG-05b | 2369 | 1872.0 | 4483.9 |
| THG-06 | 2456 | 384.9 | 881.4 |
| THG-07 | 2069 | 257.8 | 553.1 |
| THG-09 | 2194 | 83.8 | 307.2 |
| THG-12 | 2703 | 155.9 | 431.0 |
| THG-13 | 2498 | 256.9 | 772.8 |
| THG-15 | 2253 | 430.1 | 430.1 |
| THG-16 | 2693 | 210.2 | 461.8 |
| THG-17 | 2493 | 564.8 | 1605.0 |
| THG-18 | 2637 | 72.6 | 72.6 |
| Total | | 6123.1 | 14163.7 |

## C7) dg/dh plots

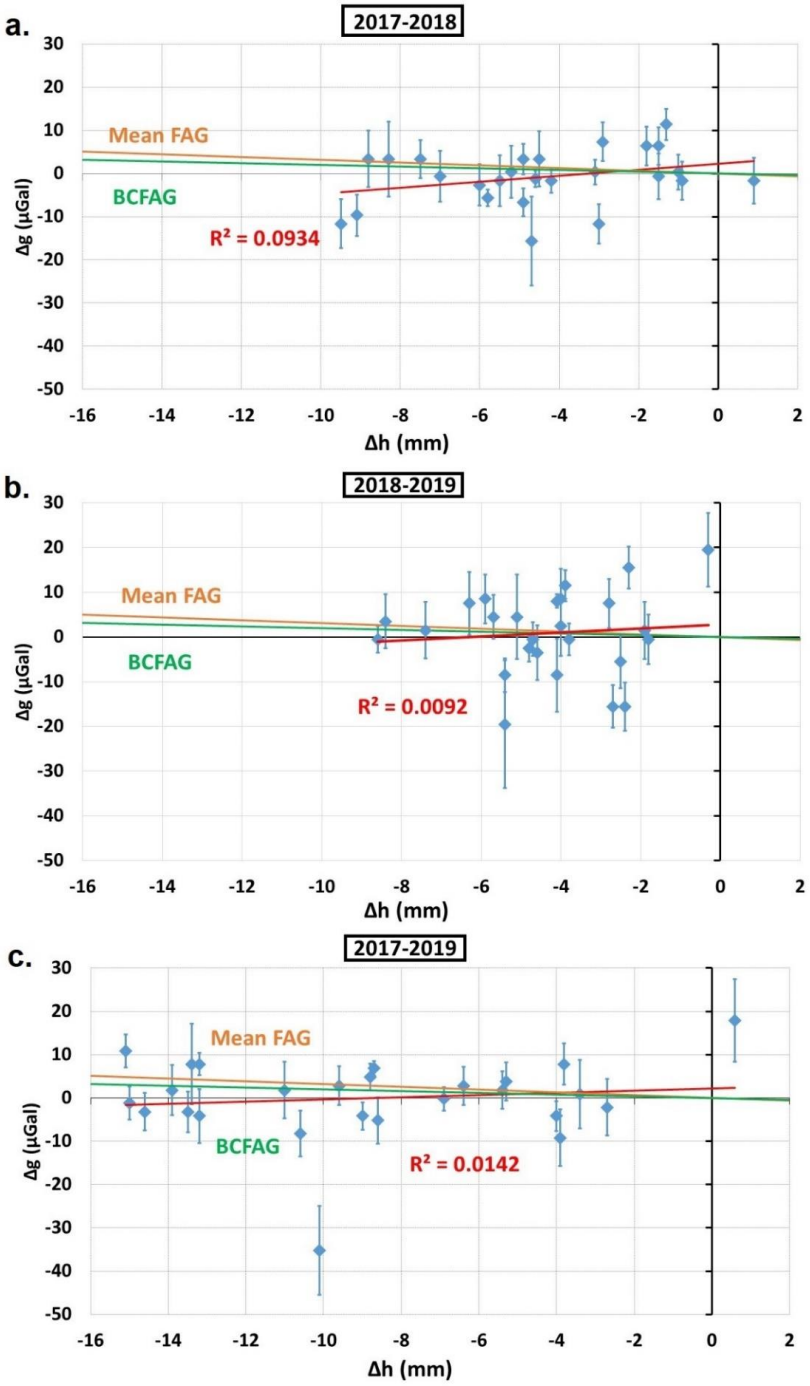


**Figure C6.** The gravity double differences Δg (μGal) as a function of vertical displacement Δh (mm) measured at the Theistareykir geothermal field for the 2017-2018 (a), 2018-2019 (b) and 2017-2019 (c) periods. The regression coefficients $R^2$ are 0.0934, 0.0092 and 0.0142, respectively. The mean measured free-air vertical gravity gradient FAG (Tab. C5) is drawn in orange; the Bouguer vertical gravity gradient BCFAG is shown in green. The mean InSAR uncertainty is 2.5 mm $yr^{-1}$.